INVESTIGATION OF THE ANTI-CORROSION PROPERTIES OF TRIVALENT CHROMIUM PROCESS COATINGS ON VARIOUS SURFACE PRETREATMENTS OF AEROSPACE ALUMINUM ALLOYS

By

Sarah McFall-Boegeman

A DISSERTATION

Submitted to
Michigan State University
in partial fulfillment of the requirements
for the degree of

Chemistry – Doctor of Philosophy

2021

ABSTRACT

INVESTIGATION OF THE ANTI-CORROSION PROPERTIES OF TRIVALENT CHROMIUM PROCESS COATINGS ON VARIOUS SURFACE PRETREATMENTS OF AEROSPACE ALUMINUM ALLOYS

By

Sarah McFall-Boegeman

The aerospace industry uses a variety of metals and alloys, primarily aluminum alloys, for the different structural components in aircraft including the fuselage, landing gear, tail fins, and the many other parts. As these components are metal based, the control and mitigation of corrosion in service is of paramount importance. The military and civilian aviation sectors spend considerable sums of money annually on corrosion prevention and maintenance. Components made with aluminum alloys are generally placed in service with a multilayer coating system to prevent corrosion. This coating system consist of a conversion coating, primer, and topcoat. The coating system can inhibit corrosion in multiple ways, but the general mechanism involves barrier layer protection that reduces contact of the environment with the underlying metal. Legacy conversion coatings and primers have chromate (Cr(VI)) as a component. While chromate is an excellent corrosion inhibitor, it is toxic and constitute a significant environmental hazard. There is a current technological need to (i) replace chromate conversion coatings and primers with non-chromate or zero-chrome coating systems and (ii) understand how to properly pretreat the aluminum alloys surfaces for application of such surface finishes. The trivalent chromium process (TCP) coating is the leading replacement non-chromate conversion coating and praseodymium- and new aluminum-based coatings are replacement primers being investigated. There is also a scientific need to better understand how to properly pretreat aluminum alloys in order to properly form conversion coatings and primers that effectively prevent environmental degradation and

corrosion. These surface pretreatments typically include abrasion and polishing, wet chemical cleaning, and deoxidation or desmutting.

In this dissertation project, fundamental research was conducted to better understand how surface pretreatments of aluminum alloys impact the formation of TCP conversion coatings and the mechanisms by which TCP conversion coatings inhibit electrochemical corrosion in laboratory measurements and during accelerated degradation testing. Research was also conducted to learn how effectively TCP coatings can seal porous anodic oxide coatings on aluminum alloys thereby improving the barrier properties and electrochemical corrosion resistance. The specific surface pretreatments investigated included laser cleaning and hyperpassivation of aluminum alloy AA2024-T3, in comparison with conventional wet chemical processing. Additionally, studies were performed to learn the mechanisms and effectiveness of TCP sealants for anodic coatings formed on this aluminum alloy during sulfuric acid (SA) and sulfuric acid/boric acid (SABA) anodization.

ACKNOWLEDGEMENTS

I would like to acknowledge the following for their support, guidance, and contributions during my time at Michigan State University.

Thanks to Professor Greg Swain, my advisor, for his continued efforts to teach and educate me in not only my research, but in the many other topics in analytical chemistry and life. Without his spirit of excitement in research, commitment to teaching and mentoring, and wisdom this dissertation would not have been possible.

I would like to thank my committee members Dr. Gary Blanchard, Dr. Liangliang Sun, and Dr. Andre Lee. Without your continued support and help I would not have been able to show much of this work to the scientific community. Thank you for motivating me to continue to learn the many areas of chemistry that are around me and to give me insight into the materials science field.

Thank you to all those current and past in Dr. Swain's research group. Jack Walton, Dr. Shruthi Kumar Raj, Dr. Romana Jarošová, Skye Henderson, and Fatemeh Parvis your friendship and help with my work will never be forgotten. Thank you all for the memories we have shared in the lab.

Finally, I would like to thank my friends and family for their support and understanding in my desire to pursue a Ph.D. Thank you to my friends Katarina Keel, Grace Hubble, Emily Dzurka, and the many others for all support during the tough times. Thank you to my mom and dad for understanding that these past years have not been easy and to rearrange our family events so I could attend. Thank you to my sister and brother-in-law for always being up for a chat and not knowing how much those helped! Thank you to my husband, Hunter, for helping me see my

work through and supporting me while also attending graduate school. You showed me the way in some parts of the program, but also gave me the love and support I needed.

Thank you to the Office of Naval Research, Honeywell, Adapt Laser, and Henkel Technologies for providing financial support and surface preparations to conduct this work.

TABLE OF CONTENTS

LIST OF TABLES

LIST OF FIGURES

KEY TO ABBREVIATIONS

AA	Aluminum Alloy
TCP	Trivalent Chrome Process
CCC	Chromate Conversion Coating
DI	Deionized
SEM	Scanning Electron Microscopy
EDX or EDS	Energy Dispersive X-ray Spectroscopy
NSS	Neutral Salt Spray
RTU	Ready to Use
SA	Sulfuric Acid
SABA	Sulfuric Acid/Boric Acid
FIB	Focused Ion Beam
HW	Hot Water
NA	Nickel Acetate
GD-OES	Glow Discharge Optical Emission Spectrometry

CHAPTER 1. INTRODUCTION

1.1 ALUMINUM

Aluminum is found to be the second most abundant metallic element on earth. Aluminum has a low density, is lightweight, and has an affinity to oxygen which gives it a natural protective oxide layer.[1-6] Aluminum on its own is not necessarily the best to use in each of these fields. Aluminum is highly reactive and easily is corroded in the environment. The native oxide that forms on aluminum does provide some self-healing properties, however, by alloying the aluminum with other metals the aluminum bulk mixed with the other metals provides many improved characteristics, such as improved corrosion resistance, that makes it ideal in these industries.

1.2 ALUMINUM ALLOYS

Aluminum is used in many areas such as automotive, ship structures, weapons, and aerospace to name a few.[1, 2, 7-11] Aluminum alloys are formed from the bulk aluminum being mixed with other metals through a forging process. The metals that are mixed with the aluminum give rise to new properties that can enhance that of the bulk such as corrosion resistance, strength, and light weight.[1, 10, 11] These aspects make the alloys of aluminum usable in many different areas of ship structure, automotive or aerospace industries. Aluminum alloys are separated into "cast aluminum" and "Wrought aluminum". These two classes of aluminum alloys are prepared by molten process (mix with other elemental metals in appropriate proportion). The cast alloys are poured into a mold of the shape of the products, while wrought alloys are poured to form ingots. These ingots are then mechanically worked (via forging, extrusion, drawing, rolling) to form desired products. Often, these

mechanically worked aluminum alloys have better engineering mechanical performance over the cast aluminum alloys as well as for sheet applications.

The properties of the aluminum alloys depend on the distribution of second phase particles, microstructure such as grain structure, and weight ratio of the alloying elements. Mechanical properties of the alloy should also be considered along with the size, shape, and distribution of the second phase particles. The Aluminum Association uses four number based on the composition with the first value being that of the principal alloying element.[12] The second digit is the designation of any modifications made to the alloy and the third and fourth digits are used to identify the alloy within the series. The different alloy families are listed in Table 1.1 with their principal alloying element.[12]

Table 1.1. Classification of Aluminum Alloys and its Principal Alloying Element

4 Digit Alloy Designation Type	Principal Alloying Element
1xxx	Pure Aluminum
2xxx	Cu
3xxx	Mn
4xxx	Si
5xxx	Mg
6xxx	Mg and Si
7xxx	Zn
8xxx	Ti, Li and/or Fe

The International Alloy Designation System also places the temper nomenclature at the end of the 4 digits to identify the type of heat treatment, if any, that the alloy was subjected

to. The major temper designations are F for fabricated, O is annealed, H is strain hardened, W solution heat treated, and T is thermally treated. Depending on the temper the digits that follow it will have different meanings.[12] In this work the thermally treated temper is used and as such those are the digits that will be explained herein. There are 10 different designations associated with the thermally treated temper and they are listed in Table 1.2[12] with the basic treatment for each designation.

Table 1.2. T Tempers and the Specific Sequences of Basic Treatments

T1	Cooled from and elevated temp., shaping process, and naturally aged
T2	Cooled from an elevated temp., shaping process, cold worked, and naturally aged
T3	Solution heat treated, cold worked, and naturally aged
T4	Solution heat treated and naturally aged
T5	Cooled from an elevated temp., shaping process, and artificially aged
T6	Solution heat treated and artificially aged
T7	Solution heat treated and over aged
T8	Solution heat treated, cold worked, and artificially aged
T9	Solution heat treated, artificially aged, then cold worked
T10	Cooled from an elevated temp., shaping process, cold worked, and artificially aged

In the aerospace sector many alloys can be found, however, the 2xxx and 7xxx series are found more widely due to the high strength during the manufacturing of the stressed aircraft components.[13] The overall goal of adding the alloying elements is to produce aluminum alloys that provide added benefits to the finished product, but some alloying elements can cause a reduction in corrosion resistance and be more susceptible to different corrosion attacks.[10, 11]

1.3 CORROSION

Corrosion is an electrochemical process that degrades materials. The electrochemical reaction takes place at the interface of the metallic surface and the electrolyte.[5, 14-17] Corrosion under open circuit conditions occurs at a rate that is determined by the equilibrium of the anodic

and cathodic reactions taking place at the interface. The anodic reaction is the oxidation of the metal and results in the release of electrons. The cathodic reaction involves the reduction of soluble redox species the electrolyte, O_2 or H^+.[15, 16] The reactions that are taking place on the aluminum alloy are[10, 11, 16-22]

$$Al \rightarrow Al^{3+} + 3e^- \quad (1)$$

$$O_2 + 2H_2O + 4e^- \rightarrow 4OH^- \quad (2)$$

Aluminum alloys are often used in the aerospace industry due to their high strength to weight ratio.[14, 15, 23-25] The aluminum alloy AA2024-T3 is alloyed with copper, iron, and magnesium. These alloys leave the substrate susceptible to corrosion because of the presence of intermetallic particles.[26] The particles can either be large with varying amounts of the different alloyed metals or small and circular and be comprised of mostly copper.[26] Copper IMPs are cathodic to the aluminum substrate and act as the cathode in the electrochemical cell.

Corrosion occurs along the aluminum substrate surface where electrons can easily flow and there is contact with the surrounding electrolyte. The above equations (1 & 2) show the anodic and cathodic reactions that take place along the substrate surface.[20] These reactions occur at an equal rate in the given electrolyte solution. Potentiostatic measurements are commonly employed when investigating corrosion. The current is measured and is done so on a logarithmic scale due to the wide range of currents getting measured (can be around 6 orders of magnitude differences).[17] The rate of the reaction can be measured by an open circuit potential (OCP) measurement where the potential is monitored over time when the specimen is subjected to the electrolyte. The OCP measurement will show the equivalent potential, E_{Corr}, of the reaction. To know the rate of corrosion these potential vs. current plots can be used.[27] The extrapolation of the anodic and cathodic currents from large overpotentials to the potential

of equilibrium, E_{corr}. This will give a point of intersection at the E_{corr} and can be used to find the corrosion current, I_{corr}. The corrosion current can then be used to determine the rate of corrosion for the specific metal.[27]

The best way to inhibit corrosion would be to reduce the rate of the oxidation or reduction reaction or both. To do this either the aluminum anode needs to be removed, the site of the reaction (the cathode which is typically an intermetallic particle) needs to be removed, the cathodic reaction needs to be mitigated through the absence of oxygen, or the pathway of the electrons needs to be blocked. The intermetallic particles along the surface are treated with a deoxidizing agent which helps to remove not only the oxide layer that is inherent to the aluminum substrate but also some of the intermetallic particles that would be the site of the corrosion to take place. This does not remove all the intermetallic particles along the surface and so the anode and cathode will continue to be present. The electrons would still be able to flow from the anode to the cathode through direct contact. In the lab it would be possible to de-aerate the solution, but in actual practice this would not be feasible. The only remaining option to reduce the rate of the oxidation, reduction or both reactions would be to block the ionic pathway between the substrate and the electrolyte. To do this a barrier layer would need to be applied to the aluminum substrate. This will be explained in greater detail below.

Many industries have come to realize that proper corrosion management can reduce the costs of corrosion over the lifetime of what is being employed. Corrosion that is not properly managed becomes a major issue. The aerospace industry uses aluminum alloys for most of the plane due to the high strength to weight ratio. The cost of corrosion control and mitigation in the aerospace industry in 2016 was $30 billion dollars.[28] Unfortunately corrosion prevention is not always successful as with the case of Aloha Airlines Flight 243, which experienced a

fuselage displacement mid-flight. The entire area surrounding first class was able to see the sky above them while at an altitude of 24,000 feet.[29] The issue that is present is that the current coating systems need to be replaced with a greener alternative. The alternative coating needs to exhibit equivalent or improved performance.

Aluminum is susceptible to corrosion due to its place in the electromotive force series which places the standard reduction potentials in order in accordance with the normal hydrogen electrode (NHE).[30] Corrosion of aluminum alloys is a bit different than just the pure aluminum. In an aluminum alloy there are elements mixed with the aluminum. Precipitates can form and that can cause galvanic coupling of the elements and thus galvanic corrosion processes take place. The process is simplified in Figure 1. The copper intermetallic particle acts as the cathodic site where corrosion begins to form around it in the aluminum bulk. Electrons can transfer from the aluminum oxidation sites to the copper intermetallic. At the copper intermetallic oxygen reduction and hydrogen reduction take place using the electrons from the aluminum oxidation reactions.

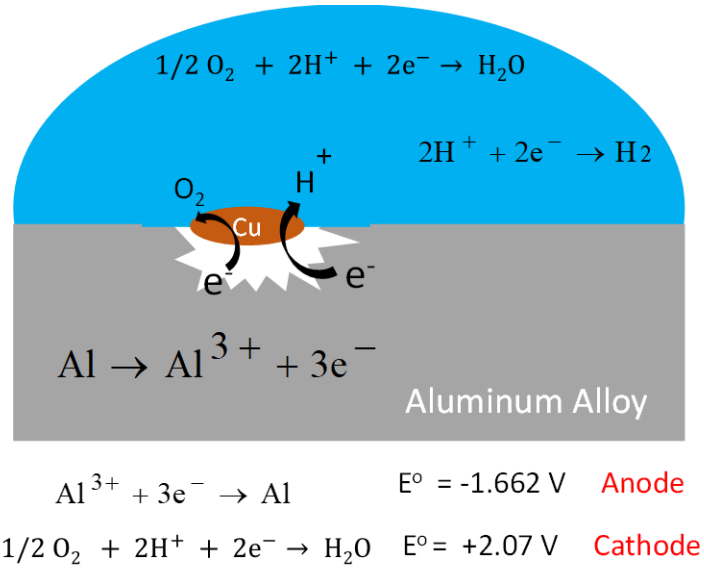

Figure 1.1. Schematic of galvanic corrosion electrochemical reactions that take place on an aluminum alloy.

Galvanic corrosion is not the only type of corrosion that takes place on an alloy. Some of the other forms of corrosion that can be found on an aluminum alloy are pitting corrosion, crevice corrosion, and intergranular corrosion.[31] There are four main building blocks that are needed for corrosion to take place 1) the anode, 2) the cathode, 3) metallic pathway, and 4) an ionic pathway. To inhibit corrosion 1 of these 4 must be removed. The aluminum alloy inherently has 1-3 present due to the intermetallic particles that are present. To inhibit corrosion the ionic pathway, or the ability of the electrolyte to interact with the alloy surface needs to be blocked. This is done in the aerospace industry by applying a layered coating system. This provides a physical barrier to the external electrolyte and retards the electrochemical reactions that can take place at the surface of the alloy.

1.4 COATING SYSTEMS

For the barrier layer protection, the aerospace industry has employed a multi-layered coating system. This includes a conversion coating or surface pretreatment, a primer layer, and a topcoat. The conversion coating can be applied by immersion, brush, spray, or a wipe-on application.[32] This layer is applied for corrosion prevention and to enhance the adhesion of the primer layer. The primer layer is typically an epoxy-based polymer. This allows for a strong bond/adhesion to the aluminum and gives another layer of protection and adds to the corrosion resistance. The final layer, the top coat, acts as the first order of protection for the aluminum surface.[32] The top coat is a paint layer that is exposed to the outside atmosphere/electrolyte.[32] Each of these layers adds to the corrosion resistance of the underlying alloy by providing multiple barrier layers that would need to be penetrated to reach the alloy.

Historically the conversion coating layer is a chromate conversion coating (CCC). These coatings have a Cr (VI) base that has many properties that are beneficial when trying to inhibit

corrosion. The three main ways the CCC inhibits corrosion are 1) through blocking active pores and defects via a Cr (III) film that precipitates out from the coating[33], 2) the CCC provides an increase in the electrical resistance by forming a barrier layer on the surface of the alloy[34], and 3) there is dynamic repair of new cracks and defects in the protective film[35]. The third reason means that the Cr (VI) is used because it can self-heal the Cr (VI) barrier layer. This comes from the migration of the Cr (VI) species in the form of CrO_4^{2-} to sites that had been damaged.[14] Because there is both Cr (III) and Cr (VI) present there is a mixed oxide that can form. It is in this mixed oxide that when covalently bound to the chromium (III) hydroxyl group there then can be storage of the Cr (VI).[14] The release of the Cr (VI) is pH dependent and damage sites cause a change in the local pH. The Cr (VI) is released via the equilibrium reaction[14]:

$$Cr^{III} - OH\ (s) + \ Cr^{VI}O_4^{2-}(aq) + H^+(aq) \ \rightleftarrows Cr^{III} - O - Cr^{VI}O_3^-\ (s) + \ H_2O \qquad (3)$$

The release chemistry was studied on multiple alloys and was found to be the same chemistry.[14]

To find out how this self-healing process proceeded McCreery and colleagues used Raman spectroscopy to find how it worked and how far the Cr (VI) species could migrate.[36] The study looked at CCC coated species placed 1.8 mm away from that of an uncoated species. There was an electrolyte solution between them that would induce corrosion. After 96 hours the uncoated specimen had minor pitting along the surface, but the polishing marks were still seen.[36] The CCC coated species also had no pitting along the surface. The control was set up in the same way, but with 2 uncoated specimens together. The uncoated control was completely corroded and no original surface could be seen.[36] It was found that the Cr (VI) had migrated through the solution to the uncoated specimen and had formed a thin film along the surface. XPS found Cr and F, both components of the CCC bath, in the thin film on the uncoated

surface.[36] Raman spectroscopy found the Cr on the uncoated specimen to be Cr (VI), but that does not mean Cr (III) wasn't present. The instrument is not very sensitive to the presence of Cr (III), but is highly sensitive to Cr (VI).[36]

Chromium (VI) was used due to the corrosion inhibition it provided and for the self-healing aspect that was also afforded, however, Cr (VI) is toxic to humans and is a known carcinogen. This makes it extremely dangerous for the workers and the waste must be disposed of using extreme caution. Workers that inhale or possibly ingest water-soluble Cr (VI) have a higher risk of developing respiratory cancer. The Cr (VI) will, however, affect all organs and leave them susceptible to its toxic or carcinogenic effects.[37] The way the Cr (VI) causes toxic or carcinogenic effects is via structurally resembling phosphate groups. Cr (VI) is actively transported into cells and undergoes reduction reactions until the Cr (III) stable state is reached. The Cr (III) then acts as an important mediator for the toxic and carcinogenic effects.[37] Cr (III) on its own will not cause these same effects. This is because the Cr (III) form is not easily absorbed by the body, the cells permeability is poor.[37] This makes Cr (III) relatively non-toxic when it does not come from the reduction process inside the cells.[37] The waste that gets generated from a Cr (VI) source is commonly a strong oxidizer and needs to be disposed of in a more regulated way. The waste is considered toxic waste if in quantities equal to or greater than 5 mg/L.[38]

Due to the toxic and carcinogenic effects of the CCC coatings, an alternative method needs to be found that can replace the CCC. There are many viable options that are being investigated due to the ban that is being imposed on Cr (VI) coated metals in 2019.[39] Some special applications have been given extensions to 2024 or 2026, but after these dates Cr (VI) will no longer be in use by plating companies.[39] Some of the alternatives to the chromate conversion

coatings are using other hypervalent transition metal oxoanions, refractive metal oxide precursors, and rare earth metals.[40] The hypervalent transition metal oxoanions refers to those that are in the highest valence state of the oxoanion. Mn, Tc, Mo, and V have all be studied and have been found to act similarly to Cr (VI). These metals reduce down to lower valence states to form insoluble oxides like the Cr (VI) based coatings do.[40] The refractive metal oxides precursors refers to metals such as Nb, Hf, Ti, Zr, and Ta. These metals all form stable oxides in the highest valence state. It has been shown that thin zirconium-based coatings can rapidly form a very thin self-limiting layer. Some of these can also form sol-gels via stable dispersions of these species from the alkoxides of them.[40] The rare earth metals have been looked into in the form of conversion coatings, but also as inhibitors in the primer layer. These rare earth metals precipitate to form a protective oxide film at active cathode sites. They can also work as a sealant for oxide layers.[40] These coatings were compared to each other by the Army Research Laboratory to find out which would be best to replace the Cr (VI) coatings. It was found that each of these had either undercutting, more damage to the underlying substrate, or damage in the scribed area that was much greater than the Cr (VI) coatings.[41]

1.5 TRIVALENT CHROMIUM PROCESS COATINGS

The one that is leading the way in replacing the CCC coating is a trivalent chromium process (TCP). The Army Research Laboratory undertook a large study to investigate all new techniques that could viably replace the CCC coatings. Coupons were tested after being coated with one of many (8) coating systems via accelerated degradation testing. The results showed that the TCP coating protected the alloy better than other coatings and in some cases even exceeded the performance of the CCC coating.[41] It was determined that the TCP coupons

showed minimal damage around the scribed region and is one of or near the leaders for chromium-free coating systems to replace the CCC coating.[41]

A TCP coating is a non-chromate conversion coating but does contain Cr (III). The coating bath also contains potassium hexafluorozirconate (K_2ZrF_6), chromium sulfate ($Cr_2(SO_4)_3$), and an acid (HF).[42] It is a zirconium-based coating and was first produced by NAVAIR.[42] The TCP conversion coating bath has a pH of 3.8-4 and forms a thin barrier layer along the surface (~100 nm thick).[42]

The TCP forms a biphasic barrier layer through an initial interfacial pH change and precipitation. The initiation of the TCP coating formation begins by attack of the alloy surface by hydrogen and fluoride ions from the bath.[42]

$$Al_2O_3 + 6HF \rightleftharpoons 2AlF_3 + 3H_2O \quad (4)$$

$$Al + 6HF + 3H^+ \rightleftharpoons AlF_6^{3+} + 3H_2 \quad (5)$$

This attack of the surface results in the dissolution of the passivating oxide layer that is intrinsic to the metal surface. This will expose the bare metal allowing cathodic reactions to ensue.

$$Al + 6F^- \longrightarrow AlF_6^{3-} + 3e^- \quad (6)$$

$$O_2 + 2H_2O + 4e^- \longrightarrow 4OH^- \quad (2)$$

$$2H^+ + 2e^- \longrightarrow H_2 \quad (7)$$

This will increase the interfacial pH which drives the process forming a hydrated zirconia layer. Because of the initial attack of the surface there is a K_xAlF_{3+x} layer that forms along the alloy surface. The hexafluorozirconate in the bath begins to hydrate and a hydrated zirconia layer precipitates onto the K_xAlF_{3+x} layer.[42]

$$ZrF_6^{2-} + 4OH^- \longrightarrow ZrO_2 \cdot 2H_2O + 6F^- \quad (8)$$

$$Cr^{3+} + 8OH^- + 3e^- \longrightarrow Cr(OH)_3 + 5OH^- \quad (9)$$

This forms the biphasic layer in Figure 1.2 and is stable with time and appears to have some hydrated channels or defects present. These hydrated channels or defects allow ions and oxygen transport to localized regions of the underlying metal. The TCP coating does provide corrosion protection even though there are these channels to the underlying metal. There are reports of the corrosion resistance being increased by 10-100x.[42] This barrier layer protection eliminates the ionic pathway needed for the galvanic corrosion to take place and inhibits the electrochemical reactions from taking place at the alloy surface.

Figure 1.2. Schematic of the biphasic TCP coating structure formed on an aluminum alloy.

1.6 ANODIZING

Anodizing aluminum is the controlled growth of aluminum oxide on the surface of the substrate through electrochemical reactions. Anodizing the aluminum alloy gives a thicker layer (~5-10 µm) above the underlying substrate to protect from corrosion.[43] This layer is a porous oxide layer that is sealed before getting put into use and the formation is modeled in Figure 1.3.[43-50]

To form the pores in Figure 1.3, the first step is applying a positive potential to the aluminum alloy to attract the anions in the anodizing electrolyte to the surface of the aluminum. The anions then discharge a loss of one or more electrons at the aluminum anode. While at the

surface the dissolved oxygen through chemisorption or absorption are restructured and a contiguous oxide film is formed. This is called the formation of the barrier layer. With further voltage applied the pores will form in the following way. The applied voltage to the aluminum will cause more anions to move toward the aluminum and the anions will strike the barrier layer surface and expel an electron. Those electrons will build up along the dielectric layer acting barrier layer so there will be no transition of the ions through the barrier layer. This will then lead to the buildup of the negative charges until they accumulate and repel each other enough to form circular patterns across the substrate in the anodizing electrolyte. This comes about due to coulombs repulsion of the negatively charged ions along the barrier layer until an equilibrium separation is achieved. The repulsion will continue until the circular shapes formed rearrange into highly ordered hexagons along the surface of the barrier layer. This new rearrangement produces a vector that acts normally downward through the barrier layer towards the aluminum substrate due to the positive charge applied to the aluminum substrate. With this new attractive force, Al^{3+} ions are attracted to the center of the hexagons from the bulk materials and the ion moves from the substrate through the barrier layer to the center of the negative charges. This is then the nucleation point for the formation of pores. This nucleation will continue until the charges are balanced and a net positive is formed, which will then attract the electrolyte anions and the process will repeat. Through the repetition of the attraction and repulsion pores will grow upwards until the voltages are no longer applied to the substrate.[23, 51-53] Depending on the electrolyte there can be more or less incorporation of the electrolyte in the oxide layer and thus different thickness ranges and densities can be achieved.[51]

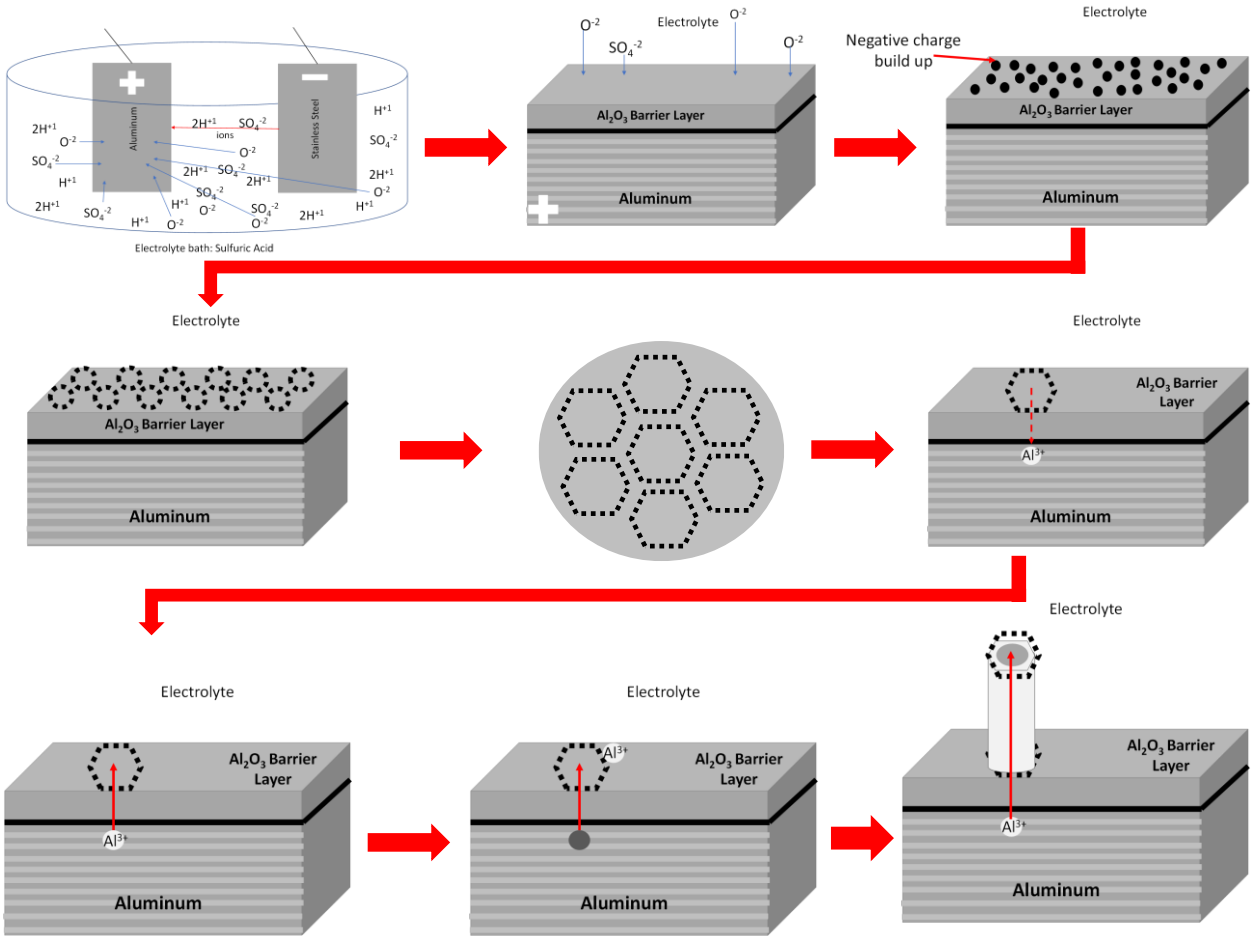

Figure 1.3. Schematic of the formation of pores for the porous oxide. One pore is demonstrated, but pores would form all along the surface in the same manner.

Anodizing the surface has some highly beneficial qualities but is limited in where it can be applied along the aircraft. Anodizing the surface is beneficial because it will not decompose and, is stable over long periods of time. This durability comes from the oxide being covalently bound to the underlying substrate.[54]

These benefits outweigh the limitations in some areas of the aircraft, such as the landing gears and flaps on the wings, however, the limitations of anodizing make it so it cannot be applied over the entire aircraft. These limitations include, but are not limited to, low thermal conductivity (cracks can form above 80˚C and the mechanical strength of the oxide is not as

strong as the substrate below due to the density of the oxide layer.[50, 55] These, among others, are the reasons that anodizing can't be used on all aluminum alloys.

Anodizing the aluminum is a surface pretreatment that is currently used and sealed by Cr (VI) containing sealants or by hot water or nickel acetate.[45, 47-49] Sulfuric acid, and others, have been found to be suitable replacements to the formation of the anodic oxide layers on aluminum alloys.[46] The sulfuric acid anodizing technique produces columnar pores and at the base of the pores lies a dense barrier layer at the oxide/substrate interface.[52, 53, 56, 57]

These oxide layers have open pores that stretch down to the base and to help prevent damage the pores are sealed typically with hot water hydrothermal sealing or a nickel acetate solution.[58] These processes, while effective, do have drawbacks and thus an alternative to these is needed to seal the porous oxide layer.

The Cr (VI) sealants typically have provided more protection in the past due to the self-healing process the Cr (VI) can undergo.[44] Nickel acetate and hot water have been used as an alternative to the toxic Cr (VI) sealant, but do not provide protection in the same way as the Cr (VI) seal does. The TCP coating could be used as a sealant for the porous oxide layer,[50] but more work needs to be done to understand the mechanism by which a TCP conversion coating seals the anodized aluminum alloys.

1.7 LASER SURFACE PRETREATMENTS

There are four general categories of laser-based material processing used industrially: (i) laser machining (cutting and drilling) that involves removing material to shape a workpiece[59, 60], (ii) laser texturing to introduce patterns into a surface that alter in beneficial ways wettability and coating or bonded component adhesion[61, 62], (iii) laser melting in 3D printing that utilizes a high power density light source to melt and fuse metallic powders producing a shaped

component[63, 64], and (iv) laser cleaning for coating or contaminant removal and surface cleaning.[65-73] Laser cleaning eliminates the need for abrasives and wet chemical processing, and their associated waste streams. The process can be used to remove contaminants, oxide layers, and coating systems from small areas, irregular surfaces, and hard-to-reach areas on aircraft. Hand-held laser systems can remove coatings and clean aerospace materials, including aluminum, steel, and other metals, without causing unacceptable damage to or alteration of the mechanical strength of the substrate.[65, 69, 73] Importantly, laser treatment, if performed properly, does not introduce pitting and pore formation in the alloy as do some chemical treatments.[63, 65, 66, 68-71, 73]

Laser cleaning involves the use of a high power, pulsed (nanosecond) light source that is rastered across a surface point to point. Key process parameters are the wavelength, pulse spot size and spacing, pulse frequency (kHz), pulse duration (nsec), pulse power (MW/cm^2), and fluence (J/cm^2). The cleaning mechanism generally involves surface heating and ablation.[61, 62, 70, 71, 73-75] If the energy supplied is greater than the ablation threshold, the material will undergo sublimation or vaporization. Oxides have an ablation threshold well below that of most base metals. Hence, one can adjust the laser parameters so that the oxide is removed without damaging the metal. The wavelength of the source (1064 nm) and the absorption properties of the material are key factors in how well the ablation proceeds. Materials with high absorption will be removed easier than materials that do not absorb the laser light. At low fluence, energy is absorbed and melting of the surface can occur, which may induce surface alloying and or reduce the exposure of second-phase particles due to melting and cooling of the surrounding aluminum matrix around and over a particle. At higher fluence, athermal processes begin to be important, and ejection of material via formation of a hot, dense plasma is observed. Oxides

absorb the laser light and are evaporated. Additionally, the interaction of the laser beam with the surface may generate significant thermal effects to induce follow-up thermal oxidation or even some near-surface melting.[66, 67, 69, 76, 77] The heating of the surface in air results in the reformation of an oxide layer that is thicker and perhaps less defective than the native oxide that forms in air at room temperature.[73] Importantly, the laser cleaning can prepare and activate a surface for the application of a coating.

1.8 MOTIVATIONS FOR STUDY

Presently, there is much information that can be found in the literature regarding the formation and use of TCP coating on various aluminum alloys to enhance corrosion resistance. These coatings are excellent alternatives to the legacy chromium (VI) conversion coatings as they are comparable in many ways. The surfaces that these TCP coatings have been applied to are generally solution or wet chemical processes that use harsh chemicals that are toxic and costly to dispose of. The TCP coatings provide excellent protection, little is known about the TCP formation and protection on other surface pretreatments such as anodized layers and laser cleaned surfaces.

Therefore, the overall goals of this research were two-fold:

(i). To gain a deeper understanding of how surface pretreatment of aluminum alloys affects the formation, adhesion and corrosion protection offered by TCP conversion coatings through detailed studies of traditional solution processed and laser pretreated surfaces and,

(ii) To understand how TCP conversion coatings form and seal anodic coatings on aluminum alloys formed by anodization in sulfuric acid (SA) and sulfuric/boric acid (SABA).

Pretreated and conversion-coated alloys were characterized by a variety of electrochemical methods to better understand the coatings impact on the aluminum oxidation and dissolved

oxygen reduction reaction kinetics (i.e., corrosion rate). Scanning electron microscopy and energy dispersive x-ray analysis were used to examine the pretreated surface and coated surface texture and elemental composition. Digital optical microscopy and scanning optical profilometry were used to quantify the pretreated surface and coated surface texture (roughness, feature height and feature dimensions). Finally, accelerated degradation testing in a neutral salt spray (1-14 days) was used to determine how the corrosion resistance of the coated alloys compared with what was predicted from the electrochemical measurements. Overall, the research provides new insights on the effectiveness of laser cleaning and hyperpassivation as surface pretreatments for non-chromate conversion coatings and the effectiveness and mechanisms by which TCP seals anodic coatings on aluminum alloys.

REFERENCES

REFERENCES

1. Davis, J. R.; Associates, *ASM International. Handbook Committee, Aluminum and Aluminum Alloys*. 1993.

2. Suib, S. L.; La Scala, J.; Nickerson, W.; Fowler, A.; Zaki, N., Determination of hexavalent chromium in NAVAIR trivalent chromium process (TCP) coatings and process solutions. *Metal Finishing* **2009,** *107* (2), 28-34.

3. Dong, X.; Wang, P.; Argekar, S.; Schaefer, D. W., Structure and Composition of Trivalent Chromium Process (TCP) Films on Al Alloy. *Langmuir* **2010,** *26* (13), 10833-10841.

4. Guo, Y.; Frankel, G. S., Active Corrosion Inhibition of AA2024-T3 by Trivalent Chrome Process Treatment. *Corrosion* **2012,** *68* (4), 045002-1-045002-10.

5. Guo, Y.; Frankel, G. S., Characterization of trivalent chromium process coating on AA2024-T3. *Surface and Coatings Technology* **2012,** *206* (19), 3895-3902.

6. Cherepy, N. J.; Shen, T. H.; Esposito, A. P.; Tillotson, T. M., Characterization of an Effective Cleaning Procedure for Aluminum Alloys: Surface Enhanced Raman Spectroscopy and Zeta Potential Analysis. **2004**.

7. Li, L.; Kim, D. Y.; Swain, G. M., Transient Formation of Chromate in Trivalent Chromium Process (TCP) Coatings on AA2024 as Probed by Raman Spectroscopy. *Journal of The Electrochemical Society* **2012,** *159* (8), C326-C333.

8. Qi, J.; Walton, J.; Thompson, G. E.; Albu, S. P.; Carr, J., Spectroscopic Studies of Chromium VI Formed in the Trivalent Chromium Conversion Coatings on Aluminum. *Journal of The Electrochemical Society* **2016,** *163* (7), C357-C363.

9. Matzdorf, C.; Beck, E.; Hilgeman, A.; Prado, R., Trivalent Chromium Process (TCP) as a Sealer for MIL-A-8625F Type II, IIB, and IC Anodic Coatings. Division, N. A. W. C. A., Ed. August 29, 2008.

10. Davis, J. R., *Alloying: Understanding the Basics-Light Metals and Alloys*. 2001.

11. Davis, J. R., *Corrosion of Aluminum and Aluminum Alloys*. 1999.

12. Kaufman, J. G., Aluminum Alloy and Temper Designation Systems of the Aluminum Association. In *Introduction to Aluminum Alloys and Tempers*, ASM International 2000; pp 9-22.

13. Rambau, P., Aluminum Alloys for Aerospace Applications. In *Aerospace Materials and Material Technologies*, Prasad, N. E.; Wanhill, R., Eds. Springer: 2017; Vol. 1, pp 29-52.

14. Xia, L.; Akiyama, E.; Frankel, G.; McCreery, R., Storage and Release of Soluble Hexavalent Chromium from Chromate Conversion Coatings: Equilibrium Aspects of Cr VI Concentration. *J. Electrochem. Soc.* **2000,** *147* (7), 2556-2562.

15. Jakab, M. A.; Little, D. A.; Scully, J. R., Experimental and Modeling Studies of the Oxygen Reduction Reaction on AA2024-T3. *J. Electrochem. Soc.* **2005,** *152* (8), B311-B320.

16. Ilevbare, G. O.; Scully, J. R., Oxygen Reduction Reaction Kinetics on Chromate Conversion Coated Al-Cu, Al-Cu-Mg, and Al-Cu-Mn-Fe Intermetallic Compounds. *Journal of The Electrochemical Society* **2001,** *148* (5), B196.

17. Instruments, G. Application Note: Getting Started with Electrochemical Corrosion Measurement. gamry.com (accessed February).

18. Huda, Z.; Taib, N. I.; Zaharinie, T., Characterization of 2024-T3: An aerospace aluminum alloy. *Materials Chemistry and Physics* **2009,** *113* (2), 515-517.

19. Jakab, M. A.; Little, D. A.; Scully, J. R., Experimental and Modeling Studies of the Oxygen Reduction Reaction on AA2024-T3. *Journal of The Electrochemical Society* **2005,** *152* (8), B311.

20. Mouanga, M.; Adreatta, F.; Druart, M. E.; Marin, E.; Fedrizzi, L.; Oliver, M. G., A Localized Approach to Study the Effect of Cerium Salts as Cathodic Inhibitor on Iron/Aluminum Galvanic Coupling. *Corrosion Sci.* **2015,** *90*, 491-502.

21. Costil, S.; Lamraoui, A.; Langlade, C.; Heintz, O.; Oltra, R., Surface modifications induced by pulsed-laser texturing—Influence of laser impact on the surface properties. *Applied Surface Science* **2014,** *288*, 542-549.

22. Dou, K.; Knobbe, E. T.; Parkhill, R. L.; Wang, Y., Surface Texturing of Aluminum Alloy 2024-T3 via Femto- and Nanosecond Pulse Excimer Laser Irradiation. *J. Selected Topics in Quantum Electronics* **2000,** *6* (4), 689-695.

23. Dufek, E. J.; Seegmiller, J. C.; Bazito, R. C.; and Buttry, D. A., Dioxygen Reduction Affects Surface Oxide Growth and Dissolution on AA2024-T3. *J. Electrochem. Soc.* **2007,** *154* (9), C458-C464.

24. Li, L.; Doran, K. P.; Swain, G. M., Electrochemical Characterization of Trivalent Chromium Process (TCP) Coatings on Aluminum Alloys 6061 and 7075. *Journal of The Electrochemical Society* **2013,** *160* (8), C396-C401.

25. Li, L.; Swain, G. P.; Howell, A.; Woodbury, D.; Swain, G. M., The Formation, Structure, Electrochemical Properties and Stability of Trivalent Chrome Process (TCP) Coatings on AA2024. *J. Electrochem. Soc.* **2011,** *158* (9), C274-C283.

26. Dufek, E. J.; Seegmiller, J. C.; Bazito, R. C.; Buttry, D. A., Dioxygen Reduction Affects Surface Oxide Growth and Dissolution on AA2024-T3. *J. Electrochem. Soc.* **2007,** *154* (9), C458-C464.

27. Software, K. T. The Chronology of a Crevice. http://www.corrosion-doctors.org/Forms-crevice/crevice3.htm (accessed March).

28. International, N. Economic Impact Report. http://impact.nace.org/economic-impact.aspx (accessed February).

29. Swopes, B. R. History Hour: Aloha Airlines Flight 243 incident. https://www.aerotime.aero/yulius.yoma/18542-history-hour-aloha-airlines-flight-243-incident (accessed March).

30. Levine, S. W.; Corporation, A. Plated parts and their production. 1984.

31. *Services, W. C. C.* Corrosion Advisory & Corrosion Consulting Services. https://www.corrosionclinic.com/index.html (accessed March).

32. Asmatulu, R.; Khan, S. I.; Jenkinson, M. L., Improving Corrosion Resistance via Graphene Nanocomposite Coatings. In *Graphene Science Handbook*, Research Gate: 2015; pp 465-476.

33. Katzman, H. A.; Malouf, G. M.; Bauer, R.; Stupain, G. W., Corrosion-protective Chromate Coatings on Aluminum. *Appl. Surf. Sci.* **1979,** *2* (3), 416-432.

34. Heine, M. A.; Pryor, M. J., Passivation of Aluminum by Chromate Solutions. *J. Electrochem. Soc.* **1967,** *114* (10), 1001-1006.

35. Kendig, M. W.; Davenport, A. J.; Isaacs, H. S., The Mechanism of Corrosion Inhibition by Chromate Conversion Coatings from X-Ray Absorption Near Edge Spectroscopy (XANES). *Corrosion Sci.* **1993,** *34* (1), 41-49.

36. J. Zhao, G. S. F. a. R. L. M., Corrosion Protection of Untreated AA-2024-T3 in Chloride Solution by a Chromate Conversion Coating Monitored by Raman Spectroscopy. *J. Electrochem. Soc.* **1998,** *145* (7), 2258-2264.

37. Costa, M., Toxicity and Carcinogenicity of Cr(VI) in Animal Models and Humans. *Critical Rev. Toxicol.* **1997,** *27*, 431-442.

38. Safety, E. H.; Safety, O. o. R. C. B., Waste Disposal Guide. In *How to Properly Dispose of Waste Materials Generated at Michigan State University*, 2009.

39. Reisch, M. S. Confronting the looming hexavalent chromium ban. https://cen.acs.org/articles/95/i9/Confronting-looming-hexavalent-chromium-ban.html (accessed March).

40. Kendig, M. W.; Buchheit, R. G., Corrosion Inhibition of Aluminum and Aluminum Alloys by Soluble Chromates, Chromate Coatings, and Chromate-Free Coatings. *J. Electrochem. Soc.* **2003,** *59* (5), 379-400.

41. Placzankis, B. E.; Miller, C. E.; Matzdorf, C. A., GM 9540P Cyclic Accelerated Corrosion Analysis of Nonchromate Conversion Coatings on Aluminum Alloys 2024, 2219, 5083, and 7075 Using DOD Paint Systems. Army, D. o. t., Ed. Army Research Laboratory, 2003; pp 1-29.

42. Li, L.; Swain, G. M., Effects of Aging Temperature and Time on the Corrosion Protection Provided by Trivalent Chromium Process Coatings on AA2024-T3. *Appl. Mater. Interfaces* **2013,** *5*, 7923-7930.

43. Specification, M., Anodic Coating for Aluminum and Aluminum Alloys. Navy, Ed. 2003.

44. Carangelo, A.; Curioni, M.; Acquesta, A.; Monetta, T.; Bellucci, F., Application of EIS to In Situ Characterization of Hydrothermal Sealing of Anodized Aluminum Alloys: Comparison between Hexavalent Chromium-Based Sealing, Hot Water Sealing and Cerium-Based Sealing. *J. Electrochem. Soc.* **2016,** *163* (10), C619-C626.

45. Wong, C.-M.; Moji, Y. Method for Anodizing Aluminum. 1990.

46. Curioni, M.; Saenz de Miera, M.; Skeldon, P.; Thompson, G.; Ferguson, J., Macroscopic and Local Filming Behavior of AA2024 T3 Aluminum Alloy during Anodizing in Sulfuric Acid Electrolyte. *Journal of The Electrochemical Society* **2008,** *155*, C387-C395.

47. Cohen, S.; Spadafora, S., A Comparison of Thin Film Sulfuric Acid Anodizing and Chromic Acid Anodizing Processes. **1995**, 40.

48. Thompson, G. E.; Zhang, L.; Smith, C. J. E.; Skeldon, P., Boric/sulfuric acid anodizing of aluminum alloys 2024 and 7075: Film growth and corrosion resistance. **1999**.

49. Zhang, J.-s.; Zhao, X.-h.; Zuo, Y.; Xiong, J.-p., The bonding strength and corrosion resistance of aluminum alloy by anodizing treatment in a phosphoric acid modified boric acid/sulfuric acid bath. *Surface and Coatings Technology* **2008,** *202* (14), 3149-3156.

50. Shruthi, T. K.; Walton, J.; McFall-Boegeman, S.; Westre, S.; Swain, G. M., Investigation of the Trivalent Chromium Process Conversion Coating as a Sealant for Anodized AA2024-T3. *Journal of The Electrochemical Society* **2020,** *167* (11), 111504.

51. Runge, J. M., The Metallurgy of Anodizing Aluminum. Springer International Publishing: 2018; pp 149-190.

52. Diggle, J. W.; Downie, T. C.; Goulding, C. W., Anodic oxide films on aluminum. *Chemical Reviews* **1969,** *69* (3), 365-405.

53. Shimizu, K.; Kobayashi, K.; Thompson, G. E.; Wood, G. C., Development of porous anodic films on aluminium. *Philosophical Magazine A* **1992,** *66* (4), 643-652.

54. Council, A. A. Anodizing's Benefits. https://www.anodizing.org/page/benefits (accessed January).

55. Tech-Faq Anodizing Aluminum. http://www.tech-faq.com/anodizing-aluminum.html (accessed January).

56. Anodic Coatings for Aluminum and Aluminum Alloys. Specification, M., Ed. September 10, 1993; Vol. MIL-A-8625F.

57. Matzdorf, C.; Beck, E.; Hilgeman, A.; Prado, R., Trivalent Chromium Process (TCP) as a Sealer for MIL-A-8625F

Type II, IIB, and IC Anodic Coatings. Division, N. A. W. C. A., Ed. August 29, 2008.

58. Zuo, Y.; Zhao, P.-H.; Zhao, J.-M., The influences of sealing methods on corrosion behavior of anodized aluminum alloys in NaCl solutions. *Surface & Coatings Technology - SURF COAT TECH* **2003,** *166*, 237-242.

59. Ahmed, N.; Pervaiz, S.; Ahmad, S.; Rafaqat, M.; Hassan, A.; Zaindin, M., LBM of aluminum alloy: towards a control of material removal and roughness. *The International Journal of Advanced Manufacturing Technology* **2019,** *105*.

60. Wang, Y.; Yang, F.; Zhang, W., Development of Laser and Electrochemical Machining Based on Internal Total Reflection. *Journal of The Electrochemical Society* **2019,** *166* (14), E481-E488.

61. Lasagni, A.; Manzoni, A.; Mücklich, F., Micro/Nano Fabrication of Periodic Hierarchical Structures by Multi-Pulsed Laser Interference Structuring. *Advanced Engineering Materials* **2007,** *9* (10), 872-875.

62. D'Alessandria, M.; Lasagni, A.; Mucklich, F., Direct Micro-Pattering of Aluminum Substrates via Laser Interference Metallurgy. *Applied Surface Science* **2008,** *255*, 3210-3216.

63. Trapp, J.; Rubenchik, A. M.; Guss, G.; Matthews, M. J., In situ absorptivity measurements of metallic powders during laser powder-bed fusion additive manufacturing. *Applied Materials Today* **2017,** *9*, 341-349.

64. Leal, M. L. B.; Bermudez-Reyes, B.; Robledo, P. d. C. Z.; Lopez-Botello, O., Parameter optimization of aluminum alloy thin structures obtained by Selective Laser Melting. *MRS Advances* **2019,** *4* (55-56), 2997-3005.

65. Tam, A. C.; Leung, W. P.; Zapka, W.; Ziemlich, W., Laser-Cleaning Techniques for Removal of Surface Particulates. *Journal of Applied Physics* **1992,** *71*, 3515-3523.

66. Lu, Y.-F.; Song, W.-D.; Tee, C.-K.; Chan, D. S.-H.; Low, T.-S., Wavelength Effects in the Laser Cleaning Process. *Japanese Journal of Applied Physics* **1998,** *37* (Part 1, No. 3A), 840-844.

67. Zhou, C.; Li, H.; Chen, G.; Wang, G.; Shan, Z., Effect of single pulsed picosecond and 100 nanosecond laser cleaning on surface morphology and welding quality of aluminium alloy. *Optics & Laser Technology* **2020,** *127*, 106197.

68. Kalvala, P.; Ram, G.; Stucker, B., Improvement in corrosion resistance of friction stir welded aluminum alloys with micro arc oxidation coatings. *Scripta Materialia - SCRIPTA MATER* **2008,** *58*, 998-1001.

69. Dimogerontakis, T.; Oltra, R.; Heintz, O., Thermal oxidation induced during laser cleaning of an aluminium-magnesium alloy. *Applied Physics A* **2005,** *81* (6), 1173-1179.

70. Zhang, S. L.; Suebka, C.; Liu, H.; Liu, Y. X.; Liu, Z.; Guo, W.; Cheng, Y. M.; Zhang, F. D.; Peng, Y. D.; Li, L., Mechanisms of Laser Cleaning Induced Oxidation and Corrosion Property Changes in AA5083 Aluminum Alloy. *J. Laser Appl.* **2019,** *31* (012001), 1-11.

71. Zhang, G.; Hua, X.; Huang, Y.; Zhang, Y.; Li, F.; Shen, C.; Cheng, J., Investigation on mechanism of oxide removal and plasma behavior during laser cleaning on aluminum alloy. *Applied Surface Science* **2020,** *506*, 144666.

72. Razab, M. K. A. A.; Jaafar, M. S.; Abdullah, N. H.; Amin, M. F. M.; Mohamed, M., Influence of Elemental Compositions in Laser Cleaning for Automotive Coating Systems. *Journal of Russian Laser Research* **2016,** *37* (2), 197-206.

73. McFall-Boegeman, S.; Yancey, D. F.; O'Neill, T.; Davidson, N.; Swain, G. M., Effect of Laser Cleaning and Hyperpassivation on the Electrochemical Behavior of AA2024-T3. *Journal of The Electrochemical Society* **2021,** *168* (3), 031501.

74. Lasagni, A.; D'Alessandria, M.; Giovanelli, R.; Mücklich, F., Advanced design of periodical architectures in bulk metals by means of Laser Interference Metallurgy. *Applied Surface Science* **2007,** *254* (4), 930-936.

75. Yilbas, B. S.; Matthews, A.; Karatas, C.; Leyland, A.; Khaled, M.; Abu-Dheir, N.; Al-Aqeeli, N.; Nie, X., Laser Texturing of Plasma Electrolytically Oxidized Aluminum 6061 Surfaces for Improved Hydrophobicity. *Journal of Manufacturing Science and Engineering* **2014,** *136* (5).

76. Psyllaki, P.; Oltra, R., Preliminary study on the laser cleaning of stainless steels after high temperature oxidation. *Materials Science and Engineering: A* **2000,** *282*, 145-152.

77. Russo, R. E.; Mao, X.; Mao, S. S., Peer Reviewed: The Physics of Laser Ablation in Microchemical Analysis. *Analytical Chemistry* **2002,** *74* (3), 70 A-77 A.

CHAPTER 2. INVESTIGATION OF CHANGES IN TENSILE STRENGTH AND CORROSION DAMAGE TO ALUMINUM ALLOY AA2024-T3 DURING NEUTRAL SALT SPRAY EXPOSURE – EFFECT OF TCP COATING TYPE

2.1 INTRODUCTION

In many industries, including aerospace, dissimilar metals come into electrical contact when joined with rivets or welds. This electrical contact between two materials having different electromotive forces can cause galvanic corrosion with the less noble material undergoing corrosion at a rate that is driven by cathodic reactions occurring at the more noble material. Usually, dissimilar materials are physically isolated from one another by an electrically insulating spacer layer or sealant. However, electrical contact can still result when a layer of electrolyte solution condenses over the surface of the two materials even when electrically isolated. Aluminum alloys that are commonly used in aerospace applications because of high strength to weight ratios[1-5] are more active and susceptible to corrosion than are other commonly used materials such as titanium, carbon composites, steel, etc. Aluminum alloys are highly susceptible to degradation when electrically contacting these materials due to galvanic corrosion.

In order to mitigate and control various types of corrosion, general, pitting and galvanic, the aerospace industry employs a multilayered coating system to protect the underlying alloy[6]. In this system the conversion coating is initially applied to the specimen. A primer layer is then added followed by finishing with the topcoat/colorant. This system provides many layers that need to be penetrated prior to corrosion formation on the underlying alloy.

The conversion coating the multilayer system has been receiving much discussion as of late due to the Cr(VI) used in the coating layer. The Cr(VI) active corrosion inhibitor in the coating is currently banned in the EU and is of great concern around the world because it is a priority pollutant and toxic to workers[7-9]. To replace this Cr(VI) coating, research has shown that the trivalent chromium process (TCP) coating is a viable alternative and is more environmentally friendly and safer for worker use[10-15].

Previous work has shown that the TCP coating provides protection to the underlying alloy when exposed to the neutral salt spray fog in accordance with ASTM B-117[15]. The multiple TCP coatings that are commercially available have variations in the coating bath composition. This can lead to differences in performance on a given aluminum alloy.

Aluminum alloys are used as structural materials in aviation because they have the high strength to weight ratio. However, depending on the main alloying elements and their distribution in the aluminum matrix other properties can emerge[16, 17]. In this work, AA2024-T3 was studied as the copper alloying element does help increase the ultimate tensile strength[16, 17]. The copper can also form secondary phases in the alloy and these acts as sites for galvanic corrosion initiation sites as these phases can support a relatively high rate of dissolved oxygen reduction. .The main problem with material degradation and corrosion is the weakening of the physical strength of the alloy that occurs leading to mechanical failure.

Much work has been performed investigating the tensile strength of AA2024[18], welds[19, 20], and other aerospace/automotive alloys[19-22], but little has been done investigating how effectively TCP conversion coatings and non-chromate primer layers inhibit corrosion on the alloy during accelerated degradation testing thereby maintaining the materials inherent mechanical strength. This research investigates how effective four commercial TCP coatings,

in combination with a non-chromate epoxy primer, are at preventing corrosion and reduced mechanical strength during a 14-day neutral salt-spray test according to ASTM B117. Tensile strength tests were performed on dogbone-shaped specimens fully coated and fitted with a titanium alloy fastener before and after the continuous salt-spray exposure for 14 days.

2.2 MATERIALS AND METHODS

Reagents

All cleaners, deoxidizers and coating baths were commercial grade quality and used as received. Turco 6849 (20% v/v, Henkel Corp., Madison Heights, MI), SurTec 133 (4% w/v, SurTec Inc., Brunswick, OH), Luster-On 401 (4% w/v, Luster-On Products Inc., Springfield, MA), and Chemeon Cleaner 1000 (45g/L, Chemeon Surface-Tech., Ninden, NV) were the degreasers used. Turco Liquid Smut-Go (20% v/v, Henkel Corp., Madison Heights, MI), Luster-On 485 (3.9% v/v, Luster-On Products Inc., Springfield, MA), and SurTec 465L (20% v/v, SurTec Inc., Brunswick, OH) served as the deoxidizers. Bonderite T-5900 RTU (Henkel Corp., Madison Heights, MI), Luster-On Aluminescent (1% w/v, Luster-On Products Inc., Springfield, MA), TCP-NP (Chemeon Surface-Tech., Ninden, NV), and SurTec 650 E (20% v/v, SurTec Inc., Brunswick, OH) were the TCP coatings. 02GN084 Chrome-Free Epoxy Polyamide Primer (PPG Aerospace Deft, Mojave, CA) was used as the primer in this work. Klean Strip Paint Thinner (W.M. Barr, Memphis, TN) was used to remove the primer from the specimens after testing. All solutions were prepared with ultrapure water (Barnstead E-Pure) having a resistivity of >17 MΩ · cm.

Specimen Preparation

Wrought aluminum alloy (AA2024-T3) was obtained as 12” x 12” rolled sheets – so-called “as received” (www.onlinemetals.com). The nominal elemental composition of this alloy from

OnlineMetals is as follows: Al (90.7-94.7 wt.%), Cr (max. 0.1 wt.%), Cu (3.5-5.0 wt.%), Fe (max 0.5 wt.%), Mg (1.2-1.8 wt.%), Mn (0.3-0.9 wt.%), Si (max. 0.5 wt.%), Ti (max. 0.1 wt.%), and Zn (max. 0.25wt.%). Specimens were machined into dogbone-shaped specimens with the dimensions presented in Figure 2.1. The panels were 12.7 cm long by 1.5 cm wide with a taper at 4 cm to a narrower 0.9 cm wide gage region that was 3.5 cm in length. A 3 mm hole was drilled into the center of the gage region to attach a metal screw for the galvanic corrosion studies. A titanium (Ti-6Al-4V) screw and nut assembly was attached to the specimen after conversion coating and priming with a torque of 100 lb-in. The ends of the specimens were masked off by using 3M waterproof electrical tape to ensure that only the gage region would be exposed to the salt- spray environment. Control specimens were not subjected to the salt spray testing, but were degreased and deoxidized and coated with Bonderite T-5900 RTU, as described below.Control specimens were not primed.

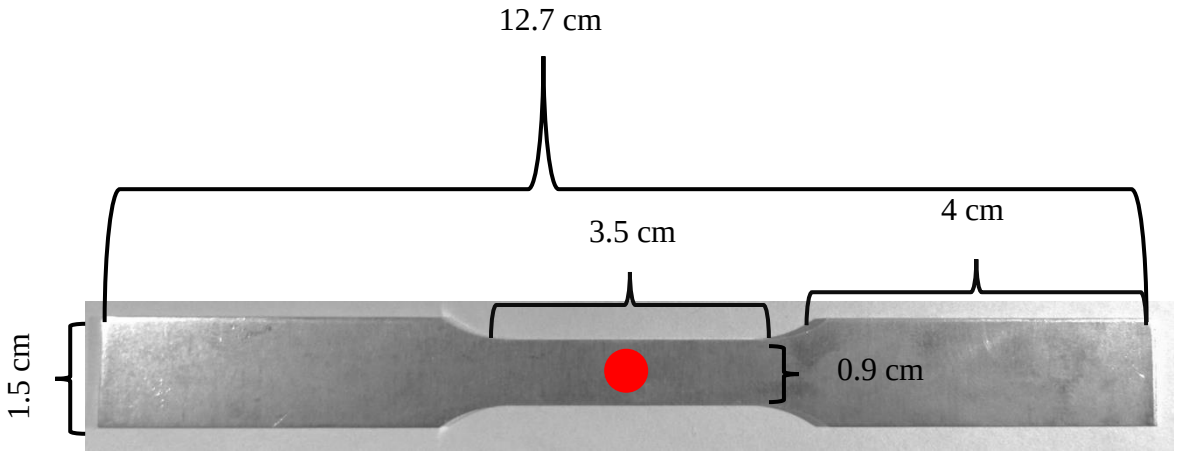

Figure 2.1. Photograph of a dogbone specimen shape used for tensile strength testing from the top side. Dimensions for the specimen are presented in the image. Red circle indicates the gage region where a drilled hole was fitted with a Ti-6Al-4V metal fastener. The drilled hole had a diameter of 3 mm.

Bonderite T-5900 RTU Coating Application

A specimen was first degreased with 20 vol.% Turco 6849 at 55°C for 10 min using periodic agitation. This was followed by a city tap water rinse for 2 min. The specimen was then deoxidized with 20 vol.% Turco Liquid Smut-Go at room temperature (~23°C) for 2 min. This was also followed by a city tap water rinse for 2 min. To form the conversion coating, the degreased and deoxidized specimen was immersed with the top side up in the RTU Bonderite T-5900 coating bath (pH 3.65) at room temperature for 10 min, with very gentle beaker agitation, as needed, to dislodge any gas bubbles (H_2) that formed. This was followed by a 2 min city tap water soak and then a 30 s soak in ultrapure water. Excess water was carefully wicked off the coated surface. This was followed by overnight drying at room temperature before use of the specimen in further testing. The typical conversion coating thickness for this and the other TCP coatings was in the range of 100-300 nm, based on past published work[12, 13, 23].

Luster-On Aluminescent Coating Application

A specimen was first degreased with 4 mass/vol.% Luster-On 401 at 60 °C for 5 min using periodic agitation. This was followed by a 2 min city tap water rinse. The specimen was then deoxidized with 3.9 vol.% Luster-On 485 at room temperature (~23°C) for 2 min. This was followed by a city tap water rinse for 2 min. To form the conversion coating, the specimen was immersed in 1 mass/vol.% Luster-On Aluminescent coating bath (pH= 3.85) for 4 min. at room temperature with a gentle agitation, as needed, to dislodge any gas bubbles (H_2) that formed. This was followed by a 2 min. city tap water soak and then a 30 s soak in ultrapure water. Excess water was carefully wicked off the surface of the coated specimen. This was followed by overnight drying at room temperature before use of the specimen in further testing.

Chemeon TCP-NP Coating Application

A specimen was first degreased with 45 g/L Chemeon Cleaner 1000 at 50°C for 10 min using periodic agitation. This was followed by a city tap water rinse for 2 min. To form the conversion coating, the cleaned specimen was immersed with the top side up in the TCP-NP coating bath (pH 3.85) at room temperature for 10 min with very gentle beaker agitation, as needed, to dislodge any gas bubbles (H_2) that formed. This was followed by a 2 min city tap water soak. Excess water was carefully wicked off the coated surface. This was followed by overnight drying at room temperature before use of the specimen in further testing.

SurTec 650 E Coating Application

A specimen was first degreased with 4 mass/vol.% SurTec 133 at 55°C for 10 min using periodic agitation. This was followed by a city tap water rinse for 2 min. The specimen was then deoxidized with 20 vol.% SurTec 465L for 1 min. This was also followed by a city tap water rinse for 2 min. To form the conversion coating, the degreased and deoxidized specimen was immersed with the top side up in 20 vol.% SurTec 650 E coating bath (pH 3.85) at 30 °C for 4 min with very gentle periodic beaker agitation, as needed, to dislodge any gas bubbles (H_2) that formed. This was followed by a 2 min city tap water soak and then a 30 s soak in ultrapure water. Excess water was carefully wicked off the coated surface. This was followed by overnight drying at room temperature before use of the specimen in further testing.

Deft® Primer Application

The ends of the dogbone specimens were taped off with 3M waterproof electrical tape to ensure only the gage region would be exposed to the salt spray. A two-component Deft® chrome-free epoxy polyamide primer 02GN084, PPG Aerospace Inc. was applied by brush within one week after TCP application. Specimens were primed one side at a time in the gage

region to allow for adequate drying of the primer. The brush was dipped into the primer before each brush stroke. Seven brush strokes were made from end to end across the gage region on each side. The brush strokes formed primer along the edges as well as the top and bottom sides. The primer thickness was 0.01-0.02 in.

2.3 TESTING AND CHARACTERIZATION

Neutral Salt-spray (ASTM B117) Testing

Conversion coated and primed specimens were placed at a ~20° angle (with respect to the vertical axis) on plastic racks inside the salt-spray chamber (Associated Environmental Systems, MX-04, 4 ft^3). The chamber was filled with a 5 wt.% NaCl solution. The salt fog test was conducted according to ASTM B117 for 14 days (35 ºC). At the end of the test period, the specimens were removed, rinsed thoroughly with ultrapure water, and dried under a stream of N_2 gas.

Camera Photographs

Photographs were taken using a Canon PowerShot SX420IS digital camera with wide-angle optical image stabilized zoom lens using the macro image setting. Photographs were processed using paint.net photograph processing software into black and white images with enhanced contrast for improved visualization of features. All photographs encompass an area slightly less than the total specimen area, to prevent edge lighting differences from influencing the specimen visualization.

Tensile Strength

A uniaxial tensile strength instrument (UTS SFM-20, United Calibration Corp.) was used. For tensile testing, a 1000 lb. load cell was used, and the extension of the sample was measured

with reflective tape and a laser extensometer, following the directions of ASTM E8. The strain rate of the specimen was 1.2 mm/min with a lab temperature of 25.8 ℃ and humidity of 34%.

Primer Removal

Specimens were immersed in Klean Strip Paint Thinner in 5 min increments to remove the primer. Between immersions the specimens were rinsed with ultrapure water and checked for primer removal. After removal of large areas of primer, any remaining primer residue was removed by pealing with a metal blade between immersions in the paint thinner. The peeling was performed while looking through a microscope to minimize contact with the aluminum alloy below the primer. The areas with remaining primer were not investigated post-tensile strength testing.

Scanning Electron Microscopy/Energy Dispersive X-Ray Spectroscopy

Scanning electron microscopy (SEM) was performed using a field emission electron microscope (JEOL 6610LV) with an energy dispersive x-ray (EDX) microanalysis attachment (Oxford, AZtec Software). Electron micrographs were obtained using an accelerating voltage of 15 kV, a working distance of 11 mm, and an electron beam spot size of 30 μm with a dwell time 16 μs/pixel.

Digital Microscopy

Digital microscopy was performed using a Keyence VHX-600 microscope at magnifications of 50 and 100x. Focused digital images of the surface were captured and combined into one fully focused (stitched) image. The microscope uses a depth of defocus method to calculate three-dimensional depth information based on the amount of defocusing of two-dimensional images. Surface roughness data were obtained from the areas measured at

different locations near damage points and further into the bulk. The depth resolution was ca. 0.2 μm.

2.4 RESULTS

Camera Photographs of Dogbone Specimens after Salt Spray Exposure

Uncoated control specimens were degreased and deoxidized, but not subjected to the neutral salt-spray test to measure the intrinsic tensile strength of the alloy. Figure 2.2 shows a representative control specimen after tensile strength testing. In the image, a clean break is seen right through the fastener hole, as expected as this is the weakest point in the gage region. This, in fact, is location of all specimen failure during tensile strength testing.

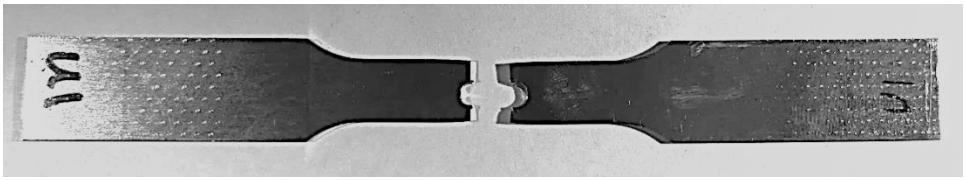

Figure 2.2. Photograph of an uncoated control AA2024-T3 dogbone specimen after tensile strength testing. The weakest point is in the gage region at the site of the fastener hole, hence the fracture at this site.

Prior to primer removal, camera images were taken to show the damage seen at the end of the 14-day neutral salt-spray (NSS) test. The specimens coated with the Bonderite T-5900 coating, in Figure 2.3, show some blistering and discoloration of the primer layer near the screw fastener on all three specimens, as indicated by the red arrows. One specimen exhibited more blistering than the other two. While blistering or bubbling can result from poor specimen cleaning, the damage here is attributed to increased pressure from moisture and corrosion product accumulation under the coating at the sites of alloy corrosion. Hydrogen gas is likely produced from the reduction of water locally on the Ti alloy using electrons generated from the oxidation of nearby aluminum alloy where solution ingress occurred. This gas evolution would be occurring in the fastener hole and could also be a cause for the blistering. The

specimens still show the 3M waterproof electrical tape that was applied to the specimen ends and the titanium screw used to evoke galvanic corrosion. The blisters indicate that there was some undercutting of the primer layer and or the conversion coating. The evidence reveals that the corrosion damage initiates in the wall of the fastener hole and progresses inward into the specimen under the coating system.

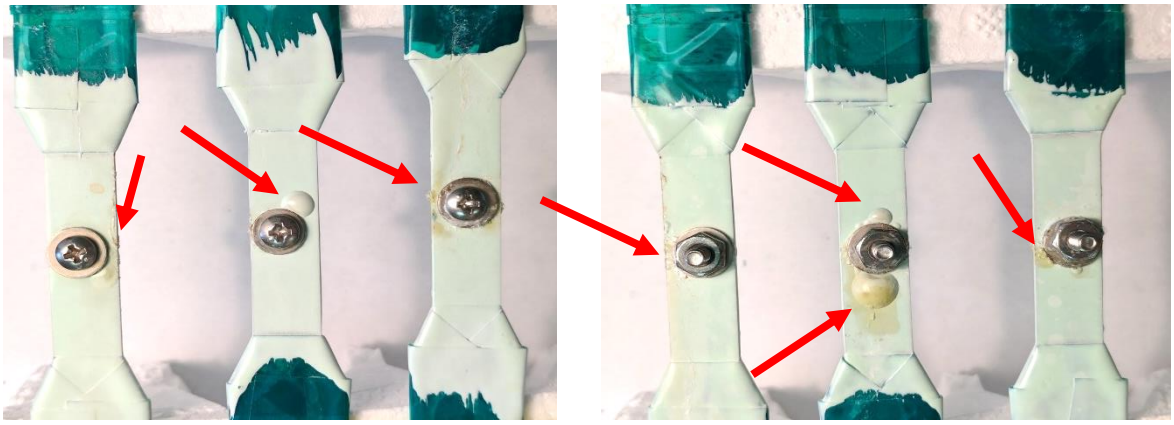

Figure 2.3. Camera photographs of Bonderite T-5900 TCP-coated specimens after a 14-day NSS exposure. Red arrows point to damage areas seen near the fastener hole . Blisters and discoloration were present due to the galvanic corrosion caused by the interactions with the titanium screw with the aluminum alloy. Photographs show the front (left) and back (right) sides of the gage region of the dogbone specimens.

The corrosion and degradation were qualitatively more severe on the Chemeon TCP-NP coated specimens, as shown in Figure 2.4. There were more small blisters present on the specimens coated with the Chemeon TCP-NP when compared to the specimens with the other conversion coatings. The many small blisters on the front and back of the specimens indicates that the TCP coating is not adhering the top primer layer well and that the TCP coating may have broken down when exposed to the neutral salt spray test.

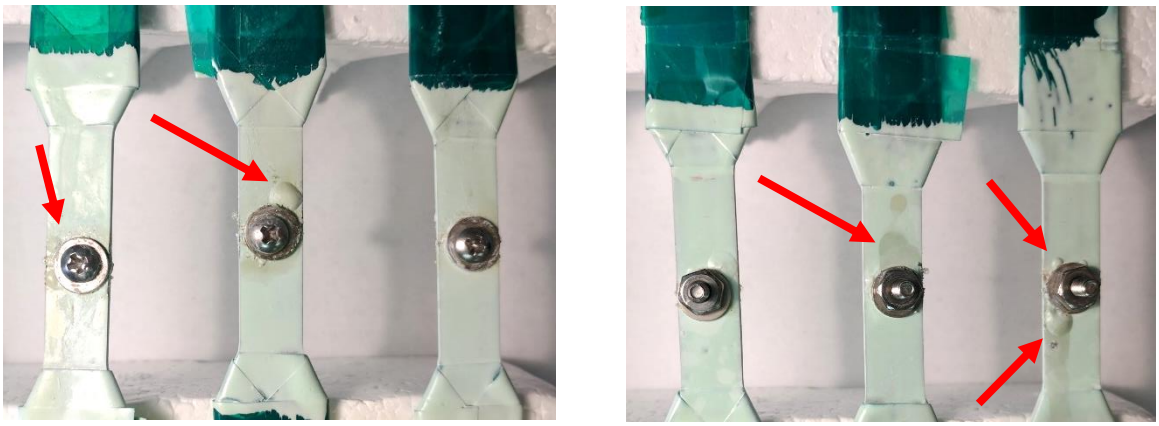

Figure 2.4. Camera photographs of Chemeon TCP-NP-coated specimens after a 14-day NSS exposure. Red arrows point to damage areas near the fastener hole. Blisters and discoloration were present due to the galvanic corrosion caused by the interactions between the titanium screw and the aluminum alloy. Photographs show the front (left) and back (right) sides of the gage region of the dogbone specimens.

Some discoloration and blistering were observed on all three of the SurTec 650 E-coated specimens. The degradation and corrosion damage were located near the fastener hole. There is little undercutting that happened on these specimens and the damage is central to the fastener area.

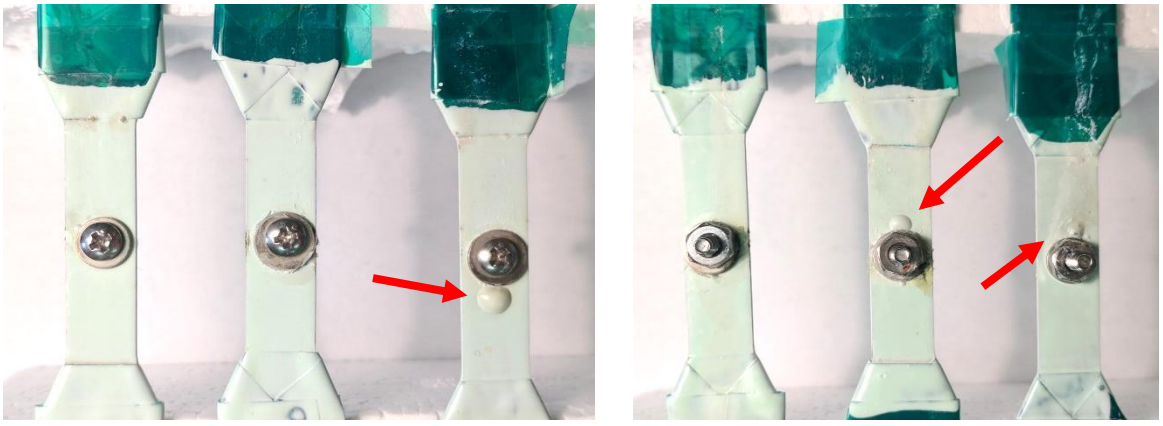

Figure 2.5. Camera photographs of SurTec 650E TCP-coated specimens after a 14-day NSS exposure. Red arrows point to damage seen while primer was still on specimens. Blisters and discoloration were present due to the galvanic corrosion caused by the interactions with the titanium rivet and the aluminum alloy. Photographs show the front (left) and back (right) sides of the specimens.

The Luster-On Aluminescent TCP coated specimens in Figure 2.6 show only one blister and one area of discoloration across multiple samples. Specimens coated with this TCP coating

and the primer visually exhibited the least damage after the 14-day neutral salt-spray exposure. There is very little undercutting of the primer layer and the damage that is seen is minimal when compared to the other TCP coated specimens.

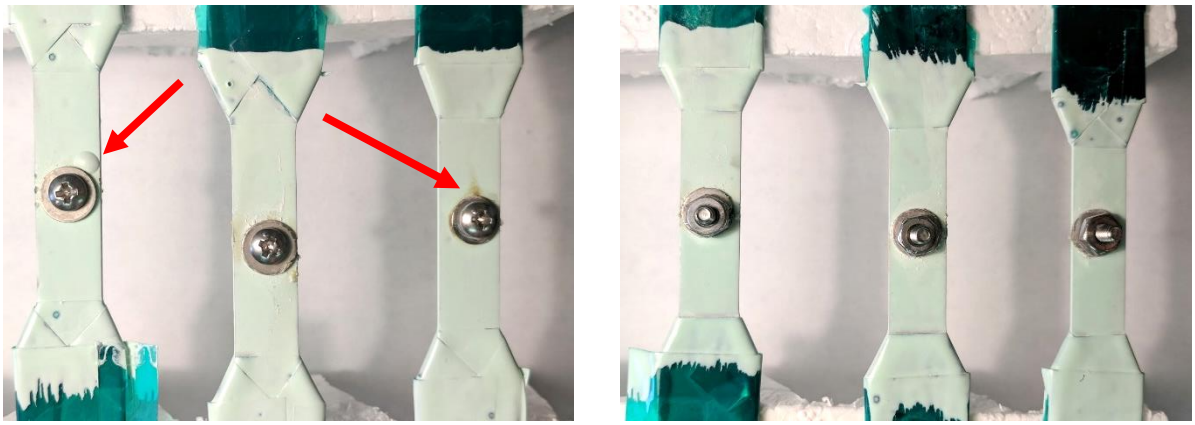

Figure 2.6. Camera photographs of Luster-On Aluminescent TCP coated specimens post-NSS exposure. Red arrows point to damage seen while primer was still on specimens. Blisters and discoloration were present due to the galvanic corrosion caused by the interactions with the titanium rivet and the aluminum alloy. Photographs show the front (left) and back (right) sides of the specimens.

Tensile Strength

Uniaxial tensile strength measurements were made on the coated specimens after the 14-day salt-spray test and removal the titanium fastener. The force required to fracture the specimen was measured in MPa and reported in Table 2.1 for each of the conversion coating/primer systems. Qualitative analysis of the corrosion damage from the photographs described above reveal that all specimens experienced a similar level of coating blistering and discoloration resulting from either degradation of the screw and or the underlying aluminum alloy. The damage appears to initiate in the fastener hole wall and progress inward undercutting the coating system.

Table 2.1. Summary of the Tensile Strength Data for the Uncoated, and T-5900, TCP-NP, 650 E, and Aluminescent Conversion Coated and Primed AA2024-T3 Specimens.

	Tensile Strength (MPa)	Difference from Control (MPa)
Uncoated	241.21 ± 2.03	--
Bonderite T-5900 RTU	130.44 ± 10.20	-110.77 ± 10.40
Chemeon TCP-NP	107.89 ± 19.66	-133.32 ± 19.77
SurTec 650 E	135.88 ± 46.93	-105.33 ± 46.98
Luster-On Aluminescent	120.09 ± 32.67	-121.12 ± 32.73

Mean ± confidence interval (95%) values for n=3 for all specimen types. The uncoated control specimen had the fastener hole machined into the gage region but was not exposed to the salt-spray test with the titanium screw in place.

Consistent with the qualitatively similar levels of observed degradation, the tests reveal similar tensile strengths for all four conversion-coated/primer systems. The nominal tensile strengths range from 100-135 MPa. ANOVA analysis revealed that there is no statistical difference in any of the mean tensile strengths for the conversion coated/primed specimens. The strength of the coated specimens is reduced by *ca.* 50 % after the salt spray exposure, as compared to the uncoated control. The control specimen was simply an aluminum alloy with the fastener hole machined into the gage region. The tensile strength was nominally 240 MPa. The tensile strength of this specimen is about half that for the dogbone specimen with no fastener hole machined in the gage region, 400-450 MPa. The uncoated control was not coupled with the titanium fastener or exposed to the 14-day NSS test. Therefore, it could be argued that this is not the most appropriate control specimen to have used in this study. The data do reveal, though, that having good conversion coating and primer formation in the fastener hole wall is critically important. A similar conclusion has been made by Frankel and coworkers for the galvanic corrosion of aluminum alloys caused by contact with steel

fasteners.[23] If poor coating exists on the hole wall, then it does not matter what the quality of the conversion coating/primer layer is on the alloy surface away from the hole.

Scanning Electron Microscopy of the Damaged Region Under the Coating

The aluminum alloy specimens in the gage region at the site of fracture were interrogated using SEM and EDS analysis after stripping the primer. SEM micrographs are presented in Figure 2.7 for the uncoated control specimen after tensile strength testing. The weakest point of the specimen is in the gage region at the site of the fastener hole, hence the specimens' fracture at this location. Minor pitting was observed on the specimen surface away from the fastener hole that is attributed to alloy dissolution during the deoxidation surface pretreatment. Red arrows indicate the small pits. Bright spots are caused by electron beam charging at the second-phase intermetallic particles present along the surface of the specimen.

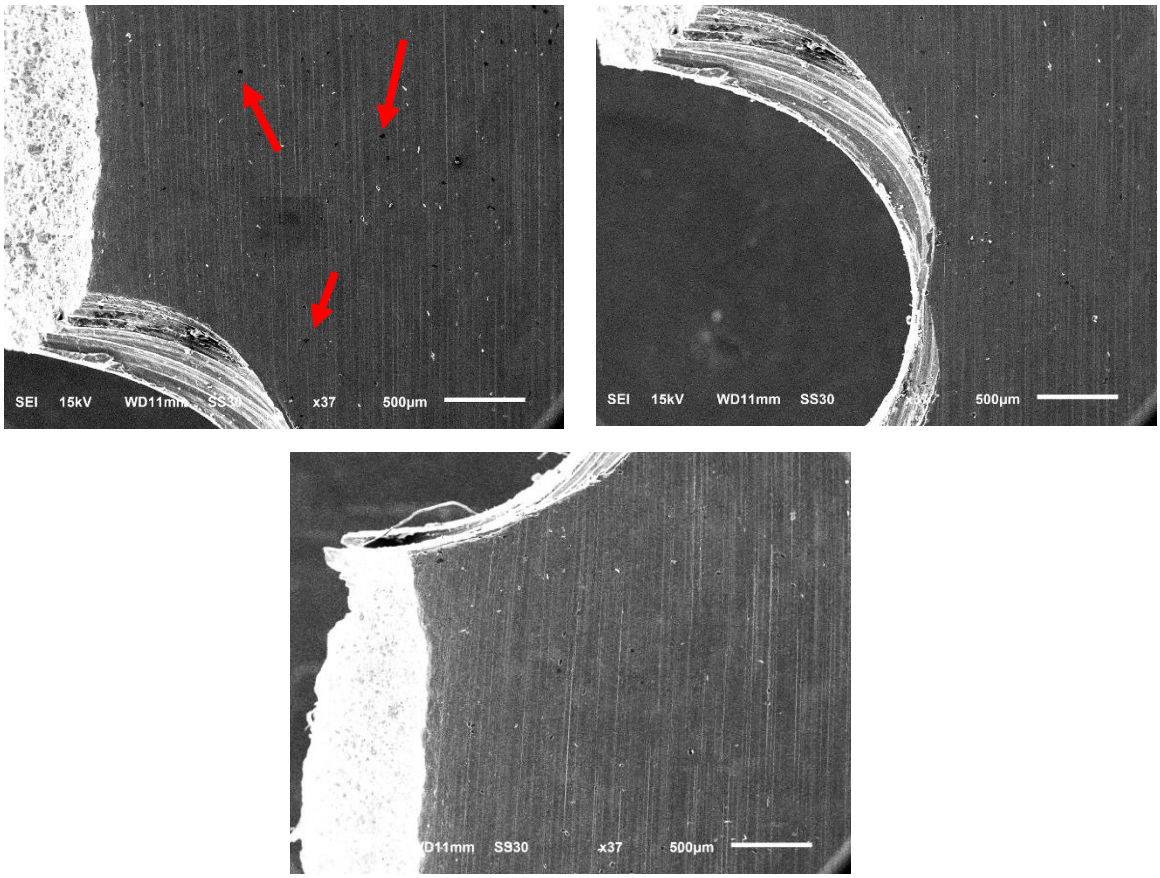

Figure 2.7. SEM micrographs of an uncoated control specimen post-tensile strength testing around one side of the fastener hole. Red arrows point to small pits produced by the deoxidation of the specimen during sample preparation.

Figure 2.8 shows an SEM micrograph and EDS elemental maps of the gage region at the site of fracture for a specimen that was conversion coated with Bonderite T-5900 and primed after the 14-day salt-spray exposure. This damage site was under a blister visible in the camera photographs presented in Figure 2.3. There is clearly corrosion damage to the hole wall, as indicated by the two red arrows. This damage led to solution ingress into the specimen under the conversion coating and primer. The damage penetrates into the specimen 2-3 mm from the hole wall. Chemically, there was aluminum present as well as oxygen in the damaged region, presumably due to the formation of Al_2O_3 corrosion product The conversion coating is still present on the undamaged regions, as evidenced by the presence of zirconium.

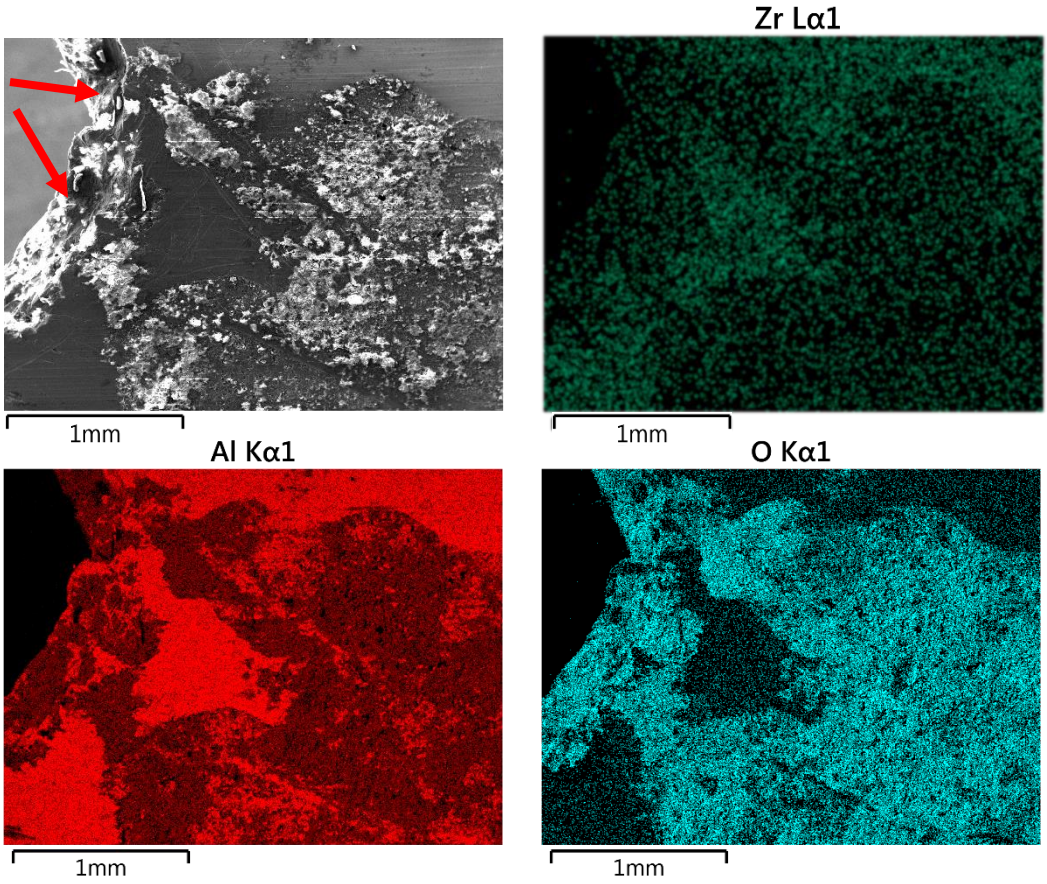

Figure 2.8. SEM micrograph and EDS elemental maps for Al, O and Zr in a region near the hole and fracture site and under a blister that was formed on a Bonderite T-5900 coated and primed dogbone specimen after a 14-day neutral salt-spray test. There was no detectable chloride along the surface.

Figure 2.9 presents an SEM micrograph and EDS elemental maps at the site of fracture for a specimen that was conversion coated with Chemeon TCP-NP and primed after the 14-day salt-spray exposure. Again, there is corrosion damage to the fastener hole wall (upper left), and this led to solution ingress under the conversion coating and primer. The corroded region of the specimen extends at least 2-3 mm away from the fastener hole. The surface is very rough due to the formation of Al_2O_3. The elemental maps for aluminum and oxygen reveal the presence of the oxide in the corroded region. However, no residual zirconium from the conversion coating was detected.

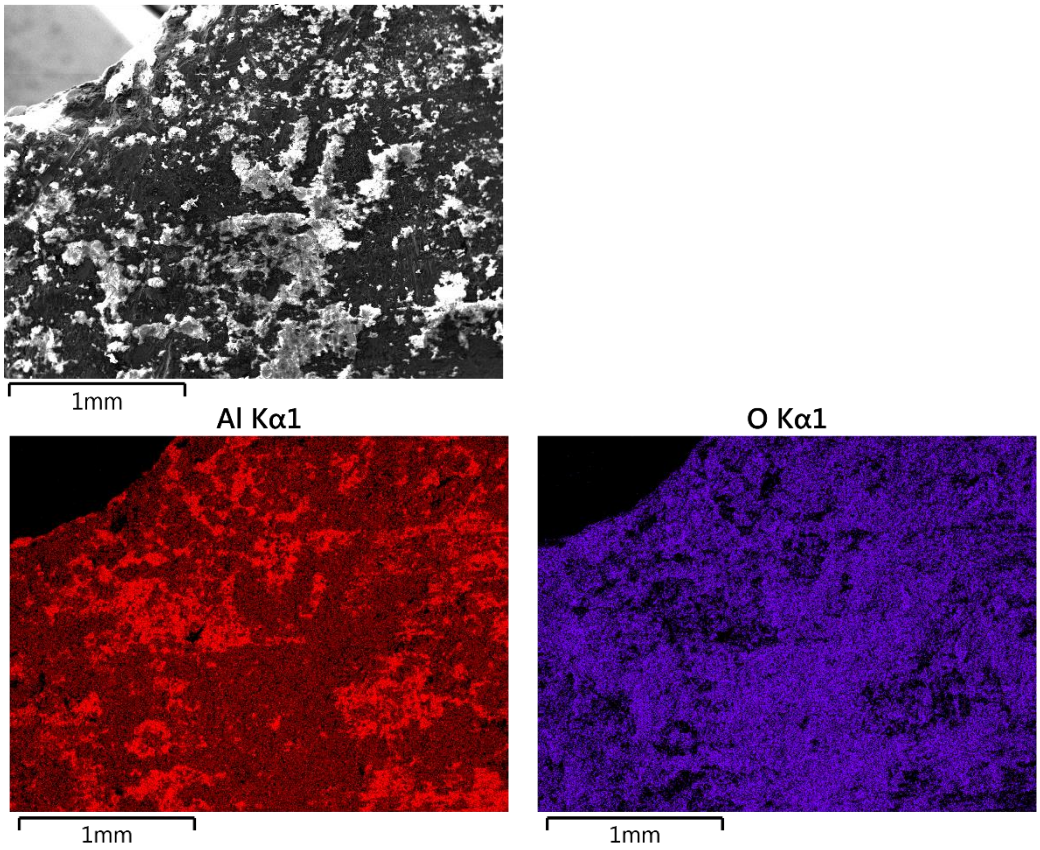

Figure 2.9. SEM micrograph and EDS elemental maps for Al and O in a region near the hole and fracture site and under a blister that was formed on a Chemeon TCP-NP coated and primed dogbone specimen after a 14-day neutral salt-spray test. There was no detectable chloride along the surface.

Figure 2.10 presents an SEM micrograph and EDS elemental maps at the site of fracture for a specimen that was conversion coated with SurTec 650E and primed after the 14-day salt spray exposure. The results are similar to those observed for the Chemeon TCP-NP coated and primed specimens. Corrosion damage to the fastener hole wall is evident (lower left) and this led to solution ingress under the coating system causing corrosion of the alloy. The extent of the damage extends away from the hole by at least 2-3 mm. The EDS elemental analysis reveals the presence of aluminum and oxygen but not zirconium in the damage region.

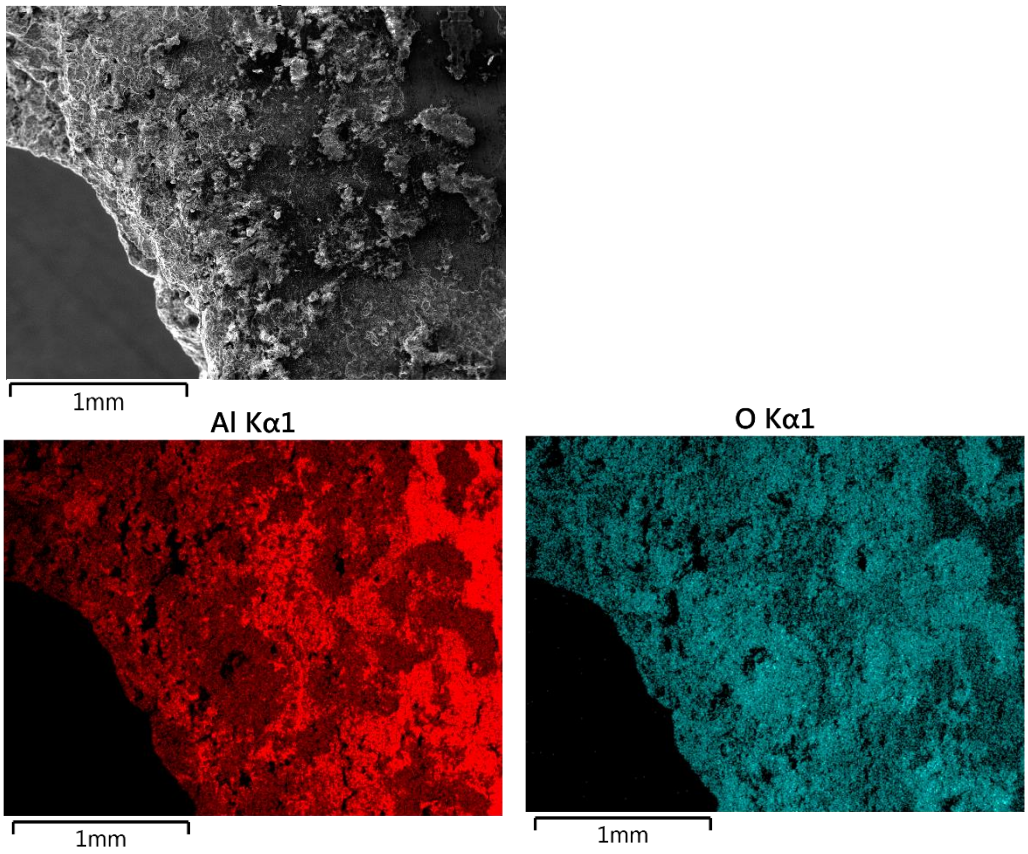

Figure 2.10. SEM micrograph and EDS elemental maps for Al and O in a region near the hole and fracture site and under a blister that was formed on a SurTec 650 E coated and primed dogbone specimen after a 14-day neutral salt-spray test. There was no detectable chloride along the surface.

Figure 2.11 presents an SEM micrograph and EDS elemental maps at the site of fracture for a specimen that was conversion coated with Luster-on Aluminescent TCP and primed after the 14-day salt spray exposure. Damage to the hole wall can be seen (upper left) and this led to solution ingress under the coating. It should be noted that part of the reason for the coating failure around the hole could also be poor adhesion and formation. Qualitatively, the damage on this specimen around the hole is less than for the other TCP-coated and primed specimens, possibly suggesting that the Luster-on TCP forms more uniformly and provide better adhesion with the primer layer than the other TCP coatings. EDS analysis reveals the presence of zirconium in the damaged and undamaged regions, along with aluminum and oxygen.

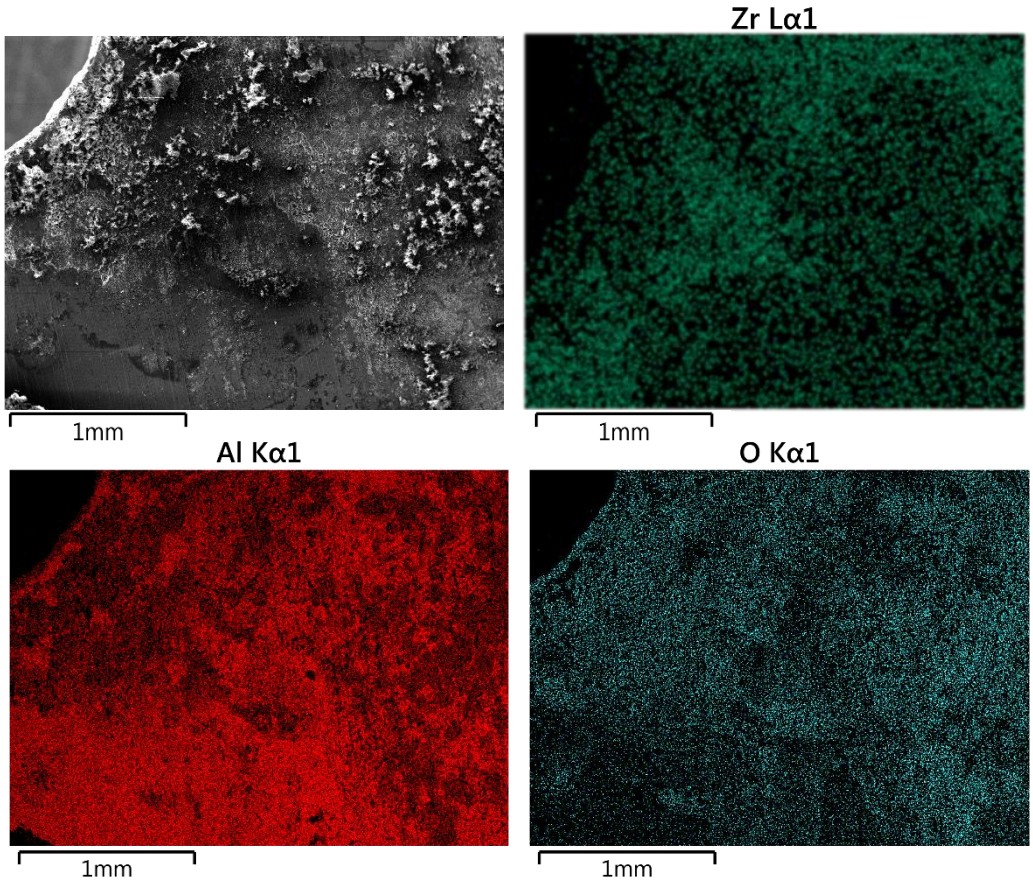

Figure 2.11. SEM micrograph and EDS elemental maps for Al and O in a region near the hole and fracture site and under a blister that was formed on a Luster-on Aluminescent coated and primed dogbone specimen after a 14-day neutral salt-spray test. There was no detectable chloride along the surface.

Digital Optical Microscopy of the Damaged Region Under the Coating

Digital optical microscopy was used to investigate the surface texture and dimensions of the damaged region under the coating system near a fastener hole. Optical micrographs of the hole region and fracture site on the uncoated control specimen are presented in Figure 2.12. For the uncoated control, as expected, there is no corrosion damage. The surface roughness for the uncoated control specimen was determined to be 0.47 ± 0.22 μm for an 80 x 110 μm^2 area based on analysis of the surface texture. This surface roughness arises from the rolling grooves resulting from the formation of the aluminum alloy sheet. The feature height, S_z, of the rolling

grooves along the uncoated control surface was 2.36 ± 0.52 µm. These data along with the surface texture analysis of the TCP-coated and primed specimens after the 14-day salt spray exposure can be found in Table 2.2.

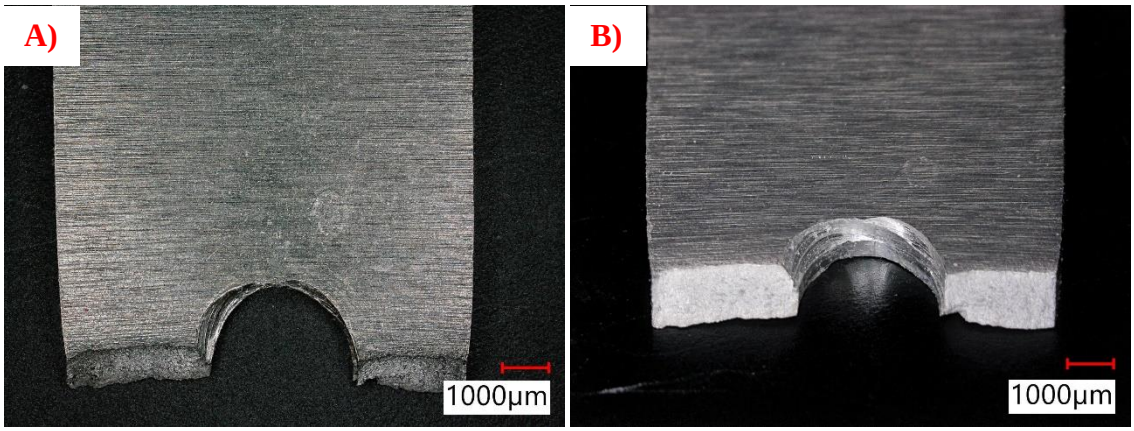

Figure 2.12. Digital optical micrographs of the bulk and area around the hole of uncoated control specimen. A) Top side of the specimen and B) image looking at the breaks and the drilled hole orthogonal to the top view.

Digital optical micrographs of the Bonderite T5900 + primed specimen after the 14-day salt spray exposure and stripping of the primer layer are shown in Figure 2.13. The micrographs show an area where a blister formed near the fastener hole. It is clear that there is significant corrosion occurring in the hole wall, and this eventually led to solution ingress under the coating system. The degradation of the conversion coating/primer interface leads to coating detachment and loss of corrosion inhibition. The degradation initially proceeds inward from the hole wall into the bulk of the specimen and then proceeds with depth into the material during the course of the salt spray exposure. It is supposed that regions of strongly adhering conversion coating and primer limit the extent of the solution ingress inward and the spread of the corrosion damage on the specimen surface. The diameter of the blister region where solution ingress occurred is 2-3 mm. The digital optical micrographs in Figures 2.13A and B reveal this damage pattern clearly. Figure 2.13 C shows a 3D surface profile created by

stitching images recorded at different focal points together. In can be seen that the inside the damaged region, a height change of up to ~15 µm is seen. The surface texture of this corroded region is rougher than the uncoated control specimen.

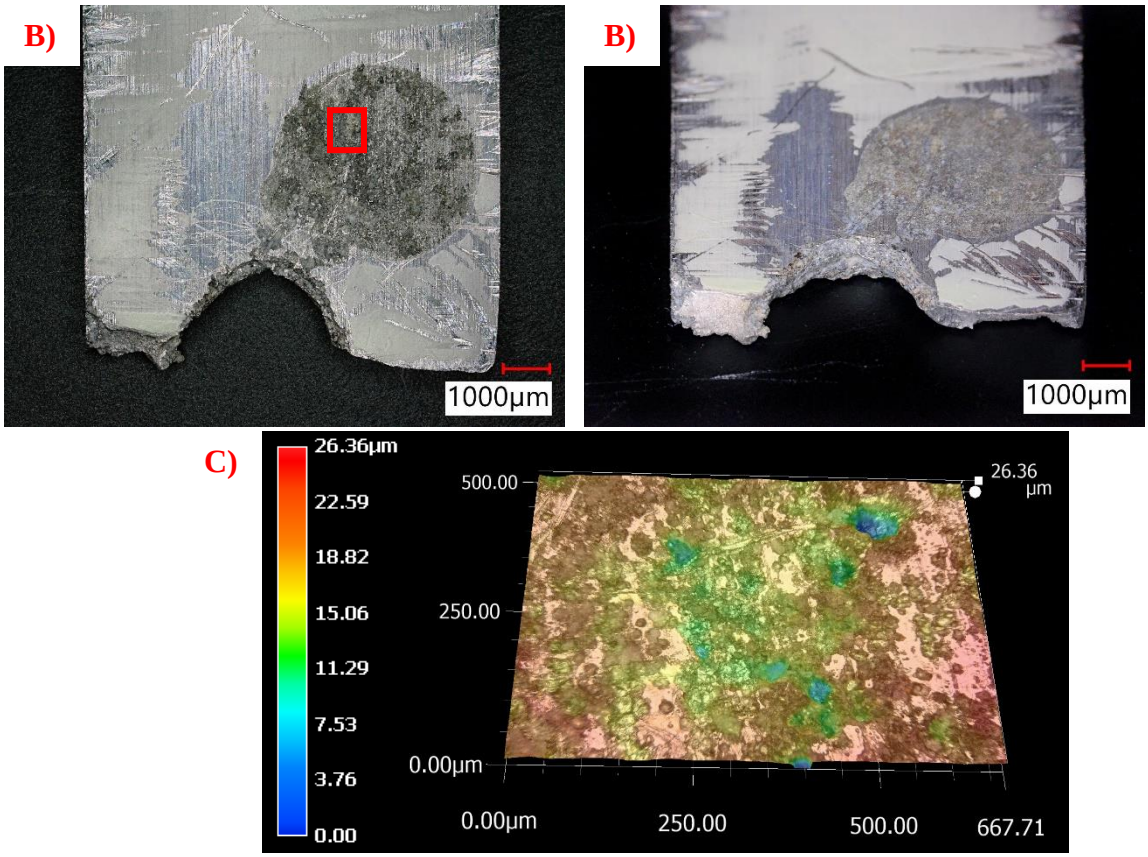

Figure 2.13. Digital optical micrographs of the bulk and area around the hole of a Bonderite T5900 TCP-coated + primed specimen after the 14-day salt-spray exposure and primer removal. A) Top side of the specimen where the screw head was positioned and B) tilted specimen revealing more of the damage pattern on the fastener hole wall. C) Height profile of the damage region where blister formation occurred. The image in presented is from the red box area in A.

Figure 2.14 shows digital optical micrographs of a Chemeon TCP-NP coated + primed specimen after the 14-day salt-spray exposure and primer removal. There is some residual primer as indicated by the two red arrows in Figure 2.14 B. Overall, the micrographs (A and B) reveal the same damage pattern seen for all of the TCP-coated and primed specimens. During the salt spray exposure, corrosion of the hole wall occurs initially. This leads to inward degradation of the material and solution ingress. Eventually the conversion coating/primer-

metal interface is compromised. This leads to corrosion damage inward into the bulk of the material in the area defined by the blister. Importantly, the extent of solution ingress into the alloy, as defined by the spatial dimension of the corroded blister area is 3-5 mm; greater than that observed for the Bonderite T5900/primer coating specimen. This is reflective of slightly less corrosion resistance provided by the Chemeon TCP-NP/primer system. Also consistent with slightly less corrosion resistance of this coating system is the 3D surface profile for the corroded area under the blister presented in Figure 2.14 C The surface texture is characterized by roughness and multiple large (~50 x 50 μm^2) and deep pits (~30 µm). In summary, the corrosion damage under the blisters was more extensive for the Chemeon TCP-NP/primer than for the Bonderite T5900/primer coating system under these test conditions.

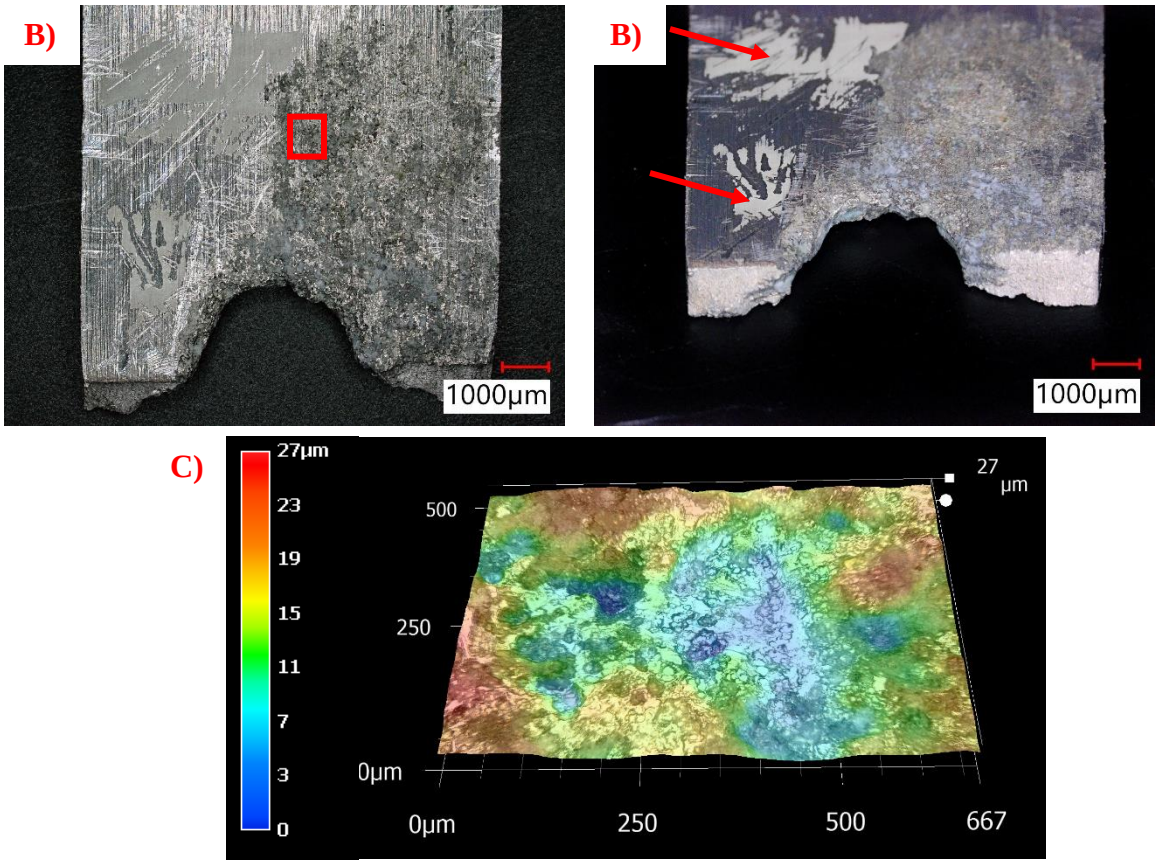

Figure 2.14. Digital optical micrographs of the bulk and area around the hole of a Chemeon TCP-NP coated + primed specimen after the 14-day salt spray exposure and primer removal. A) Top side of the specimen where the screw head was positioned and B) tilted specimen revealing more of the damage pattern on the fastener hole wall. C) Height profile of the damage region where blister formation occurred. The image in presented is from the red box area in A.

Digital optical micrographs for the SurTec 650 E conversion coated + primed specimen after the 14-day salt-spray exposure and primer removal are presented in Figure 2.15 A and B. Qualitatively, the extent of corrosion damage in the fastener hole wall and extending into the bulk alloy is far greater for this TCP/primer coating system than the other three TCP/primer coating systems. As was the case for the other coating systems, there was initial corrosion along the hole wall followed by solution ingress into the material. This led to degradation of the coating/metal alloy interface and corrosion of the unprotected alloy. The 3D surface profile for the corroded area under blister presented Figure 2.15 C reveals some significant surface

roughness and feature height variations. For example, some pits ~195 µm deep and ~200 x 200 μm^2 in area are seen.

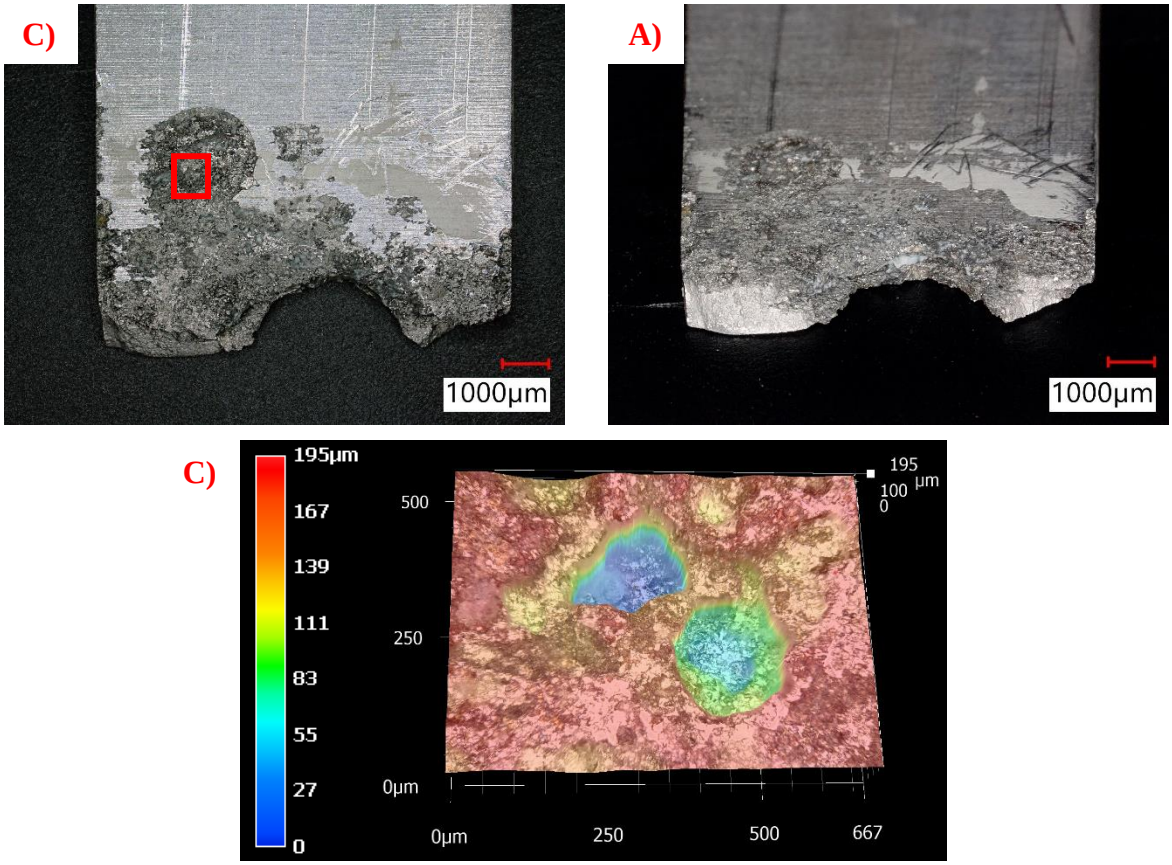

Figure 2.15. Digital optical micrographs of the bulk and area around the hole of a SurTec 650E coated + primed specimen after the 14-day salt spray exposure and primer removal. A) Top side of the specimen where the screw head was positioned and B) tilted specimen revealing more of the damage pattern on the fastener hole wall. C) Height profile of the damage region where blister formation occurred. The image in presented is from the red box area in A.

Figure 2.16A and B show digital optical micrographs of a Luster-On Aluminescent coated + primed specimen after the 14-day salt spray test and primer removal. Like the Bonderite T5900 and Chemeon TCP-NP, this TCP/primer coating system provided a similar level of corrosion protection. There is corrosion damage on the hole wall extending away from the hole by 1-2 mm where a blister formed. The micrographs reveal the area of the blister. The 3D surface profile for the corroded area under blister presented Figure 2.16 C reveals some minor

changes in surface roughness and feature height variations. No significant pitting was observed.

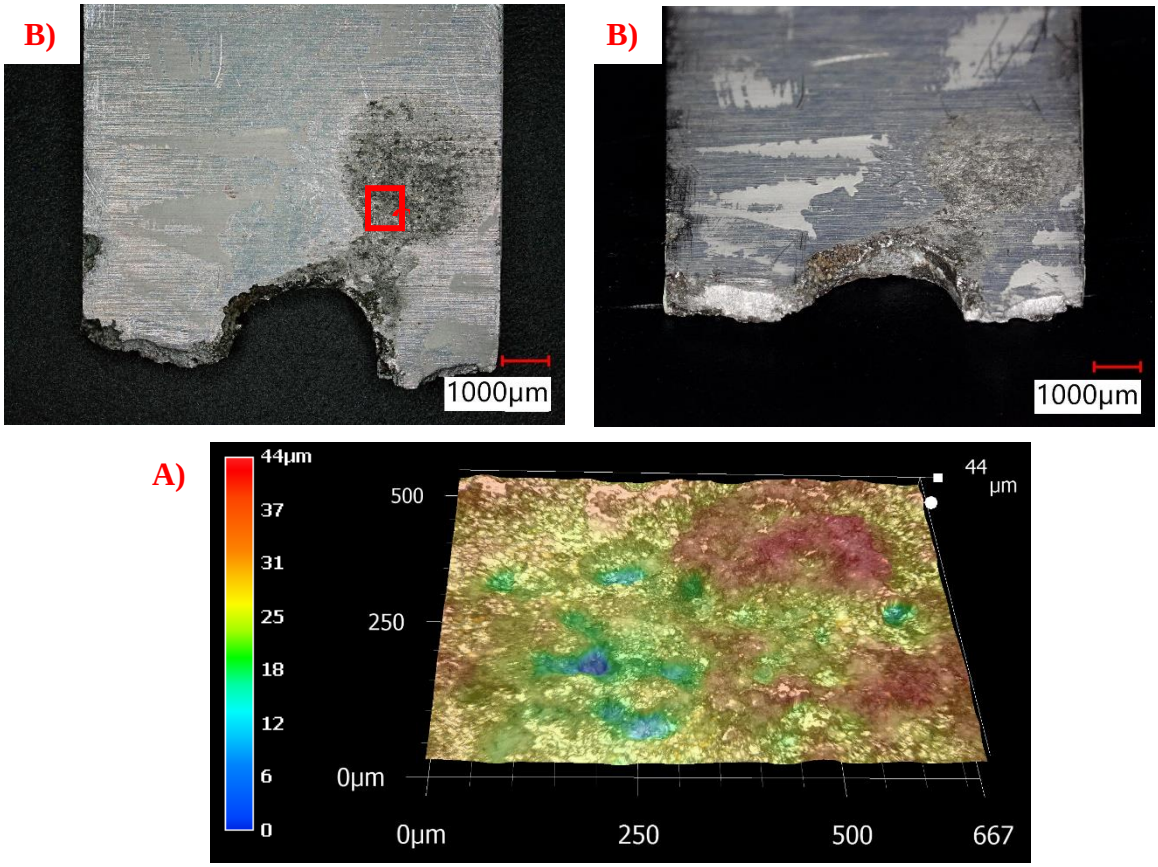

Figure 2.16. Digital optical micrographs of the bulk and area around the hole of a Luster-on Aluminescent coated + primed specimen after the 14-day salt-spray exposure and primer removal. A) Top side of the specimen where the screw head was positioned and B) tilted specimen revealing more of the damage pattern on the fastener hole wall. C) Height profile of the damage region where blister formation occurred. The image in presented is from the red box area in A.

The surface roughness, S_q, and the overall surface height change, S_z, are given for each of the coated specimens after the 14-day salt spray exposure in Table 2.2. The data are divided into two groups: data for the blister or damaged region and data for the bulk undamaged region. The data reveal that the greatest level of corrosion damage, based on the roughness and feature height analysis, was observed for the SurTec 650E/primer coating system. In the blister or corroded area, there is no statistical difference in the mean values roughness or feature height

for the other three TCP/primer coating systems. This trend in the data suggests that of the four TCP/primer coating systems, the SurTec 650/primer provides the least galvanic corrosion protection to the aluminum alloy.

Table 2.2. Summary of the Surface Texture Data for the Uncoated, and Bonderite T-5900, Chemeon TCP-NP, SurTec 650 E and Aluminescent Coated AA2024-T3 and Primed Specimens After the 14-Day Salt-Spray Exposure.

	Blister		Bulk	
	S_q (μm)	S_z (μm)	S_q (μm)	S_z (μm)
Uncoated	--	--	0.47 ± 0.22	2.36 ± 0.52
Bonderite	2.46 ± 1.01	15.08 ± 3.97	0.35 ± 0.03	2.29 ± 0.27
Chemeon	2.62 ± 0.64	17.78 ± 3.68	0.26 ± 0.02	1.94 ± 0.11
SurTec	7.02 ± 3.33	39.36 ± 7.30	0.32 ± 0.02	1.95 ± 0.10
Luster-On	2.23 ± 0.53	13.91 ± 1.71	0.51 ± 0.07	2.70 ± 0.15

80 x 110 μm^2 geometric area investigated with n=3

2.5 DISCUSSION

The goal of this work was to determine if the commercial TCP + primer coating systems provide significantly different levels of galvanic corrosion protection to AA2024-T3 as assessed during a 14-day continuous salt-spray exposure. The data reveal that the mechanical strength of the dogbone alloy specimens is reduced equivalently for all the coated specimens so, based on this test, the coatings systems provide a similar level of corrosion protection. After the 14-day salt spray exposure, all specimens exhibited discoloration and blistering near the fastener hole. The discoloration could be due to degradation of the Ti-6Al-4V screw or corrosion of the underlying aluminum alloy. The blistering may result from corrosion of the aluminum and accumulation of corrosion products at the interface of coating and metal. During the salt-spray exposure, alloy corrosion develops initially in the fastener hole wall. This is followed by ingress of water and aggressive chloride anions. This appears to cause degradation and failure by filiform corrosion under the coating system and blistering followed by delamination of the TCP/primer coating.

It appears that defects exist in these coatings on the fastener hole wall or the sharp whole edges from the time of their application. Alternately, defects may form over time leading to galvanic interaction between the fastener in the hole and the underlying aluminum alloy. These coating defects on the hole walls are detrimental to coating performance. It appears that forming well adhering and low defect coatings in the hole wall is critical for minimizing galvanic corrosion in these types of specimens.

While the mechanical strength reduction was similar for all four TCP/primer coatings, there were some differences in the extent of the corrosion damage away from the hole and the surface texture of the corroded aluminum alloy under the coating blisters. The least extensive corrosion damage away from the fastener hole and the lowest surface roughness and feature height differences were seen equivalently for the Bonderite T5900, Chemeon TCP-NP and Luster-on Aluminescent/primer coating systems. In contrast significantly more corrosion damage away from the hole and greater changes in the surface texture were observed for the SurTec 650E/primer system.

2.6 CONCLUSIONS

In this work, four commercial TCP coatings were applied to AA2024-T3 dogbone specimens to compare the tensile strength changes and galvanic corrosion damage after 14-day continuous salt-spray exposure. The specimens were primed with a non-chromate primer a Ti-6Al-4V fastener was connected in the gage region to simulate a galvanic corrosion situation. The surfaces showed corrosion damage around the fastener hole, closest to the more noble fastener, and undercutting of the coating system. Blisters were generally formed due to the generation of gas on the nearby fastener (water reduction to generate H_2 on the nearby Ti-6Al-4V surface, $2H_2O + 2e^- \rightarrow H_2 + 2OH^-$) and corrosion product build up on the nearby

exposed aluminum alloy (e.g., $2Al + 3H_2O \rightarrow Al_2O_3 + 6e^-$) . Overall, the least amount of alloy corrosion damage was found for the Luster-On Aluminescent + primer coating system. The reduced corrosion damage was evidenced by lower surface roughening and feature heights when compared to the other TCP+ primer coating systems. There was wide-spread damage found for the Chemeon NP and SurTec 650E coated specimens and the later showed the largest change in surface roughness and feature height in the damaged regions of the specimens. The variations in the formulation of the TCP coatings do influence the amount of damage and severity of the damage. With the damage to the specimens there was a decrease in tensile strength for the exposed specimens from the unexposed, but there was no statistical difference found among the four TCP coatings in tensile strength after exposure.

REFERENCES

REFERENCES

1. Davis, J. R., *Alloying: Understanding the Basics-Light Metals and Alloys*. 2001.

2. Davis, J. R.; Associates, *ASM International. Handbook Committee, Aluminum and Aluminum Alloys*. 1993.

3. Davis, J. R., *Corrosion of Aluminum and Aluminum Alloys*. 1999.

4. Polmear, I. J., *Light Alloys*. 2005.

5. Mavhungu, S. T.; Akinlabi, E. T.; Onitiri, M. A.; Varachia, F. M., Aluminum Matrix Composites for Industrial Use: Advances and Trends. *Procedia Manufacturing* **2017,** *7*, 178-182.

6. Twite, R. L.; Bierwagen, G. P., Review of Alternatives to Chromate for Corrosion Protection of Aluminum Aerospace Alloys. *Prog. Org. Coat.* **1998,** *33* (2), 91-100.

7. Costa, M., Toxicity and Carcinogenicity of Cr(VI) in Animal Models and Humans. *Critical Rev. Toxicol.* **1997,** *27*, 431-442.

8. Akiyama, E.; Markworth, A. J.; McCoy, J. K.; Frankel, G. S.; Xia, L.; McCreery, R. L., Storage and Release of Soluble Hexavalent Chroium from Chromate Conversion Coatings. *J. Electrochem. Soc.* **2000,** *150* (2), B83-B91.

9. Xia, L.; Akiyama, E.; Frankel, G.; McCreery, R., Storage and Release of Soluble Hexavalent Chromium from Chromate Conversion Coatings: Equilibrium Aspects of Cr VI Concentration. *J. Electrochem. Soc.* **2000,** *147* (7), 2556-2562.

10. Whitman, B. W.; Li, L.; Swain, G. M., Anti-Corrosion Properties of a TCP Pretreatment Conversion Coating on Aluminum Alloy 2024-T3 during Moist SO_2 Atmospheric Testing: Effects of Galvanic Coupling. *J. Electrochem. Soc.* **2017,** *164* (4), C135-C147.

11. Li, L.; Swain, G. M., Effects of Aging Temperature and Time on the Corrosion Protection Provided by Trivalent Chromium Process Coatings on AA2024-T3. *Appl. Mater. Interfaces* **2013,** *5*, 7923-7930.

12. Li, L.; Swain, G. P.; Howell, A.; Woodbury, D.; Swain, G. M., The Formation, Structure, Electrochemical Properties and Stability of Trivalent Chrome Process (TCP) Coatings on AA2024. *J. Electrochem. Soc.* **2011,** *158* (9), C274-C283.

13. Li, L.; Whitman, B. W.; Munson, C. A.; Estrada, R.; Matzdorf, C. A.; Swain, G. M., Structure and Corrosion Performance of a Non-chromium Process (NCP) Zr/Zn Pretreatment Conversion Coating on Aluminum Alloys. *J. Electrochem. Soc.* **2016,** *163* (13), C718-C728.

14. Ely, M.; Swiatowska, J.; Seyeux, A.; Zanna, S.; Marcus, P., Role of Post-Treatment in Improved Corrosion Behavior of Trivalent Chromium Protection (TCP) Coating Deposited on Aluminum Alloy 2024-T3. *J. Electrochem. Soc.* **2017,** *164* (6), C276-C284.

15. Placzankis, B. E.; Miller, C. E.; Matzdorf, C. A., GM 9540P Cyclic Accelerated Corrosion Analysis of Nonchromate Conversion Coatings on Aluminum Alloys 2024, 2219, 5083, and 7075 Using DOD Paint Systems. Army, D. o. t., Ed. Army Research Laboratory, 2003; pp 1-29.

16. Shabestari, S. G.; Moemeni, H., Effect of Copper and Solidification Conditions on the Microstructure and Mechanical Properties of Al-Si-Mg Alloys. *Journal of Materials Processing Technology* **2004,** *153*, 193-198.

17. Rana, R. S.; Purohit, R.; Das, S., Reviews on the Influences of Alloying Elements on the Microstructure and Mechanical Properties of Aluminum Alloys and Aluminum Alloy Composites. *International Journal of Scientific Research Publications* **2012,** *2* (6), 1-7.

18. Nakai, M.; Eto, T., New aspect of development of high strength aluminum alloys for aerospace applications. *Materials Science and Engineering: A* **2000,** *285* (1), 62-68.

19. Kuo, T. Y.; Lin, H. C., Effects of pulse level of Nd-YAG laser on tensile properties and formability of laser weldments in automotive aluminum alloys. *Materials Science and Engineering: A* **2006,** *416* (1), 281-289.

20. Clauer, A. H.; Fairand, B. P.; Wilcox, B. A., Laser Shock Hardening of Weld Zones in Aluminum Alloys. *Metallurgical Transactions A* **1977,** *8A*, 1871-1876.

21. Inoue, A.; Kimura, H., High-strength aluminum alloys containing nanoquasicrystalline particles. *Materials Science and Engineering: A* **2000,** *286* (1), 1-10.

22. Kobayashi, T., Strength and fracture of aluminum alloys. *Materials Science and Engineering: A* **2000,** *280* (1), 8-16.

23. Guo, Y.; Frankel, G. S., Characterization of trivalent chromium process coating on AA2024-T3. *Surface and Coatings Technology* **2012,** *206* (19), 3895-3902.

CHAPTER 3. SEALING SULFURIC ACID ANODIZED ALUMINUM ALLOY 2024-T3 WITH THE TRIVALENT CHROMIUM PROCESS CONVERSION COATING

3.1 INTRODUCTION

Aluminum alloys are used in the aerospace industry due to their high strength to weight ratio, but the susceptibility to corrosion is high for the 2xxx alloy series due to the incorporation of copper as a main alloying element.[1-6] The aerospace industry faces a continuous battle with the control and mitigation of corrosion. The primary way environmental corrosion is inhibited is using a multi-layer coating system. The coating system generally consists of a thin conversion coating layer (100-300 nm thick), a primer layer (microns thick) and a topcoat or paint overlayer (microns thick).[7] The conversion coating layer aids with the corrosion resistance but also promotes adhesion with the primer layer. Proper surface pretreatment is essential for forming low defect and well adhering coatings to aluminum alloys[8,9]

A surface pretreatment that is used to passivate the aluminum and the aluminum alloys is by using an anodic oxide insulating layer. Anodizing is a durable and corrosion resistant layer formed through electrochemical processes by using an acid and either constant current or constant voltages. Chromic acid anodizing enhances the corrosion resistance of the underlying alloy, but with the use of the toxic Cr(VI) as the base for the acid, a suitable replacement is needed.[7, 10-12] Sulfuric acid, and others, have been found to be suitable replacements to the formation of the anodic oxide layer on aluminum alloys.[12] The sulfuric acid anodizing technique produces columnar pores and at the base of the pores lies a dense barrier layer at the oxide/substrate interface.[11, 13-15]

These oxide layers are open pores that stretch down to the base and to help prevent damage the pores are sealed typically with hot water hydrothermal sealing or a nickel acetate solution.[16] These processes, while effective, do have drawbacks and thus an alternative to these is needed to seal the porous oxide layer. Trivalent Chromium Process (TCP) coatings have shown excellent protection to aluminum alloys,[8, 9, 17-20] and has been shown by our group to be a viable sealing method.[21]

This work focuses on the *i*) surface morphology and sealing of the TCP coatings, *ii*) the corrosion resistance of two TCP coatings as sealants for anodic oxides produced through sulfuric acid anodizing, and *iii*) the correlation of the electrochemical behavior to accelerated degradation testing.

3.2 MATERIALS AND METHODS

Reagents

Turco 6849 (20% v/v, Henkel Corp., Madison Heights, MI) and Luster-On 401 (4% w/v, Luster-On Products Inc., Springfield, MA) were the commercial degreasing solutions used. Turco Liquid Smut-Go (20% v/v, Henkel Corp., Madison Heights, MI) and Luster-On 485 (3.9% v/v, Luster-On Products Inc., Springfield, MA) served as the deoxidizing solutions. Bonderite T-5900 RTU (Henkel Corp., Madison Heights, MI) and Luster-On Aluminescent (1% w/v, Luster-On Products Inc., Springfield, MA) were the commercial TCP coating baths studied. Sulfuric acid (95-98%), sodium sulfate (Na_2SO_4), sodium chloride (NaCl), nickel (II) acetate, potassium dichromate, sodium carbonate, and calcium chloride were all purchased from Sigma Adrich (St. Louis, MO). Cobalt acetate was purchased from Spectrum Chemical Manufacturing Corp. (Gardena, CA). Nitric acid was purchased from Fisher Scientific (Hampton, NH). All chemicals were technical or reagent grade quality, or better, and used

without additional purification. All solutions were prepared with ultrapure water (Barnstead E-Pure) having a resistivity of >17 MΩ · cm.

Specimen Preparation

Aluminum alloy 2024-T3, purchased as 12 in. x 12 in. sheets from OnlineMetals.com, was used in these studies. The metal sheet was 2-mm thick and cut into 1 in^2 squares. The 1 in^2 specimens were then abraded on a wet 1500-grit Al_2O_3 sandpaper and then polished sequentially with 0.3 and 0.05 μm diam. alumina powder slurried with ultrapure water. Each polishing step was performed by hand on a dedicated felt polishing pad until a mirror-like finish was achieved. The specimens were rinsed with and ultrasonically cleaned in ultrapure water for 20 min then ultrasonically cleaned in isopropyl alcohol for 20 min after each abrading and polishing step to remove debris. The cleaned specimens were then degreased for 10 min at 55°C and rinsed with flowing city tap water for 2 min. The specimens were deoxidized for 2 min followed by a 2 min flowing city tap water rinse and dried with N_2 gas for anodizing.

Sulfuric Acid Anodization

The electrolyte used was 9.8 wt.% sulfuric acid (SA). The cathode was a stainless steel (type 316) plate. The stainless-steel cathode and aluminum alloy anode were equivalent geometric areas (1 in^2). The cathode was positioned parallel to and 1.5 inches from the anode in the electrolyte solution. The electrodes were connected to a DC power supply (Tenma) that provided the constant voltage for anodization. The specimens were immersed in the solution vertically with three-quarters of each immersed into the electrolyte solution. For anodization, the applied voltage to the anode was stepped at 5 V/min from 0 to 15 V (3 min total period) and then held at this voltage for an additional 20 min. Thus, the total anodization time was 23 min. For SA anodization, MIL-A-8625F (Military Specification: Anodic Coatings for

Aluminum and Aluminum Alloys) calls for an anodic coating weight (oxide layer weight) of 1000 mg/ft^2, or greater. The ASTM B137 ((Standard Test Method for Measurement of Coating Mass Per Unit Area on Anodically Coated Aluminum) method describing the chromic acid anodic stripping method for determining the oxide coating weight was applied to some anodized specimens. After anodization, the specimens were immersion rinsed in ultrapure water for 10 min and then left to dry overnight in a desiccator. This post-treatment produced the most consistent oxide weight and coating morphology after anodization. The current density was recorded each minute during the anodization. Figure 3.1 shows the electrochemical set-up used for the anodization process.

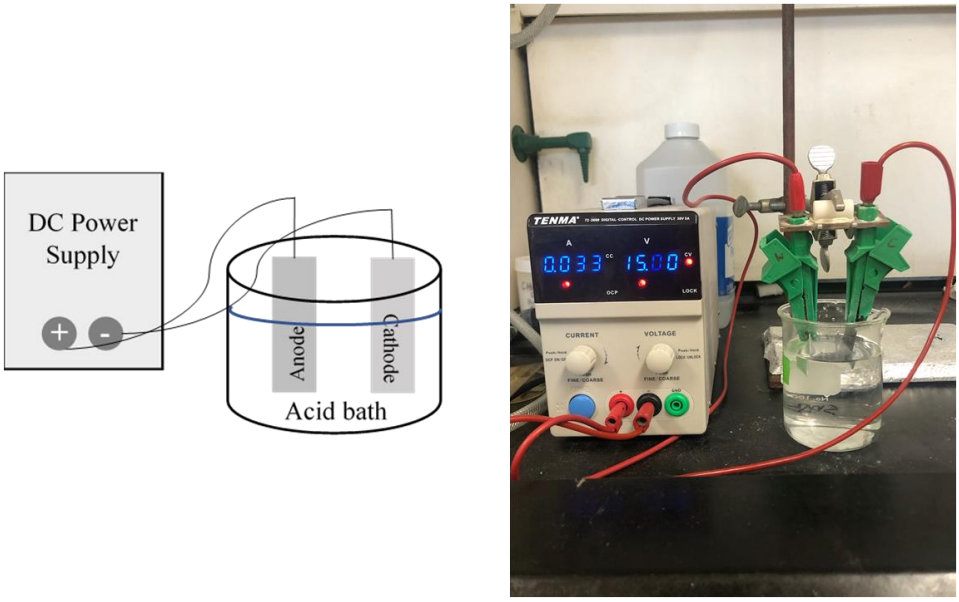

Figure 3.1. Experimental set-up used for all anodizing procedures. A clamp was used to immerse the anode and cathode in the sulfuric acid electrolyte with 75% of specimen immersed. The cathode was cleaned after each anodization by a light polish and the electrolyte replenished after three anodization treatments. The left is a cartoon version of the setup d on the right.

Bonderite T-5900 (Henkel) TCP Seal

Anodized specimens were immersion sealed with Bonderite T-5900 TCP. The optimized sealing conditions were determined to be room temperature using an immersion time of 10 min. Electrochemical measurements were used to determine that the 10-min sealing period was

optimum. This determination was based on which sealing time (1, 5, or 10 min) provided the greatest improvement in the corrosion resistance of the anodized alloy. The electrochemical parameters used for this assessment were the anodic and cathodic currents in potentiodynamic polarization curves, the low frequency ($Z_{0.01}$ Hz) impedance modulus in EIS measurements, and the polarization resistance (R_p), as determined from linear sweep voltametric curves. The specimens were immersion sealed with periodic agitation, as needed, to remove any gas bubbles that formed at the surface. After sealing, the specimens were rinsed by immersion in city tap water for 2 min and then rinsed with flowing ultrapure water for 30 s. Excess water was wicked from the surface and the specimens were left face up to dry overnight in the lab air before any further testing.

Luster-On Aluminescent TCP Seal

Anodized specimens were also immersion sealed with Luster-On Aluminescent TCP. The optimized sealing conditions were determined to be room temperature and an immersion time of 5 min. Again, the optimum sealing time was determined based on electrochemical assessment of the sealing time (1, 5 or 10 min) that provided the greatest improvement in corrosion resistance of the anodized alloy. The specimens were immersion sealed with periodic agitation, as needed, to remove any gas bubbles. After sealing, the specimens were immersion rinsed in city tap water for 2 min and then rinsed with flowing ultrapure water for 30 s. Excess water was wicked from the surface and the specimens were left face up to dry overnight in lab air before any further testing.

Hot Water Seal

Ultrapure water was also used to hydrothermally seal the anodized specimens, for comparison. Hot water immersion is a common sealing method for anodic coatings on

aluminum alloys. The water was heated to 90 ± 3 °C and was held at that temperature throughout the sealing process. Sealing the anodized specimens was performed by immersion in the hot water for 30 min. After sealing, excess water was wicked from the surface and the specimens were left face up to dry overnight in lab air before any further testing.

Nickel Acetate Seal

Nickel acetate immersion was also used to seal the anodized specimens, for comparison. This too is a common method for sealing anodic coatings on aluminum alloys. The nickel acetate solution composition consisted of 5 g/L nickel acetate, 1 g/L cobalt acetate, and 8 g/L boric acid. The pH of the sealant bath was maintained between 5 and 6. The sealing was performed by immersing the anodized specimens for 15 min at 80 °C. After sealing, excess water was wicked from the surface and the specimens were left face up to dry overnight before any further testing.

Oxide Weight Determination

The weight of the oxide formed by SA anodization of AA2024-T3 was determined using the chromic acid anodic stripping method described in ASTM B137 (Standard Test Method for Measurement of Coating Mass Per Unit Area on Anodically Coated Aluminum). In this method, the anodized AA2024-T3 specimen was aged for 24 h before stripping the oxide to allow for complete drying. The sample was then weighed before placement in the stripping solution. The stripping solution (1L) contained 20 g CrO_3 + 35 mL of phosphoric acid. The specimen was immersed in the stripping solution for 5 min to dissolve the oxide. The specimen was then rinsed with ultrapure water and dried thoroughly with a stream of N_2 gas before measuring the weight change. The 5-min immersion and weight loss measurements were repeated until a stable weight was achieved (± 0.001 g). Typically, a total immersion time of

15 min was required to entirely dissolve the oxide and achieve a constant specimen weight. Three anodized specimens were tested for statistical analysis with the results presented in Table 3.1. For the 23 min/15 V DC SA anodization, the nominal oxide weight was 1900 ± 154 mg/ft^2 (n = three anodic coatings)

Table 3.1. Oxide Weights for SA Anodized AA2024-T3 Specimens (23 min/ 15 V DC)

	Before Stripping (µg)	After Stripping (µg)	Difference (µg)	Oxide Weight (mg/ft^2)
Specimen 1	1727200	1716050	11150	2073
Specimen 2	1729810	1720260	9550	1775
Specimen 3	1740000	1730036	9964	1852

Area of Oxide was 0.00538 ft^2. The nominal oxide weight was 1900 ± 154 mg/ft^2

3.3 TESTING AND CHARACTERIZATION

Electrochemical Measurements

The unsealed and sealed anodized specimens were electrochemically characterized using open circuit potential (OCP) measurements, full frequency electrochemical impedance spectroscopy (EIS) measurements at the OCP, linear polarization resistance measurements, and potentiodynamic polarization curves. The electrolyte used in all the measurements was naturally aerated 0.5 M Na_2SO_4 + 0.01 M NaCl. All electrochemical measurements were conducted in a 1 cm^2 flat cell (Biologic Science Instruments) using a computer-controlled electrochemical workstation (Gamry Instruments, Inc, Reference 600, Warminster, PA). The cell design is shown in Figure 3.2. An aluminum alloy specimen was mounted in the cell against a Viton® O-ring that defined the exposed geometric area, 1 cm^2. All currents reported herein are normalized to this geometric area. The counter electrode was a Pt flag, and the reference was a home-made Ag/AgCl electrode (4 M KCl, E^0 = +0.197 V vs. NHE) that was

housed in a Luggin capillary with a cracked glass tip. Data were collected at the OCP using 7 points per frequency decade from 10^5 to 10^{-2} Hz to determine the frequency dependence of the real (ohmic) and imaginary (capacitive) components of the total impedance. Linear polarization resistance measurements were performed by linear sweep voltammetry at potentials ±20 mV vs. OCP. Potentiodynamic polarization curves were recorded from ±20 mV vs. OCP to either 500 mV for the anodic curves or -1.2 V for the cathodic curves. These curves provided insight on the anodic (oxide formation and localized pitting) and cathodic (oxygen reduction) reaction rates. Electrochemical measurements were collected in the following way: OCP, EIS at OCP, a second OCP was measured to ensure no changes, then short linear polarization resistance measurement, followed by either anodic or cathodic potentiodynamic polarization curves. The anodic and cathodic potentiodynamic polarization curves were collected on separate specimens.

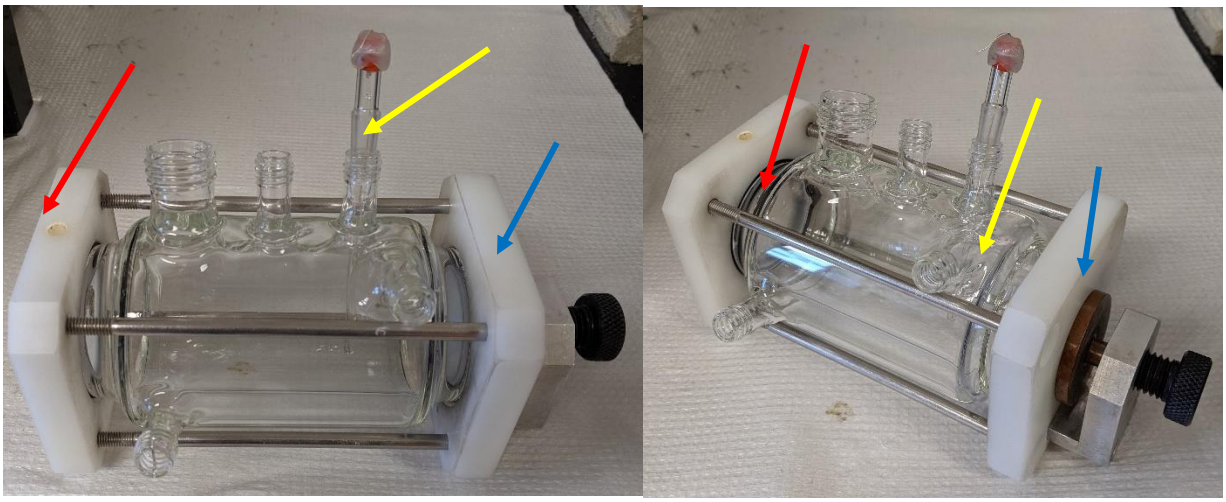

Figure 3.2. Single compartment glass H-cell used for the electrochemical measurements. The counter electrode was a platinum flag mounted at the left end of the cell (red arrow), the reference electrode, Ag/AgCl, was placed close to the working electrode (yellow arrow), and the working electrode was held in place via o-ring and copper plate (blue arrow). The two photographs are of the same cell but at different angles to display the copper plate current collector (working electrode end).

Continuous Neutral Salt-Spray (ASTM B117) Exposure

Specimens 1 in^2 in area were placed at a ~20° angle (with respect to the vertical axis) on plastic racks inside a salt-spray chamber (Associated Environmental Systems, MX-40, 4 ft^3). The solution reservoir was filled with a 5 wt. % NaCl solution. The test specimens had an exposed area near the top that was not anodized, and this area was masked off with corrosion tape. The salt fog exposure was conducted according to ASTM B117 (Standard Practice for Operating Salt Spray (Fog) Apparatus) for 14 days (35°C). At the end of the test period, the specimens were removed, rinsed thoroughly with ultrapure water, and dried under a stream of N_2 gas. Ultrasonic cleaning in ultrapure water was performed to dissolve salts and remove weakly adhering corrosion product from the surface. Nitric acid ultrasonic cleaning, as is commonly used to remove corrosion produce from aluminum alloy specimens after salt spray exposure, was not performed after the salt spray exposure in these experiments so as to not remove any of the oxide through etching or alter the surface of the sealant layer after the 14-day test.

Scanning Electron Microscopy/Energy Dispersive X-ray Spectroscopy

Scanning electron microscopy (SEM) and energy dispersive x-ray spectroscopy (EDS) were performed using a field emission electron microscope (JOEL 7500F) equipped with an Oxford EDS system for elemental analysis. These measurements were performed to assess the porous oxide layer surface morphology and the location of TCP coating elements (Zr, Cr, F, and O) within the oxide. The latter measurements were performed on cross-sections of specimens that were prepared by focused ion beam milling. The measurements were performed using instruments at the Center for Advanced Microscopy (MSU).

Scanning Electron Microscopy/ Focused Ion Beam Milling

A field emission scanning electron microscope (Auriga XB Crossbeam) was used for imaging that was equipped with a gallium focused ion beam (FIB) for performing milling. The gallium ion beam was generated at 30 kV. An ion beam current of 4 nA was applied to the specimen at a 45˚ angle for large cross-section cuts. A 600-pA ion beam current was used for fine cleaning of the cross-section. The microscopy and milling were performed on an instrument at the Composite Materials and Structures Center (MSU).

Digital Optical Microscopy

Digital microscopy was performed to assess the surface morphology/texture of the oxide layer and alloy surfaces prior to and after a 14-day neutral salt spray exposure. A digital microscope (Keyence VHX-6000) was used to record images at variable magnifications. Digital images of the surface were captured as each different area comes into focus, combining them into one fully focused (stitched) image. The microscope uses a depth of defocus method to calculate three-dimensional depth information based on the amount of defocusing of two-dimensional images. Surface roughness data were obtained from the areas measured at different points on a specimen. The depth resolution was ca. 0.2 µm. The measurements were made on an instrument at the Center for Advanced Microscopy (MSU).

Scanning Optical Profilometry

Surface contour profiles were obtained using a WYKO Optical Profilometer along with the associated instrument software, Vision for RST Plus (version 1.8). The instrument used an 10x magnification lens along with a field of view lens of 2x that produced images at a 20x magnification. Five areas across each specimen were probed in a grid like pattern to verify the overall surface texture. The topography was profiled by stitching focused images from 10 µm

above to 10 μm below the surface at each measurement point. The WYKO Optical Profilometer collects this same image 5 times and removes any unfocused areas by averaging the scans together giving one fully focused image. 3D images and contour plots were collected over an area of 306 x 230 μm^2 to profile the surface texture and to calculate the surface roughness.

Glow Discharge Optical Emission Spectroscopy/EDS

Glow discharge optical emission spectroscopy (GD-OES) was performed using a Leco GDS 850 A Glow Discharge Optical Emission spectrometer at Henkel Technologies (Madison Heights, MI). GD-OES is a useful measurement method for investigating the elemental composition of coatings and films from the surface down to tens of microns with a depth resolution that can be as good as 1 nm. SEM/EDX was done with a JSM 5900-LV. For EDS analysis, samples were secured to an aluminum stage with double sided copper tape. Samples were analyzed at a working distance of 12 mm in high vacuum with a spot size of 71. All analysis was done at 500x magnification. Samples were then analyzed by GD-OES, using program Henkel RF QDP (Ar RF plasma, 20 W and 1,000 V), and was allowed to run for 10 min. The sputter rate is determined through the time of 6,000 s and the frequency of 10 Hz. A spot size of 4 mm was investigated at 3 locations along the specimen. Argon was used to generate the plasma.

3.4 RESULTS

Current Density Passed During Controlled Voltage Anodization

The current density was measured during each minute of the controlled voltage anodization in the SA bath. The results for multiple specimens are presented in Figure 3.3. The current density nominally increased with time during the early stages of anodization trending toward

a constant value at later stages. This increase in current is due to the oxide layer growth over time as progressively more of the alloy surface gets anodized. The near-constant current reflects a constant rate of oxide film formation. The current density at 20 min is ~35 mA/cm^2.

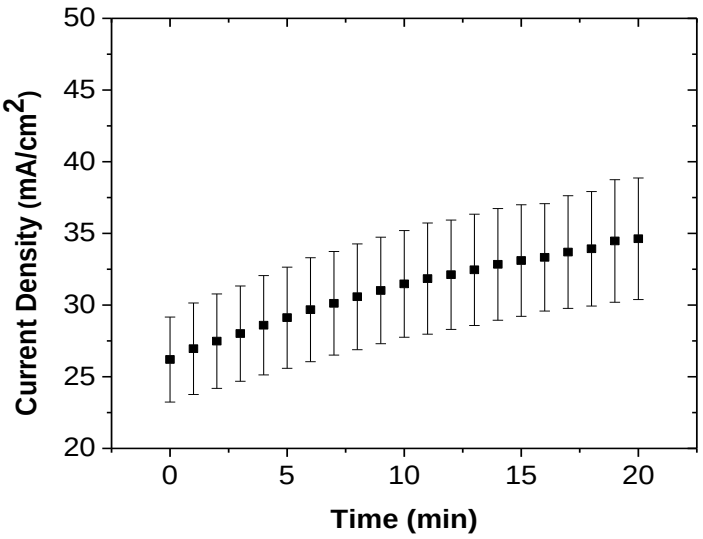

Figure 3.3. Current density recorded for AA2024-T3 specimens during each minute of the SA anodization after reaching 15 V. Data are presented as mean ± standard deviation for n ≥ 15 specimens.

Oxide Morphology for SA Anodized Specimens Before and After Sealing

Figure 3.4 presents scanning electron micrographs (secondary electron) of specimens anodized in SA similarly and sealed by the different methods. As compared to the micrograph for the unanodized specimen (Figure 3.4 upper left), the SA anodization forms a porous oxide coating over the surface (Figure 3.4 upper right). The pores range in size from 20-50 nm for the smaller ones and 85-120 nm for the larger ones.

The micrograph of the hot water or hydrothermally sealed specimen reveals some very small, hair-like fibers protruding from the oxide surface. Most notable though is the reduced porosity after this sealing method (Figure 3.4 middle left). The hot water sealing causes swelling of the outer region of the oxide that reduces the size of the pores.[22] Underneath this swelled outer oxide around a micron deep; however, the porous oxide still exists, but with

smaller pore sizes as compared to the anodized and unsealed oxide. The reduction in outer porosity of the oxide increases the barrier properties. The micrograph of the nickel acetate-sealed specimen reveals that the surface porosity still remains (Figure 3.4 middle right). This sealing involves formation of relatively insoluble $Ni(OH)_2$ inside the pores, thus blocking the pore and increasing the barrier properties. The electron micrograph of the oxide surface after Ni acetate sealing reveals no change in the oxide morphology as this sealing method simply blocks the interior of pores with a relatively insoluble salt and does not alter the oxide coating physically or chemically.

For the TCP-sealed specimens (Figure 3.4 bottom left and right), the porous oxide is no longer visible as it is covered with the TCP conversion coating. Under the vacuum conditions of the SEM, the TCP coating exhibits mud cracking resulting from dehydration. Importantly, research has shown that these cracks are not inherently present in the coating but develop upon vacuum exposure.[23-27] The morphology of both TCP-sealed layers looks similar. Clearly, the sealant forms across the outer oxide surface with some penetration into the oxide pores, as will be shown below and has been reported previously.[21] A minor difference between the two conversion coating sealants is that the Luster-On Aluminescent has coating bath aggregates, white deposits, that decorate the surface, that are generally absent on the Bonderite T5900 coating.

Rather than simply altering the outer morphology of the oxide layer to densify it or to block pores, as is the case for the hot water and nickel acetate sealing methods respectively, the TCP sealing works by formation of a conversion coating across and within the outer oxide surface.[21] Glow discharge optical emission spectroscopy measurements (discussed below) reveal the TCP layer across the oxide coating is around 200 nm thick. Below the conversion coating the

porous oxide structure is still intact. This suggests that the TCP sealants do not seal up the pores from the very bottom of the pores, but instead forms a thin barrier layer on the outer oxide with penetration of the pores down to a depth of ~1 μm.

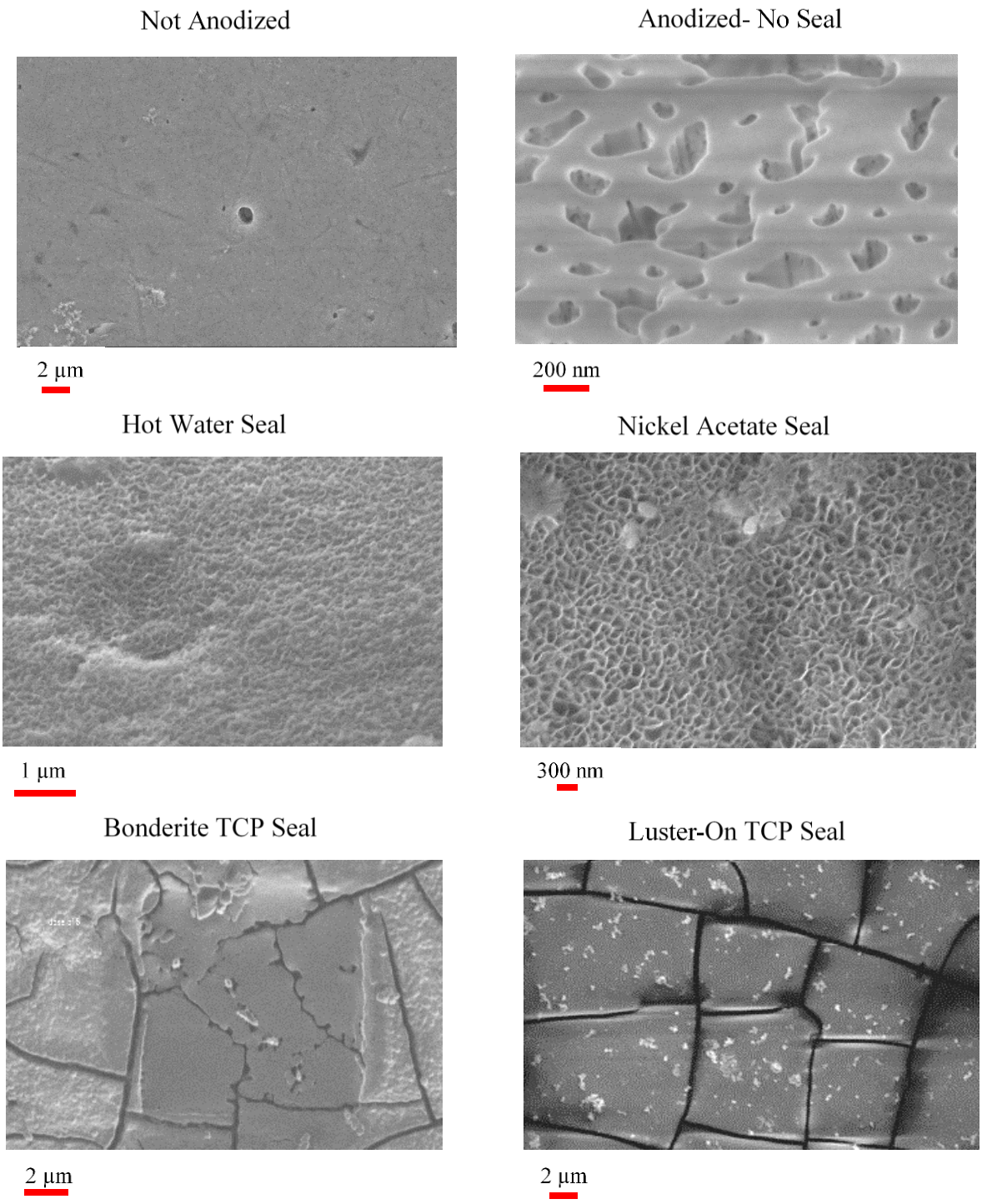

Figure 3.4. SEM micrographs showing the surfaces of each anodized and anodized + sealed AA2024-T3 specimen type. Top row shows an unanodized specimen and one anodized for 23 minutes in SA. The middle row shows SA anodized specimens (23 minutes) sealed with hot water (left) and nickel acetate (right) . The bottom row shows SA anodized specimens (23 minutes) sealed with TCP - Bonderite T5900 (left) and Luster-On Aluminescent (right). 15kV and 5 mm working distance.

Energy Dispersive X-Ray Spectroscopy

SEM-FIB cross sections presented in Figure 3.5, followed by EDS analysis, reveal the thickness of the TCP layer to be 150-300 nm depending on the location and then around 4-5 μm into the oxide. The oxide coating thickness was determined to be ca. 4-5 μm. The TCP coating elements were previously found to penetrate about 1 μm deep into the ~5 μm thick SA oxide layer.[21] The TCP sealant provides added corrosion protection by forming a barrier layer across the oxide surface, covering and partially filling the outer pores. The TCP does not reach the bottom of the pores, but it does fill most of the pores. The strength of the conversion coating adhesion was not assessed, however, qualitatively the adhesion was strong. The sealant layer inhibits the penetration of water and electrolyte to the underlying metal alloy thereby reducing the rate of corrosion and degradation.

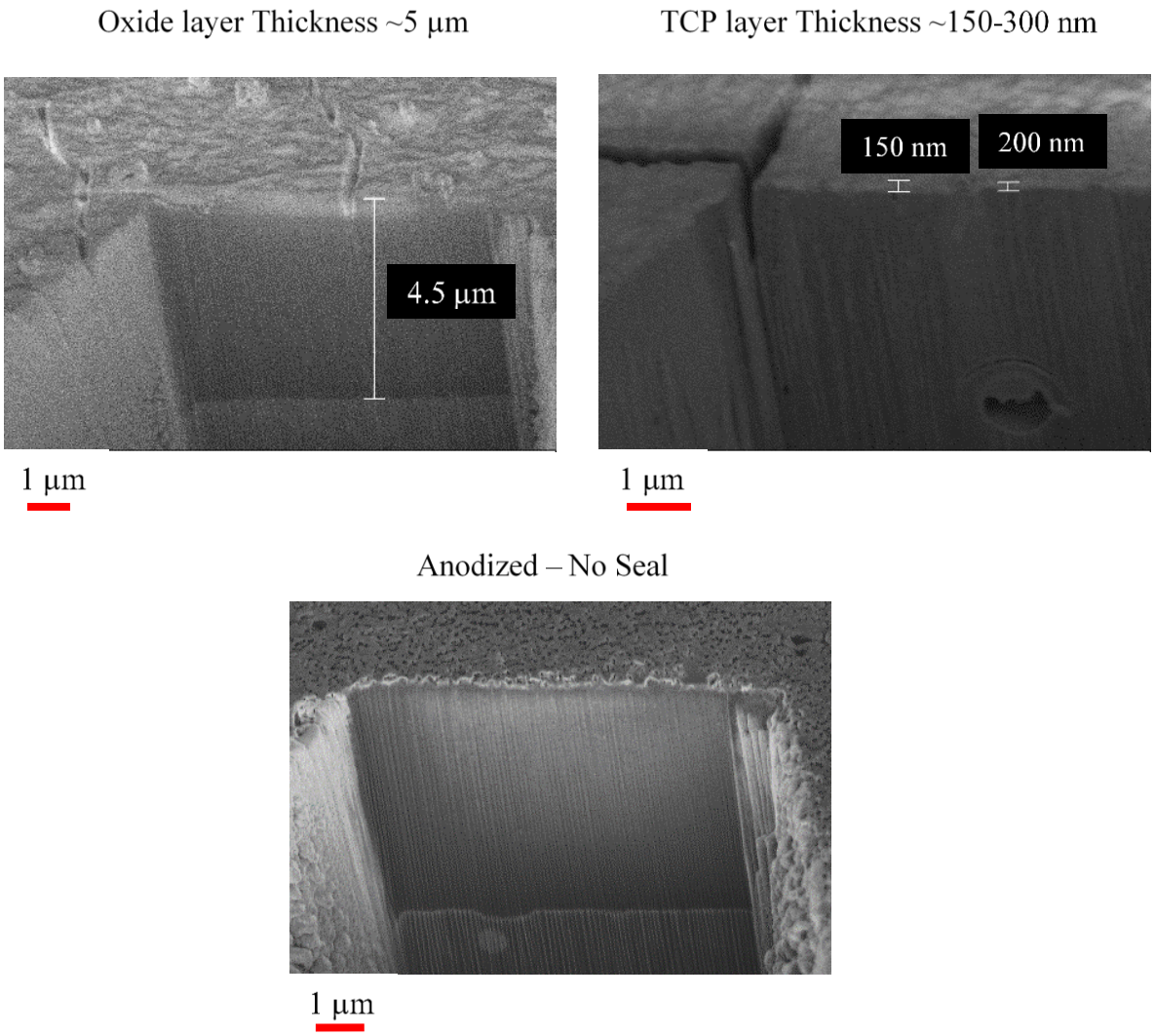

Figure 3.5. SEM-FIB micrographs showing the thickness of the oxide layer to be 4.5 µm (top left) and the thickness of the TCP barrier layer on top of the oxide to be 150-200 nm (top right). Specimens shown were anodized in sulfuric acid and sealed with Bonderite TCP (10-min immersion). Collection of depths was collected at an angle of 45°. Columnar pores normal to alloy surface are visible in bottom image. Micrographs were collected using a 2 kV accelerating voltage at 6 mm working distance. The FIB milling parameters are given in the Experimental Methods section.

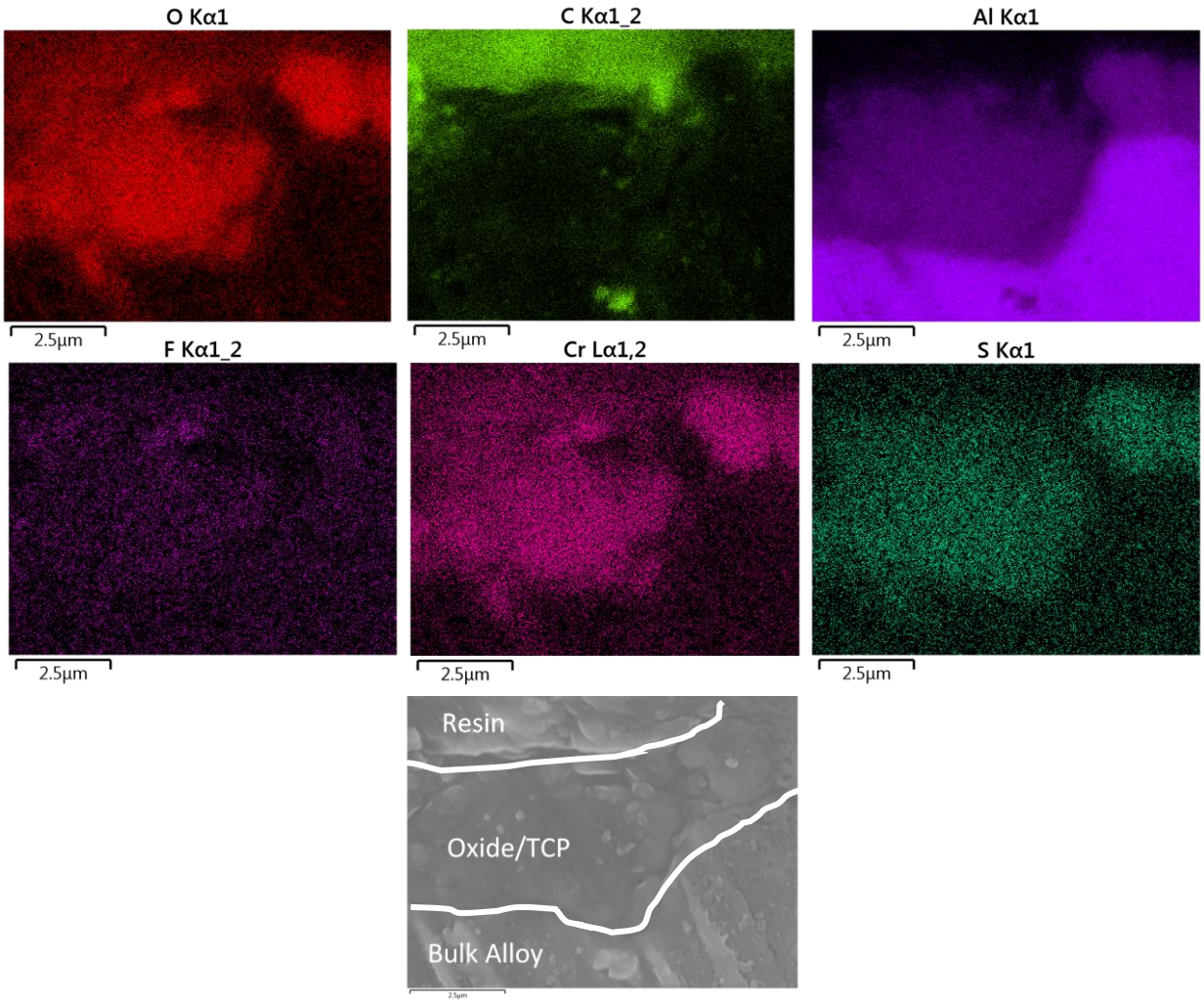

Figure 3.6. Scanning electron micrograph of a cut cross section of an anodized AA2024-T3 specimen sealed with Bonderite T5900. EDX elemental maps recorded over the cross section are presented for Al, C, O, F, Cr, and S. The white lines indicate where the organic resin meets the oxide layer and where the oxide meets the bulk aluminum alloy.

The two TCP sealant layers were further characterized by SEM-EDX to inform on the sealing mechanism and to determine how deep into the SA oxide the TCP coating penetrates. Across the sealed oxide surface, the main elements detected by EDX were Cr, F and O for both TCP coatings. These are the characteristic elements of the TCP coating baths, and the detection of these elements indicates that the coating formed over and adhered to the oxide surface. The TCP/oxide was sealed in an epoxy resin prior to collecting a cross-section and is visible in the electron image in Figure 3.6. The three regions in the electron image (resin, TCP/Oxide, and

bulk alloy) are separated by the white lines. The EDX maps show the location of the sulfur showing the oxide with incorporation of the sulfur from the bath along with the higher amounts of oxygen and a reduction in the aluminum content. This is where the oxide resides, and the TCP components were also found. The Cr and F are found to fill the oxide region suggesting that the TCP fills the pores fully. Zr was not found as the excitation energy was not high enough to detect the Zr. This was a decision made to help reduce the charging effects caused by the insulating oxide layer and the insulating epoxy resin.

Glow Discharge Optical Emission Spectrometry

GD-OES data for the elemental distribution through a TCP-sealed anodized AA2024-T3 specimen are shown in Figure 3.7 A and B. This analysis was performed to gauge the depth of penetration of the TCP coating into the passivating oxide layer. We did not perform any post-sputtering measurement of the crater depth to determine the sputter rate. The elemental signal intensities have been plotted as a percentage of the sealant/oxide layer thickness with the full thickness being the point where the signal for oxygen falls to zero. There appears to be sealant on the surface (SEM micrographs above) and within the outer oxide coating. The signals for the TCP coating elements (Zr and Cr) are highest at the oxide surface and decay in intensity in the near-surface region of the oxide coating. For example, these elemental signals are largest from 0-5% into the oxide. The Zr and Cr signal intensities extend 50-60% into the oxide coating. Given the oxide coating is ca. 5 μm, the sealant appears to penetrate 2.5-3 μm into the outer oxide, similar to what we have previously for another commercial TCP in SA anodized AA2024-T3. S is incorporated into the oxide during the anodizing process and the abundance at the outer oxide surface is greater than within the oxide as this element, as SO_4^{2-}, is present in the coating bath. The barrier layer incorporates the anions from electrolyte bath at

the start of the anodizing processes and generally has a higher amount of S present in the sulfuric acid anodized specimens.[28] At around 60% of the total oxide thickness the oxide begins to end, and the bulk of the alloy is reached. This is further confirmed with the presence of the Cu from the bulk in the presence of secondary phase particles become more evident at the 60% depth.

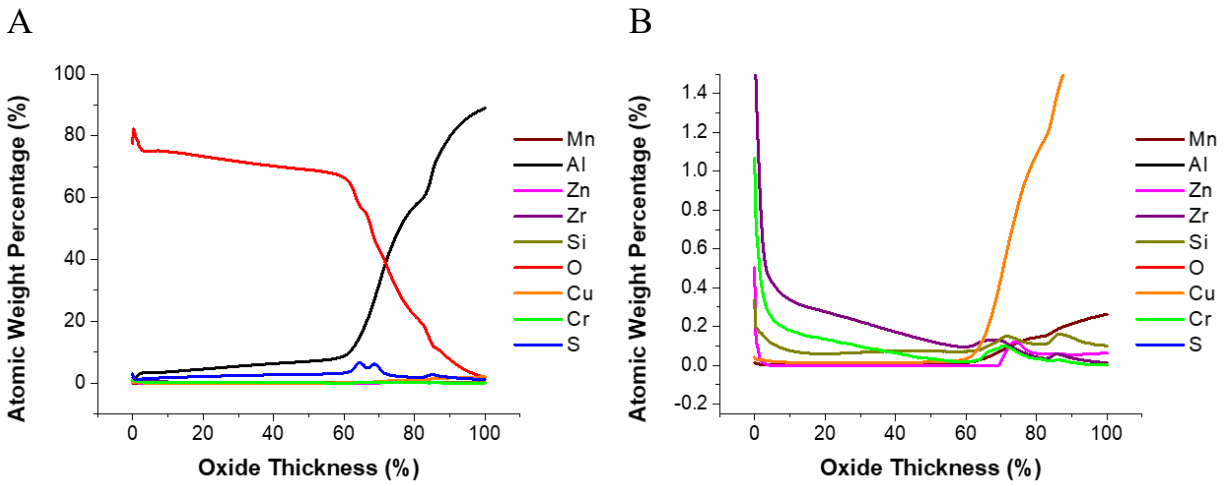

Figure 3.7. GD-OES elemental profiles for the SA anodized specimen sealed with Bonderite TCP coating. A) Full spectrum showing the full oxide depth to the bulk of the alloy. B) Oxide weight percentages from 0-5 enlarged from A to show the TCP components more clearly. Zr and Cr are found at the surface and are continued to be found throughout the oxide to the barrier layer start. Plots are average of 3 data sets.

Optimization of the TCP Sealant Time

Experiments were conducted to determine the effect of immersion time (1, 5 and 10 min) on the TCP sealant formation in terms of the sealant's impact on the electrochemical corrosion resistance. Figure 3.8 shows characteristic potentiodynamic polarization curves in the anodic direction for unanodized, SA anodized and unsealed, and SA anodized and TCP sealed specimens in naturally aerated 0.5 M Na_2SO_4 + 0.01 M NaCl. Curves are presented for SA specimens sealed for various immersion times in the Bonderite T5900 TCP bath. These curves were recorded starting at 50 mV negative of the OCP. The currents for all the TCP-sealed and the anodized and unsealed specimens are significantly lower than the current for the

unanodized specimen by 2-6 orders of magnitude. Clearly, the anodic coating and sealed anodic coating function to reduce the rate of aluminum oxidation/dissolution. The currents for the 1- and 10-min TCP-sealed specimens are lower than the current for the anodized and unsealed specimen. The specimen sealed for 5 minutes unexpectedly has increased current as compared to the anodized and unsealed specimen. In this set of data, the current for the 1-min TCP-sealed specimen is considerably lower than the currents for the 5 min TCP-sealed specimen. However, it proved difficult to reproduce this level of current reduction for the 1-min TCP sealing time as only 50% of the specimens exhibited this trend. The sealant layers tend to shift the specimen OCP toward more positive potentials consistent with greater surface passivation. Overall, analysis of the data revealed that the 10-min immersion produced a sealant layer that provided the most reduction in anodic current at these potentials (2-3 orders of magnitude), and hence the greatest level of enhanced corrosion protection. The current at these potentials arises from the oxidation of the underlying aluminum to form Al_2O_3 according to the reaction, $2Al + 3H_2O \rightarrow Al_2O_3 + 6H^+ + 6e^-$. The sealant serves to limit water and electrolyte penetration through the oxide to the underlying metal (reduced area of metal in contact), thus reducing the current for this reaction.

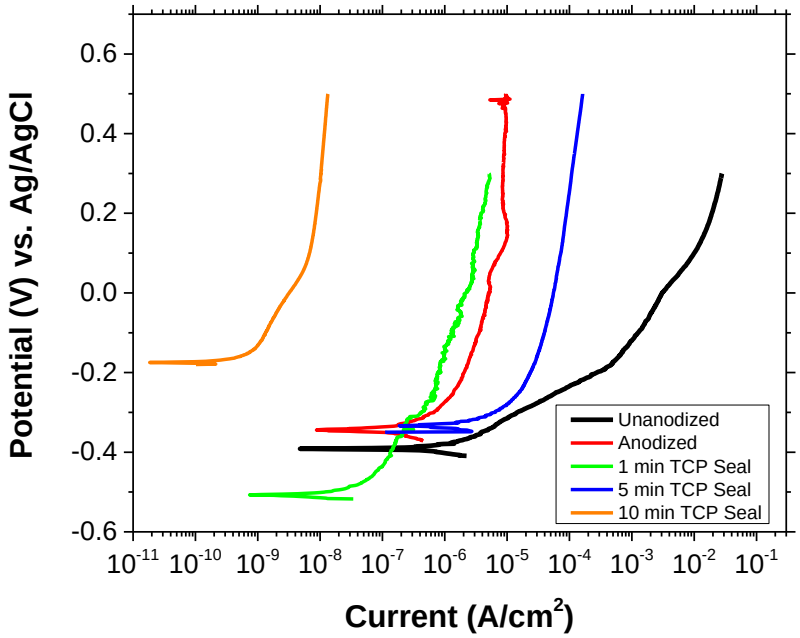

Figure 3.8. Potentiodynamic polarization curves in the anodic direction from the OCP for AA2024-T3 specimens anodized in sulfuric acid and sealed for different immersion times in Bonderite T5900. Curves for unanodized and SA anodized and unsealed specimens are presented for comparison. The measurements were made in naturally aerated 0.5 M Na_2SO_4 + 0.01 M NaCl at room temperature. The specimens were anodized in SA as described above.

Experiments were performed to determine if the immersion bath temperature has a significant effect on the sealant formation. SA anodized specimens were sealed for 10 min in Bonderite T5900 at room temperature (~23 ^oC) and 40 ^oC. Figure 3.9 presents potentiodynamic polarization curves in the anodic direction for unanodized, anodized and unsealed, and anodized and TCP sealed specimens. Again, the currents at all potentials for the anodized and anodized and sealed specimens are significantly lower than the current for the unanodized specimen. The immersion at room temperature produced the best seal of the oxide coating based on the current suppression. The effects of immersion temperature on the TCP sealant layer and oxide coating were not investigated in detail so it is unknown why the higher temperature immersion produced an inferior sealant layer. It could be that the acidic fluoride-containing TCP coating bath damages the oxide coating more at the elevated temperature making the sealing less effective.

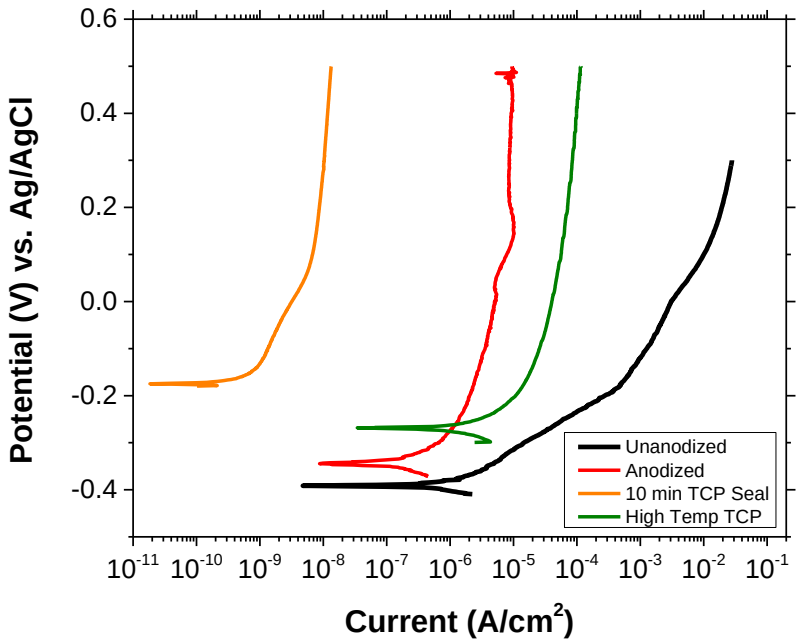

Figure 3.9. Potentiodynamic polarization curves in the anodic direction from the OCP for AA2024-T3 specimens anodized in sulfuric acid and sealed at two temperatures in Bonderite T5900. Curves for unanodized and SA anodized and unsealed specimens are presented for comparison. The measurements were made in naturally aerated 0.5 M Na_2SO_4 + 0.01 M NaCl at room temperature. The specimens were anodized in SA as described above.

Figure 3.10 presents representative potentiodynamic polarization curves in the anodic direction from the OCP for SA anodized specimens sealed with Luster-on TCP for immersion times of 1-, 5- and 10-min. Curves for unanodized and SA anodized and unsealed specimens are presented for comparison. The lowest current was observed for the anodized specimen sealed for 5 min. The sealant layers tend to shift the specimen OCP toward more positive potentials consistent with greater surface passivation. Based on these results, 5 min was determined to be optimum for sealing the anodic coatings with this TCP.

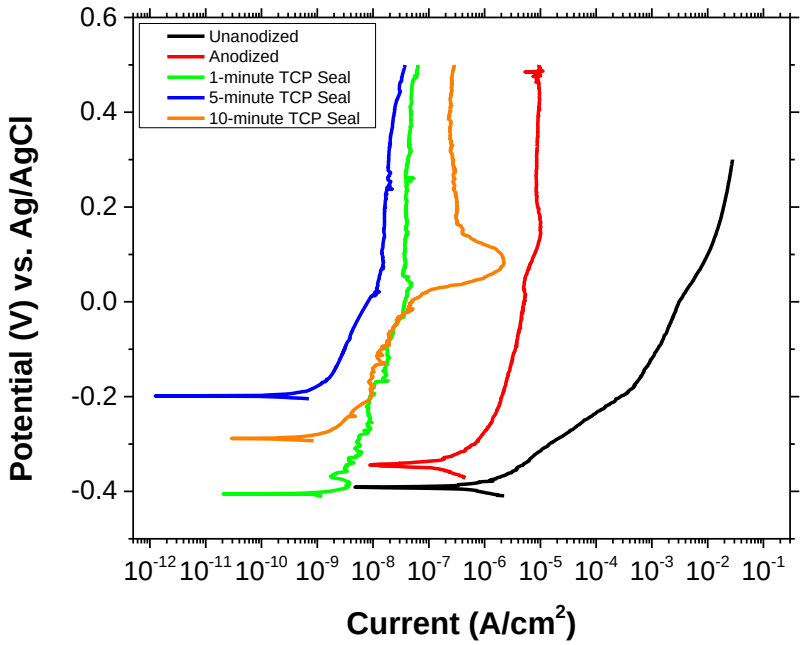

Figure 3.10. Potentiodynamic polarization curves in the anodic direction from the OCP for AA2024-T3 specimens anodized in sulfuric acid and sealed for different times (1, 5 and 10 min) in Luster-On Aluminescent. The measurements were made in naturally aerated 0.5 M Na_2SO_4 + 0.01 M NaCl at room temperature. The specimens were anodized in SA as described above.

Electrochemical Evaluation of Optimally Sealed SA Anodized Specimens

It is important to investigate how sealing with TCP compared with oxide coating sealing by other standard non-chromate methods. Figure 3.11 presents potentiodynamic polarization curves in the anodic direction from the OCP for SA anodized AA2024-T3 specimens sealed by the different methods: hot water, nickel acetate, and TCP. Curves for the unanodized and anodized and unsealed specimens are presented for comparison. The largest currents are seen for the unanodized specimen by 2-3 orders of magnitude, as expected. Lower currents are seen for the anodized and unsealed with slightly lower currents for the differentially sealed specimens. The lowest currents are observed for the specimens sealed in hot water and with the two TCP coatings. Slightly larger currents are seen for the nickel acetate sealed specimen. Notably, the currents for all the differentially sealed specimens are lower than the current for the anodized and unsealed specimen. The OCP values for all of the sealed specimens are quite

similar at -0.2 V and are shifted positive by ca. 0.2 V of the values for the unanodized and anodized and unsealed specimens. Shown are the initial curves for all the specimens recorded first right after preparation. This positive OCP shift for the sealed specimens indicates the sealing process has a greater effect on the anodic reaction rate (underlying aluminum oxidation to Al_2O_3) than on the cathodic reaction rate (dissolved O_2 reduction) and is reflective of greater surface passivation. In summary, these data suggest the two TCP sealants provide the greatest anodic current suppression for the anodized alloys.

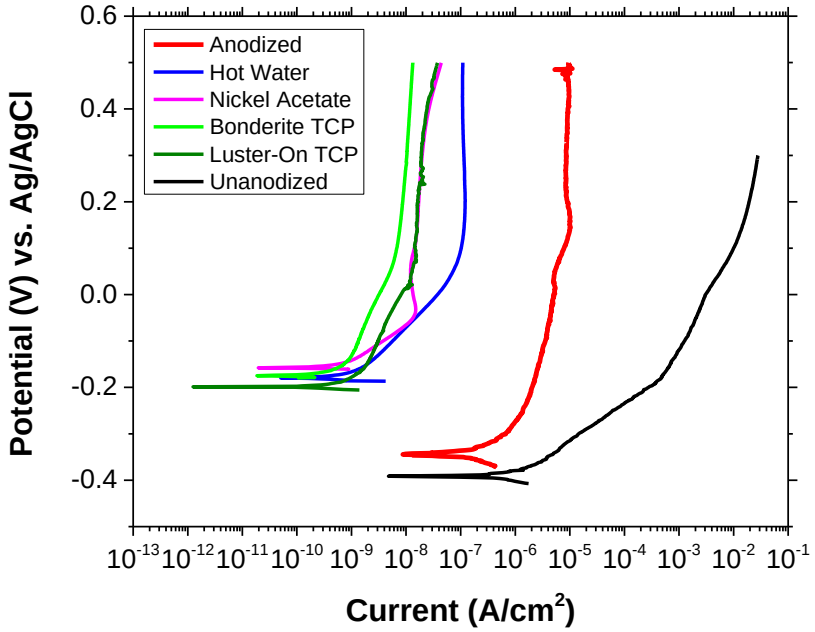

Figure 3.11. Potentiodynamic polarization curves in the anodic direction from the OCP for AA2024-T3 specimens anodized in sulfuric acid. Data are presented for SA anodized specimens sealed in hot water, nickel acetate and the two TCP coatings. Comparison curves for unanodized and anodized and unsealed specimens are also presented. The measurements were made in naturally aerated 0.5 M Na_2SO_4 + 0.01 M NaCl at room temperature. The SA anodization was performed as described above.

Figure 3.12 shows potentiodynamic polarization curves in the cathodic direction from the OCP for AA2024-T3 specimens unanodized, anodized and unsealed, anodized and sealed in hot water, nickel acetate and the two TCP coatings. These curves were recorded in naturally aerated 0.5 M Na_2SO_4 + 0.01 M NaCl with the scans being initiated 50 mV positive of the

OCP. The largest current is seen for the unanodized specimen, as expected. Reduced currents are the norm for the anodized and unsealed specimen with the lowest currents observed for the sealed specimens. The current at potentials between -0.3 and -1.0 V is mainly due to the diffusion-limited reduction of dissolved oxygen, presumably according to the reaction, $O_2 + 2H_2O + 4e^- \rightarrow 4OH^-$. The two TCP-sealed anodized specimens exhibit the lowest currents; ~2 orders of magnitude lower than the current for the anodized and unsealed specimen. Greater variability in the OCP values for the different specimens than was found when recording the anodic potentiodynamic curves. The OCP values are more negative of the values observed in the anodic polarization curves, at least for some of the specimens. There is a consistent general trend, however, that the OCP values for the TCP sealed specimens are shifted positive of the value for the anodized and unsealed specimen by 0.2 to 0.3 V. The variability and shift of the OCP values seen in Figure 3.12 may be linked to changes in the surface condition caused by defects in the oxide that can form with the inclusion of second phase particles.[21] In summary, these electrochemical data indicate that both TCP sealants provide the most cathodic current suppression for the anodized alloys.

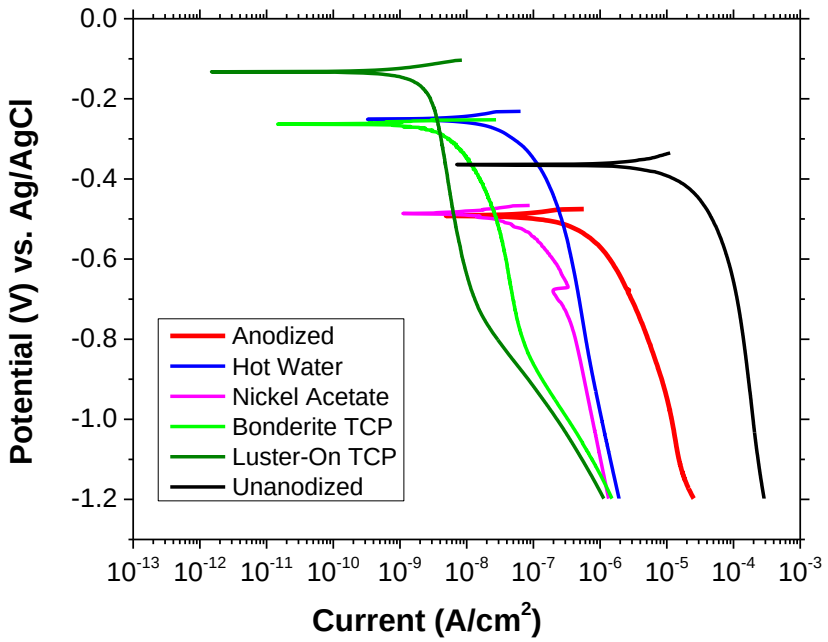

Figure 3.12. Potentiodynamic polarization curves recorded in the cathodic direction from the OCP for AA2024-T3 specimens unanodized, SA anodized and unsealed, and anodized and sealed in hot water, nickel acetate and the two TCP coatings. The measurements were made in naturally aerated 0.5 M Na_2SO_4 + 0.01 M NaCl at room temperature. The SA anodization was performed as described above.

Replicate electrochemical measurement data for the anodized and sealed AA2023-T4 specimens were statistically analyzed and the results are presented in the figures and table below. Figure 3.13 displays the anodic current measured at +0.20 V for the different specimens. The largest nominal current is observed for the anodized and unsealed specimen. There is considerable variability in some of the measurement data. Data are presented for N=3 specimens of each type. Assuming the variability results from random fluctuations in the processing or random error, including more measurement data would be expected to reduce the variability. The currents for the SA anodized specimens sealed by the different methods are nominally the same and about 1-2 orders of magnitude lower than the current for the

anodized and unsealed control. The lowest nominal anodic current is seen for the Luster-On sealed specimens.

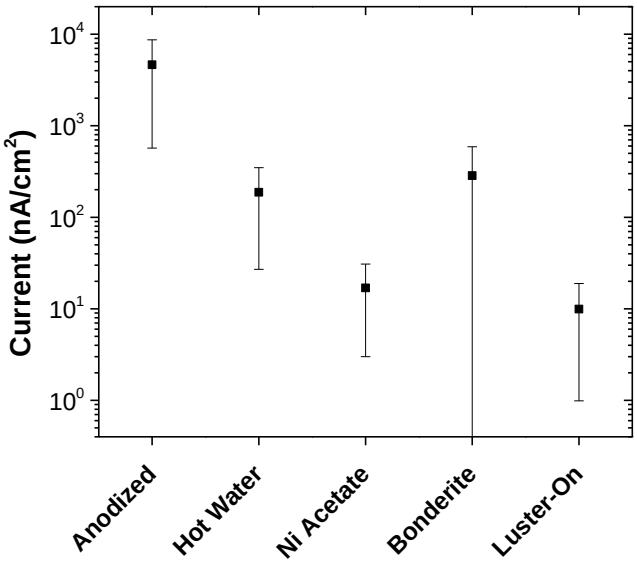

Figure 3.13. Comparison of the current measured in anodic potentiodynamic polarization curves at 0.2 V for AA2024-T3 specimens SA anodized and unsealed and anodized and sealed in hot water, nickel acetate, and the two TCP coatings. Shown are mean ± confidence intervals (95%) for $n \geq 3$. Statistical comparison was made against the anodized and unsealed control specimen using a one-tailed Student t-test at the 95% confidence level.

Figure 3.14 shows plots of the nominal cathodic current measured at -0.70 V for the different specimens. The largest nominal current is seen for the anodized and unsealed specimen. The nominal current for the different sealed specimens are about 1-2 orders of magnitude lower. Again, the largest variability in the current is seen for the anodized specimens. The lowest cathodic current is observed for the Luster-On sealed specimens.

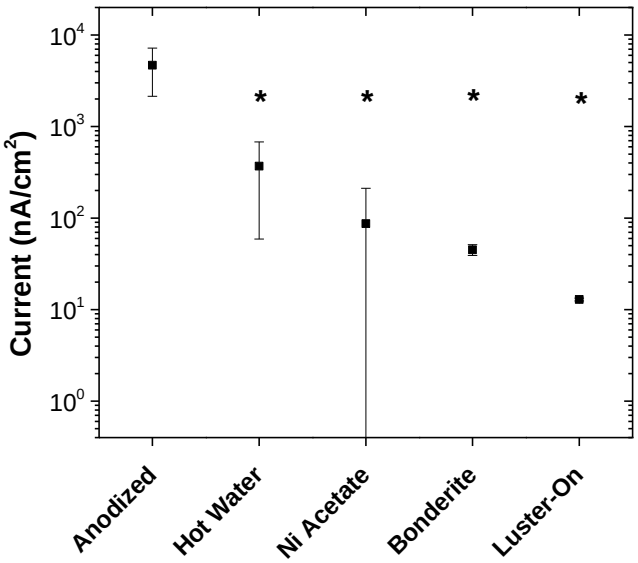

Figure 3.14. Comparison of the current measured in cathodic potentiodynamic polarization curves at -0.7 V for AA2024-T3 specimens SA anodized and unsealed and anodized and sealed in hot water, nickel acetate, and the two TCP coatings. Shown are mean ± standard deviations for n ≥ 3. Statistical analysis was made using a one-tailed Student t-test at 95% confidence level with mean data for the individually sealed specimens compared against the unsealed control.

Table 3.2. Tabular Data for Specimens Anodized in Sulfuric Acid for 20 minutes.

	Anodized	Hot Water Seal	Nickel Acetate Seal	Bonderite (TCP) Seal	Luster-On (TCP) Seal
OCP (mV)	-363 ± 62	-277 ± 142	-219 ± 146	-187 ± 41	-140 ± 52
Current (nA) at +200 mV	4630 ± 4030	188± 161	17.0± 14.0	8.18 ± 0.92	9.94± 8.95
Current (nA) at -700 mV	4670 ± 2540	370± 311*	87.0± 12.6*	45.1± 6.08*	13.0± 0.46*
$Z_{0.01}$ Hz (Mohm-cm^2)	0.24 ± 0.19	3.68 ± 2.96*	5.51 ± 1.72*	4.49 ± 1.36*	5.49 ± 0.01*

Shown are Mean ± Confidence Interval (95%) for n ≥ 3 electrodes of all specimen types in naturally aerated 0.5 M Na_2SO_4 + 0.01 M NaCl.
*Statistically significant difference from the values for the anodized specimens that served as controls assessed using a two-tailed paired Student's t-Test with significance at $p < 0.05$.

The numerical data presented in Table 3.2 present the open circuit potentials (OCP), anodic and cathodic current densities at +200 and -700 mV respectively, and the total impedance taken from the impedance spectroscopy at 10 mHz. The OCP values for the specimens that were sealed after anodizing showed a slight positive shift. This shift positive would indicate that the reaction kinetics for the aluminum dissolution reaction are further reduced when compared to the specimen that was anodized and left unsealed. When looking at the current densities in both directions the current is drastically reduced after sealing. The specimen that was anodized and left unsealed and in the anodic direction had a large deviation in the total current that was passed at +200 mV causing there to t be no statistical difference after sealing. However, when looking at the nominal values the sealing processes decrease the total amount of current flowing at those potentials which is suggestive of the reduced kinetics of both the aluminum dissolution reaction and the oxygen reduction reaction at +200 and -700 mV respectively. The total impedance for the specimens that are not anodized are around 10^3-10^4 and thus it is expected to increase with anodizing and increase further when the anodized specimens are sealed.[8, 18, 20] This is what is seen with the specimens that are anodized and those that are anodized and sealed. The specimens that were sealed are statistically different from those that were solely anodized. The specimens that were sealed with Luster-On TCP showed very little difference over the 6 specimens investigated. This combined with the anodic and cathodic potentiodynamic polarization curves and OCP values suggests that the Luster-On TCP may be the best TCP to seal the anodic oxide layer that is formed on AA2024-T3 in the sulfuric acid bath. The electrochemical data revealed the two conventional TCP coatings provide as effective or superior corrosion protection as do conventional hot water and nickel acetate sealing.

Continuous Neutral Salt Spray Exposure

The anodized and anodized and sealed specimens were subjected to a 14-day continuous neutral salt spray in accordance with ASTM B117. A 5 wt.% NaCl solution was used with the chamber temperature held at 35°C . The specimens were positioned in the chamber on plastic trays at an angle of ~20°. This allowed for mist to flow down the specimen surfaces by gravity. The area at the top of each specimen that was unanodized was masked off with corrosion protection tape to ensure salt spray contact with only the anodized region. After testing, the corrosion protection tape was removed, and the specimens were rinsed with ultrapure water. They were then ultrasonicated in ultrapure water to remove salt deposits that collected on the surface. Figure 3.15 shows plan view optical micrographs of unanodized, anodized and unsealed, and anodized and sealed specimens before and after a 14-day NSS exposure. The unanodized specimens were pulled after just 3 days of exposure because of the extensive corrosion damage that developed across the entire surface. The specimen surface was extensively roughened, and large pits (dark circular features in micrographs) developed. The micrographs for the anodized specimens have some subtle changes. The normal surface roughness increased by a factor of 3x, and the feature heights increased by a factor of 2x. These data are seen in Table 3.3. In contrast, and consistent with, the reduced anodic and cathodic polarization currents, the 14-day NSS produced no significant change in surface morphology, roughness, or peak-to-valley distance for any of the anodized + sealed specimens including the two TCP-sealed specimens.

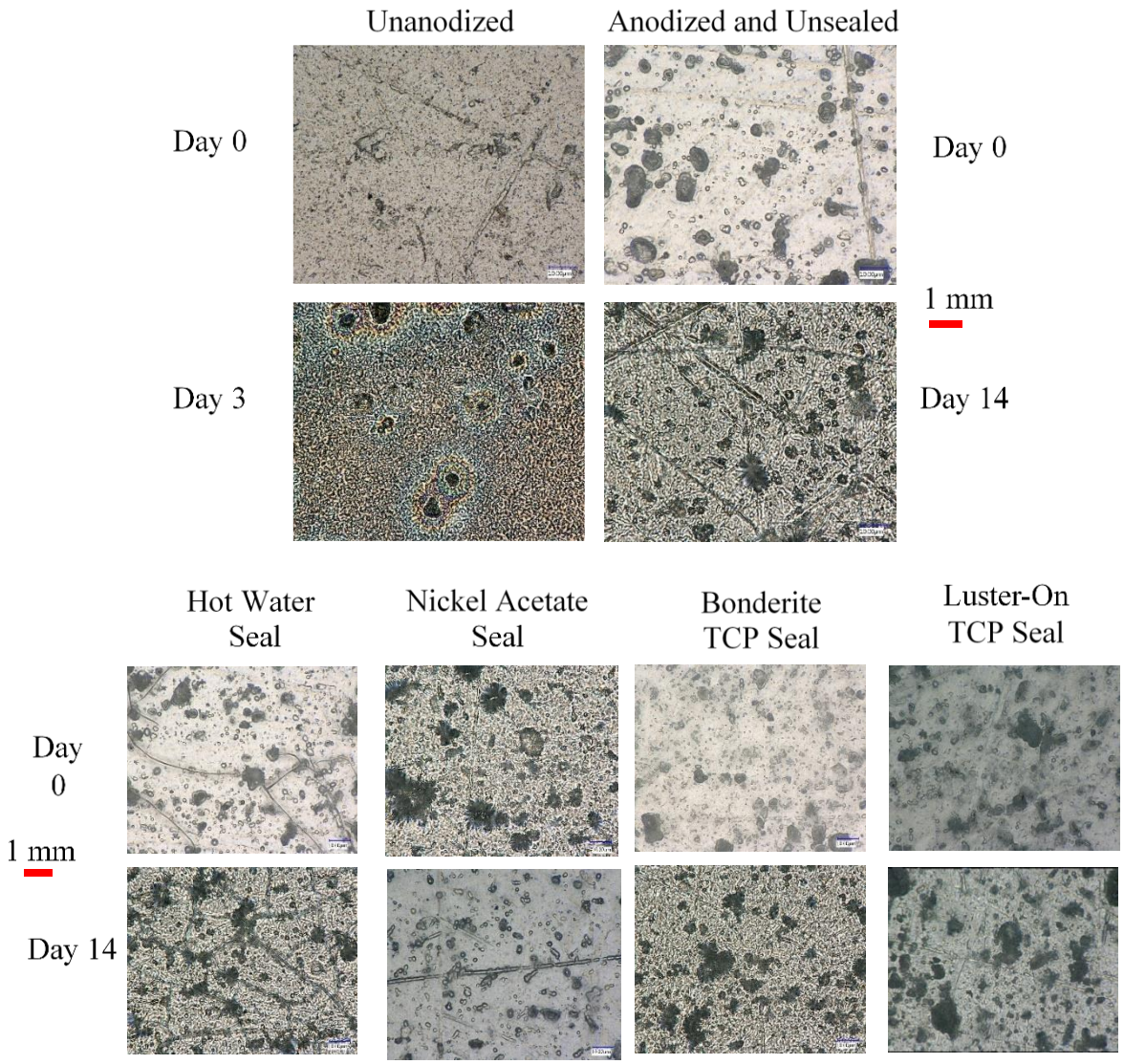

Figure 3.15. Neutral salt spray images for specimens anodized using sulfuric acid. Top images (row 1 and 2) are of specimens that were not anodized compared to those that were. The bottom images (row 3 and 4) show the different seals compared to each other. Rows 1 and 3 show images from before exposure to the 5 wt.% NaCl fog for 14 days. Rows 2 and 4 show the same specimen after exposure. Specimens that were not anodized were removed after just 3 days due to large amounts of visible pitting. All other specimens were removed after the 14-day test ended. Images taken using digital microscopy at 3,000x magnification.

The two TCP seals did not show much difference between from each other after the 14-day exposure. Both before and after the test, the samples showed no signs of corrosion product build up or pitting along the surface, even close to the edges.

Table 3.3. Root Mean Square Surface Roughness (S_q) and Surface Feature Heights (S_z) for Anodized Specimens Exposed to 14-Day Neutral Salt Spray

	S_q before exposure (µm)	S_q after exposure (µm)	S_z before exposure (µm)	S_z after exposure (µm)
Unanodized	0.17 ± 0.03	1.33 ± 0.23*	0.55 ± 0.25	5.81 ± 2.11*
Anodized Unseal	0.46 ± 0.14	1.18 ± 0.44*	6.42 ± 1.06	11.11 ± 2.67*
Hot Water Seal	1.02 ± 0.58	1.49 ± 0.68	8.81 ± 2.41	12.91 ± 2.60
Nickel Acetate Seal	0.71 ± 0.13	0.43 ± 0.22*	8.86 ± 1.05	4.77 ± 1.73*
Bonderite TCP Seal	2.20 ± 0.40	0.67 ± 0.15*	9.22 ± 0.91	9.55 ± 1.55
Luster-On TCP Seal	1.81 ± 0.13	1.19 ± 0.22*	11.50 ± 2.86	7.15 ± 1.16*

Mean ± standard deviation at the confidence interval (95%) values for N=15. 5 measurements across one specimen, with total of 3 specimens of each type over an area of 80 x 110 μm^2. Surface roughness is presented as a root mean square value.
*Statistically significant difference ($p \leq 0.05$) from the before exposure value as assessed by One-tailed Students t-Test.

Surface Roughness and Feature Height Data Determined by Digital Optical Microscopy

Table 3.3 summarizes surface roughness and feature height data for the different specimens before and after NSS exposure. S_q is the root mean surface roughness that assesses the root mean square average of the profile heights over the evaluation area. S_z is the average maximum height of the surface area and is found by the average of the successive values of the vertical distance between the highest and lowest points of the surface profile across the entire surface area. The values were determined from digital optical micrographs obtained at a 3000x magnification. Significant increases in the surface roughness (2x) and feature height (10x) are seen in the data for the unanodized specimen after just 3 days of NSS exposure. This is

consistent with the widespread corrosion damage visible in the optical micrographs above. The anodized and unsealed specimen also experienced corrosion damage over a 14-day exposure as the surface roughness (3x) and feature height (2x) both increased. In contrast, there were much less significant changes in the anodized specimens after different sealing. There was no change in the surface roughness or feature height of the hot water sealed specimens. A slight decrease in both the surface roughness and feature height data is seen for the nickel acetate sealed specimens. For the two TCP sealed specimens, the surface roughness for both decreased after the 14-day NSS exposure. This is likely due to chemical removal of some of the TCP coating across the outside of the oxide coating. For the Bonderite T5900 TCP sealed specimen, the data reveal no change in the feature height consistent with the chemical removal of some of the TCP coating across the outside of the oxide coating. For the Luster-on TCP sealed specimen, a slight decrease in the feature height is seen. Taken together, these data indicate that both TCP sealants provide good corrosion resistance to SA anodized AA2024-T3 specimens after this 14-day NSS test, comparable to the corrosion resistance provided by hot water and nickel acetate sealing.

Mass loss data in Table 3.4 show the two TCP sealants had a very large variation in the mass prior to and after neutral salt spray. It was statistically different from the specimens that were not sealed. This change in mass could be due to salt stuck to the surface after removal from the chamber or could be due to the “washing” off or stripping of the TCP aggregates from the surfaces of the specimens. None of the other data shows corrosion product built up on the surface, thus it is likely that the change in mass is from the removal of coating precipitates or a chemical loss of the TCP coating from the oxide surface.

Table 3.4. Weight Percent Change After 14-Day Neutral Salt Spray Exposure

Bonderite TCP Sealed	Luster-On TCP Sealed	Nickel Acetate Sealed	Hot Water Sealed	Anodized Unsealed
0.09 ± 0.03*	0.07 ± 0.02*	0.04 ± 0.02*	0.003 ± 0.005*	0.18 ± 0.02

Mean ± confidence interval (95%) values for n=3 for all specimen types.
*Significant difference ($p \leq 0.05$) from Anodized + No Seal specimens assessed with One-tailed Students t-Test.

3.5 DISCUSSION

The sulfuric acid electrolyte produced columnar pores that extend normal to the alloy surface. This allowed the Bonderite TCP and Luster-On TCP sealants to penetrate the pores and to help seal the pores up to 4-5 μm in depth. With the TCP plugging the pores and forming a layer above the surface of the oxide this provides better protection to the alloy below as the layer that must be penetrated is thicker with the TCP coatings. The TCP coating reaches to the bottom of the pores and thus leaves little room for electrolyte penetration to initiate corrosion.

The sulfuric acid anodizing produced anodic oxide layers that were found to be approximately 5-10 μm in depth and were found to have the columnar pores typically found with sulfuric acid anodizing. The pores at the surface were found to be varying in size at the surface and likely converged at the surface to form openings as large as 120 nm. The sealing process for the TCP coating has been investigated elsewhere,[21] but with further analysis done through GD-OES a better understanding was found for these TCP sealants. The TCP is able to fill portions of the oxide pores but does not fill the pores fully in the work that has been previously done. Those TCP coatings did not fully penetrate to the base of the pores, but in this work the TCP coatings do in fact fully fill the pores from the bottom and create a thin, 150-300 nm, thick barrier layer at the oxide/electrolyte interface.

Electrochemically the data showed that the corrosion resistance was increased with anodizing and was further increased upon sealing the oxide layer with both the conventional methods and the TCP coatings. The TCP coatings showed excellent corrosion resistance and were found to be similar to that of the nickel acetate and hot water seals at 15-22x that of the oxide layer alone. The TCP coating uses less energy than the nickel acetate and the hot water seals. Both traditional sealing techniques require elevated temperatures. The TCP coatings both provide similar corrosion protection to the underlying alloy and are comparable to that of the traditional sealants.

Correlation between specimens investigated with electrochemical measurements and neutral salt spray were made for specimens anodized in sulfuric acid. The electrochemical data suggests that the specimens that were not anodized would have the least corrosion resistance due to the high current at low over potentials from the open circuit potential. This was corroborated with the results from the neutral salt spray test because after just 3 days there was significant pitting found along the surface of the specimens that had not been anodized. This pitting occurred much more rapidly than that of the pitting found on the specimens that were anodized and not sealed. This too correlates well with the electrochemical data because the current was much lower for the specimens anodized without being sealed than it was for the specimens that had not been anodized, but there was still a slightly higher current density for the specimens that were anodized and not sealed than those that were anodized and sealed. The specimens that were anodized and sealed did not show much statistical difference in the electrochemical data besides that Luster-On as a TCP sealant had less current density at higher over potentials than the Bonderite TCP did. However, when correlating to the neutral salt-spray test results there was no difference found in the salt spray test for any of the sealants like

there was in the electrochemical data. Another accelerated degradation test, thin layer mist test, may be needed to find any differences in the TCP baths used as a sealant.

3.6 CONCLUSIONS

In this work two TCP coatings were applied as a sealant to the anodic oxide formed on AA2024-T3 and were investigated for sealing morphology, penetration of the coating into the oxide layer, corrosion protection, and correlation to accelerated degradation tests. The surfaces showed that the TCP coatings formed as a barrier layer covering the outer surface and penetrating the oxide 2.5-3 μm filling up the pores. The TCP does not fully fill the pores of the anodic oxide layer, but it does provide added corrosion protection. The oxide layer sealed with the TCP coatings provides similar amounts of protection to the underlying alloy as other commercial sealants, but with less energy consumption by being applied at room temperature. The TCP sealed specimens showed no damage after 14 days of exposure to 5 wt.% NaCl in the neutral salt spray test. There was no statistical difference found between the two TCP coatings and both would be excellent options as sealants for anodic oxide films on AA2024-T3 formed with sulfuric acid anodizing.

REFERENCES

REFERENCES

1. Davis, J. R., *Alloying: Understanding the Basics-Light Metals and Alloys*. 2001.

2. Davis, J. R.; Associates, *ASM International. Handbook Committee, Aluminum and Aluminum Alloys*. 1993.

3. Davis, J. R., *Corrosion of Aluminum and Aluminum Alloys*. 1999.

4. Mavhungu, S. T.; Akinlabi, E. T.; Onitiri, M. A.; Varachia, F. M., Aluminum Matrix Composites for Industrial Use: Advances and Trends. *Procedia Manufacturing* **2017,** *7*, 178-182.

5. Shabestari, S. G.; Moemeni, H., Effect of Copper and Solidification Conditions on the Microstructure and Mechanical Properties of Al-Si-Mg Alloys. *Journal of Materials Processing Technology* **2004,** *153*, 193-198.

6. Rana, R. S.; Purohit, R.; Das, S., Reviews on the Influences of Alloying Elements on the Microstructure and Mechanical Properties of Aluminum Alloys and Aluminum Alloy Composites. *International Journal of Scientific Research Publications* **2012,** *2* (6), 1-7.

7. Twite, R. L.; Bierwagen, G. P., Review of Alternatives to Chromate for Corrosion Protection of Aluminum Aerospace Alloys. *Prog. Org. Coat.* **1998,** *33* (2), 91-100.

8. Li, L.; Swain, G. P.; Howell, A.; Woodbury, D.; Swain, G. M., The Formation, Structure, Electrochemical Properties and Stability of Trivalent Chrome Process (TCP) Coatings on AA2024. *J. Electrochem. Soc.* **2011,** *158* (9), C274-C283.

9. Li, L.; Whitman, B. W.; Munson, C. A.; Estrada, R.; Matzdorf, C. A.; Swain, G. M., Structure and Corrosion Performance of a Non-chromium Process (NCP) Zr/Zn Pretreatment Conversion Coating on Aluminum Alloys. *J. Electrochem. Soc.* **2016,** *163* (13), C718-C728.

10. Thompson, G. E.; Zhang, L.; Smith, C. J. E.; Skeldon, P., Boric/sulfuric acid anodizing of aluminum alloys 2024 and 7075: Film growth and corrosion resistance. **1999**.

11. Shimizu, K.; Kobayashi, K.; Thompson, G. E.; Wood, G. C., Development of porous anodic films on aluminium. *Philosophical Magazine A* **1992,** *66* (4), 643-652.

12. Curioni, M.; Saenz de Miera, M.; Skeldon, P.; Thompson, G.; Ferguson, J., Macroscopic and Local Filming Behavior of AA2024 T3 Aluminum Alloy during Anodizing in Sulfuric Acid Electrolyte. *Journal of The Electrochemical Society* **2008,** *155*, C387-C395.

13. Anodic Coatings for Aluminum and Aluminum Alloys. Specification, M., Ed. September 10, 1993; Vol. MIL-A-8625F.

14. Matzdorf, C.; Beck, E.; Hilgeman, A.; Prado, R., Trivalent Chromium Process (TCP) as a Sealer for MIL-A-8625F Type II, IIB, and IC Anodic Coatings. Division, N. A. W. C. A., Ed. August 29, 2008.

15. Diggle, J. W.; Downie, T. C.; Goulding, C. W., Anodic oxide films on aluminum. *Chemical Reviews* **1969,** *69* (3), 365-405.

16. Zuo, Y.; Zhao, P.-H.; Zhao, J.-M., The influences of sealing methods on corrosion behavior of anodized aluminum alloys in NaCl solutions. *Surface & Coatings Technology - SURF COAT TECH* **2003,** *166*, 237-242.

17. Whitman, B. W.; Li, L.; Swain, G. M., Anti-Corrosion Properties of a TCP Pretreatment Conversion Coating on Aluminum Alloy 2024-T3 during Moist SO_2 Atmospheric Testing: Effects of Galvanic Coupling. *J. Electrochem. Soc.* **2017,** *164* (4), C135-C147.

18. Li, L.; Swain, G. M., Effects of Aging Temperature and Time on the Corrosion Protection Provided by Trivalent Chromium Process Coatings on AA2024-T3. *Appl. Mater. Interfaces* **2013,** *5*, 7923-7930.

19. Munson, C. A.; McFall-Boegeman, S. A.; Swain, G. M., Cross comparison of TCP conversion coating performance on aluminum alloys during neutral salt-spray and thin-layer mist accelerated degradation testing. *Electrochimica Acta* **2018,** *282*, 171-184.

20. McFall-Boegeman, S.; Yancey, D. F.; O'Neill, T.; Davidson, N.; Swain, G. M., Effect of Laser Cleaning and Hyperpassivation on the Electrochemical Behavior of AA2024-T3. *Journal of The Electrochemical Society* **2021,** *168* (3), 031501.

21. Shruthi, T. K.; Walton, J.; McFall-Boegeman, S.; Westre, S.; Swain, G. M., Investigation of the Trivalent Chromium Process Conversion Coating as a Sealant for Anodized AA2024-T3. *Journal of The Electrochemical Society* **2020,** *167* (11), 111504.

22. Carangelo, A.; Curioni, M.; Acquesta, A.; Monetta, T.; Bellucci, F., Application of EIS to In Situ Characterization of Hydrothermal Sealing of Anodized Aluminum Alloys: Comparison between Hexavalent Chromium-Based Sealing, Hot Water Sealing and Cerium-Based Sealing. *J. Electrochem. Soc.* **2016,** *163* (10), C619-C626.

23. Qi, J.; Walton, J.; Thompson, G. E.; Albu, S. P.; Carr, J., Spectroscopic Studies of Chromium VI Formed in the Trivalent Chromium Conversion Coatings on Aluminum. *Journal of The Electrochemical Society* **2016,** *163* (7), C357-C363.

24. Guo, Y.; Frankel, G. S., Characterization of trivalent chromium process coating on AA2024-T3. *Surface and Coatings Technology* **2012,** *206* (19), 3895-3902.

25. Arrowsmith, D. J.; Dennis, J. K.; Sliwinski, P. R., Chromate conversion coatings on aluminium: Growth of layers of spherical particles. *Transactions of the IMF* **1984,** *62* (1), 117-120.

26. Treverton, J. A.; Amor, M. P., High-resolution SEM studies of chromate conversion coatings. *Journal of Materials Science* **1988,** *23* (10), 3706-3710.

27. Laget, V.; Jeffcoate, C. S.; Isaacs, H. S.; Buchheit, R. G., Dehydration-Induced Loss of Corrosion Protection Properties in Chromate Conversion Coatings on Aluminum Alloy 2024-T3. *Journal of The Electrochemical Society* **2003,** *150* (9), B425.

28. Runge, J. M., The Metallurgy of Anodizing Aluminum. Springer International Publishing: 2018; pp 149-190.

CHAPTER 4. SEALING SULFURIC ACID/ BORIC ACID ANODIZED ALUMINUM ALLOY 2024-T3 WITH THE TRIVALENT CHROMIUM PROCESS CONVERSION COATING

4.1 INTRODUCTION

Besides sulfuric acid (SA) anodization as an alternative to the chromic acid anodization, sulfuric/boric acid (SABA) anodization is an effective alternate surface treatment.[1-3] Sulfuric acid is a fine alternative in terms of corrosion protection to the underlying alloy, but it is not recommended for use as it can be detrimental to the fatigue life of the material.[1, 4, 5] Work in the past has shown that the addition of the boric acid has negligible effect on the current time profiles from sulfuric acid baths.[1] SABA anodization produces oxide thicknesses that vary with temperature ranging from 2-11 μm..[4] With TEM a thin barrier layer if found at the metal/oxide interface and the oxide is formed as a mixture of linear continuous pores and lamellar shape grown preferentially in one direction at the grain boundaries creating a tortuous pore morphology.[4]

The SABA oxide layer does not possess the same physical structure that the SA oxide layer has as the boric acid produces a less porous and more compact oxide layer that protects the underlying aluminum alloy.[1, 6, 7] Previous work has shown that the SABA oxide forms with a non-oriented grain like structure along the grain boundaries and is separated by open channels.[4] This is opposition to the anodized linear pores perpendicular to the substrate across the entirety of the oxide layer formed in sulfuric acid.[2, 3, 7, 8] The SABA oxide should provide more intrinsic corrosion protection and it should be more effectively sealed as it is less porous and has fewer

defects. TEM has shown the barrier layer formed by SABA to be defect free and more of a gel-like layer through a mechanism of a peptization of the hydroxide particles.[9, 10]

Sulfuric acid is a great alternative to the chromate anodizing bath, but the downside to using the sulfuric acid only in the anodizing bath is that it has been shown to weaken the substrate.[1, 4, 9, 11, 12] With the incorporation of the boric acid to the electrolyte bath the aggressive attack of the surface by the sulfuric acid is lessened and the mechanical strength of the substrate can be maintained while still providing similar, if not greater, corrosion protection.[1, 4]

The sealing of the SABA oxide with hot water on aluminum alloys is less effective than the oxide on its own for improving corrosion resistance.[4, 5, 9, 11] From the previous work the sealants that must hydrate the oxide or to push the oxide towards dissolution to then seal the oxide layer have more difficulty properly sealing the SABA oxide.[9, 13] It is important to demonstrate that more environmentally friendly sealants, like TCP, are effective at sealing the SABA oxide grown on aluminum alloys and that the corrosion resistance can be further improved. [14-18]

Basic research was conducted to investigate the mechanism by which two different commercial TCP conversion coatings, Bonderite T5900 and Luster-on Aluminescent, seal SABA anodic coatings on AA2024-T3 and to assess the corrosion resistance enhancement that these sealants provide, as compared to unsealed anodized specimens. Electrochemical techniques including open circuit potential measurements (OCP), potentiodynamic polarization curves, and electrochemical impedance spectroscopy at the OCP were employed to assess the corrosion resistance of the unsealed and sealed anodized alloy. Scanning electron microscopy (SEM) with energy dispersive x-ray spectroscopy (EDS) was used to determine

the oxide and sealed oxide morphology, as well as the location of the TCP coating bath constituents, Zr and Cr. SEM-FIB was used in the cross-section to examine the oxide morphology and thickness, as well as the TCP coating thickness. These were then confirmed through the use of GD-OES. Unsealed and sealed anodized specimens were exposed to a 14-day neutral salt-spray (ASTM B117) test to evaluate the corrosion resistance under accelerated degradation conditions. Optical profilometry was used to assess the corrosion damage on the alloy surfaces after the salt-spray exposure.

4.2 MATERIALS AND METHODS

Reagents

Turco 6849 (20% v/v, Henkel Corp., Madison Heights, MI) and Luster-On 401 (4% w/v, Luster-On Products Inc., Springfield, MA) were the commercial degreasing solutions used. Turco Liquid Smut-Go (20% v/v, Henkel Corp., Madison Heights, MI) and Luster-On 485 (3.9% v/v, Luster-On Products Inc., Springfield, MA) served as the deoxidizing solutions. Bonderite T-5900 RTU (Henkel Corp., Madison Heights, MI) and Luster-On Aluminescent (1% w/v, Luster-On Products Inc., Springfield, MA) were the commercial TCP coating baths studied. Sulfuric acid (95-98 wt.%), boric acid, sodium sulfate (Na_2SO_4), sodium chloride (NaCl), nickel (II) acetate, potassium dichromate, sodium carbonate, and calcium chloride were all purchased from Sigma Adrich (St. Louis, MO). Cobalt acetate was purchased from Spectrum Chemical Manufacturing Corp. (Gardena, CA). Nitric acid was purchased from Fisher Scientific (Hampton, NH). All chemicals were technical or reagent grade quality, or better, and used without additional purification. All solutions were prepared with ultrapure water (Barnstead E-Pure) having a resistivity of >17 MΩ · cm.

Specimen Preparation

Aluminum alloy 2024-T3, purchased as 12 in. x 12 in. sheets from OnlineMetals.com, was used in these studies. The metal sheet was 2-mm thick and cut into 1 in^2 squares. The 1 in^2 specimens were then abraded on wet 1500-grit Al_2O_3 sandpaper and then polished sequentially with 0.3 and 0.05 μm diam. alumina powder slurried with ultrapure water. Each polishing step was performed by hand on a dedicated felt polishing pad until a mirror-like finish was achieved. The specimens were rinsed with and ultrasonically cleaned in ultrapure water for 20 min then ultrasonically cleaned in isopropyl alcohol (distilled/activated carbon) for 20 min after each abrading and polishing step to remove debris. The cleaned specimens were then degreased for 10 min at 55°C and rinsed with flowing city tap water for 2 min. The specimens were deoxidized for 2 min followed by a 2 min flowing city tap water rinse and dried with N_2 gas prior to anodization.

Sulfuric Acid/ Boric Acid Anodization

The bath consisted of 9.8 wt. % sulfuric acid and 10 g/L boric acid (or 1 wt.%) (SABA). The cathode was a stainless steel (type 316) plate. The stainless-steel cathode and aluminum alloy anode were equivalent geometric areas (1 in^2). The cathode was positioned parallel to and 1.5 inches from the anode in the electrolyte solution. The electrodes were connected to a DC power supply (Tenma) that provided the constant voltage for anodization. The specimens were immersed in the solution vertically with three-quarters of each immersed in the electrolyte solution. For anodization, the applied voltage to the anode was stepped at 5 V/min to 15 V (3 min total period) and then held at this voltage for 20 min. Thus, the total anodization time was 23 min.[1, 5, 11] The anodization conditions were selected to be identical to those used for the SA anodization described in Chapter 3. Afterward, the anodized specimens were rinsed with

ultrapure water for 10 min and left to dry overnight in a desiccator. The anodizing set up was the same as that in Chapter 3 and is shown in Figure 3.1.

Bonderite T-5900 (Henkel) TCP Seal

Anodized specimens were immersion sealed with Bonderite T-5900 TCP. The optimized sealing conditions were determined to be room temperature using an immersion time of 10 min. Electrochemical measurements were used to determine that the 10-min sealing period was optimum. This determination was made based on the sealing time (1, 5, and 10 min) that provided the greatest improvement in the corrosion resistance of the anodized alloy. The electrochemical parameters used for this assessment were the anodic and cathodic currents in potentiodynamic polarization curves, the low frequency ($Z_{0.01}$ Hz) impedance modulus in EIS measurements, and the polarization resistance (R_p), as determined from linear sweep polarization curves. The specimens were immersion sealed with periodic agitation, as needed, to remove any gas bubbles that formed at the surface. After sealing, the specimens were rinsed by immersion in city tap water for 2 min and then rinsed with flowing ultrapure water for 30 s. Excess water was wicked from the surface and the specimens were left face up to dry overnight in the lab air before any further testing.

Luster-On Aluminescent TCP Seal

Anodized specimens were also immersion sealed with Luster-On Aluminescent TCP. The optimized sealing conditions were determined to be room temperature and an immersion time of 5 min. Again, the optimum sealing time was determined based on electrochemical assessment of the sealing time (1, 5 and 10 min) that provided the greatest improvement in corrosion resistance of the anodized alloy. The specimens were immersion sealed with periodic agitation, as needed, to remove any gas bubbles. After sealing, the specimens were immersion

rinsed in city tap water for 2 min and then rinsed with flowing ultrapure water for 30 s. Excess water was wicked from the surface and the specimens were left face up to dry overnight in lab air before any further testing.

Hot Water Seal

Ultrapure water was also used to seal the anodized specimens, for comparison. Hot water immersion (e.g., hydrothermal) is a common sealing method for anodic coatings on aluminum alloys.[17, 19, 20] The water was heated to 90 ± 3 °C and maintained at that temperature throughout the sealing process. Sealing the anodized specimens was performed by immersion in the hot water for 30 min. After sealing, excess water was wicked from the surface and the specimens were left face up to dry overnight in lab air before any further testing.

Nickel Acetate Seal

Nickel acetate immersion was also used to seal the anodized specimens, for comparison. This too is a common method for sealing anodic coatings on aluminum alloys.[17, 21] The nickel acetate solution composition consisted of 5 g/L nickel acetate, 1 g/L cobalt acetate, and 8 g/L boric acid. This composition was developed by Boeing. The pH of the sealant bath was maintained between 5 and 6. The sealing was performed by immersing the anodized specimens for 15 min at 80 °C. After sealing, excess water was wicked from the surface and the specimens were left face up to dry overnight before any further testing.

4.3 TESTING AND CHARACTERIZATION

Electrochemical Measurements

The unsealed and sealed anodized specimens were electrochemically characterized using open circuit potential (OCP) measurements, full frequency electrochemical impedance spectroscopy (EIS) measurements at the OCP, linear polarization resistance measurements,

and potentiodynamic polarization curves. The electrolyte used in all the measurements was naturally aerated 0.5 M Na_2SO_4 + 0.01 M NaCl at room temperature. All electrochemical measurements were conducted in a 1 cm^2 flat cell (Biologic Science Instruments) using a computer-controlled electrochemical workstation (Gamry Instruments, Inc, Reference 600, Warminster, PA). The cell design is the same as that used in Chapter 3 and is shown in Figure 3.2. An aluminum alloy specimen was mounted in the cell against a Viton® O-ring that defined the exposed geometric area, 1 cm^2. All currents reported herein are normalized to this geometric area. The counter electrode was a Pt flag, and the reference was a home-made Ag/AgCl electrode (4 M KCl, E^0 = +0.197 V vs. NHE) that was housed in a Luggin capillary with a cracked glass tip. Data were collected at the OCP using 7 points per frequency decade from 10^5 to 10^{-2} Hz to determine the frequency dependence of the real (ohmic) and imaginary (capacitive) components of the total impedance. Linear polarization resistance measurements were performed by linear sweep voltammetry at potentials ±20 mV vs. OCP. Potentiodynamic polarization curves were recorded from ±20 mV vs. OCP to either 500 mV for the anodic curves or -1.2 V for the cathodic curves. These curves provided insight on the anodic (oxide formation and localized pitting) and cathodic (oxygen reduction) reaction rates.

Neutral Salt-Spray (ASTM B117) Exposure

Specimens 1 in^2 in area were placed at a ~20° angle (with respect to the vertical axis) on plastic racks inside a salt-spray chamber (Associated Environmental Systems, MX-40, 4 ft^3). The solution reservoir was filled with a 5 wt. % NaCl solution. The test specimens had an exposed area near the top for electrical connection that was not anodized, and this area was masked off with corrosion protection tape (3M Scotchrap™). The salt fog exposure was conducted according to ASTM B117 (Standard Practice for Operating Salt Spray (Fog)

Apparatus) for 14 days (35°C). At the end of the test period, the specimens were removed, rinsed thoroughly with ultrapure water, and dried under a stream of N_2 gas. Ultrasonic cleaning in ultrapure water was performed to dissolve salts and remove weakly adhering corrosion product from the surface. Nitric acid ultrasonic cleaning, as is commonly used to remove corrosion produce from aluminum alloy specimens after salt spray exposure. However, such cleaning was not performed in these experiments so as to not damage or remove any of the oxide or alter the surface of the sealant layer after the 14-day test.[22]

Scanning Electron Microscopy/Energy Dispersive X-ray Spectroscopy

Scanning electron microscopy (SEM) and energy dispersive x-ray spectroscopy (EDS) were performed using a field emission electron microscope (JOEL 7500F) equipped with an Oxford EDS system for elemental analysis. Electron micrographs were obtained using an accelerating voltage of 15 kV, a working distance of 11 mm, and an electron beam spot size of 30 with a dwell time 16 µs/pixel. EDS was collected with the same voltage, but the spot size was increased to 50 for x-ray dead time to increase to 20%. These measurements were performed to assess the porous oxide layer surface morphology and the location of TCP coating elements (Zr, Cr, F, and O) within the oxide. The latter measurements were performed on cross-sections of specimens that were prepared by focused ion beam milling. The measurements were performed using instruments at the Center for Advanced Microscopy (MSU).

Scanning Electron Microscopy/ Focused Ion Beam Milling

A field emission scanning electron microscope (Auriga XB Crossbeam) was used for imaging that was equipped with a gallium focused ion beam (FIB) for performing the milling. The gallium ion beam was generated at 30 kV. An ion beam current of 4 nA was applied to the

specimen at a 45˚ angle for large cross-section cuts. A 600-pA ion beam current was used for fine cleaning of the cross-section. The microscopy and milling were performed on an instrument at the Composite Materials and Structures Center (MSU).

Digital Optical Microscopy

Digital microscopy was performed to assess the surface morphology/texture of the oxide layer and alloy surfaces prior to and after a 14-day neutral salt-spray exposure. A digital microscope (Keyence VHX-6000) was used to record images at variable magnification. Digital images of the surface were captured as each different area comes into focus, combining them into one fully focused (stitched) image. The microscope uses a depth of defocus method to calculate three-dimensional depth information based on the amount of defocusing of two-dimensional images. Surface roughness data were obtained from the areas measured at different points on a specimen. The depth resolution was ca. 0.2 µm. The measurements were made on an instrument at the Center for Advanced Microscopy (MSU).

Scanning Optical Profilometry

Surface profiles was obtained using a WYKO Optical Profilometer along with the associated instrument software, Vision for RST Plus (version 1.8). The instrument used an 10x magnification lens along with a field of view lens of 2x that produced images at a 20x magnification. Five areas across each specimen were probed in a grid like pattern to verify the overall surface texture. The topography was profiled by stitching focused images from 10 µm above to 10 µm below the surface at each measurement point. The WYKO Optical Profilometer collects this same image 5 times and removes any unfocused areas by averaging the scans together giving one fully focused image. 3D images and contour plots were collected

over an area of 306 x 230 μm^2 to profile the surface texture and to calculate the surface roughness.

Glow Discharge Optical Emission Spectroscopy/EDS

Glow discharge optical emission spectroscopy (GD-OES) was performed using a Leco GDS 850 A Glow Discharge Optical Emission spectrometer at Henkel Technologies (Madison Heights, MI). GD-OES is a useful measurement method for investigating the elemental composition of coatings and films from the surface down to tens of microns with a depth resolution that can be as good as 1 nm. SEM/EDX was done with a JSM 5900-LV. For EDS analysis, samples were secured to an aluminum stage with double sided copper tape. Samples were analyzed at a working distance of 12 mm in high vacuum with a spot size of 71. All analysis was done at 500x magnification. Samples were then analyzed by GD-OES, using program Henkel RF QDP (Ar RF plasma, 20 W and 1,000 V), and was allowed to run for 10 min. The sputter rate is determined through the time of 6,000 s and the frequency of 10 Hz. A spot size of 4 mm was investigated at 3 locations along the specimen. Argon was used to generate the plasma.

4.4 RESULTS

The current density was measured during each minute of the controlled voltage anodization in the SABA bath. The current-time profiles for multiple anodized specimens are presented in Figure 4.1. The current density nominally increases with time during early stages of anodization trending toward a constant value at longer times. At this stage, the highest growth rate is observed. Over time as progressively more of the alloy surface gets oxidized and the current approaches a near-constant value reflective of a constant rate of oxide film formation. The maximum current density is ~35 mA/cm^2. These current densities are very comparable to

those recorded during sulfuric acid anodization (see Chapter 3). This is anticipated as previously reported data show that the current density during the anodizing process should have negligible differences with the addition of boric acid to the anodizing bath.[1, 4] Greater variability in the current density was observed during the SABA anodization at times longer than 20 minutes at 15 V. The conditions used for the SABA anodization were identical to the ones used for the SA anodization discussed in the previous chapter (20 minutes was used for the total anodizing time at 15 V after the 3 min ramp).

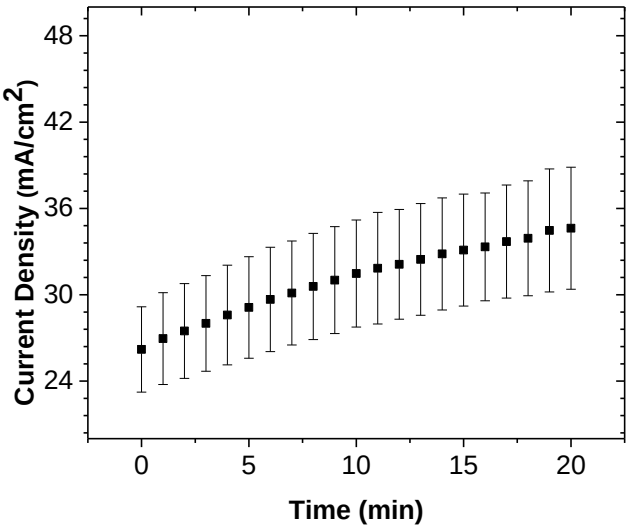

Figure 4.1. Current density recorded for AA2024-T3 specimens during each minute of the SABA anodization after reaching 15V. Data are presented as mean and standard deviation for N ≥ 15 different anodized specimens at each time point.

Weight Change as a Function of Anodizing Time

For SA anodization, MIL-A-8625F (Military Specification: Anodic Coatings for Aluminum and Aluminum Alloys) calls for an anodic coating weight (oxide layer weight) of 1000 mg/ft^2, or greater. The ASTM B137 (Standard Test Method for Measurement of Coating Mass Per Unit Area on Anodically Coated Aluminum) method was used to determine the anodic coating weight for the SABA anodized AA2024-T3 specimens. In this method, chromic

acid anodic stripping was used to dissolve the oxide with a specimen weight change before and after the stripping. The 15 VDC, 23-min anodization in SABA produced a nominal oxide weight of ~1200 mg/ft^2. In ASTM B137, the anodized AA2024-T3 specimen was aged for 24 h before stripping the oxide to allow for complete drying. The dried specimen was first weighed before placement in the stripping solution. The stripping solution (1L) contained 20 g CrO_3 + 35 mL of phosphoric acid. The specimen was immersed in the stripping solution for 5 min to dissolve the oxide. The specimen was then removed, rinsed with ultrapure water, and dried thoroughly with a stream of N_2 gas before measuring the weight change. The 5-min immersion and weight loss measurements were repeated until a stable weight was achieved (± 0.001 g). Typically, a total immersion time of 15 min was required to entirely dissolve the oxide and achieve a constant specimen weight. Three anodized specimens were tested for statistical analysis with the results presented in Table 4.1. For the 23 min/15 V DC SABA anodization, the nominal oxide weight was 1192 ± 43 mg/ft^2.

Table 4.1. Oxide Weights for SABA Anodized AA2024-T3 Specimens (23 min/ 15 V DC)

	Before Stripping (mg)	After Stripping (mg)	Difference (mg)	Oxide Weight (mg/ft^2)
Specimen 1	1833.41	1827.21	6.20	1190
Specimen 2	1758.37	1751.93	6.44	1236
Specimen 3	1809.08	1803.34	5.74	1150

Area of oxide was 0.00538 ft^2. The nominal oxide weight was 1192 ± 43 mg/ft^2.

Oxide Morphology for SABA Anodized Specimens Before and After Sealing

Scanning electron microscopy allowed for higher resolution investigation of the oxide coating morphology and thickness before and after each of the sealing post-treatments. Figure 4.2 presents electron micrographs of an unanodized, a SABA anodized, and SABA anodized

specimens sealed by different methods. The anodized specimen is clearly rougher than the unanodized one, but interestingly, the SABA anodized surface does not consist of an oxide coating with open pores. Rather the surface of the coating has low porosity and appears denser than the oxide formed in SA (reported in Chapter 3). This trend was reported in the literature as well.[11] The reduction in the outer porosity of the SABA oxide increases the barrier properties of the coating and improves corrosion resistance.[4, 5]

Electron micrographs shown in the center left of Figure 4.2 are the SABA anodized specimen sealed in hot water, which showed hair-like fibers protruding from the surface. The hot water sealing causes a hydrated aluminum oxide, boehmite ($Al_2O_3 + H_2O \rightarrow 2AlOOH$), to be formed in the pores. Boehmite has a greater volume than the aluminum oxide and thus serves to fill and block the outer pores of the oxide coating.[20, 23] The anodic coating after hot water sealing had small pores between the fibers protruding from the surface. These are the small black dots that can be seen in the micrograph. A reduction in the outer porosity of the oxide coating improves the barrier properties and increases the corrosion resistance.

The nickel acetate sealing produced negligible changes to the outer coating morphology, as evidenced by little to no structures on the surface. SEM-FIB images below investigate the nature of the oxide that formed, and it will be noted how the structure of the anodic layer is much more condensed and there are really no pores remaining that are open. The Ni acetate sealing involves changes in the oxide morphology Nickel acetate seals react to form precipitates of nickel hydroxide $Ni(OH)_2$ within oxide coating pores. In all cases with all seals, dissolution of the surface structure of the oxide is part of the reaction that leads to the formation of the pore-blocking $Ni(OH)_2$ particles.[24] Then the surface features are formed, depending on how compact the layer below is, by the forcing of air up and out of the pores that are collapsing.

The air bubbles that become trapped on the surface form boehmite structures, or when the air bubbles freely leave the surface while sealing is occurring, then the surface is left virtually featureless.[21] The SABA oxide being much denser than that of the sulfuric acid grown oxide in Chapter 3, results in the air bubbles reaching the surface and being able to freely leave, leaving behind a relatively smooth surface for the nickel acetate sealing.

Both TCP sealants can be seen to have cracks and polyps along the surface. The small polyps on the surface are excess TCP coating, and the cracks are associated with the high vacuum exposure that has caused mud-cracks to form. This is seen typically on surfaces that are not anodized and are coated with TCP conversion coatings.[14, 25-28] The difference between these two TCP sealants is that the Luster-On Aluminescent has more aggregates of coating around the surface than the Bonderite T5900. This could lead to increased protection because the chromium III in the TCP coatings is able to oxidize to chromium VI and can move to damaged areas and be reduced to chromium III again.[14, 29] This oxidation and then reduction process gives more protection because of the portable protection and not just stationary protection from the chromium in the TCP.

Some regions in the micrographs presented in Figure 4.2 exhibit charging affects along the surface; very bright spots mixed with very dark spots. This affect arises from the electrically insulating nature of the oxide coating. To reduce the charging the specimens were coated with a conducting layer of platinum.

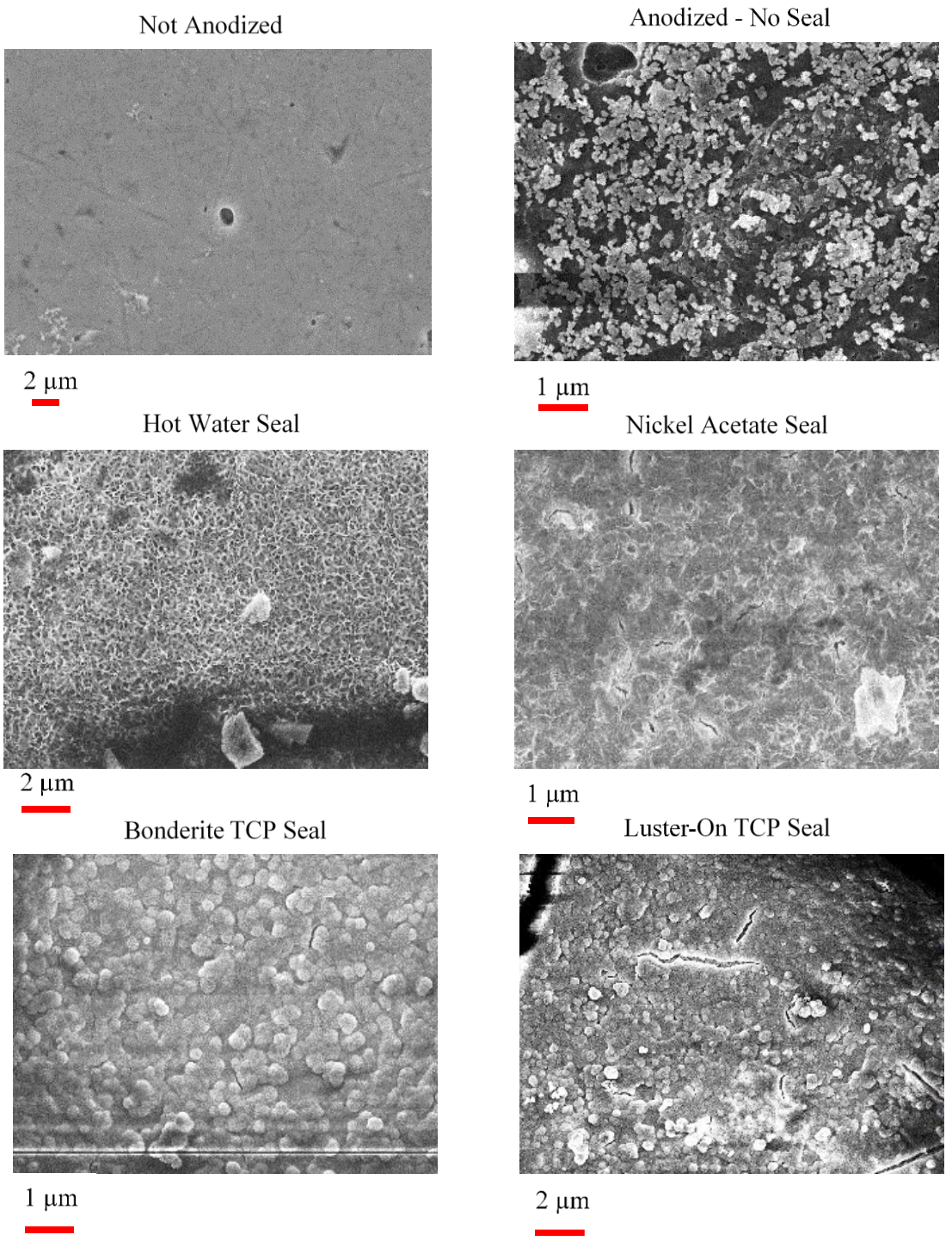

Figure 4.2. SEM micrographs showing the surfaces of unanodized and SABA anodized AA2024-T3 specimens with different sealing post-treatments. Top row shows an unanodized specimen and a specimen anodized for 20 minutes at 15 V in SABA. Bottom two rows show anodized specimens (20 minutes) in sulfuric/boric acid and sealed via different processes. Left to right: (middle row) hot water, nickel acetate; (bottom row) Bonderite TCP, and Luster-On TCP. 15 kV and 5 mm working distance.

The oxide coating thickness was estimated from SEM-FIB micrographs in the cross section to be between 5 and 6 µm. Figure 4.3 presents an example micrograph. The oxide coating is compact with no visible columnar pores, as was seen for the SA oxide coating. It is clear the SABA oxide is about the same thickness as that formed in SA under similar conditions, but it appears denser. For this particular specimen, sealing was performed using Luster-On TCP prior to the FIB milling. The oxide layer forms around the grain boundaries and some small cracking is evidenced in Figure 4.3 in the cross section. As the cracks penetrate into the oxide cross section and is not localized to the surface, it is likely a mixture of mud cracking of the TCP[14, 25-28] with some openings into the oxide around the grain boundaries.[4] While there was no open porous structure running throughout the oxide, there were some larger openings at the surface that were not filled in with the TCP sealant in Figure 4.3. These openings are, again, likely from the formation of the oxide layer being in the dense packing of the stacked features in the oxide layer forming along the grain boundaries and leaving what appear to be pores along the surface.

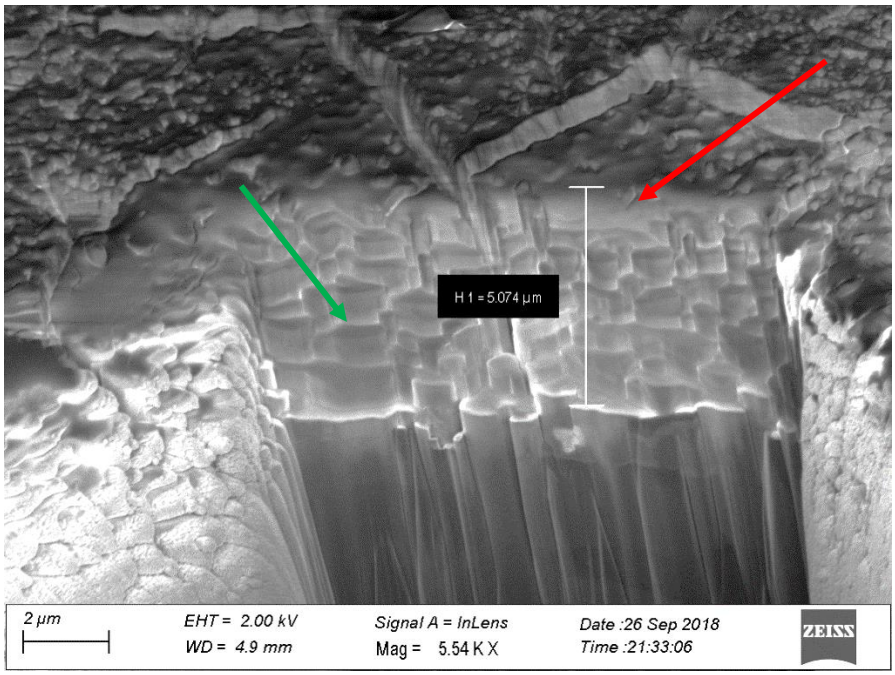

Figure 4.3. Cross section of the SABA grown oxide layer sealed with Luster-On TCP measured using SEM-FIB. The thickness of the oxide coating is 5-6 µm. The green arrow points to the block formation of the oxide layer, while the red arrow points to the TCP coating on the outer edge of the oxide.

The TCP layer can be seen across the surface of the oxide. This was confirmed by EDX analysis (Zr, Cr and F) as shown in Figure 4.4. The thickness of the TCP layer across the surface is several hundred nanometers. The EDX analysis of the TCP sealed SABA oxide was performed in the cross section at an angle. The entire oxide cross section was visible and only the bulk substrate at the bottom of the cut-out section is not visible via the x-rays. The red line in the SEM micrograph shows where the bottom of the oxide layer would be found. The Zr, Cr, and F are most abundant across the surface as evidenced by the intensity in the EDX maps. The TCP elements are found in lower intensity further into the oxide layer as seen in Figure 4.4. The TCP coating elements do not appear to reach the bottom of the oxide, but due to the tilt needed to collect the data, other analysis options are needed to quantify the depth of penetration of the TCP coating.

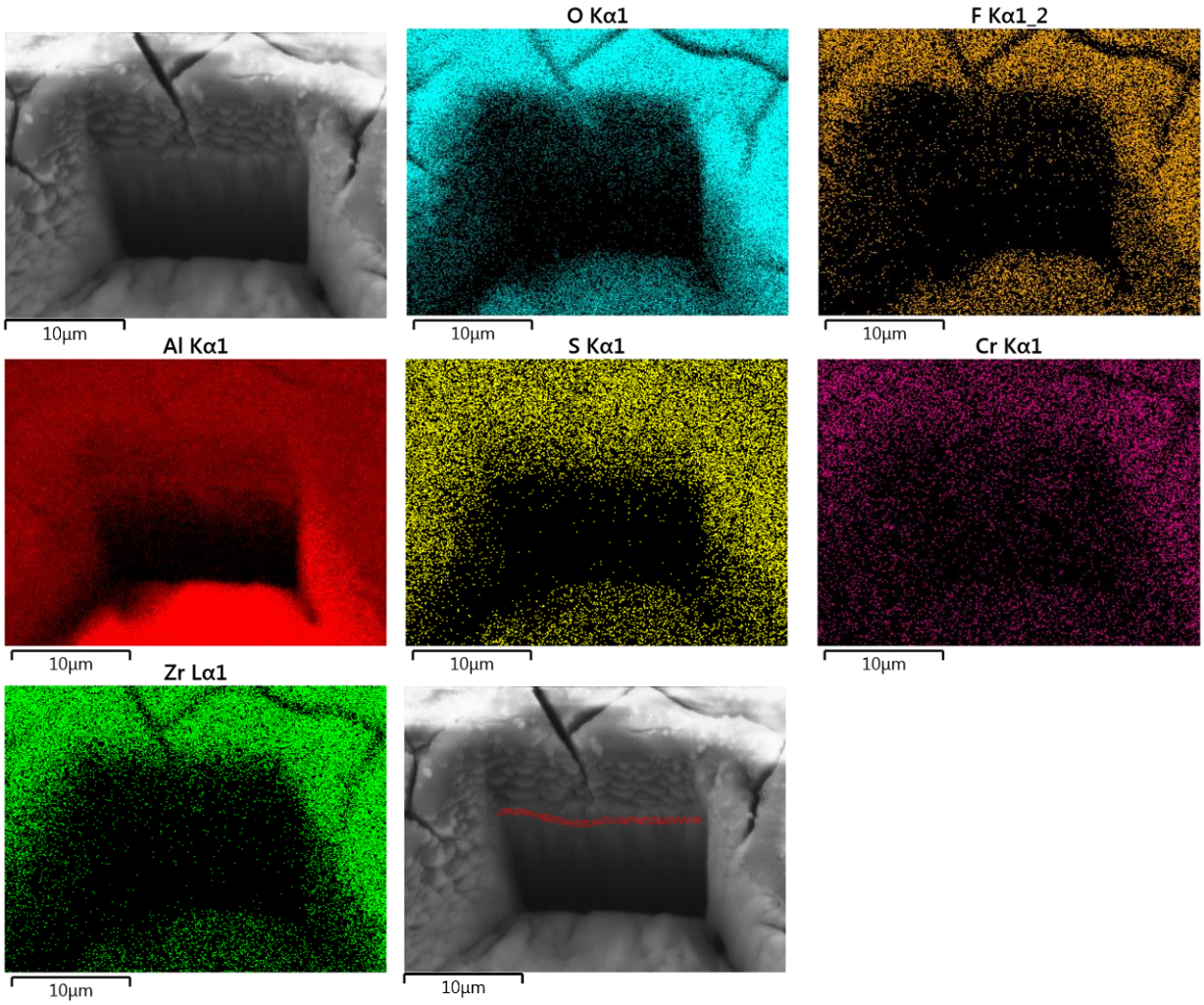

Figure 4.4. Scanning electron micrograph of an ion milled cross section of a SABA anodized AA2024-T3 specimen sealed with Luster-On Aluminescent. EDX elemental maps recorded over the cross section are presented for Al, Zr, O, F, Cr, and S. The red line indicates where the oxide layer meets the bulk aluminum alloy. Dark areas in the Al map indicate where the depth of the cut region was too far down for X-rays to escape without being blocked. The absence of the element in the maps in this region does not mean it wasn't present, but that the X-rays were blocked before they could reach the detector.

Glow Discharge Optical Emission Spectroscopy

GD-OES elemental profiles for the anodized specimens sealed with Bonderite TCP are presented in Figure 4.5. This analysis was done to investigate the depth of penetration of the TCP coating into the passivating oxide layer. At the very surface, around 0-5%, there appears to be the TCP coating barrier layer as suggested by the Zr and Cr found in higher amounts at

the surface and the reduction in the amount of the oxygen present in that same region. The Al_2O_3 layer has a higher concentration of the sulfur and oxygen and thus it appears that the TCP forms a layer above the oxide layer and then penetrates into the oxide. This is evidenced through the uptick of S at the very edge of the oxide showing that the S is incorporated in the oxide layer as it is part of the SABA bath. B can also be found in low weight percentages in Figure 4.5 B. There S and B both show an uptick in weight around 60% of the oxide thickness and is indicative of the barrier layer that forms at the start of anodizing. This barrier layer appears to be from around 60-80% and is roughly 20% of the total oxide thickness. This barrier layer is much thicker than the one formed in sulfuric acid (~10% of oxide layer). This thicker barrier layer provides added protection as it is defect free and is very compact from the incorporation of boron.[9] The Zr and Cr are present at the top of the oxide layer, and into the oxide until around 45-50% of the oxide thickness. After this depth, the TCP components were no longer found, and the oxide was all the remained along with the sulfur/boron from the acid bath. At around 70-80% of the oxide thickness the oxide begins to end, and the bulk of the alloy is present and with further penetration Cu is found in greater amounts which also signals the bulk substrate has been reached.

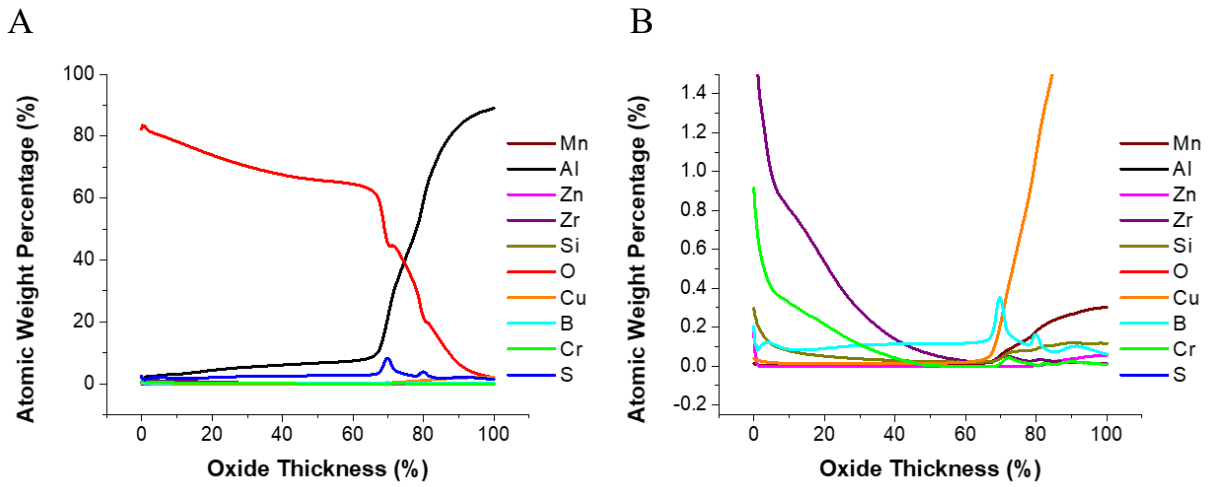

Figure 4.5. GD-OES elemental profiles for the SA anodized specimen sealed with Bonderite TCP coating. A) Full spectrum showing the full oxide depth to the bulk of the alloy. B) Oxide weight percentages from 0-5 enlarged from A to show the TCP components more clearly. Zr and Cr are found at the surface and are continued to be found throughout the oxide to ~50% of the oxide thickness. Plots are average of 3 data sets.

The TCP coating elements were found to penetrate to the bottom of the more compact oxide created with the SABA bath. While the oxide is more compact and does not show the porous columnar structure, the oxide forms in blocks along the grain with channels between them at the grain boundries.[9] These channels allow the TCP coating bath to penetrate further into the oxide layer. This suggests that the TCP and other sealants can penetrate the oxide layer through these large cracks to help seal the defects that are formed in the oxide layer during formation.

Electrochemical Studies of the Sealed SABA Anodized Specimens

Figure 4.6 presents potentiodynamic polarization curves in the anodic direction for SABA anodized AA2024-T3 specimens sealed by the different methods - hot water, hot nickel acetate, and TCP. Curves for the unanodized and anodized and unsealed specimens are presented for comparison. The largest currents for aluminum oxide formation ($2Al + 3H_2O \rightarrow Al_2O_3 + 6H^+ + 6e^-$) are seen for the unanodized specimen by 5-6 orders of magnitude. Lower currents are seen for the anodized and unsealed with slightly lower currents for the differently sealed

specimens. The anodic current in this passivation region reaches a steady state for all the specimens with no evidence of any oxide breakdown and stable pit formation out to 0.5 V in this supporting electrolyte. The anodic current density for the hot water sealed specimen surprisingly exhibited a higher current than that of the unsealed anodized specimen. This has been seen where the hot water sealant is not able to easily penetrate into the tortuous pore system making it difficult for hydration of the alumina at greater depths. This leads to only the outer oxide being sealed and thus the current would remain higher for the less perfect seal with the hot water.[4] The other sealants also form a nonporous barrier at the outer oxide and thus have a reduced current. The lowest currents are seen for the specimens sealed with the two TCP coatings.

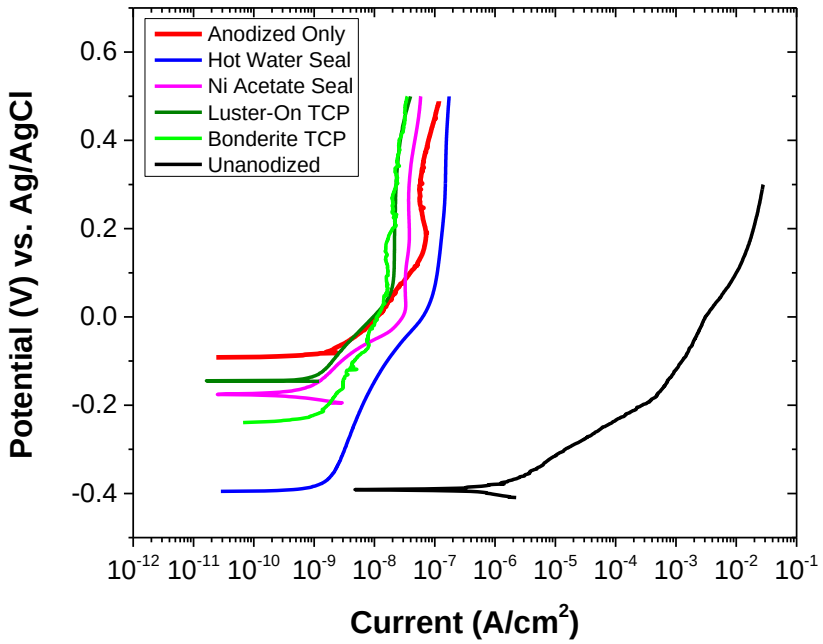

Figure 4.6. Potentiodynamic polarization curves in the anodic direction from the OCP for AA2024-T3 specimens anodized in sulfuric acid/boric acid (SABA). Data are presented for SABA anodized specimens sealed in hot water, nickel acetate and the two TCP coatings. Comparison curves for un anodized and anodized and unsealed specimens are also presented. The measurements were made in naturally aerated 0.5 M Na_2SO_4 + 0.01 M NaCl at room temperature. The SABA anodization was performed as described above.

The OCP values for all the sealed specimens are similar at around -0.1 V, except for the hot water sealed specimen that was around -0.4 V. The OCP value for the hot water sealed specimen is similar to that of the unanodized specimen. Generally, anodizing and anodizing with sealing has more of an effect on the alloy oxidation kinetics as evidenced by the positive shift of the OCP. This is consistent with increased passivation of the alloy. In summary, these polarization curve data indicate the two TCP sealants provide the greatest anodic current suppression for the anodized alloy.

Figure 4.7 shows potentiodynamic polarization curves in the cathodic direction for AA2024-T3 specimens unanodized, anodized and unsealed, and anodized and sealed in hot water, nickel acetate and the two TCP coatings. These curves were recorded on specimens after recording the OCP with the scans being initiated +50 mV relative to the OCP. The largest current by two orders of magnitude is seen for the unanodized specimen. Reduced currents are seen for the anodized and unsealed specimen with the lowest currents seen for the different sealed specimens. The current at potentials between -0.3 and -1.2 V is mainly due to the diffusion-limited reduction of dissolved oxygen ($O_2 + 2H_2O + 4e^- \rightarrow 4OH^-$). The lowest current is seen for the Bonderite TCP-sealed specimen. The hot water, nickel acetate, and Luster-On TCP-sealed specimens all exhibited similar currents. In summary, these data suggest that both TCP coatings effectively seal SABA anodic coatings providing increased barrier layer protection and reduced cathodic currents as compared to the unsealed anodized alloy. Both TCP coatings are equally as effective at sealing SABA anodic coatings as is hydrothermal and nickel acetate sealing.

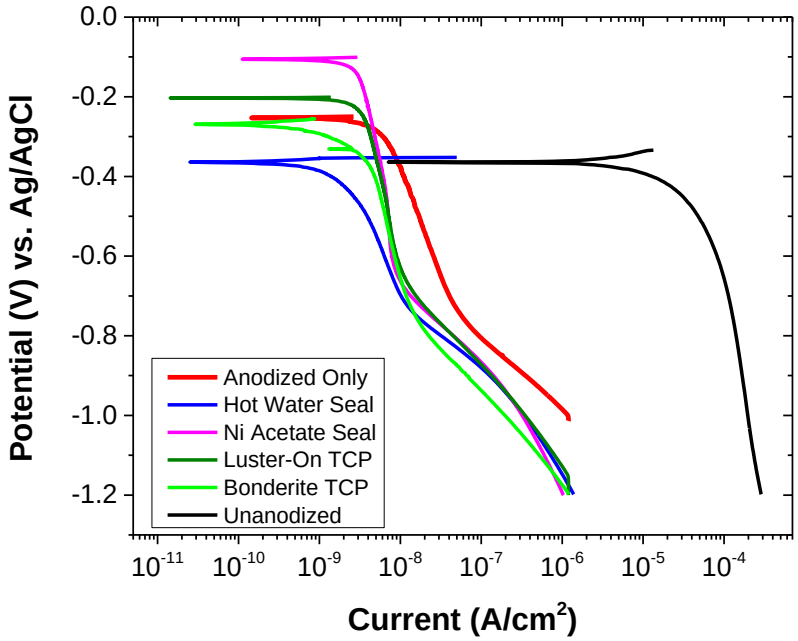

Figure 4.7. Potentiodynamic polarization curves recorded in the cathodic direction from the OCP for AA2024-T3 specimens unanodized, SABA anodized and unsealed, and anodized and sealed in hot water, nickel acetate and the two TCP coatings. The measurements were made in naturally aerated 0.5 M Na_2SO_4 + 0.01 M NaCl at room temperature. The SABA anodization was performed as described above.

Replicate electrochemical measurement data for the differently sealed anodized AA2023-T4 alloys were statistically analyzed with the results presented in the figures and table below. Figure 4.8 displays the nominal anodic current measured at +0.20 V for all the different specimens. The largest nominal current is observed for the anodized specimen and the specimen anodized and sealed with hot water. This has been seen where the hot water sealant is not able to easily penetrate into the tortuous pore system, which makes it difficult for hydration of the alumina at greater depths, and thus, the current would remain higher for the less perfect seal with the hot water.[4] There is considerable variability in the measurement data for both specimen types. Data are presented for N=3 specimens. Assuming the variability results from random fluctuations in the processing or random error, including more measurement data would be expected to reduce the variability. The currents for the nickel acetate and the TCP sealed specimens are nominally the same and around 3-4x lower in

magnitude than that for the anodized specimens. There was much less variability in the current data for the nickel acetate and TCP-sealed specimens. The lowest nominal current and the least variability are seen for the two TCP-sealed specimens. Nominally the currents for these specimens are significantly lower than the currents for the hot water-sealed and anodized and unsealed specimens but given the large variability in the data for these two specimens, this difference in current is not statistically demonstrated.

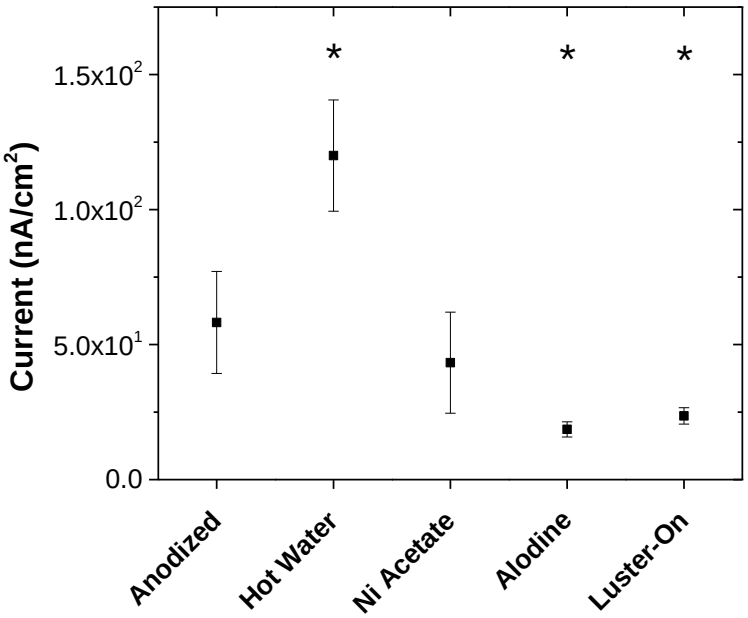

Figure 4.8. Comparison of the anodic current measured in potentiodynamic polarization curves at 0.2 V for AA2024-T3 specimens after SABA anodization that were unsealed, and sealed in hot water, nickel acetate, and the two TCP coatings. Shown are mean ± standard deviations for $n \geq 3$. Statistical analysis was made using a two-tailed Students t-Test at 95% confidence with mean data for the individually sealed specimens compared against the unsealed control.

Figure 4.9 displays the nominal cathodic current measured at -0.70 V for all the different specimens. The largest normalized current is seen for the unsealed anodized specimen. The nominal current for the differently sealed anodized specimens is about 4x lower. The lowest nominal currents are observed for the hot water, nickel acetate, and Bonderite TCP-sealed specimens.

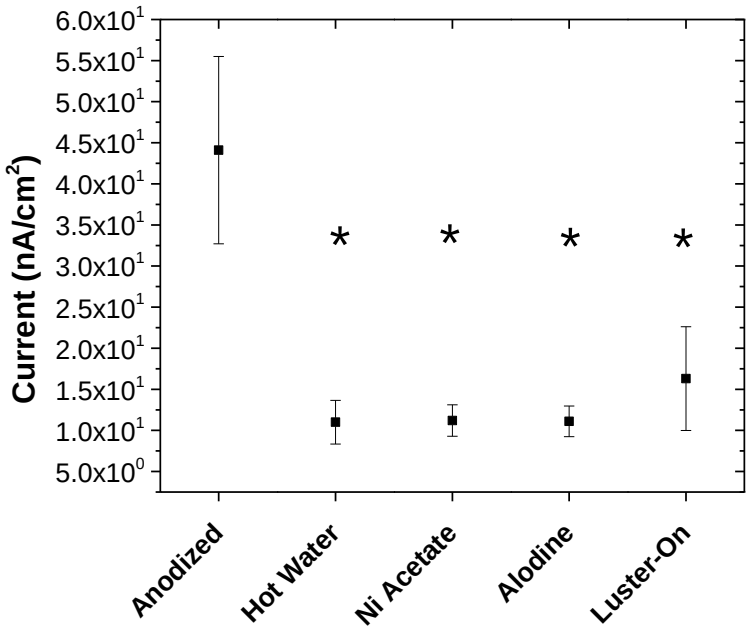

Figure 4.9. Comparison of the current measured in cathodic potentiodynamic polarization curves at -0.7 V for AA2024-T3 specimens SABA anodized and unsealed and anodized and sealed in hot water, nickel acetate, and the two TCP coatings. Shown are mean ± standard deviations for $n \geq 3$. Statistical analysis was made using a One-tailed Students t-Test at 95% confidence with mean data for the individually sealed specimens compared against the unsealed control.

Table 4.2 a summary of numerical electrochemical measurement data for the different specimens. The OCP values shows the polarization resistance taken from the impedance spectroscopy at 10 mHz. The polarization resistance for the specimens that are not anodized are around 10^3-10^4 and thus it is expected to increase with anodizing and increase further when the anodized specimens are sealed. What is seen though is that the specimens that were not sealed there is still a very large polarization resistance (10^6 ohm-cm^2). This is a little higher than expected for a specimen that was not sealed. This is hypothesized to be due to the dense oxide layer that is formed and the lack of open pores to the bottom of the oxide to the substrate below. The specimens that were sealed are not statistically different from those that were solely anodized. These tabular data taken together indicate that the TCP coatings provide added corrosion protection to the SABA anodized specimens.

Table 4.2. Tabular Data for Specimens Anodized in Sulfuric Acid/ Boric Acid for 20 Minutes

	Anodized No Seal	Hot Water Seal	Nickel Acetate Seal	Bonderite (TCP) Seal	Luster-On (TCP) Seal
OCP (mV)	-204 ± 64	-369 ± 96*	-175 ± 68*	-294 ± 108	-123 ± 63*
Current (nA) at +200 mV	58.2 ± 18.9	120 ± 20.6*	43.4± 18.8	18.6± 2.81*	23.7± 3.05*
Current (nA) at -700 mV	44.1± 11.5	11.0± 2.67*	11.3± 1.93*	11.2± 1.87*	16.3± 6.31*
R_p (Mohm-cm^2) at 10 mHz	3.79 ± 1.48	4.69 ± 1.74	7.09 ± 2.17*	6.09 ± 1.52	5.17 ± 0.47

Shown are Mean ± Confidence Interval (95%) for $n \geq 3$ for all specimen types in 0.5 M Na_2SO_4 + 0.01 M NaCl.
*Statistical Difference ($p \leq 0.05$) from Anodized specimens using a two-tailed Students t-Test.

Neutral Salt Spray Evaluation

The anodized and anodized and sealed specimens were subjected to a 14-day neutral salt spray in accordance with ASTM B117. A 5 wt.% NaCl solution was used with the chamber temperature held at 35°C . The specimens were positioned in the chamber on plastic trans at an angle of ~20°. This allowed for mist to flow down the specimen surfaces by gravity. The area at the top of each specimen that was unanodized was masked off with corrosion protection tape to ensure salt spray contact with only the anodized region. After testing, the corrosion protection tape was removed, and the specimens were rinsed with ultrapure water. They were then ultrasonicated in ultrapure water to remove salt deposits that collected on the surface. The electrochemical data revealed the two conventional TCP coatings provide as effective or superior corrosion protection as do conventional nickel acetate and hot water sealing. Figure 4.10 shows plan view optical micrographs of unanodized, anodized and unsealed, and anodized and sealed specimens before and after a 14-day NSS exposure. In the micrographs for the

unanodized specimen there are a few polishing striations that were still present prior to exposure, but with the damage they were not present after exposure. The micrographs for the anodized specimens that were sealed and the unsealed specimens all show the features along the surface that come from the uneven growth of the oxide. This uneven growth is due to the secondary phase particles reached during the anodizing process. These features are present before and after the neutral salt-spray testing.

The unanodized specimens were pulled after just 3 days of exposure because of the extensive corrosion damage that developed across the entire surface. The specimen surface was extensively roughened, and large pits (dark circular features in micrographs) developed. The micrographs for the anodized specimen have some subtle changes. The normal surface roughness increased by a factor of 4x, and the highest peak-to-valley distance increased by a factor of 0.5x. These data are in Table 4.3. In contrast and consistent with the reduced anodic and cathodic polarization currents, the 14-day NSS produced no significant change in the surface morphology, roughness, or peak-to-valley distance for any of the sealed + anodized specimens including the two TCP-sealed ones. If there was any change it appears that any imperfections along the surface were removed via exposure to the NSS.

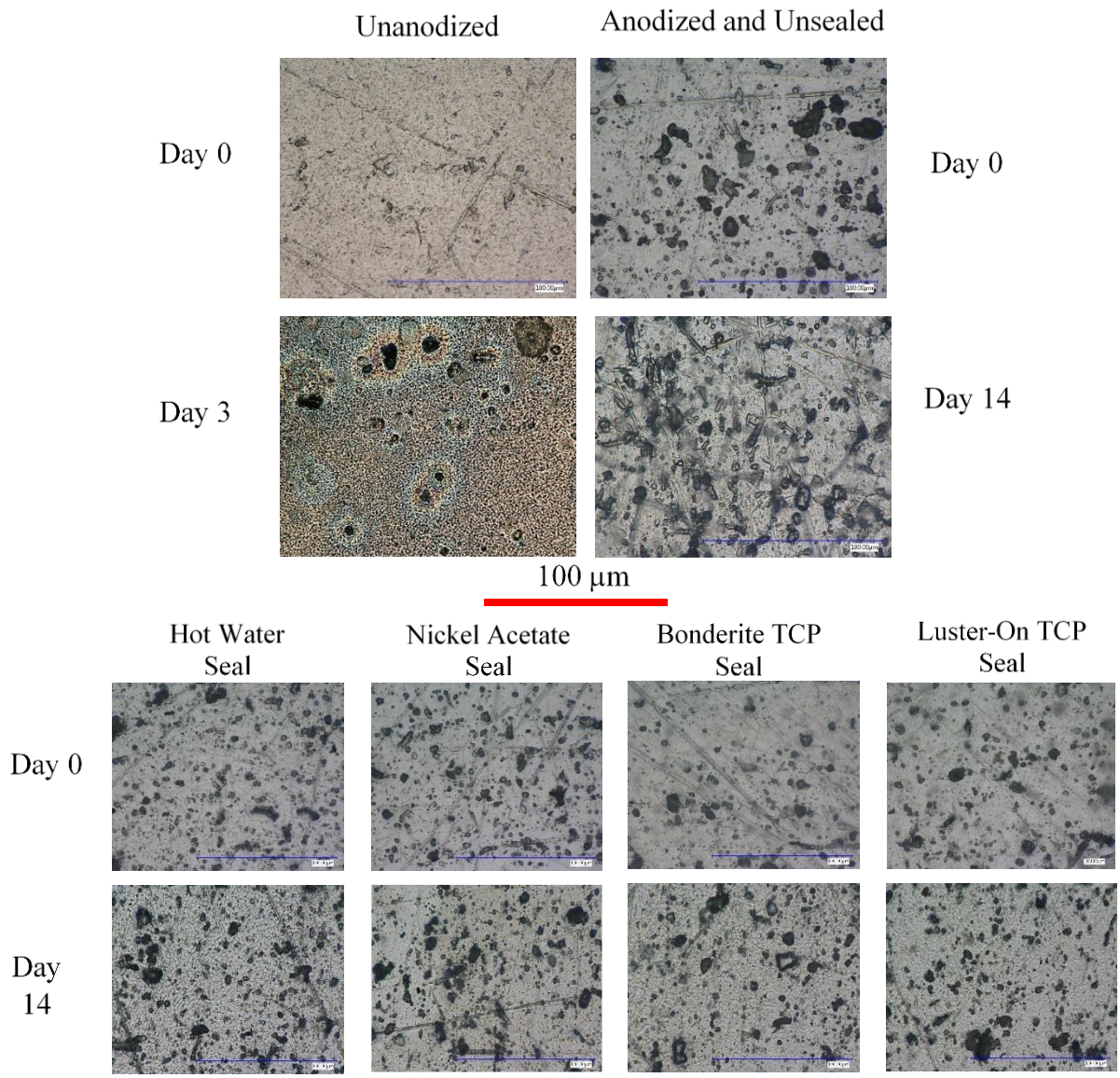

Figure 4.10. Digital optical micrographs of unanodized, anodized and unsealed, and anodized and sealed AA2024-T3 specimens before and after NSS exposure. The top images (row 1 and 2) are of specimens that were not anodized compared to those that were. The bottom images (row 3 and 4) show the different seals compared to each other. Rows 1 and 3 show images from before exposure to the 5 wt.% NaCl fog for 14 days. Rows 2 and 4 show the same specimen after exposure. Specimens that were not anodized were removed after just 3 days due to large amounts of visible pitting. All other specimens were removed after the 14-day test ended. Images taken using digital microscopy at 3,000x magnification.

The corrosion damage was minimal with no differences being evident for the two TCP sealed specimens. Both before and after the test, the specimens showed no evidence of corrosion product build up or pitting across the surface, even close to the edges.

Surface Roughness and Feature Height Data Determined by Digital Optical Microscopy

Table 4.3 summarizes surface roughness and feature height data for the different specimens before and after NSS exposure. S_q is the root mean surface roughness that assesses the root mean square average of the profile heights over the evaluation area. S_z is the average maximum height of the surface area and is found by the average of the successive values of the vertical distance between the highest and lowest points of the surface profile across the entire surface area. The values were determined from digital optical micrographs obtained at a 3000x magnification. Significant increases in the surface roughness (8x) and feature height (10x) are seen in the data for the unanodized specimen after just 3 days of NSS exposure. This is consistent with the widespread corrosion damage visible in the optical micrographs above. The anodized and unsealed specimen also experienced corrosion damage over a 14-day exposure as the surface roughness (4x) and feature height (1.3x) both increased.

In contrast, there were much less significant changes in the anodized specimens after different sealing. There was no change in the surface roughness or feature height of the hot water sealed specimens. A slight increase in both the surface roughness and feature height data is seen for the nickel acetate sealed specimens. The feature height was not changed statistically from exposure, but the average height was slightly larger (3x). For the two TCP sealed specimens, the surface roughness for both decreased after the 14-day NSS exposure. This is likely due to chemical removal of some of the TCP coating across the outside of the oxide coating. For both TCP sealed specimens, the data reveal a decrease in the feature height consistent with the chemical removal of some of the TCP coating across the outside of the oxide coating. Taken together, these data indicate that both TCP sealants provide good

corrosion resistance to SABA anodized AA2024-T3 specimens after this 14-day NSS test, comparable to the corrosion resistance provided by hot water and nickel acetate sealing.

Table 4.3. Surface Roughness (S_q) and Surface Feature Heights (S_z) for SABA Anodized and Anodized and Sealed Specimens Before and After Exposure to a 14-Day Neutral Salt Spray

	S_q before exposure (µm)	S_q after exposure (µm)	S_z before exposure (µm)	S_z after exposure (µm)
Unanodized	0.17 ± 0.03	1.33 ± 0.23*	0.55 ± 0.25	5.81 ± 2.11*
Anodized & Unsealed	0.52 ± 0.07	2.21 ± 2.03	7.66 ± 2.27	10.22 ± 3.27
Hot Water Seal	0.39 ± 0.08	0.47 ± 0.24	7.37 ± 1.97	6.13 ± 3.78
Nickel Acetate Seal	0.54 ± 0.13	1.88 ± 0.56*	9.90 ± 3.18	10.23 ± 3.33
Bonderite TCP Seal	1.59 ± 0.23	0.64 ± 0.10*	11.24 ± 2.48	7.98 ± 1.89*
Luster-On TCP Seal	2.06 ± 0.62	0.60 ± 0.07*	19.77 ± 7.22	7.13 ± 0.94*

Mean ± standard deviation at the confidence interval (95%) values for N=15 measurements (3 specimens with 5 spots on each specimen) of each type over an area of 80 x 110 µm^2. Surface roughness is presented as a root mean square value.
*Statistically significant difference ($p \leq 0.05$) from the before exposure value as assessed by a two-tailed Students t-Test.

Surface Roughness Data Determined by Optical Profilometry

Scanning optical profilometry was also performed to analyze the surface roughness on a larger scale to investigate the changes in area size. Figure 4.11 and Figure 4.12 show the 3D plots from before and after exposure, respectfully. Before neutral salt spray and after testing was done at 3 spots on the most representative specimen for the set. Before neutral salt spray the roughness values were all very similar between the different sealants and can be found in Table 4.4.

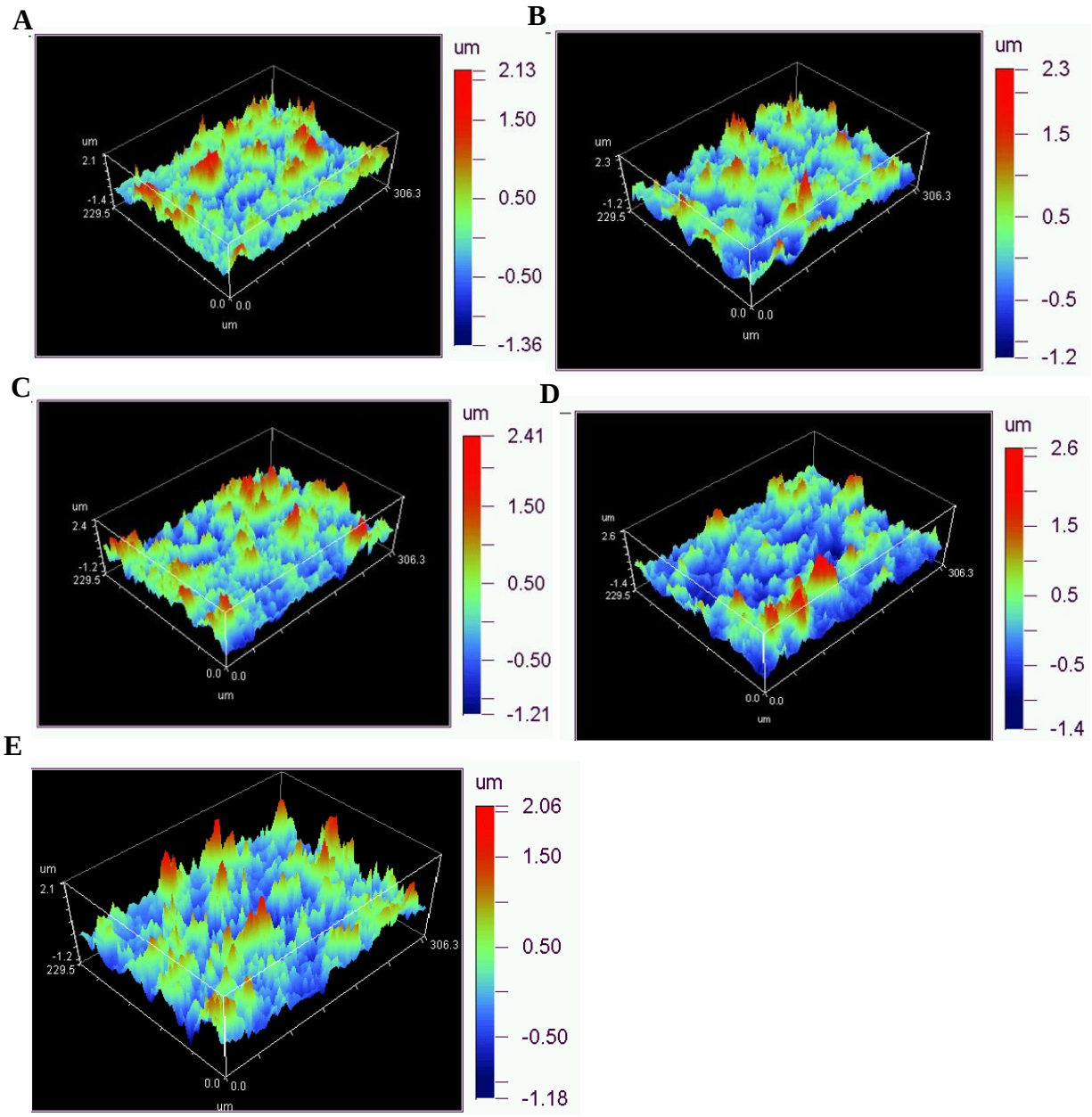

Figure 4.11. Optical profilometry 3D plots of the different sealants prior to the 14-day neutral salt spray test. Images collected at 20x magnification using Vision software. (A) Bonderite sealed, (B) Luster-On sealed, (C) Nickel Acetate sealed, (D) Hot Water sealed, (E) Anodized no seal.

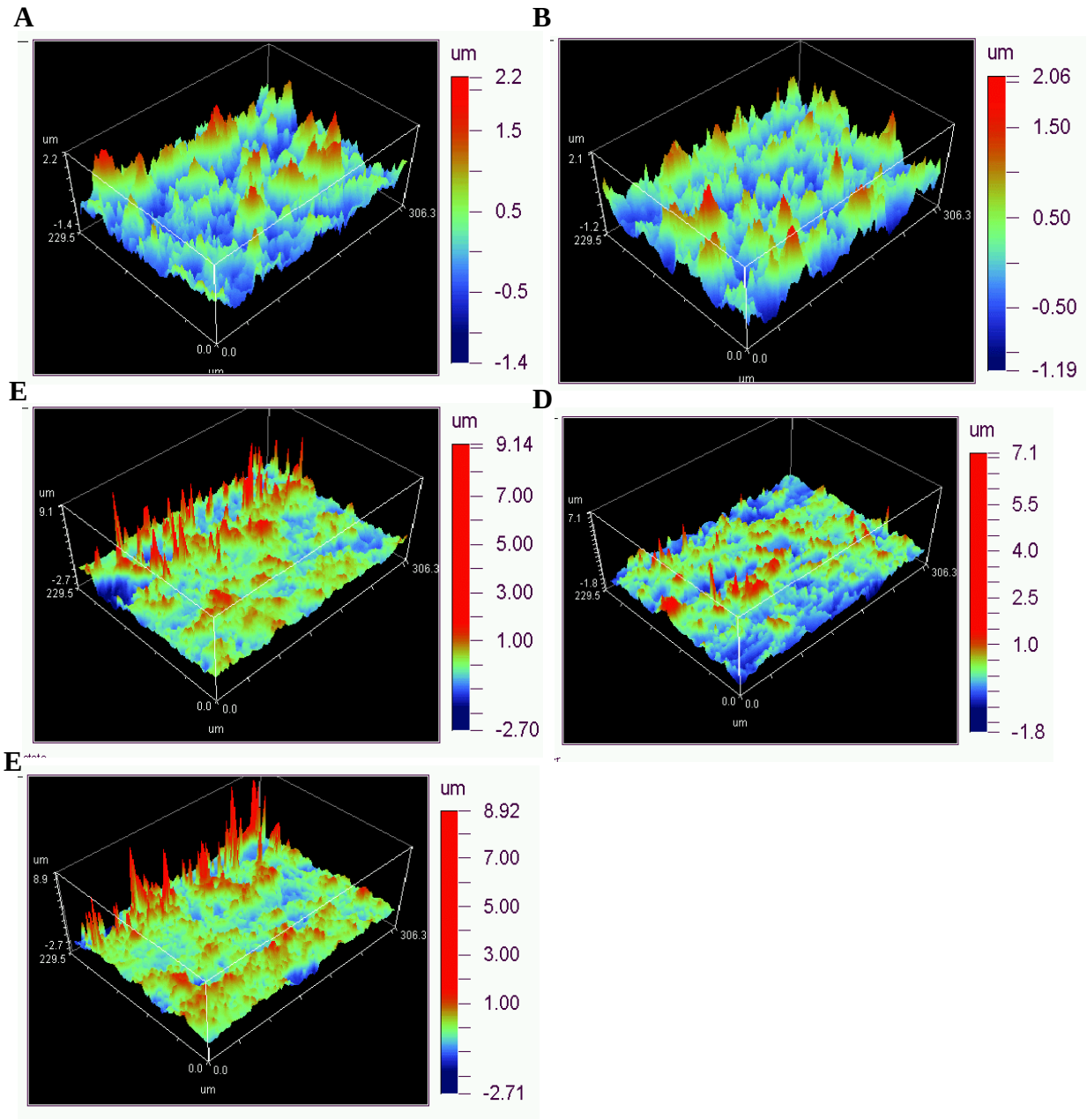

Figure 4.12. Optical profilometry 3D plots of the different sealants after exposure to the 14-day neutral salt spray test. Images collected at 20x magnification using Vision software. (A) Bonderite sealed, (B) Luster-On sealed, (C) Nickel Acetate sealed, (D) Hot Water sealed, (E) Anodized no seal.

After neutral salt spray there was a statistical difference in the roughness for the specimens that were anodized and not sealed presented in Table 4.4. The specimens that were sealed with nickel acetate also showed a statistical difference in roughness after exposure to the salt spray

fog. The two TCP coatings both showed no statistical difference in roughness. And the images in Figure 4.12 show that there was no difference in the surface features on the two TCP coatings. While the values are different from that reported above, this is accounted for in the total area investigated. Over larger areas, the average roughness is incorporating more data points and any larger deviations from the average are less pronounced in the data.

Table 4.4. Roughness (R_q) Data for Scanning Optical Profilometry Before and After 14-day Exposure for the SABA Anodized and Anodized and Sealed Specimens

	Bonderite Sealed	Luster-On Sealed	Nickel Acetate Sealed	Hot Water Sealed	Anodized & Unsealed
R_q Before (μm)	0.41 ± 0.04	0.44 ± 0.05	0.50 ± 0.02	0.44 ± 0.05	0.46 ± 0.03
R_q After (μm)	0.42 ± 0.05	0.46 ± 0.03	0.82 ± 0.09*	0.49 ± 0.02	0.86 ± 0.11*

Mean ± confidence interval (95%) values for n=3 for all specimen types.
*Significant difference ($p \leq 0.05$) from before exposure for that specimen type assessed with One-tailed Students t-Test.

Mass loss data in Table 4.5 show the two TCP sealants had a very large variation after neutral salt spray. This change in mass could be due to salt stuck to the surface after removal from the chamber or could be due to the "washing" off or stripping of the TCP aggregates from the surfaces of the specimens. None of the other data shows corrosion product built up on the surface, thus it is likely that the change in mass is from the removal of coating precipitates or a chemical loss of the TCP coating from the oxide surface.

Table 4.5. Weight Percent Change After 14-Day Neutral Salt Spray Exposure

Bonderite TCP Sealed	Luster-On TCP Sealed	Nickel Acetate Sealed	Hot Water Sealed	Anodized Not Sealed
0.08 ± 0.03	0.07 ± 0.02	0.07 ± 0.06	0.02 ± 0.02*	0.10 ± 0.02

Mean ± confidence interval (95%) values for n=3 for all specimen types.
*Significant difference from Anodized + No Seal specimens assessed with One-tailed Students t-Test.

4.5 DISCUSSION

The sulfuric acid/boric acid anodizing produced anodic oxide layers that were found to be approximately 5-10 μm in depth. These layers did not have the columnar pores typically found with sulfuric acid anodizing. Instead, the SABA anodizing produced blocks of oxide with small channels between the blocks and was cracked which allowed for sealants to penetrate to the base of the oxide layer to seal the compact oxide layer fully.

The SABA electrolyte did not produce the nice columnar pores like with the sulfuric acid bath and thus the TCP seal formed a thick layer on top of the oxide layer with penetration to around 50% of the total oxide thickness as was found through EDX analysis and GD-OES analysis. The EDX of the cross-section was difficult to obtain as the x-rays are not easy to read at the depths cause by the milling process, but in total the TCP components were found to penetrate into the oxide slightly as there were open channels from the oxide forming on the grains and having the channels at the grain boundaries.

The SABA anodizing produced oxide layers that were more corrosion resistant (16x) than that of the sulfuric acid anodized specimens. The currents were found to be 2-3 orders of magnitude less for the SABA vs the SA anodized and unsealed specimens. The oxide being more compact and having fewer pores or defects allows the oxide generated through SABA anodizing to be more passivating than the SA anodized and unsealed specimens.

Electrochemically the data showed that the corrosion resistance was increased with SABA anodizing and was further increased upon sealing the oxide layer. The TCP coatings showed excellent corrosion resistance and was found to be like that of the nickel acetate and hot water seals at 1.5-2x that of the oxide layer alone. The TCP coating uses less energy as the nickel

acetate and the hot water seals both require elevated temperatures and provides similar corrosion protection to the underlying alloy.

Correlation between specimens investigated with electrochemical measurements and neutral salt spray were made for specimens anodized in SABA. The electrochemical data suggests that the specimens that were not anodized would have the least corrosion resistance due to the high current at low over potentials from the open circuit potential. This was corroborated with the results from the neutral salt spray test because after just 3 days there was significant pitting found along the surface of the specimens. This pitting occurred much more rapidly than that of the pitting found on the specimens that were anodized and unsealed. This too correlates well with the electrochemical data because the current was much lower for the specimens anodized without being sealed than it was for the specimens not anodized at all, but there was still a slightly higher current density for the specimens that were anodized and unsealed than those that were anodized and sealed.

The specimens that were anodized and sealed did not show much statistical difference in the electrochemical data besides that the hot water seal did have higher currents than the other sealants. However, when correlating to the neutral salt-spray test results, there was no difference found in the salt spray test for any of the sealants like there was in the electrochemical data. For the two TCP sealed specimens, the surface roughness for both decreased after the 14-day NSS exposure. This is likely due to chemical removal of some of the TCP coating across the outside of the oxide coating. For both TCP sealed specimens, the data reveal a decrease in the feature height consistent with the chemical removal of some of the TCP coating across the outside of the oxide coating. The surface roughness and feature heights were also altered for the nickel acetate sealed specimens. This could be due to minor

pitting that was not really noticed via the naked eye. The boehmite structures may have been damaged but remained attached to other boehmite structures and thus caused a larger height and roughness. Another possible reason for the height change was that there was some removal of the boehmite structures and some of the underlying nickel acetate was beginning to dissociate and had some minor pits in the surface. This would increase the roughness and have minor changes in the height if some of the boehmite structures remained intact. Thus, the chemical removal of the outer layer of the nickel acetate was the most likely reason for the changes in feature height and roughness. Another accelerated degradation test, thin layer mist test, may be needed to find any differences in the TCP baths used as a sealant.

4.6 CONCLUSIONS

In this work two TCP coatings were applied as a sealant to the anodic oxide formed by sulfuric acid/boric acid on AA2024-T3 and were investigated for sealing morphology, penetration of the coating into the oxide layer, corrosion protection, and correlation to accelerated degradation tests. The oxide that was formed was done so in a block like format the follows the grain boundaries leading to tortuous channels along those grain boundaries for sealing. The oxide had very few pores at the surface that were open for penetration of electrolyte or sealants. The TCP formed through the fluoride etching of the oxide and penetration into the open channels. The TCP coatings then formed in the oxide by filling and sealing the open channels. The TCP also provided a protective barrier layer at the outer oxide that was found to be around 150-200 nm in thickness. The nickel acetate was also able to penetrate into the oxide layer to form boehmite structures to fill the channels. The hot water was able to only form a small protective layer as the electrochemistry saw an increase in current. The oxide layer sealed with the TCP coatings provides similar amounts of protection

to the underlying alloy as other commercial sealants, but with less energy consumption by being applied at room temperature. The TCP sealed specimens showed no damage after 14 days of exposure to 5 wt.% NaCl in the neutral salt spray test. There was no statistical difference found between the two TCP coatings and both would be excellent options as sealants for anodic oxide films on AA2024-T3 formed with sulfuric acid/boric acid anodizing.

REFERENCES

REFERENCES

1. Thompson, G. E.; Zhang, L.; Smith, C. J. E.; Skeldon, P., Boric/sulfuric acid anodizing of aluminum alloys 2024 and 7075: Film growth and corrosion resistance. **1999**.

2. Cohen, S.; Spadafora, S., A Comparison of Thin Film Sulfuric Acid Anodizing and Chromic Acid Anodizing Processes. **1995**, 40.

3. Boisier, G.; Pebere, N.; Druez, C.; Villatte, M.; Suel, S., FESEM and EIS Study of Sealed AA2024-T3 Anodized in Sulfuric Acid Electrolytes: Influence of Tartaric Acid. *J. Electrochem. Soc.* **2008,** *155* (11), C521-C529.

4. Domingues, L.; Fernandes, J. C. S.; Da Cunha Belo, M.; Ferreira, M. G. S.; Guerra-Rosa, L., Anodising of Al 2024-T3 in a modified sulphuric acid/boric acid bath for aeronautical applications. *Corrosion Science* **2003,** *45* (1), 149-160.

5. Wong, C.-M.; Moji, Y. Method for Anodizing Aluminum. 1990.

6. Shimizu, K.; Kobayashi, K.; Thompson, G. E.; Wood, G. C., Development of porous anodic films on aluminium. *Philosophical Magazine A* **1992,** *66* (4), 643-652.

7. Curioni, M.; Saenz de Miera, M.; Skeldon, P.; Thompson, G.; Ferguson, J., Macroscopic and Local Filming Behavior of AA2024 T3 Aluminum Alloy during Anodizing in Sulfuric Acid Electrolyte. *Journal of The Electrochemical Society* **2008,** *155*, C387-C395.

8. Keller, F.; Hunter, M. S.; Robinson, D. L., Structural Features of Oxide Coatings on Aluminum. *Journal of The Electrochemical Society* **1953,** *100* (9), 411.

9. Runge, J. M., The Metallurgy of Anodizing Aluminum. Springer International Publishing: 2018; pp 149-190.

10. Pashchanka, M.; Schneider, J. J., Origin of self-organisation in porous anodic alumina films derived from analogy with Rayleigh–Bénard convection cells. *Journal of Materials Chemistry* **2011,** *21* (46), 18761-18767.

11. Zhang, J.-s.; Zhao, X.-h.; Zuo, Y.; Xiong, J.-p., The bonding strength and corrosion resistance of aluminum alloy by anodizing treatment in a phosphoric acid modified boric acid/sulfuric acid bath. *Surface and Coatings Technology* **2008,** *202* (14), 3149-3156.

12. ASTM, Constant Amplitude Axial Fatigue Tests of Metallic Materials. Materials, A. S. f. T. a., Ed. Annual Book of ASTM Standards, 1984; pp E466-82.

13. Brace, A. W., *The Technology of Anodizing Aluminum*. 3rd ed. ed.; Interall Srl.: Modena, Italy, 2000.

14. Guo, Y.; Frankel, G. S., Characterization of trivalent chromium process coating on AA2024-T3. *Surface and Coatings Technology* **2012,** *206* (19), 3895-3902.

15. Munson, C. A.; McFall-Boegeman, S. A.; Swain, G. M., Cross comparison of TCP conversion coating performance on aluminum alloys during neutral salt-spray and thin-layer mist accelerated degradation testing. *Electrochimica Acta* **2018,** *282*, 171-184.

16. Li, L.; Swain, G. P.; Howell, A.; Woodbury, D.; Swain, G. M., The Formation, Structure, Electrochemical Properties and Stability of Trivalent Chrome Process (TCP) Coatings on AA2024. *J. Electrochem. Soc.* **2011,** *158* (9), C274-C283.

17. Shruthi, T. K.; Walton, J.; McFall-Boegeman, S.; Westre, S.; Swain, G. M., Investigation of the Trivalent Chromium Process Conversion Coating as a Sealant for Anodized AA2024-T3. *Journal of The Electrochemical Society* **2020,** *167* (11), 111504.

18. Matzdorf, C.; Beck, E.; Hilgeman, A.; Prado, R., Trivalent Chromium Process (TCP) as a Sealer for MIL-A-8625F Type II, IIB, and IC Anodic Coatings. Division, N. A. W. C. A., Ed. August 29, 2008.

19. Abd El-Hameed, A. M.; Abdel-Aziz, Y. A.; El-Tokhy, F. S., Anodic Coating Characteristics of Different Aluminum Alloys for Spacecraft Materials Applications. *Materials Sciences and Applications* **2017,** *8* (2), 197-208.

20. Carangelo, A.; Curioni, M.; Acquesta, A.; Monetta, T.; Bellucci, F., Application of EIS to In Situ Characterization of Hydrothermal Sealing of Anodized Aluminum Alloys: Comparison between Hexavalent Chromium-Based Sealing, Hot Water Sealing and Cerium-Based Sealing. *J. Electrochem. Soc.* **2016,** *163* (10), C619-C626.

21. Zuo, Y.; Zhao, P.-H.; Zhao, J.-M., The influences of sealing methods on corrosion behavior of anodized aluminum alloys in NaCl solutions. *Surface & Coatings Technology - SURF COAT TECH* **2003,** *166*, 237-242.

22. Ferrer, K. S.; Kelly, R. G., Comparison of Methods for Removal of Corrosion Product from AA2024-T3. *Corrosion* **2001,** *57* (02).

23. Arenas, M. A.; Conde, A.; de Damborenea, J. J., Effect of acid traces on hydrothermal sealing of anodising layers on 2024 aluminium alloy. *Electrochimica Acta* **2010,** *55* (28), 8704-8708.

24. Hu, N.; Dong, X.; He, X.; Browning, J.F.; Schaefer, D.W. Effect of sealing on the morphology of anodized aluminum oxide. *Corros. Sci.* **2015,** 97, 17-24.

25. Arrowsmith, D. J.; Dennis, J. K.; Sliwinski, P. R., Chromate conversion coatings on aluminium: Growth of layers of spherical particles. *Transactions of the IMF* **1984,** *62* (1), 117-120.

26. Treverton, J. A.; Amor, M. P., High-resolution SEM studies of chromate conversion coatings. *Journal of Materials Science* **1988,** *23* (10), 3706-3710.

27. Laget, V.; Jeffcoate, C. S.; Isaacs, H. S.; Buchheit, R. G., Dehydration-Induced Loss of Corrosion Protection Properties in Chromate Conversion Coatings on Aluminum Alloy 2024-T3. *Journal of The Electrochemical Society* **2003,** *150* (9), B425.

28. Qi, J.; Walton, J.; Thompson, G. E.; Albu, S. P.; Carr, J., Spectroscopic Studies of Chromium VI Formed in the Trivalent Chromium Conversion Coatings on Aluminum. *Journal of The Electrochemical Society* **2016,** *163* (7), C357-C363.

29. Xia, L.; Akiyama, E.; Frankel, G.; McCreery, R., Storage and Release of Soluble Hexavalent Chromium from Chromate Conversion Coatings: Equilibrium Aspects of Cr VI Concentration. *J. Electrochem. Soc.* **2000,** *147* (7), 2556-2562.

CHAPTER 5. EFFECT OF LASER CLEANING AND HYPERPASSIVATION ON THE ELECTROCHEMICAL BEHAVIOR OF ALUMINUM ALLOY – AA2024-T3

Chapter adapted from *J. Electrochem. Soc.* **168** 031501 (2021).

Article: Sarah McFall-Boegeman, David F. Yancey, Tyler O'Neill, Nick Davidson, and Greg M. Swain. *Effect of Laser Cleaning and Hyperpassivation on the Electrochemical Behavior of AA2024-T3.*

5.1 INTRODUCTION

There is a need to implement more environmentally friendly surface pretreatments and finishes in aerospace material processing to mitigate corrosion, particularly for aluminum alloys. Laser cleaning is one such surface pretreatment. There are four general categories of laser-based material processing used industrially: (i) laser machining (cutting and drilling) that involves removing material to shape a workpiece[1,2], (ii) laser texturing to introduce patterns into a surface that alter in beneficial ways wettability and coating or bonded component adhesion[3,4], (iii) laser melting in 3D printing that utilizes a high power density light source to melt and fuse metallic powders producing a shaped component[5,6], and (iv) laser cleaning for coating or contaminant removal and surface cleaning.[7-17]

Abrasives and wet chemical treatments are still routinely used for coating removal, cleaning, and surface pretreatment of aerospace materials. Surface pretreatment (cleanliness, texture, and chemistry) is necessary to properly prepare alloys for adhesive bonding to other materials or for the application of a coating system for corrosion protection. The use of abrasives and solution processing is time consuming, labor intensive, an issue for worker health

and safety, and requires expensive environmental controls for chemical use and waste disposal. Hand-held laser systems can remove coatings and clean aerospace materials, including aluminum, steel, and other metals, without causing unacceptable damage to or alteration of the mechanical strength of the substrate.[7-17] Laser cleaning eliminates the need for abrasives and wet chemical processing, and their associated waste streams. The process can be used to remove contaminants, oxide layers, and coating systems from small areas, irregular surfaces, and hard-to-reach areas on aircraft. To date, there has not been widespread adaptation of this material processing technology in the aerospace sector. Furthermore, there is limited scientific literature on parameter optimization, the mechanisms associated with the laser cleaning of aluminum alloys, and the effect of the treatment on the electrochemical behavior of the alloys.[7-17] Given the short pulse duration (100's of nanoseconds) used, the local heating that occurs is limited to the near-surface region. Using a thermal diffusivity value of 9.7×10^{-5} m^2/s (pure aluminum) and a pulse time of 180 nsec (the time used in this work), the heat penetration depth is on the order of about 6 μm ($(2Dt)^{1/2}$). With proper selection of the processing parameters, lasers used in surface pretreatment will only remove a thin layer of material without affecting the bulk composition and bonding. In other words, laser treatments can effectively clean aluminum alloys without introducing major changes in the surface texture and microstructure that could reduce the bulk mechanical strength.

Using lasers for cleaning and oxide removal affords many advantages over wet chemical treatments including remote application, localized cleaning (such as a repair at a depot), cleaning of components with complex shapes, and elimination of hazardous waste.[7-22] Importantly, laser treatment, if performed properly, does not introduce pitting and pore formation in the alloy as do some chemical treatments.[7-22] Laser cleaning can remove

contaminants and surface oxides by one of two mechanisms: direct ejection of material achieved by vaporization or hydrodynamic sputtering, or by thermoplastic expansion of the underneath parent material.[7,9,11-17,22] Laser treatment is a complex process that involves ablation, phase expansion, and evaporation.[23,24] Key process parameters are the laser wavelength, pulse duration, pulse energy, repetition rate, scanning speed, and laser fluence.[7,9,11-17,20] Basic research is needed to address some of the fundamental knowledge gaps that exist about how laser cleaning affects the surface texture, chemistry, and microstructure of different aluminum alloys – knowledge that will serve as a foundation for wider adaptation of the technology in the aerospace sector.

We report herein on how two different pulsed laser surface pretreatments, cleaning (5.2 J/cm^2) and hyperpassivation (10.8 J/cm^2), affect the surface texture, surface chemistry, and electrochemical behavior of "as received" aluminum alloy AA2024-T3. Surfaces were pretreated using a pulsed (180 ns pulse duration) Nd-YAG laser at 1064 nm. Control experiments with alloys pretreated by wet chemical processing (degreasing and deoxidation) were performed for comparison. The electrochemical behavior was evaluated in naturally aerated 0.5 M Na_2SO_4 at room temperature. Preliminary electrochemical results are also provided for AA6061-T6 and AA7075-T6.

5.2 EXPERIMENTAL

Reagents

All salts were analytical grade quality, or better, and were used without additional purification. Sodium sulfate (Na_2SO_4) was purchased from Fisher Chemical (Fairlawn, NJ). Industrial grade Bonderite C-AK 6849 (also known as Turco 6849) and Bonderite C-IC Smut-go NC Aero (also known as Turco Liquid Smut-Go) solutions (Henkel Corp., Madison

Heights, MI) served as the degreaser and deoxidizer, respectively. Both were diluted with ultrapure water to 20 vol. % for use. All solutions were prepared with ultrapure water (Barnstead E-Pure) having a resistivity >17 MΩ - cm.

Specimen Preparation

Wrought aluminum alloys, AA2024-T3, AA6061-T6, and AA7075-T6, were obtained as 12" x 12" rolled sheets – so-called "as received" (www.onlinemetals.com). The nominal elemental composition of these alloy types is found in Table 5.1.

Table 5.1. Nominal Elemental Composition of AA2024-T3, AA6061-T6 and AA7075-T6 in Weight Percent

	Al	Cr	Cu	Fe	Mg	Mn	Si	Ti	Zn
AA2024-T3	Bal.	Max 0.1	3.5-5.0	Max 0.5	1.2-1.8	0.3-0.9	Max 0.5	Max 0.1	Max 0.25
AA6061-T6	Bal.	0.04-0.35	0.15-0.4	Max 0.7	0.8-1.2	Max 0.15	0.4-0.8	Max 0.15	Max 0.25
AA7075-T6	Bal.	0.18-0.28	1.2-2	Max 0.5	2.1-2.9	Max 0.3	Max 0.4	Max 0.2	5.1-6.1

The laser pretreatments were performed on specimens "as received". As such, the surfaces were rough with rolling groove undulations and covered by cutting oil, grease, fingerprints, etc. from past handling prior to pretreatment. A 0.08" (2-mm) thick sheet was cut into 1-in^2 specimens for the experiments. Specimens for control measurements were prepared by conventional solution processing – degreasing and deoxidation. This involved "as received" specimen immersion in Bonderite C-AK 6849 degreaser at 55°C for 10 min. This was followed by a 2-min tap water immersion rinse. The specimen was then immersed in Bonderite C-IC Smut-go NC Aero for deoxidation at room temperature for 2 min followed by another 2-min tap water immersion rinse. All specimens were then dried with N_2 prior to use in additional experiments. These control specimens are referred to in the text as "solution processed".

Laser Cleaning and Hyperpassivation

"As received" alloy specimens were (i) laser cleaned (low fluence) or (ii) laser hyperpassivated (high fluence). Laser treatment was performed by Adapt-Laser (Kansas City, MO) using a pulsed Nd:YAG laser with output wavelength of 1064 nm. The spot size was 428 μm in both treatments with a spot overlap of 50% during the spatial treatment process. Only one laser pulse per spot was applied over a treatment area of *ca.* 1 in^2. The parameters used were selected based on the company's knowledge of cleaning aluminum alloys without introducing any microstructural alterations. No process parameter variation was performed in this work. For the laser cleaning, the following parameters were used: (i) a pulse frequency of 40 kHz, (ii) a pulse duration of 180 ns, (iii) a pulse intensity of 29 MW/cm^2, and a (iv) laser fluence of 5.16 J/cm^2. For the laser hyperpassivation, the following parameters were used: (i) a pulse frequency of 15 kHz, (ii) a pulse duration of 80 ns, (iii) a pulse intensity of 140 MW/cm^2, and (iv) a laser fluence of 10.84 J/cm^2. Treated specimens were stored in Ziploc storage bags and shipped back to MSU. The bagged specimens were stored in a refrigerator until time for electrochemical testing.

Fundamentals of Laser Treatment

Laser cleaning involves the use of a high power, pulsed (nanosecond) light source that is rastered across a surface point to point. Key process parameters are the wavelength, pulse spot size and spacing, pulse frequency (kHz), pulse duration (nsec), pulse power (MW/cm^2), and fluence (J/cm^2). The cleaning mechanism generally involves surface heating and ablation.[7-17,18,23-25] If the energy supplied is greater than the ablation threshold, the material will undergo sublimation or vaporization. Oxides have an ablation threshold well below that of most base metals. Hence, one can adjust the laser parameters so that the oxide is removed without

damaging the metal. The wavelength of the source (1064 nm) and the absorption properties of the material are key factors in how well the ablation proceeds. Materials with high absorption will be removed easier than materials that do not absorb the laser light. For example, oxides absorb 1064 nm light strongly while aluminum exhibits little absorption at this wavelength. At low fluence, energy is absorbed and melting of the surface can occur, which may induce surface alloying and or reduce the exposure of second-phase particles due to melting and cooling of the surrounding aluminum matrix around and over a particle. At higher fluence, athermal processes begin to be important, and ejection of material via formation of a hot, dense plasma is observed. Oxides absorb the laser light and are evaporated. Additionally, the interaction of the laser beam with the surface may generate significant thermal effects to induce follow-up thermal oxidation or even some near-surface melting.[8-11,23-25] The heating of the surface in air results in the reformation of an oxide layer that is thicker and perhaps less defective than the native oxide that forms in air at room temperature. Importantly, the laser cleaning can prepare and activate a surface for the application of a coating.

Electrochemical Measurements

All electrochemical measurements were performed in a 1 cm^2 flat cell (Bio-Logic Science Instruments, France) using a computer-controlled electrochemical workstation (Gamry Instruments, Inc, Reference 600, Warminster, PA). An aluminum alloy specimen was mounted against a Viton® O-ring that defined the exposed geometric area, 1 cm^2. All currents reported herein are normalized to this geometric area. The counter electrode was a Pt flag, and the reference was a home-made Ag/AgCl electrode (4 M KCl, E^0 = +0.197 V vs. NHE) that was housed in a Luggin capillary with a cracked glass tip. All measurements were made in naturally aerated 0.5 M Na_2SO_4 (pH 5-6) at room temperature (23 ± 2 ^oC).

The following measurements were performed to evaluate the electrochemical behavior of the solution processed and laser treated alloy specimens: (i) a 30-min open circuit potential (OCP) measurement, (ii) an electrochemical impedance spectroscopy (EIS) measurement at the OCP at frequencies from 10^{-2} to 10^{6} Hz, (iii) a linear polarization curve measurement from ± 20 mV vs. OCP to determine the polarization resistance, and (iv) recording an anodic and cathodic potentiodynamic polarization curve from the OCP to 0.2 and -1.0 V vs. Ag/AgCl, respectively. The scan rate was 1 mV/s in the potentiodynamic polarization measurements. The cathodic potentiodynamic polarization curve was recorded first followed by the anodic curve on the same specimen. The polarization curves were recorded last after the OCP, EIS, and linear polarization curves.

Scanning Electron Microscopy

Scanning electron microscopy (SEM) was performed using a field emission electron microscope (JEOL 6610LV) with an energy dispersive x-ray microanalysis attachment (Oxford, AZtec Software). Electron micrographs were obtained using an accelerating voltage of 25 kV, a working distance of 11 mm, and an electron beam spot size of 30 μm with a dwell time 16 μs/pixel.

Digital Optical Microscopy

Digital microscopy was performed using a Keyence VHX-6000 microscope at magnifications of 50 and 2000x. Digital images of an entire surface were captured as each different area comes into focus, combining them into one fully focused (stitched) image. The microscope uses a depth of defocus method to calculate three-dimensional depth information based on the amount of defocusing of two-dimensional images. Roughness data were obtained

from line scans of 1 mm in length measured at different points near the center of each three-dimensional image. The depth resolution was ca. 0.2 μm.

Optical Profilometry

Optical profilometry was performed using a WYKO Optical Profilometer along with the associated instrument software, Vision for RST Plus (version 1.8). The instrument was calibrated using a gold step sputter deposited on a glass slide. The instrument used an 10x magnification lens along with a field of view lens of 2x that produced images at a 20x magnification. Five areas across each specimen were probed in a grid like pattern. The topography was profiled by stitching focused images from 10 μm above to 10 μm below the surface for each scan. The WYKO Optical Profilometer collects this same image 5 times and removes any unfocused areas of the image by averaging the scans together giving one fully focused image. 3D images and contour plots were collected over an area of 306 x 230 μm^2 to profile the surface texture and to calculate the surface roughness.

SEM-FIB Analysis

Focused ion beam milling coupled with scanning electron microscopy was performed using an AURIGA Compact FIB-SEM (Carl Zeiss) equipped with a gallium ion beam for material milling. The beam current was set to 120 pA for making cross-section cuts and was performed to a depth of 3 μm into the aluminum bulk. Cross-sections were milled by mounting the specimen normal to the gallium ion beam, but at an angle 54^o relative to the secondary electron collection optics for the microscope. Specimens were not coated with Pt, or any other metal, to protect the oxide prior to milling. The SEM micrographs were collected using a 3 kV electron beam accelerating voltage. Even though the oxide is an electrical insulator, only minor charging was observed with this voltage, even at the higher magnifications. The working

distance was 11 mm and the aperture size was 30 μm. Backscattered electron micrographs were collected at an accelerating voltage of 20 kV. All other settings were the same as above.

XPS Depth Profiling

The elemental composition with respect to depth on the treated alloy specimens was assessed by x-ray photoelectron spectroscopy. The solution processed or laser treated specimens were attached to an analysis platen with conductive copper tape. Data were collected on a VersaProbe II Microprobe XPS (Dow Chemical Co.). Elemental signals were collected for Al (2p), O (1s), Cu ($2p_{3/2}$), Mg (2p), C (1s), and F (1s). The dwell time was adjusted from element to element to achieve a suitable signal-to-noise ratio. No evidence of Cu 3p signal in the Al 2p region was observed, so the contribution of Cu signal in the Al 2p region was not considered. Data analysis was performed using CasaXPS software. Relative sensitivity factors (RSFs) for the elements of interest were taken from the instrument manufacturer.

For the depth profile analysis, a pass energy of 58.7 eV was used with a step size of 0.125 eV/step. The analysis spot size was 200 μm. Data were collected with an initial 60-second Ar ion sputtering cycle, followed by longer sputter times with increasing depth into the oxide: (i) 60 second increments: 6 min (6 cycles), (ii) 120 second increments: 10 min (5 cycles), (iii) 180 second increments: 6 min (2 cycles), (iv) 240 second increments: 8 min (2 cycles), and (v) 300 second increments: 60 min (12 cycles). The total sputter time was 90 min for each spot on each specimen. The sputtering conditions used Ar ions with an accelerating voltage of 2 kV. A beam raster size of 1 mm x 1 mm was used with a target ion current of ~2.5 μA. Based on past depth profiling work on conversion-coated aluminum alloy specimens, a sputter rate of 5 nm/min was assumed for the oxide using these settings. This means that 3000 seconds corresponds to

about 250 nm. The alloy surfaces were too rough to confirm the sputter rate with profilometric analysis of the sputter crater depth. XPS elemental compositions are reported with respect to sputter time (not depth) because sputter rate is expected to differ between the oxide surface layer and the underlying metal alloy.

5.3 RESULTS

Electrochemical Behavior

Figure 5.1 shows cathodic potentiodynamic polarization curves for solution processed (control) and laser treated AA2024-T3 specimens. The current at potentials between -0.4 and -0.8 V is due to the diffusion-limited reduction of dissolved oxygen. As can be seen, this current is significantly attenuated for both the laser cleaned and hyperpassivated specimens. The current at -0.6 V, for example, is over an order of magnitude lower for the hyperpassivated specimens and about 5x lower for the cleaned specimens, as compared to the solution processed controls. The curves for the specimen types are reproducible in terms of the current magnitude with potential. Taken together, these data indicate that the rate of diffusion-limited oxygen reduction on this alloy is lower for the laser cleaned and hyperpassivated specimens, as compared to the control. This is attributed to some surface melting and cooling of the aluminum matrix around second-phase particles that reduces their exposed area on the alloy surface, as these sites are the most active kinetically for the oxygen reduction reaction.[26-28] Additionally, aluminum oxide (Al_2O_3) reformation will occur around and over the second-phase particle at the end of the laser pulse. Given the brief elevated temperature of the surface at the end of a laser pulse, a thicker oxide layer is expected to reform, and this passivation layer could serve to inhibit oxygen reduction.

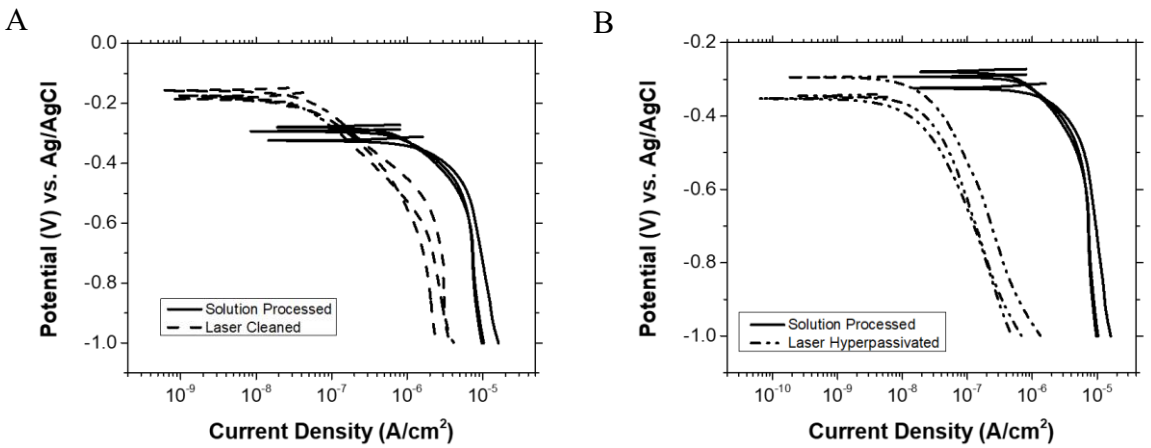

Figure 5.1. Cathodic potentiodynamic polarization curves for solution processed (controls) and (A) laser cleaned and (B) hyperpassivated AA2024-T3 specimens. All measurements were made in naturally aerated 0.5 M Na_2SO_4 at room temperature. Scan rate = 1 mV/s.

Figure 5.2 presents anodic potentiodynamic polarization curves for solution processed (control) and laser treated AA2024-T3 specimens. The current at these potentials arises from the oxidation of the aluminum and formation of an oxide (Al_2O_3 or $AlOOH/Al_2O_3$) layer. There is no evidence in the curves for increased current associated with stable pit formation and growth, at least out to 0.2 V. As was the case for the cathodic curves recorded first on these specimens, the OCP for the laser cleaned specimens is *ca.* -0.2 V, and for the laser hyperpassivated and control specimens is ca. -0.3 V. The fact that the OCP of the laser cleaned specimens is slightly more positive means that the cleaning, oxide and contaminant removal, and reformation of the oxide layer provides greater passivation to the alloy. It is difficult, however, to infer much about differences in the OCP because the same specimen was used in all the measurements, and this created changes in the surface condition over time. The current observed near 0 V for some of the solution processed specimens is believed to be due to the oxidation of Cu in exposed second-phase particles to CuO. The anodic current at -0.1 V, for example, for all laser cleaned and hyperpassivated specimens is over an order of magnitude

lower than the current for the controls. The lower current for the laser hyperpassivated than for the laser cleaned specimens is indicative of a more passivating oxide film. The curves for all three specimen types are reproducible in terms of current magnitude with potential. The results demonstrate that the rate of aluminum oxidation is suppressed by an equivalent amount on both laser treated surfaces. This is likely due to cleaning and reformation of a thicker and perhaps less defective oxide layer than exists natively on the solution processed controls. Greater variability in the OCP was observed for the laser cleaned and solution processed than for the laser hyperpassivated specimens.

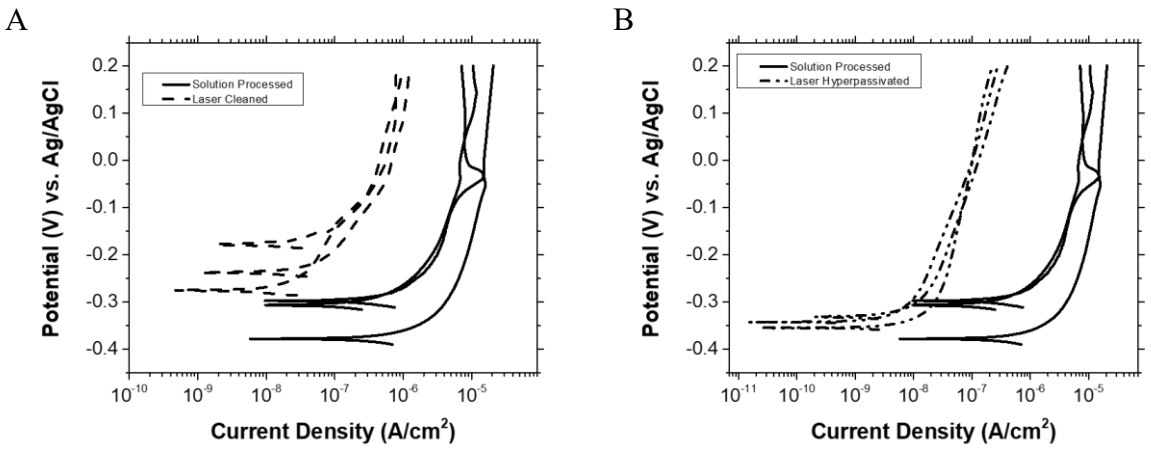

Figure 5.2. Anodic potentiodynamic polarization curves for solution processed (controls) and (A) laser cleaned and (B) hyperpassivated AA2024-T3 specimens. All measurements were made in naturally aerated 0.5 M Na_2SO_4 at room temperature. Scan rate = 1 mV/s.

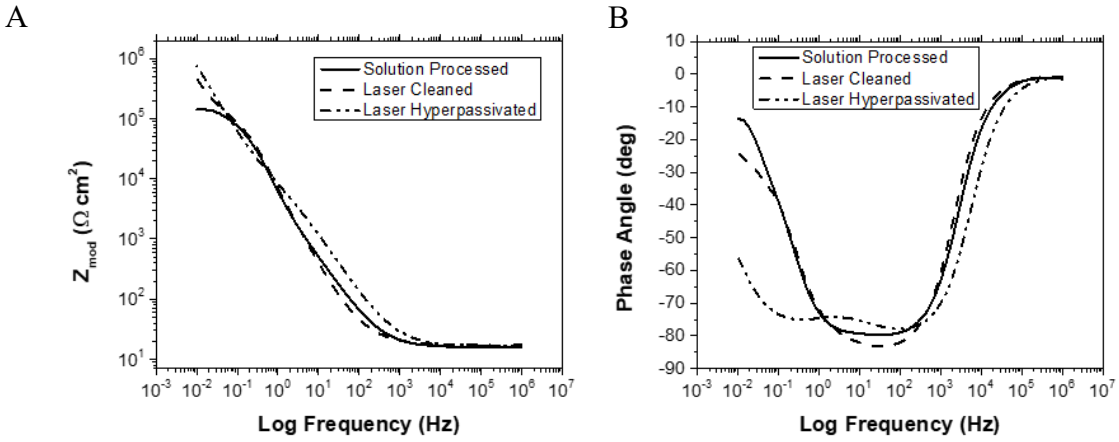

Figure 5.3. Electrochemical impedance spectroscopy data (Bode plots) for solution processed, laser cleaned and laser hyperpassivated AA2024-T3 specimens showing (A) total impedance and (B) phase shift plots over a frequency range from 10^6 to 10^{-2} Hz. The measurements were made in naturally aerated 0.5 M Na_2SO_4 and recorded at the OCP.

Electrochemical impedance spectroscopic (EIS) data for the different treated AA2024-T3 specimens, recorded at the OCP, are presented in Figure 5.3. Figure 5.3A shows Bode plots of the total impedance as a function of frequency. Similar impedance profiles are seen for the laser cleaned and solution processed specimens except at the lowest frequencies. For example, the total impedance at 0.01 Hz ($Z_{0.01\,Hz}$) is greater (13x) for the former. In fact, the $Z_{0.01\,Hz}$ values for the laser cleaned and hyperpassivated specimens are both larger than the value for the

solution processed control. This difference is reflective of an increase in the polarization resistance (*i.e.*, corrosion resistance). This appears due, based on the data in Figure 5.2, to reduced second-phase particle exposure and the formation of a more passivating (*i.e.*, thicker, and less defective) oxide layer. The high frequency range is dominated by the solution and electrode ohmic resistance, and for the three specimen types, there are no distinct differences.

Figure 5.3B shows Bode plots of phase shift as a function of frequency for the same specimens. All three specimens exhibit capacitive behavior at frequencies from 500 down to 50 Hz as evidenced by the -80 degree phase shift. The response differences for the specimen types are noticeable only at the lowest frequencies. At these frequencies, the phase shifts for the solution processed and laser cleaned specimens are similar and decrease to less than -30 degrees. In contrast, the laser hyperpassivated specimen retains more capacitive behavior with a phase shift of greater than -50 degrees. This suggests that there is a less permeable and thicker passivating oxide layer present on the surface of the hyperpassivated specimen than on the laser cleaned or solution processed specimens.

Table 5.2 presents a summary of electrochemical data for the three treated AA2024-T3 specimen types obtained from the polarization curve and the EIS data. The first column presents the low frequency impedance modulus, $Z_{0.01\ Hz}$, determined from the EIS measurements at the OCP. The larger the impedance, the less susceptible the alloy is to corrosion under the open circuit conditions. The nominal values for the laser cleaned and hyperpassivated specimens, respectively, are 13 and 31x greater than the nominal value for the solution processed controls. The data also reveal that the low frequency impedance modulus for the solution processed controls is reproducibly achieved. The second column shows the polarization resistance, R_p, for the different specimens, as determined from the slope of the

linear polarization curves recorded ±20 mV vs. OCP. This value, like $Z_{0.01\ Hz}$, is a direct measure of the corrosion resistance. The nominal values for the laser cleaned and hyperpassivated specimens are significantly greater, 9 and 25x respectively, as compared to the nominal value for the solution processed controls. These increases are like the increases seen for $Z_{0.01\ Hz}$. The center column presents the OCP values for the different specimens. These are the OCP values measured initially for the different specimens before any of the other electrochemical measurements were performed. According to the trends, the OCP values for the laser treated alloy are similar or slightly more positive of the nominal value for the solution processed controls. The right two columns compare the cathodic and anodic current densities at -0.6 and -0.1 V vs. Ag/AgCl, respectively. The nominal currents at both potentials are lower than the values for the solution processed controls, with the values being lowest for the laser hyperpassivated specimens. Taken together, these numerical electrochemical parameters indicate that the laser cleaning and hyperpassivation produce a surface condition that renders the alloy more resistant to electrochemical corrosion than the solution processed specimens.

Table 5.2. Summary of Electrochemical Parameters for the Solution Processed, Laser Cleaned, and Laser Hyperpassivated AA2024-T3 Specimens

	$Z_{0.01\ Hz}$ (kΩ-cm^2)	R_p (kΩ-cm^2)	OCP (mV vs. Ag/AgCl)	Current Density at -0.6 V (μA/cm^2)	Current Density at -0.1 V (μA/cm^2)
Solution Processed	38 ± 11	77 ± 34	-312 ± 35	7.17 ± 0.77	7.66 ± 4.38
Laser Cleaned	449 ± 16*	667 ± 111*	-178 ± 25*	1.53 ± 0.62*	0.19 ± 0.09*
Laser Hyperpassivated	1580 ± 650*	2810 ± 1510*	-344 ± 33	0.11 ± 0.06*	0.06 ± 0.01*

Mean ± confidence interval (95%) values for solution processed (n=6), laser cleaned (n=4), and laser hyperpassivated (n=5) specimens. *Statistically significant difference determined, relative to the solution processed control, using a one-tailed Student's t-test at the 95% confidence interval.

The EIS data were fit (ZView® 3.0) using a Randles equivalent circuit consisting of an electrolyte resistance, R_s, in series with the parallel combination of a constant phase element (CPE-Q) in place of a traditional double-layer capacitance and an impedance of a faradaic reaction, R_p.

The numerical values for the CPE, Q, were converted to an effective capacitance, C_{eff}, using the following equation according to the method described by Hirschorn et al.[29]

$$C_{eff} = \left(\frac{R_s R_p}{R_s + R_p}\right)^{\frac{1-\alpha}{\alpha}} Q^{\frac{1}{\alpha}}$$

This method for calculating C_{eff} was selected given the fact that this interfacial capacitance reflects charge stored at the oxide surface, in any cracks or defects in the oxide exposing the underlying metal and exposed second-phase particles. As expected, given the thicker and presumably less defective oxide, C_{eff} for the laser cleaned (2.83 ± 0.79 μF/cm^2) and hyperpassivated (0.89 ± 0.12 μF/cm^2) specimens was nominally lower than the value for the solution processed (4.03 ± 0.82 μF/cm^2) specimens at the OCP. The values are normalized to the geometric area of each specimen and can be found in Table 5.3.

Table 5.3. Summary of the Fitting Parameters from the EIS Data Recorded at the OCP for the Solution Processed, Laser Cleaned, and Laser Hyperpassivated AA2024-T3 Specimens

	R_s (Ω-cm^2)	CPE-Q (s^n/Ω-cm^2) x 10^{-6}	α	R_p (kΩ-cm^2)	C_{eff} (μF/cm^2)
Solution Processed	15.49 ± 0.12	13.2 ± 6.3	0.88 ± 0.03	96.2 ± 58.8	4.03 ± 0.82
Laser Cleaned	16.18 ± 0.24	7.19 ± 1.78	0.91 ± 0.01	514 ± 188	2.83 ± 0.79
Laser Hyperpassivated	15.69 ± 0.50	4.56 ± 0.52	0.85 ± 0.01	6110 ± 3220	0.89 ± 0.12

Mean ± confidence interval (95%) values for solution processed (n=6), laser cleaned (n=4), and laser hyperpassivated (n=5) specimens.

Electrochemical Behavior of AA6061-T6

Figure 5.4A presents anodic potentiodynamic polarization curves for solution processed (control) and laser treated AA6061-T6 specimens. The current at these potentials arises from the oxidation of the aluminum and formation of an oxide (Al_2O_3 or $AlOOH/Al_2O_3$) layer. There is no evidence in the curves for increased current associated with stable pit formation and growth, at least out to 0.4 V. The OCP for the control specimens is *ca.* -0.3 V, and for the laser cleaned and laser hyperpassivated is ca. -0.6 V. With both laser treatments producing an OCP with a negative shift from the control, this indicates that the surfaces are more active and will have more of an effect on the cathodic (diffusion-limited reduction of dissolved oxygen) reaction kinetics than on the anodic reaction (oxidation of aluminum and formation of an oxide) kinetics. In turn the currents at larger overpotentials are not highly reduced or changed from the control specimens for either laser treatment on AA6061-T6. It is difficult, however, to infer much about differences in the OCP because the same specimen was used in all the measurements, and this created changes in the surface condition over time. The anodic current at 0.2 V, for example, for all laser cleaned and hyperpassivated specimens is around 2x lower than the current for the controls. The current density was not suppressed for the hyperpassivated specimens further than the laser cleaned specimens and thus the oxide film is likely to be similar after each of the laser treatments on AA6061-T6. A small sample set was collected, and reproducibility tests would need to be conducted, but as was seen with the AA2024-T3 specimens, reproducibility is likely. The results demonstrate that the rate of aluminum oxidation is mildly suppressed by an equivalent amount on both laser treated surfaces. This is likely due to cleaning and reformation of a thicker and perhaps less defective oxide layer than exists natively on the solution processed controls.

Figure 5.4B shows cathodic potentiodynamic polarization curves for solution processed (control) and laser treated AA6061-T6 specimens. The current at potentials between -0.2 and -1.0 V is due to the diffusion-limited reduction of dissolved oxygen. As can be seen, this current is significantly attenuated for both the laser cleaned and hyperpassivated specimens. The current at -0.8 V, for example, is over an order of magnitude lower for the hyperpassivated specimens and about 20x lower for the cleaned specimens, as compared to the solution processed controls. A small sample set was collected, and reproducibility tests would need to be conducted. Taken together, these data indicate that the rate of diffusion-limited oxygen reduction on this alloy is lower for the laser cleaned and hyperpassivated specimens, as compared to the control. This is also attributed to some surface melting and cooling of the aluminum matrix around second-phase particles that reduces their exposed area on the alloy surface, as these sites are the most active kinetically for the oxygen reduction reaction.[26-28] Additionally, aluminum oxide (Al_2O_3) reformation will occur around and over the second-phase particle at the end of the laser pulse. Given the brief elevated temperature of the surface at the end of a laser pulse, a thicker oxide layer is expected to reform, and this passivation layer could serve to inhibit oxygen reduction.

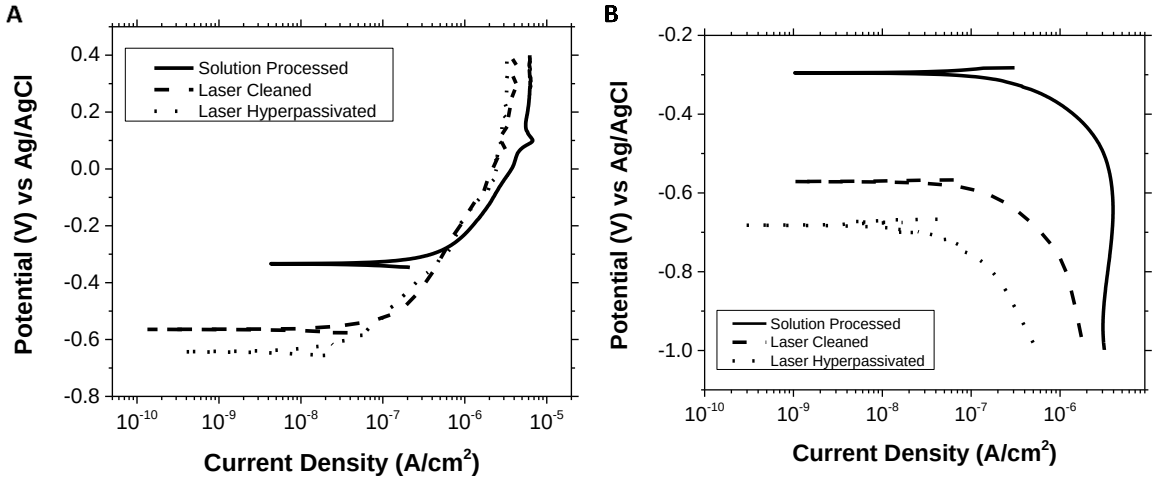

Figure 5.4. (A) Anodic and (B) cathodic potentiodynamic polarization curves for solution processed (controls), laser cleaned, and hyperpassivated AA6061-T6 specimens. All measurements were made in naturally aerated 0.5 M Na_2SO_4 at room temperature. Scan rate = 1 mV/s.

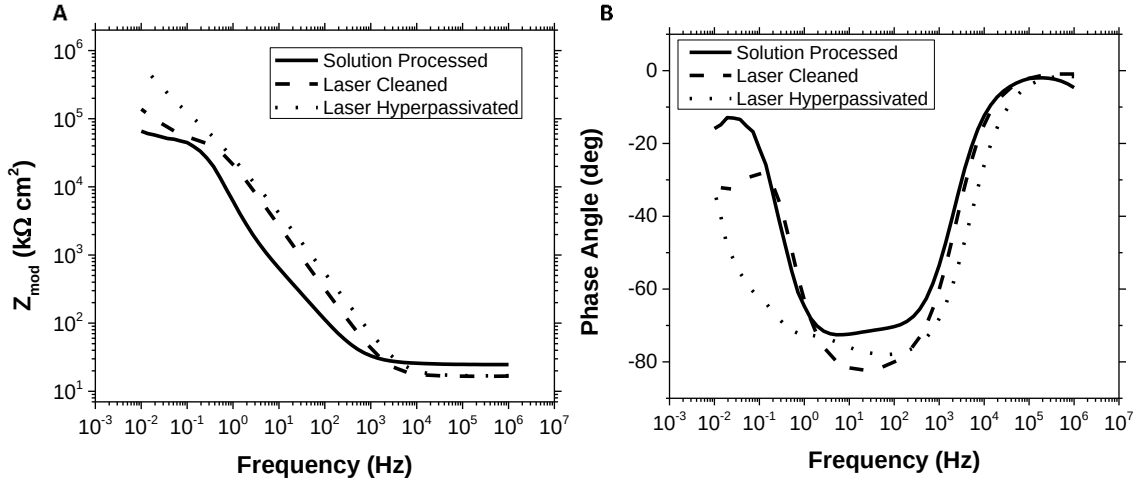

Figure 5.5. Electrochemical impedance spectroscopy data (Bode plots) for solution processed, laser cleaned and laser hyperpassivated AA6061-T6 specimens showing (A) total impedance and (B) phase shift plots over a frequency range from 10^6 to 10^{-2} Hz. The measurements were made in naturally aerated 0.5 M Na_2SO_4 and recorded at the OCP.

Electrochemical impedance spectroscopic (EIS) data for the different treated AA6061-T6 specimens, recorded at the OCP, are presented in Figure 5.5. Figure 5.5A shows Bode plots of the total impedance as a function of frequency. Similar impedance profiles are seen for the

laser cleaned and solution processed specimens except at the mid and lowest frequencies. For example, the total impedance at 0.01 Hz ($Z_{0.01\ Hz}$) is greater (10x) for the laser hyperpassivated than the control. In fact, the $Z_{0.01\ Hz}$ values for the laser cleaned and hyperpassivated specimens are both larger than the value for the solution processed control. This difference is reflective of an increase in the polarization resistance (*i.e.*, corrosion resistance). This appears due, based on the data in Figure 5.4, to reduced second-phase particle exposure and the formation of a more passivating (*i.e.*, thicker, and less defective) oxide layer. The high frequency range is dominated by the solution and electrode ohmic resistance, and for the three specimen types, there are no distinct differences.

Figure 5.5B shows Bode plots of phase shift as a function of frequency for the same specimens. All three specimens exhibit capacitive behavior at frequencies from 500 down to 50 Hz as evidenced by the -70 to -80 degree phase shift. The response differences for the specimen types are noticeable only at the lowest frequencies. At these frequencies, the phase shifts for the solution processed specimen decrease to less than -20 degrees. In contrast, the laser cleaned and laser hyperpassivated specimens retains more capacitive behavior with a phase shift of greater than -30 degrees. This suggests that there is a less permeable and thicker passivating oxide layer present on the surface of the laser cleaned and laser hyperpassivated specimens than on the solution processed specimen.

Table 5.4 presents a summary of electrochemical data for the three treated AA6061-T6 specimen types obtained from the polarization curve and the EIS data. The first column presents the low frequency impedance modulus, $Z_{0.01\ Hz}$, determined from the EIS measurements at the OCP. The larger the impedance, the less susceptible the alloy is to corrosion under the open circuit conditions. The nominal values for the laser cleaned and

hyperpassivated specimens, respectively, are 2 and 9x greater than the nominal value for the solution processed controls. The data also reveal that the low frequency impedance modulus for the solution processed controls is reproducibly achieved. The second column shows the polarization resistance, R_p, for the different specimens, as determined from the slope of the linear polarization curves recorded ±20 mV vs. OCP. This value, like $Z_{0.01\ Hz}$, is a direct measure of the corrosion resistance. The nominal values for the laser cleaned and hyperpassivated specimens are significantly greater, 2 and 9x respectively, as compared to the nominal value for the solution processed controls. These increases are like the increases seen for $Z_{0.01\ Hz}$. The center column presents the OCP values for the different specimens. These are the OCP values measured initially for the different specimens before any of the other electrochemical measurements were performed. According to the trends, the OCP values for the laser treated alloy are similar and are more negative of the nominal value for the solution processed controls. The right two columns compare the cathodic and anodic current densities at -0.8 and 0.2 V vs. Ag/AgCl, respectively. The nominal currents at both potentials are lower than the values for the solution processed controls, with the values being lowest for the laser hyperpassivated specimens. Taken together, these numerical electrochemical parameters indicate that the laser cleaning and hyperpassivation produce a surface condition that renders the alloy more resistant to electrochemical corrosion than the solution processed specimens.

Table 5.4. Summary of Electrochemical Parameters for the Solution Processed, Laser Cleaned, and Laser Hyperpassivated AA6061-T6 Specimens

	$Z_{0.01\ Hz}$ ($k\Omega$-cm^2)	R_p ($k\Omega$-cm^2)	OCP (mV vs. Ag/AgCl)	Current Density at -0.8 V ($\mu A/cm^2$)	Current Density at 0.2 V ($\mu A/cm^2$)
Solution Processed	66 ± 2	84 ± 7	-314 ± 17	3.60 ± 0.56	5.83 ± 0.38
Laser Cleaned	139**	194**	-568**	1.17	3.48
Laser Hyperpassivated	629 ± 113*	736 ± 97*	-656 ±18*	0.18 ± 0.004*	2.93 ± 0.33

Mean ± confidence interval (95%) values for solution processed (n=3), laser cleaned (n=1), and laser hyperpassivated (n=2) specimens. *Statistically significant difference determined, relative to the solution processed control, using a one-tailed Student's t-test at the 95% confidence interval. **Laser cleaned statistical differences at 95% confidence are presumed but may not be statistically different until further specimens can be tested.

Electrochemical Behavior of AA7075-T6

Figure 5.6A presents anodic potentiodynamic polarization curves for solution processed (control) and laser treated AA7075-T6 specimens. The current at these potentials arises from the oxidation of the aluminum and formation of an oxide (Al_2O_3 or $AlOOH/Al_2O_3$) layer. There is no evidence in the curves for increased current associated with stable pit formation and growth, at least out to 0.4 V. The OCP for the control specimens is *ca.* -0.3 V, and for the laser cleaned and laser hyperpassivated is ca. -0.55 V. With both laser treatments producing an OCP with a negative shift from the control, this indicates that the surfaces are more active and will have more of an effect on the diffusion-limited reduction of dissolved oxygen reaction kinetics than on the oxidation of aluminum and oxide formation kinetics. It is difficult, however, to infer much about differences in the OCP because the same specimen was used in all the measurements, and this created changes in the surface condition over time. While the current

was only slightly reduced for the laser cleaned specimen from the control specimen (1x) at 0.3 V, the laser hyperpassivated showed around 1 order of magnitude current decrease from the control specimen. The lower current for the laser hyperpassivated than for the laser cleaned specimens is indicative of a more passivating oxide film. The curves for all three specimen types are reproducible in terms of current magnitude with potential for the small sample size studied. The results demonstrate that the rate of aluminum oxidation is suppressed by a greater amount for the laser hyperpassivated surfaces vs the laser cleaned specimen, and both provide some protection to the surface when compared to the solution processed control. This is likely due to cleaning and reformation of a thicker and perhaps less defective oxide layer than exists natively on the solution processed controls.

Figure 5.6B shows cathodic potentiodynamic polarization curves for solution processed (control) and laser treated AA7075-T6 specimens. The current at potentials between -0.4 and -1.0 V is due to the diffusion-limited reduction of dissolved oxygen when the current is at the plateau for each specimen type. As can be seen, this current is significantly attenuated for both the laser cleaned and hyperpassivated specimens. The current at -0.8 V, for example, is over an order of magnitude lower for the hyperpassivated specimens and about 1x lower for the cleaned specimens, as compared to the solution processed controls. A small sample set was collected, and reproducibility tests would need to be conducted, but as was seen with the AA2024-T3 specimens, reproducibility is likely. Taken together, these data indicate that the rate of diffusion-limited oxygen reduction on this alloy is lower for the laser cleaned and hyperpassivated specimens, as compared to the control. This is also attributed to some surface melting and cooling of the aluminum matrix around second-phase particles that reduces their exposed area on the alloy surface, as these sites are the most active kinetically for the oxygen

reduction reaction.[26-28] Additionally, aluminum oxide (Al_2O_3) reformation will occur around and over the second-phase particle at the end of the laser pulse. Given the brief elevated temperature of the surface at the end of a laser pulse, a thicker oxide layer is expected to reform, and this passivation layer could serve to inhibit oxygen reduction.

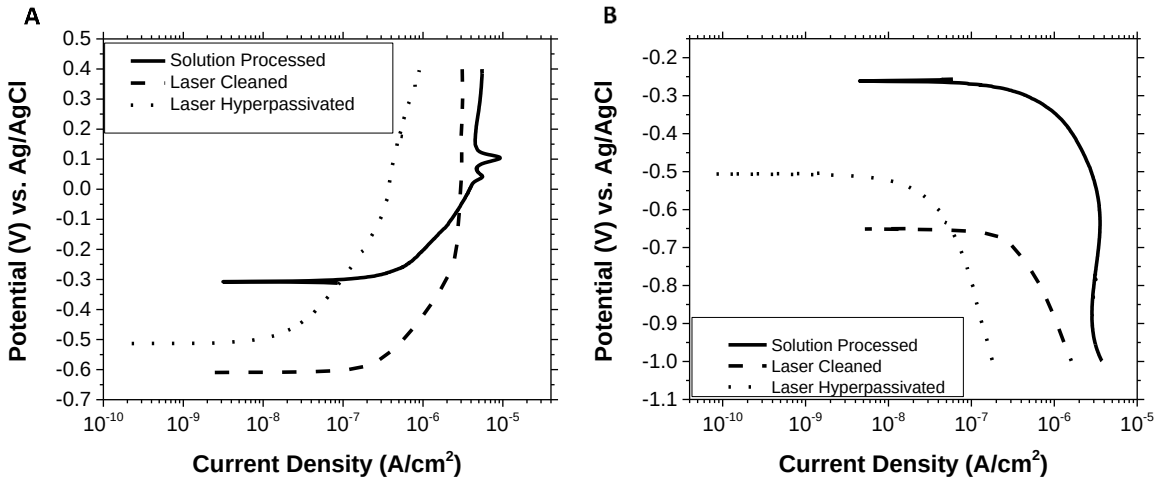

Figure 5.6. (A) Anodic and (B) cathodic potentiodynamic polarization curves for solution processed (controls), laser cleaned, and hyperpassivated AA7075-T6 specimens. All measurements were made in naturally aerated 0.5 M Na_2SO_4 at room temperature. Scan rate = 1 mV/s.

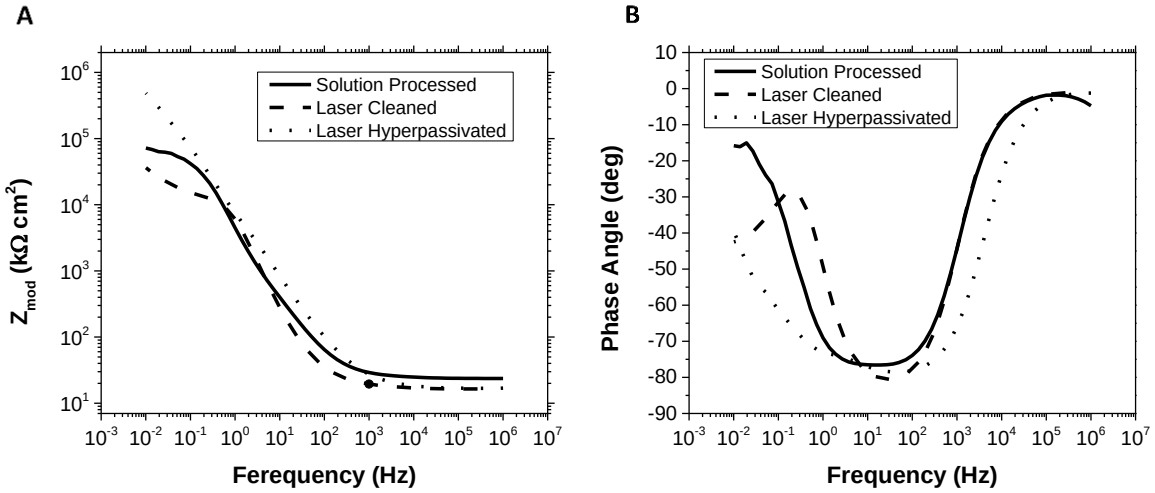

Figure 5.7. Electrochemical impedance spectroscopy data (Bode plots) for solution processed, laser cleaned and laser hyperpassivated AA7075-T6 specimens showing (A) total impedance and (B) phase shift plots over a frequency range from 10^6 to 10^{-2} Hz. The measurements were made in naturally aerated 0.5 M Na_2SO_4 and recorded at the OCP.

Electrochemical impedance spectroscopic (EIS) data for the different treated AA7075-T6 specimens, recorded at the OCP, are presented in Figure 5.7. Figure 5.7A shows Bode plots of the total impedance as a function of frequency. Similar impedance profiles are seen for the laser cleaned and solution processed specimens except at the lowest frequencies. For example, the total impedance at 0.01 Hz ($Z_{0.01\ Hz}$) is reduced (1.7x) for the former. In fact, the $Z_{0.01\ Hz}$ values for the laser hyperpassivated specimens are larger than the value for the solution processed control (7x), but the laser cleaned specimen showed a slight decrease in the total impedance at 0.01 Hz. This difference is reflective of an increase in the polarization resistance (*i.e.*, corrosion resistance) for the hyperpassivated specimens. This appears due, based on the data in Figure 5.6, to reduced second-phase particle exposure and the formation of a more passivating (*i.e.*, thicker, and less defective) oxide layer. The laser cleaned specimen only had 1 specimen tested and thus the reliability of that one measurement is low and further testing is needed to understand the decrease in the total impedance. With more specimens, the $Z_{0.01}$ may in fact increase slightly and be the same statistically as the solution processed. The high frequency range is dominated by the solution and electrode ohmic resistance, and for the three specimen types, there are no distinct differences.

Figure 5.7B shows Bode plots of phase shift as a function of frequency for the same specimens. All three specimens exhibit capacitive behavior at frequencies from 500 down to 50 Hz as evidenced by the -80 degree phase shift. The response differences for the specimen types are noticeable only at the lowest frequencies. At these frequencies, the phase shifts for the solution processed specimen decrease to less than -20 degrees. In contrast, the laser cleaned and laser hyperpassivated specimens retains more capacitive behavior with a phase shift of greater than -40 degrees. This suggests that there is a less permeable and thicker passivating

oxide layer present on the surface of the laser cleaned and laser hyperpassivated specimens than on the solution processed specimen.

Table 5.5 presents a summary of electrochemical data for the three treated AA7075-T6 specimen types obtained from the polarization curve and the EIS data. The first column presents the low frequency impedance modulus, $Z_{0.01\ Hz}$, determined from the EIS measurements at the OCP. The larger the impedance, the less susceptible the alloy is to corrosion under the open circuit conditions. The nominal values for the laser hyperpassivated specimens, 7x greater than the nominal value for the solution processed controls while the laser cleaned specimen showed a slight decrease in the low frequency impedance modulus nominally. The data also reveal that the low frequency impedance modulus for the solution processed controls is reproducibly achieved. The second column shows the polarization resistance, R_p, for the different specimens, as determined from the slope of the linear polarization curves recorded ±20 mV vs. OCP. This value, like $Z_{0.01\ Hz}$, is a direct measure of the corrosion resistance. The nominal values for the laser hyperpassivated specimens are significantly greater, 9x, as compared to the nominal value for the solution processed controls. Again, the laser cleaned AA7075-T6 showed a decrease in the total corrosion resistance with a nominal value lower than that of the solution processed control. This decrease may be due to the protection of the oxide being slightly defective after laser treatment, but further testing would need to be completed to further understand if there is or is not a statistical difference from the solution processed controls. These differences are like those seen for $Z_{0.01\ Hz}$. The center column presents the OCP values for the different specimens. These are the OCP values measured initially for the different specimens before any of the other electrochemical measurements were performed. According to the trends, the OCP values for the laser treated

alloy are similar to or slightly more negative of the nominal value for the solution processed controls. The right two columns compare the cathodic and anodic current densities at -0.8 and 0.3 V vs. Ag/AgCl, respectively. The nominal currents at both potentials are lower than the values for the solution processed controls, with the values being lowest for the laser hyperpassivated specimens. Taken together, these numerical electrochemical parameters indicate that the laser cleaning and hyperpassivation produce a surface condition that renders the alloy more resistant to electrochemical corrosion than the solution processed specimens.

Table 5.5. Summary of Electrochemical Parameters for the Solution Processed, Laser Cleaned, and Laser Hyperpassivated AA7075-T6 Specimens

	$Z_{0.01\ Hz}$ (kΩ-cm^2)	R_p (kΩ-cm^2)	OCP (mV vs. Ag/AgCl)	Current Density at -0.8 V (μA/cm^2)	Current Density at 0.3 V (μA/cm^2)
Solution Processed	88 ± 16	103 ± 18	-262 ± 26	2.93 ± 0.06	4.65 ± 0.48
Laser Cleaned	50	67	-384**	2.66	4.28
Laser Hyperpassivated	591 ± 59*	926 ± 32*	-292 ± 24	0.82 ± 0.10*	1.41 ± 0.12*

Mean ± confidence interval (95%) values for solution processed (n=3), laser cleaned (n=1), and laser hyperpassivated (n=2) specimens. *Statistically significant difference determined, relative to the solution processed control, using a one-tailed Student's t-test at the 95% confidence interval. **Laser cleaned statistical differences at 95% confidence are presumed but may not be statistically different until further specimens can be tested.

Surface Texture and Chemical Composition of the Laser Treated Alloys

Digital optical microscopy and scanning optical profilometry were used to measure changes in the surface texture (*i.e.*, surface roughness) of the alloy specimens after the two laser treatments. Figure 5.8 shows digital optical micrographs of representative (A) solution processed, (B) laser cleaned, and (C) laser hyperpassivated AA2024-T3 surfaces. The micrographs of the solution processed (Fig. 5.8A) and laser cleaned (Fig. 5.8B) specimens

reveal a similar texture as the only features visible at this magnification are the grooves from the plate rolling process. The inset (Fig. 5.8B) reveals these undulations more clearly. The lay of these grooves is in the vertical direction in this micrograph. The micrographs reveal there are no macroscale changes in the surface texture after the laser cleaning. In other words, there is no visible pitting, cracking or other surface damage caused by the laser treatment. It is critical that any laser treatment process not introduce any defects, such as micro cracks or other microstructural changes that could reduce the alloy hardness and mechanical strength. The micrograph for the laser hyperpassivated specimen (Fig. 5.8C) reveals a rougher and wavier surface texture. This ripple surface likely forms because of greater heating in the beam probe volume and convective flow of the melt toward the cooler surrounding regions. Similar surface textures have been previously reported for laser treated surfaces.[13,15,30,31]

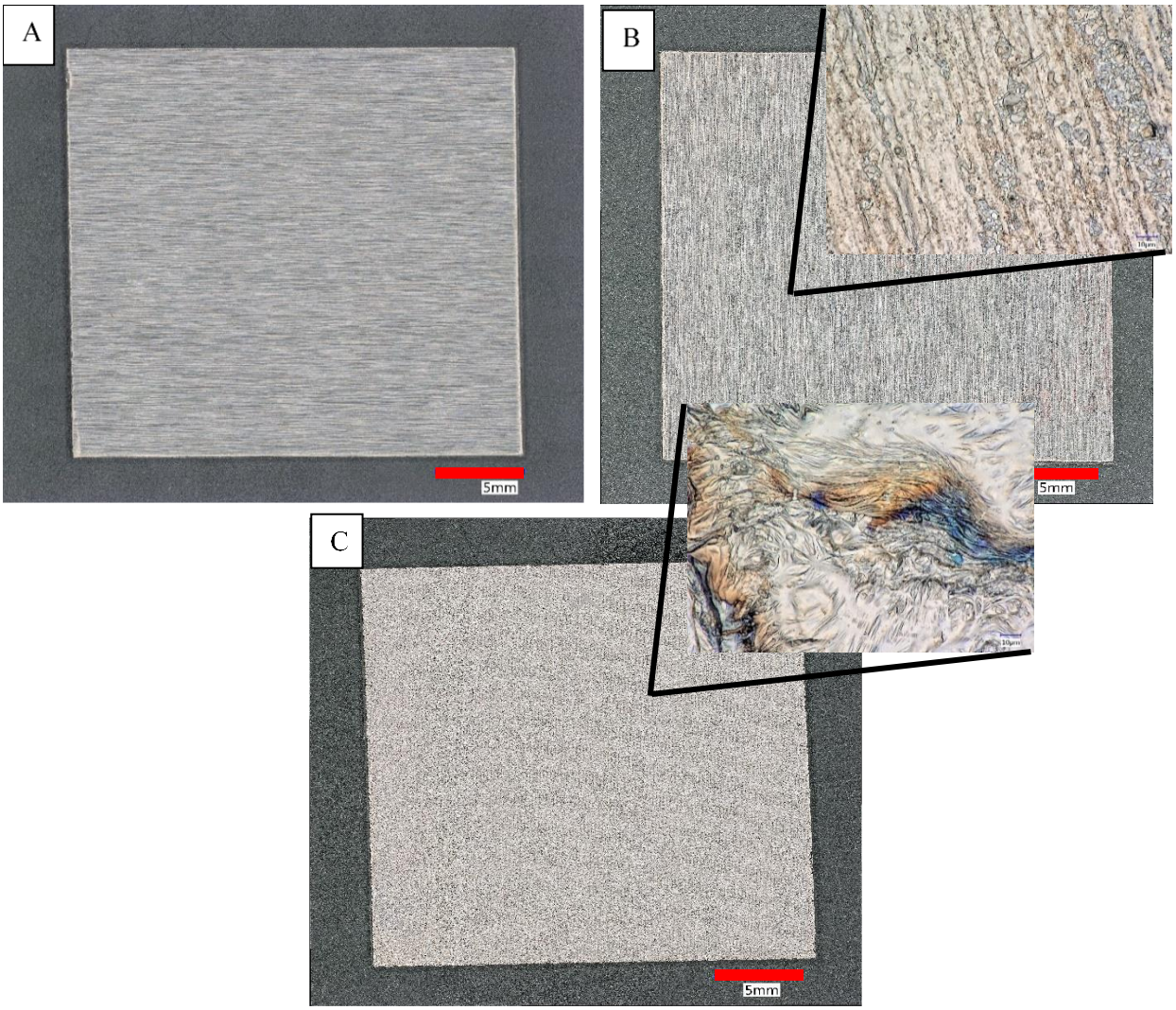

Figure 5.8. Digital optical micrographs of (A) solution processed and (B) laser cleaned AA2024-T3 specimens (5.2 J/cm^2). The higher magnification inset in (B) reveals the rolling grooves. The micrograph in (C) is for a laser hyperpassivated specimen (10.8 J/cm^2). The higher magnification inset in (D) reveals a wavy surface texture with no visible rolling lines. The magnification for all the micrographs was the same, 50x. The insets for (B) and (C) are at a 2,000x magnification with area 170 x 125 µm^2.

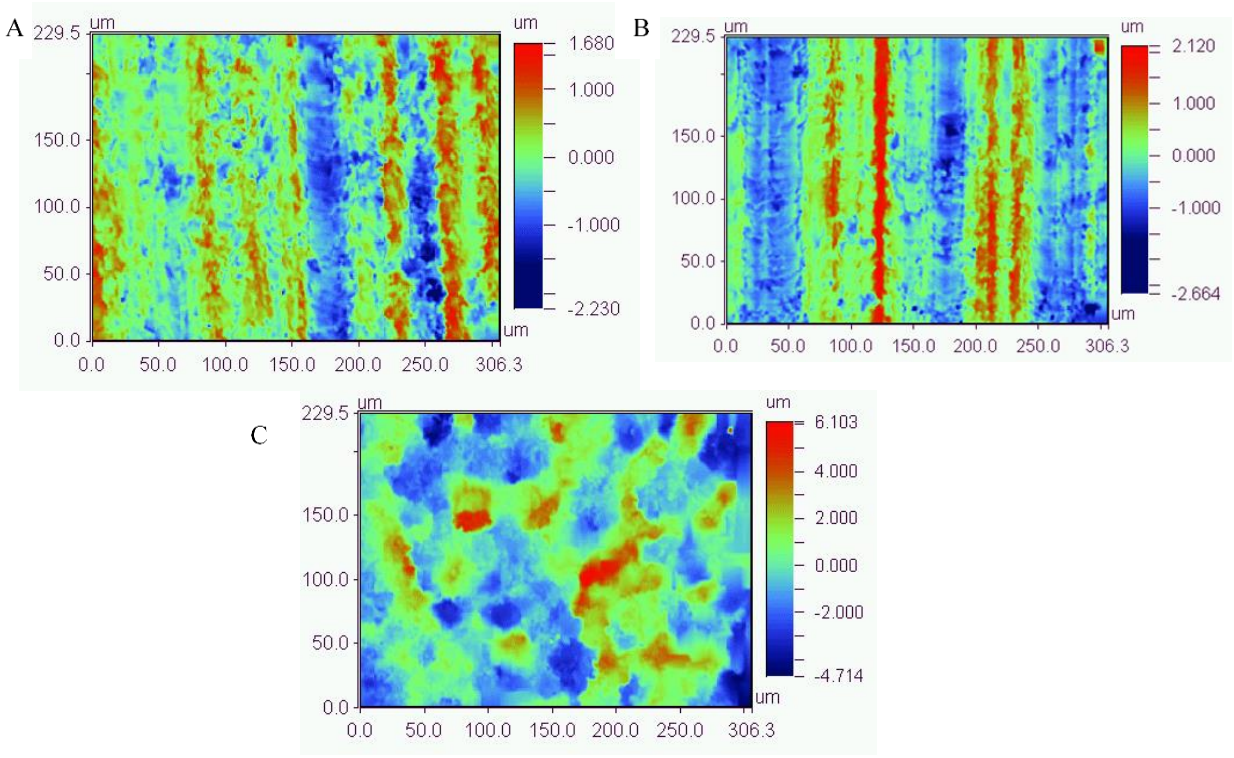

Figure 5.9. Contour plots of optical profilometry data for AA2024-T3 specimens (A) solution processed, (B) laser cleaned (5.2 J/cm^2), and (C) laser hyperpassivated (10.8 J/cm^2). All plots are 300 x 230 μm^2 in dimension. The z-axis scales are different in each of the contour plots. Maximum feature heights for the solution processed and laser cleaned specimens are 4-5 μm. In contrast, maximum feature heights for the laser hyperpassivated specimen are 8-10 μm.

Optical profilometry was used to generate contour plots of the surface texture to quantify the roughness, lay, and feature height. Representative profiles for the three specimen types are shown in Figure 5.9. The rolling grooves are distinguishable across the surface of both the (A) solution processed and (B) laser cleaned specimens. The lay of these is in the vertical direction. The periodicity of the features is similar for these two specimens and feature heights are 4-5 μm for both. These feature dimensions are comparable to those determined from the digital microscopy data. The (C) laser hyperpassivated specimen has a much different surface texture. The surface consists of irregularly distributed; elongated features consistent with the wavy texture seen in the optical micrograph (Fig. 5.9C). The length of some of these features is *ca.* 100 μm. The height of these features is 8-10 μm. Clearly, the laser hyperpassivation with a

higher pulse laser fluence produces some changes in the surface texture of this alloy, more so than does the laser cleaning as there is greater near-surface heating during the hyperpassivation treatment. Table 5.6 summarizes the surface roughness (R_q) and feature height (R_z) data for the three specimen types. R_q and R_z values for the laser cleaned specimens are statistically similar to the values for the solution processed ones. This indicates the laser conditions used for cleaning produce no major changes in surface texture (roughness, lay, or waviness). There is, however, a statistically significant increase in the roughness and feature height of the laser hyperpassivated specimens, as compared to the solution processed controls.

Table 5.6. Surface Roughness Data Obtained from Contour Plots of Optical Profilometry Data for the Solution Processed, Laser Cleaned, and Laser Hyperpassivated Specimens

	Solution Processed (μm)	Laser Cleaned (μm)	Laser Hyperpassivated (μm)
R_q roughness	0.54 ± 0.08	0.56 ± 0.09	1.47 ± 0.08*
R_z height	3.43 ± 0.31	3.87 ± 0.74	9.20 ± 0.44*

Mean ± confidence interval (95%) values for n=5 measurements across a single specimen of each type. Roughness values were determined over 300 x 230 μm^2 area on each specimen type at a 20x magnification. *Statistically significant difference determined, relative to the solution processed control using a one-tailed Student's t-test at the 95% confidence interval.

Scanning electron microscopy was used to examine the surface morphology on a smaller length scale. Figure 5.10 shows representative electron micrographs of (A) solution processed, (B) laser cleaned, and (C) laser hyperpassivated specimens. Both secondary electron and backscattered electron micrographs are presented. Bright spots in the backscattered electron micrographs reveal the location of second-phase particles exposed at the surface that consist of elements higher in atomic number than Al. The electron micrographs reveal, consistent with the digital microscopy and optical profilometry data, that there are no changes in the surface

topography of the laser cleaned specimen at this length scale, as compared to the solution processed control. The lay of the rolling grooves is similar on both specimens. Importantly, there is no evidence of any crack formation or other microstructural damage on the laser cleaned specimen. Pits are seen across the surface of both specimens, but the number density appears reduced for the laser cleaned specimen. There is a noticeable reduction in both the pit density and the second- phase particle exposure for the laser hyperpassivated specimen. The elongated surface features are apparent with some of the longer ridge-like features being 200 μm in dimension. A wavy surface texture is evident with an irregular distribution of the raised features, consistent with the digital micrographs and optical profilometry contour plots.

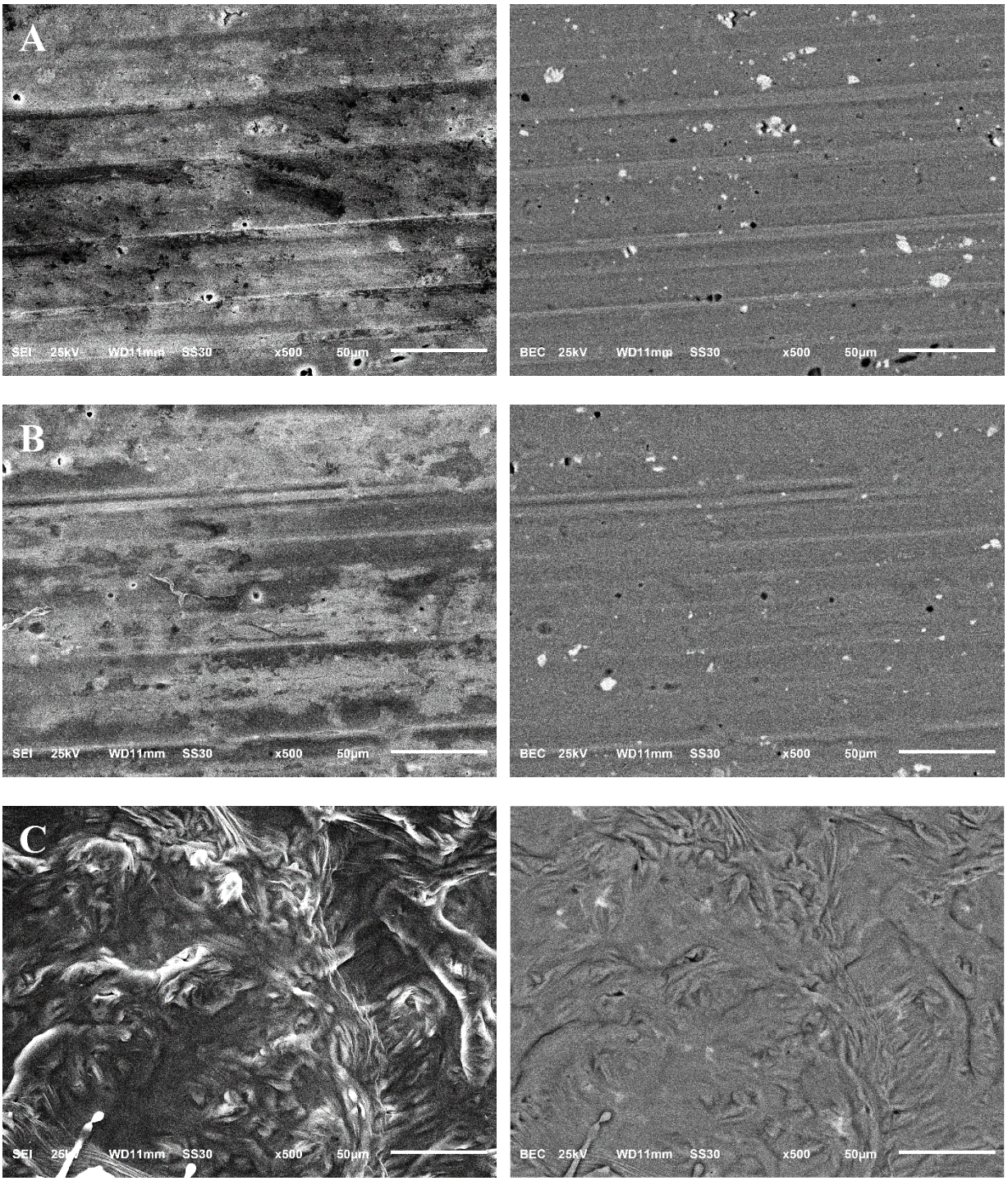

Figure 5.10. SEM micrographs of representative (A) solution processed, (B) laser cleaned (5.2 J/cm^2), and (C) laser hyperpassivated (10.8 J/cm^2) specimens. Secondary electron (left) and backscattered electron (right) micrographs are presented. Bright spots in the backscattered electron micrographs indicate second-phase particles at the surface. All micrographs were recorded at a 500x magnification.

More quantitative analysis of the second-phase particle size and distribution across each specimen type was performed by digitizing the backscattered electron micrographs and analyzing them using ImageJ software. A digital pattern was created to only include the second-phase particles detected as bright spots in the electron micrographs. The patterns were analyzed quantitatively for particle size and number density. Electron micrographs obtained at a 500x magnification were used in this analysis. Five regions in a grid pattern (center and four corner regions) were analyzed and the data aggregated. Figure 5.11 shows the digital patterns created from the corresponding backscattered electron micrographs (Fig. 5.10) for each of the specimen types.

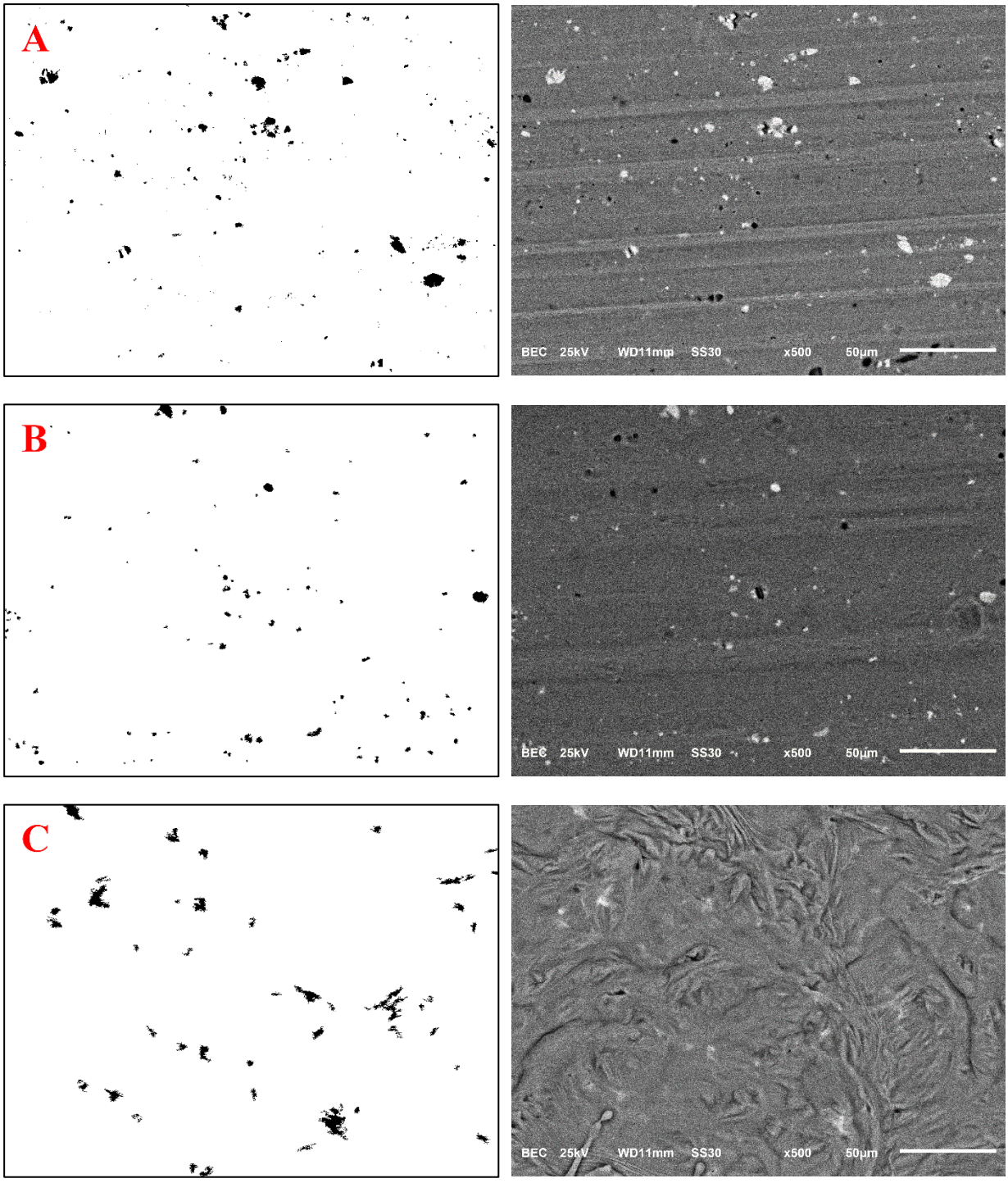

Figure 5.11. Digital maps (left) created from SEM backscattered electron micrographs (right) of specimens (A) solution processed, (B) laser cleaned (5.2 J/cm^2), and (C) laser hyperpassivated (10.8 J/cm^2). Bright spots that represent second-phase particles in the micrographs appear as black spots in the digital maps. All micrographs used were obtained at a 500x magnification.

Table 5.7 summarizes the results from the image analysis. The nominal number of second-phase particles is lower for the laser cleaned, as compared to the solution processed specimen, but not statistically different. The total particle area is nominally larger for the laser cleaned specimen, but not statistically different from the value for the solution processed specimen. The average particle size is similar for both the laser cleaned and solution processed specimens. In contrast, there is a statistically significant decrease in particle number and an increase in the average particle size for the laser hyperpassivated specimens, as compared to the solution processed controls. There is no statistically significant difference in the total area or percent of the total area the particles occupy. There is clearly some particle aggregation or coalescence occurring because of the near-surface heating during the laser hyperpassivation. A higher surface temperature is expected to be reached during each pulse of the hyperpassivation treatment.

Table 5.7. Second-Phase Particle Characterization on AA2024-T3 Specimens Solution Processed, Laser Cleaned, and Laser Hyperpassivated Using Imagej Image Analysis

	Total Number	Total Area (μm^2)	Average Size (μm)	% Area
Solution Processed	149 ± 35	455 ± 117	3.32 ± 1.40	0.90 ± 0.23
Laser Cleaned	126 ± 43	635 ± 314	4.91 ± 1.02	1.25 ± 0.62
Laser Hyperpassivated	46 ± 13*	518 ± 163	11.18 ± 1.77*	1.02 ± 0.32

Mean ± confidence interval (95%) values are reported for n=5 measurements from a single specimen of each type collected in grid pattern over surface. *Statistically significant difference determined, relative to the solution processed control using a one-tailed Student's t-test at the 95% confidence interval. Area investigated 260 x 195 μm^2.

The histogram in Figure 5.12 shows the distribution of the second-phase particle areas across the three specimen types. In the smallest area grouping, 0-20 μm^2, there is a nominal

decrease in the number of particles for the laser cleaned and hyperpassivated. In the 20-40 μm^2 grouping, the laser cleaned and hyperpassivated specimens have a higher particle count than the solution processed controls. It appears that there is some coalescence of nearby particles to form larger sized ones during the local heating from the laser treatments. Consistent with the particle sintering, the laser cleaned and hyperpassivated specimens have a greater number of particles above the 60 μm^2 in area.

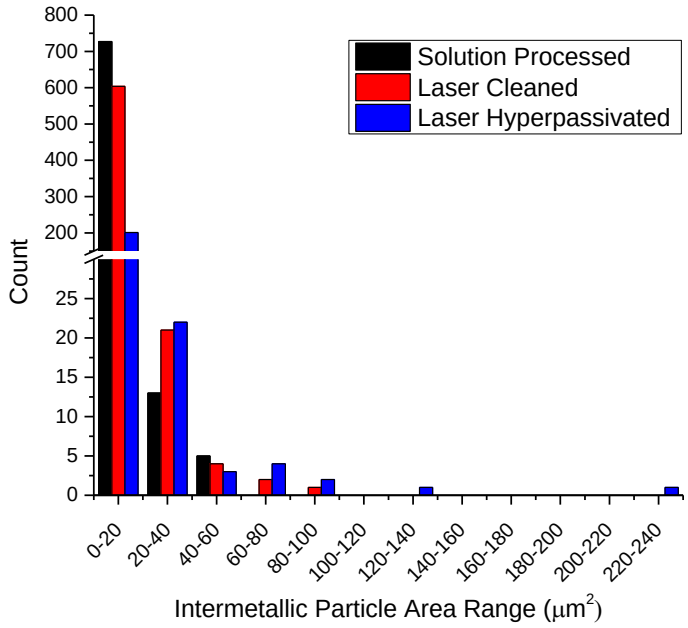

Figure 5.12. Histogram of second-phase particle areas grouped into 20 μm^2 ranges. All particles detected across five areas (260 x 195 μm^2 each) on a single specimen of each type were counted and binned by particle area.

XPS Depth Profiling

As discussed above, the electrochemical parameters indicate the laser cleaning and hyperpassivation pretreatments produce a surface condition that renders the alloy more resistant to electrochemical corrosion than does the solution processing. It is hypothesized that the reason for this is a thicker and less defective oxide layer and reduced exposure of Cu-containing, second-phase particles after the laser treatments. Figure 5.13 presents XPS depth

profile data for solution processed (A and B), laser cleaned (C and D), and laser hyperpassivated (E and F) specimens. Data are presented for the elements Al, O, F, Cu, Mg and C with depth through the oxide and into the near surface region of the alloy. The C present only on the oxide surface is adventitious hydrocarbon material adsorbed during atmospheric exposure. Importantly, O is present for longer sputter times for the laser hyperpassivated specimen, as compared to the solution processed and laser cleaned specimens. This is consistent with a thicker oxide layer. The oxide layer thickness appears slightly greater for the laser cleaned than for the solution processed specimen. For example, at a sputter time of 1000 s (*est.* 5 nm/min sputter rate) or *ca.* 80 nm of depth, the atomic percentage of O is 20, 30 and 50%, respectively, for the solution processed, laser cleaned, and laser hyperpassivated specimens. These data reflect a slightly thicker oxide layer for the laser cleaned and a much thicker layer for the laser hyperpassivated specimens, as compared to the solution processed ones.

The other important piece of information is the reduced atomic percentage of Cu at the surface of both the laser cleaned and hyperpassivated specimens. Cu is associated with second-phase particles in this alloy including s-phase (Al_2CuMg), θ-phase (Al_2Cu), and AlFeCuMn particles. Cu-containing second-phase particles at the alloy surface are particularly detrimental to the corrosion resistance as they provide preferential cathodic sites supporting the oxygen reduction reaction.[26-28,30-32] This alloy contains 3.5 – 5.0 wt. % of Cu or 3.4 – 4.9 at.%. It can be seen from the data that the Cu for the solution processed specimen is 4.2 at.% at the surface and then levels off at 3.5 at.% after about 200 seconds of sputter time. In contrast, the Cu signal for the laser cleaned and hyperpassivated specimens is considerably lower at the surface but reaches a similar concentration of 3.5 at.% in the near surface of the alloy. The reduced Cu

at the surface can be better assessed by examining the Cu/Al ratio. Discounting the surface layer where the adventitious carbon layer was present, the Cu/Al atomic ratios were 0.14, 0.05 and 0.03, respectively, for the solution processed, laser cleaned, and laser hyperpassivated specimens.

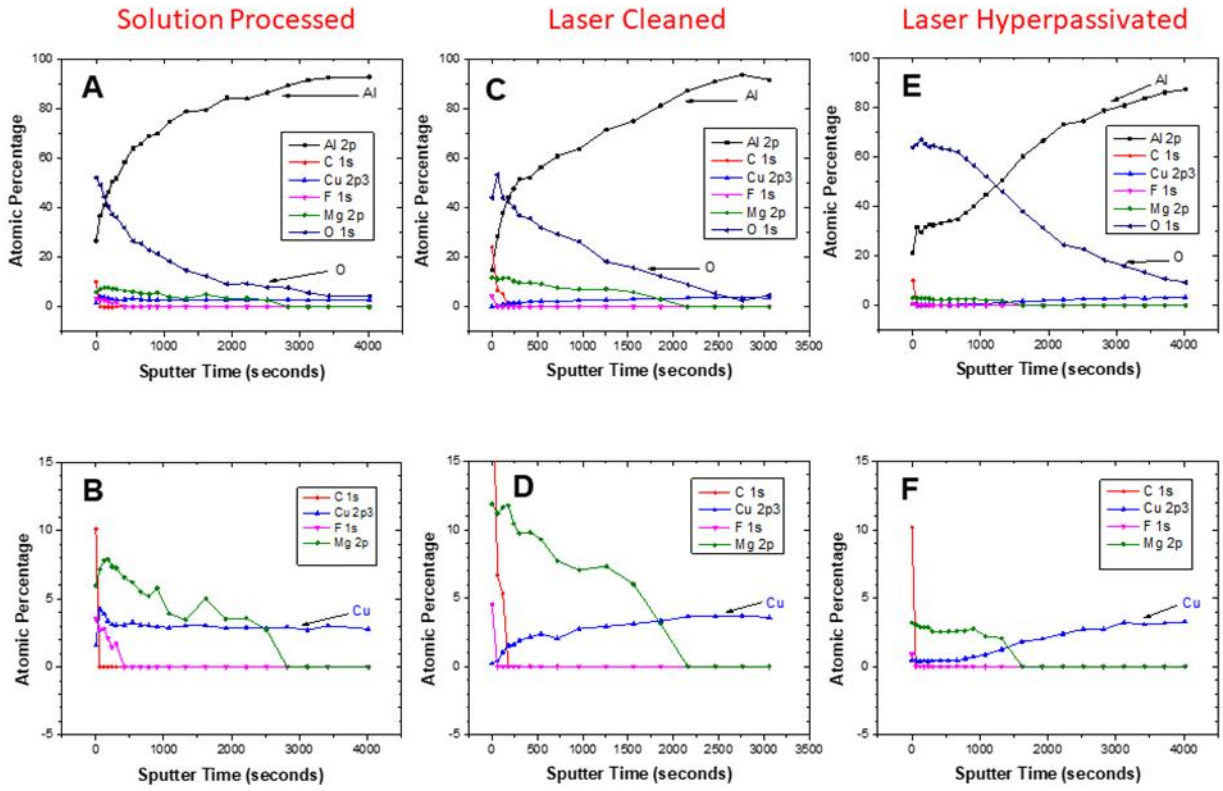

Figure 5.13. XPS depth profiles (atomic percentage) for Al, O, Cu, F, Mg and C through the oxide films on the surface of solution processed (A and B), laser cleaned (C and D) (5.2 J/cm^2), and laser hyperpassivated (E and F) (10.8 J/cm^2) AA2024-T3 specimens. The data in B, D and F are the same data plotted in A, C and E on a reduced full-scale atomic percentage range.

Figure 5.14 shows (A) XPS depth profile data for the oxide component of the Al 2p region as a function of depth on each of the three specimen types and (B) a cascade of Al 2p XPS spectra recorded with depth through the oxide layer on the laser hyperpassivated specimen. Two distinct regions on each specimen type were probed with comparable elemental compositions found at each. The data in Figure 5.14A were obtained by fitting spectra like

those presented in Figure 5.14B. For aluminum, the upper layers contained a mixture of metallic Al and Al_2O_3. As the sputtering continued, the Al_2O_3 was removed, and only metallic Al remained. For example, the peak at 72.6 eV is the aluminum metal, while the broader peak at higher binding energy is from the oxide. The last ten spectra are similarly shaped with a peak position at 72.6 eV reflective of "bulk" aluminum metal. The peak between 74 and 77 eV seen in the spectra recorded more toward the surface is from the oxide component. The O atomic percentage with depth data, which was generated from the higher binding energy oxide component of the Al 2p region, reveal the oxide layer is much thicker for the laser hyperpassivated specimen. The oxide layer appears slightly thicker for the laser cleaned, as compared to the solution processed specimen. The oxide layer thickness was estimated from the tangent crossing points shown in Figure 5.14A for the laser cleaned and hyperpassivated specimens. Assuming a 5 nm/min sputter rate, the oxide layer thicknesses for the two are 17 and 125 nm, respectively. The typical native Al_2O_3 oxide layer thickness on aluminum, upon exposure to oxygen or dry air at room temperature is 2-4 nm in several hours and reaches a value of about 5 nm after a long time.[33,34]

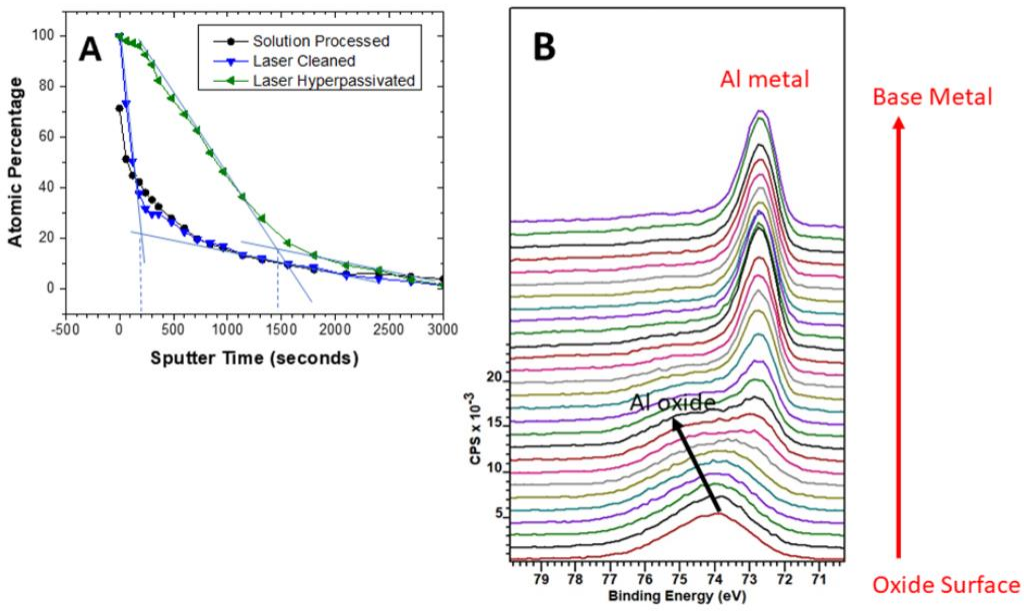

Figure 5.14. (A) XPS depth profiles showing the atomic percentage of aluminum that is in the aluminum oxide state vs. metallic aluminum state for solution processed, laser cleaned (5.2 J/cm2), and laser hyperpassivated (10.8 J/cm2) AA2024-T3 specimens. (B) XPS spectra for the Al 2p region as a function of depth into the oxide layer for the laser hyperpassivated specimen. These spectral data, and similar data for the other two specimen types, were fit to enable the plots the relative percentage of oxide vs. metal in the Al 2p signals for the specimens shown in A.

The elemental depth profile data in Figure 5.13 also reveal the presence of F on the oxide surface of all three specimen types. We attribute this to specimen storage in polytetrafluoroethylene (PTFE) containers prior to the XPS analysis. Interestingly, the data also reveal the presence of elevated levels of Mg within the oxide and in the near-surface region of the laser cleaned and hyperpassivated specimens. The elevated Mg percentage with sputter depth is most notable for the laser cleaned specimen. Presumably, the Mg is associated with s-phase (Al_2CuMg) second-phase particles. Mg 2p shows a monotonic decrease in intensity with depth. Cu $2p_{3/2}$ shows a corresponding increase. The Cu near the surface appears to be oxidized, but metallic Cu is found below. The Mg 2p spectrum is consistent with MgO with depth. The cause for the surface enrichment of Mg is unclear and needs further investigation.

SEM-FIB Analysis

Figure 5.15 presents an SEM micrograph in the cross section of a laser hyperpassivated specimen after focused ion beam milling. The micrograph reveals the wavy surface texture formed during laser hyperpassivation (see Figs. 5.8 and 5.9). There is some variability in the oxide layer thickness depending on the location. For example, the micrograph reveals one region that is 125 nm thick and surrounding regions that are 50-60 nm thick. The alloy specimens were used as received so the rolling grooves were part of the surface texture. The oxide does not appear to grow conformally with this surface texture during the laser hyperpassivation but grows thicker in the valleys between the grooves. Given the uncertainty in sputter rate of the oxide layer, the thickness determination from the micrograph is consistent with the thickness estimated from the XPS depth profiling data. The apparent thickness of the oxide layer on the solution processed and laser cleaned specimens is at or below the resolution limit of our microscope, so no efforts were made to measure these in the cross section.

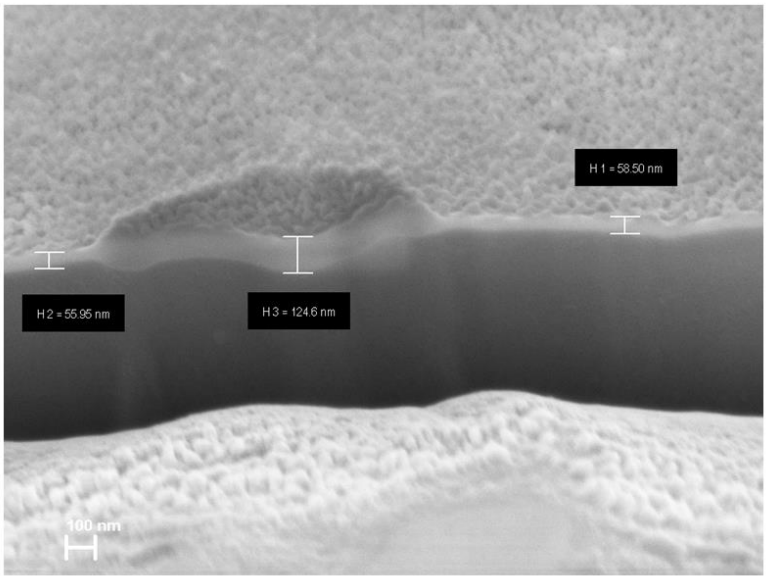

Figure 5.15. Scanning electron micrograph in the cross section (secondary electron image) of the oxide layer formed on the surface of AA2024-T3 after laser hyperpassivation. The specimen was sectioned by focused ion beam milling.

5.4 DISCUSSION

The data reveal that both the laser cleaning and laser hyperpassivation pretreatments increase the corrosion resistance of AA2024-T3, more so than pretreatment by traditional solution processing. All the electrochemical numerical parameters are consistent with increased corrosion resistance of the aluminum alloy after both laser treatments. The low frequency impedance, $Z_{0.01Hz}$, and polarization resistance, R_p, are nominally 8-10x greater for the laser cleaned and 35-40x greater for the laser hyperpassivated specimens, as compared to the solution processed controls. The cathodic current for dissolved oxygen reduction at -0.6 V vs. Ag/AgCl is 5 and 65x lower for the laser cleaned and hyperpassivated specimens, respectively. The anodic current for aluminum dissolution at -0.1 V vs. Ag/AgCl is 40 and 65x lower for the laser cleaned and hyperpassivated specimens, respectively. There are two reasons for the improved corrosion resistance. The first is the formation of a thicker and presumably less defective oxide layer after the laser treatments. The formation of a more compact and less permeable oxide layer across the clean alloy surface is expected after laser treatment.[11,13] The second is reduced exposure of Cu-rich second-phase particles due to thermal-induced sintering or coalescence of smaller particles into larger ones on the surface, burying of the particles by the thicker oxide layer, and possibly burying of the particles due to melting of nearby aluminum and flow of the metal over some of the smaller particles. Material characterization was performed to confirm these causations.

The surface texture of the laser cleaned specimens was unaltered when compared to the solution processed controls. This was revealed by both the digital microscopy and optical profilometry data, in particular, the presence of the unaltered rolling grooves. The laser cleaning process, with the fluence, pulse duration and repetition rate used, only ablated the top

layer of contaminants and the oxide without altering the morphology of the underlying aluminum. The laser interaction is long enough to vaporize/ablate the native oxide layer, but not long enough to change the surface texture through surface melting.

In contrast, more significant near-surface heating of the alloy occurs during the laser hyperpassivation. The pulsed laser fluence is greater for the hyperpassivation treatment (10.8 vs. 5.2 J/cm^2) and this produces higher thermal energy at each pulse point. The increased thermal energy likely produces some near surface melting. Thermal diffusion of the heated metal causes movement of the molten material away from the irradiated area after the laser pulse producing the wavy surface texture observed in Figures 5.8-5.10.

XPS depth profiling data clearly indicate that a thicker passivating oxide layer forms on the aluminum alloy after both the laser cleaning and hyperpassivation pretreatments. Oxide thicknesses of *ca.* 17 and 125 nm are estimated from the data for the laser cleaning and hyperpassivation pretreatments, respectively. The oxide layer thickness on the solution processed controls is expected to be on the order of 2-5 nm. Cross sectional SEM micrographs of the oxide layer on the laser hyperpassivated specimen are consistent with the thickness estimated from the XPS data. This thicker, and presumably less defective passivation layer, reduces the current for metal dissolution. The thicker oxide also buries the Cu-rich second-phase particles, and this contributes to reduced O_2 reduction currents, likely by inhibited mass transport and the blocking of surface sites for O_2 chemisorption (*i.e.*, the first step in the O_2 reduction reaction). Reduced Cu presence on the surface is evidenced by the decreased Cu/Al atomic ratios at the alloy surface with values of 0.05 and 0.03 for the laser cleaned and hyperpassivated surfaces, respectively. A higher ratio of 0.14 is seen for the solution processed control. Initially, laser light is absorbed by the oxide layer and contaminants, and both are

ablated (evaporation or sublimation) from the surface. At the end of the pulse, the surface is cleaned, activated, and at elevated temperature in the air atmosphere. The oxide layer will reform, and the rate of surface oxidation is higher than at room temperature, and this leads to the reformation of a thicker and presumably a less defective oxide layer.

The second reason for the improved corrosion resistance is reduced exposure of Cu in second-phase particles at the alloy surface. Cu-containing second phase particles are active sites for cathodic reactions, such as oxygen reduction, and, as such, they reduce the corrosion resistance of the alloy.[26-28,30-32,35] The Cu/Al atomic ratios found by XPS were 0.14, 0.05 and 0.03, respectively, for the solution processed, laser cleaned and laser hyperpassivated specimens. The particle size analysis (see Table 5.5 and Figure 5.12) revealed a smaller second-phase particle number and an increased particle size, particularly after the laser hyperpassivation. The particle size histogram presented in Figure 5.12 indicates a greater distribution of larger particle sizes (> 60 μm) for the laser treated specimens, as compared to the solution processed controls. Taken together, the data reveal reduced exposure of Cu on the laser cleaned and hyperpassivated specimens because of (i) a thicker oxide covering them and (ii) some near-surface heating that causes sintering or aggregation of some closely spaced second-phase particles.[36-40] Fewer particles larger in size also leads to the formation of a less defective oxide layer.

There is a statistically significant reduction in total number and an increase in the nominal second-phase particle size for the laser hyperpassivated specimens. While there is evidence for sintering and second-phase particle aggregation, which leads to a reduced dissolved oxygen flux and reduced diffusion-limited current, we have no demonstrable proof that some of the second-phase particles are buried by the flow of nearby melted aluminum. The alloy can be

viewed as a microelectrode for O_2 reduction with the second-phase particles serving as the microelectrodes. Changes in the second-phase particle size and distribution over the surface can affect diffusional transport to these "microelectrodes".[35] The key parameters are the size of the second-phase particles, their spacing across the surface, and the diffusion layer thickness.

The data reveal that both the laser cleaning and laser hyperpassivation pretreatments increase the corrosion resistance of AA6061-T6 and AA7075-T6, more so than pretreatment by traditional solution processing. All the electrochemical numerical parameters are consistent with increased corrosion resistance of the aluminum alloy after both laser treatments with the one exception being for the laser cleaned AA7075-T6 showing $Z_{0.01}$ and R_p data lower than that of the solution processed specimens. The low frequency impedance, $Z_{0.01\ Hz}$, and polarization resistance, R_p, are nominally 2x greater for the laser cleaned and 9-10x greater for the laser hyperpassivated specimens, as compared to the solution processed controls on AA6061-T6. R_p and $Z_{0.01\ Hz}$ are nominally 1.5-2x lower for the laser cleaned and 7-9x greater for the laser hyperpassivated specimens, as compared to the solution processed controls for AA7075-T6. The cathodic current for dissolved oxygen reduction at -0.8 V vs. Ag/AgCl is 3 and 20x lower for the laser cleaned and hyperpassivated specimens, respectively on AA6061-T6. The anodic current for aluminum dissolution at 0.2 V vs. Ag/AgCl is 2x and 2x lower for the laser cleaned and hyperpassivated specimens, respectively. On AA7075-T6 the cathodic current for dissolved oxygen reduction at -0.8 V vs. Ag/AgCl is 1x and 4x for the laser cleaned and hyperpassivated specimens, respectively, while the anodic current density for aluminum dissolution at 0.3 V vs. Ag/AgCl is 1 and 3x lower for the laser cleaned and hyperpassivated specimens, respectively. There are two reasons for the improved corrosion resistance. The first

is the formation of a thicker and presumably less defective oxide layer after the laser treatments. The formation of a more compact and less permeable oxide layer across the clean alloy surface is expected after laser treatment.[11,13] The second is reduced exposure of second-phase particles due to thermal-induced sintering or coalescence of smaller particles into larger ones on the surface, burying of the particles by the thicker oxide layer, and possibly burying of the particles due to melting of nearby aluminum and flow of the metal over some of the smaller particles. Material characterization is needed to confirm these causations.

5.5 CONCLUSIONS

The results reported herein show how laser cleaning and hyperpassivation affects the surface texture, surface elemental composition, and electrochemical behavior of AA2024-T3. The following are the key findings based on the data:

1) Laser cleaning removes contaminants and ablates the surface oxide but does not change the surface texture of the aluminum alloy, as compared to solution processed controls. The laser hyperpassivation does increase the feature height and surface roughness.
2) Laser treatment, particularly the laser hyperpassivation, reduces the total second-phase particle number and increases the nominal particle size. This is accounted for by aggregation or sintering nearby particles.
3) Laser cleaning and hyperpassivation produce a thicker and presumably less defective surface oxide layer, as compared to solution processed controls. This is based on XPS depth profiling data for the atomic O percentage with sputter time.
4) The corrosion resistance of AA2024-T3 is improved after both laser cleaning and hyperpassivation, as compared to solution processed controls.

5) The low frequency impedance, $Z_{0.01Hz}$, and polarization resistance, R_p, are nominally 8-10x greater for the laser cleaned and 35-40x greater for the laser hyperpassivated specimens, as compared to the solution processed controls.
6) The cathodic current for dissolved oxygen reduction at -0.6 V vs. Ag/AgCl is 5 and 65x lower for the laser cleaned and hyperpassivated specimens, respectively. The anodic current for aluminum dissolution at -0.1 V vs. Ag/AgCl is 40 and 65x lower for the laser cleaned and hyperpassivated specimens, respectively, as compared to solution processed controls.
7) The reasons for the improved corrosion resistance are (i) a thicker and less defective surface oxide layer and (ii) reduced Cu exposure in second-phase particles.
8) AA6061-T6 and AA7075-T6 both show improved corrosion resistance for the laser treated specimens electrochemically, but further material characterization is needed to fully understand the reasons for the improved corrosion resistance.

5.6 ACKNOWLEDGEMENTS

This research was supported, in part, through funding from the Office of Naval Research, Sea-Based Aviation Program through grant # N00014-15-1-2005. We thank Kristina Tkacz and Kirk Kramer of Henkel Corporation for providing the cleaning solutions used in this work. We also thank Dr. Per Askland (Composite Materials and Structural Characterization Facility, MSU) for his assistance with the SEM-FIB measurements.

REFERENCES

REFERENCES

1. N. Ahmed, S. Pervaiz, S. Ahmad, M. Rafaqat, A. Hassam, and M. Zaindin, "LBM of Aluminum Alloy: Towards a Control of Material Removal and Roughness", *Int. J. Adv. Manuf. Technol.* 105, 1901 (2019).

2. Y. F. Wang, F. Yang and W. W. Zhang, "Development of Laser and Electrochemical Machining Based on Internal Total Reflection", *J. Electrochem. Soc.* 166, E481 (2019).

3. A. Lasagni, A. Manzoni, and F. Mucklich, "Micro/Nano Fabrication of Periodic Hierarchical Structures by Multi-Pulsed Laser Interference Structuring", *Adv. Engr. Mater.* 9, 872 (2007).

4. M. D'Alessandria, A. Lasagni and F. Mucklich, "Direct Micro-Patterning of Aluminum Substrates via Laser Interference Metallurgy", *Appl. Surf. Sci.* 255, 3210 (2008).

5. J. Trapp, A. M. Rubenchik, G. Guss, and M. J. Matthews, "In Situ Absorptivity Measurements of Metallic Powders During Laser Powder-Bed Fusion Additive Manufacturing", *Appl. Mater. Today* 9, 341 (2017).

6. L. Bun, L. Malena, B. Bermudez-Reyes, R. Zambrano, P.D.Z. Robledo, and O. Lopez-Botello, "Parameter Optimization of Aluminum Alloy Thin Structures Obtained by Selective Laser Melting", *MRS Adv.* 4, 2997 (2019).

7. A. C. Tam, W. P. Leung, W. Zapka, and W. Ziemlich, "Laser-Cleaning Techniques for Removal of Surface Particulates", *J. Appl. Phys.* 71, 3515 (1992).

8. Y. F. Lu, W. D. Song, C. K. Tee, D. S. H. Chan, and T. S. Low, "Wavelength Effects in the Laser Cleaning Process", *Jap. J. Appl. Phys.* 37 840 (1998).

9. C. Zhou, H. Li, G. Chen, G. Wang, and Z. Shan, "Effect of Single Pulsed Picosecond and 100 Nanosecond Laser Cleaning on Surface Morphology and Welding Quality of Aluminum Alloy", *Optics Laser Technol.* 127, 106197 (2000).

10. S. Williams, R. Ambat, D. Price, M. Jariyaboon, A. Davenport, and A. Wescott, "Laser Treatment Method for Improvement of the Corrosion Resistance of Friction Stir Welds", *Mater. Sci. Forum,* 426-432, 2855 (2003).

11. Th. Dimogerontakis, R. Oltra, and O. Heintz, "Thermal Oxidation Induced During Laser Cleaning of an Aluminum-Magnesium Alloy", *Appl. Phys. A: Mater. Sci. Proc.* 81, 1173 (2005).

12. F. D. Zhang, H. Liu, C. Suebka, Y. X. Liu, Z. Liu, W. Gou, Y. M. Cheng, S. L. Zhang, and L. Li, "Corrosion Behaviour of Laser-Cleaned AA7024 Aluminum Alloy", *Appl. Surf. Sci.* 435, 452 (2018).

13. S. L. Zhang, C. Suebka, H. Liu, Y. X. Liu, Z. Liu, W. Guo, Y. M. Cheng, F. D. Zhang, Y. D. Peng, and L. Li., " Mechanisms of Laser Cleaning Induced Oxidation and Corrosion Property Changes in AA5083 Aluminum Alloy", *J. Laser Appl*. 31, 012001 (2019).

14. T. Shi, C. Wang, G. Mi, and F. Yan, "A Study of Microstructure and Mechanical Properties of Aluminum Alloy Using Laser Cleaning", *J. Manuf. Process* 42, 60 (2019).

15. G. Zhang, X. Hua, F. Li, Y. Zhang, C. Shen, and J. Cheng, "Effect of Laser Cleaning Process Parameters on the Surface Roughness of 5754-grade Aluminum Alloy", *Int. J. Adv. Manuf. Technol*. 105, 2481 (2019).

16. Z. Tian, Z. Lei, X. Chen, and Y. Chen, "Evaluation of Laser Cleaning for Defouling of Marine Biofilm Contamination on Aluminum Alloys", *Appl. Surf. Sci*. 499, 144060 (2020).

17. G. Zhang, X. Hua, Y. Huang, Y. Zhang, F. Li, C. Chen, and J. Cheng, "Investigation on Mechanism of Oxide Removal and Plasma Behavior During Laser Cleaning on Aluminum Alloy", *Appl. Surf. Sci.* 506, 144666 (2020).

18. F. Moroni, L. Romoli, and M. M. A. Khan, "Design of Laser-Textured Surfaces to Enhance the Strength of Adhesively Bonded Joints", *Int. J. Adhesion and Adhesives* 85, 208 (2018).

19. R. Kromer, S. Costil, J. Cormier, D. Courapied, L. Berthe, P. Peyre, and M. Boustie, "Laser Surface Patterning to Enhance Adhesion of Plasma Sprayed Coatings", *Surf. Coat. Technol.* 278, 171 (2015).

20. A. W. AlShaer, L. Li, and A. Mistry, "The Effects of Short Pulse Laser Surface Cleaning on Porosity Formation and Reduction in Laser Welding of Aluminum Alloy for Automotive Component Manufacture", *Optics & Laser Technol*., 64 162171 (2014).

21. B. S. Yilbas, A. Matthews, A. Leyland, C. Karatas, S. S. Akhtar, and B. J. A. Aleem, "Laser Surface Modification Treatment of Aluminum Bronze with B4C", *Appl. Surf. Sci.* 263, 804 (2012).

22. C. P. Chan, T. M. Yue, and H. C. Man, "The Effect of Excimer Laser Surface Treatment on the Pitting Corrosion Fatigue Behaviour of Aluminum Alloy 7075 ", *J. Mater. Sci.* 38, 2689 (2003).

23. R. E. Russo, X. Mao, and S. S. Mao, "The Physics of Laser Ablation in Microchemical Analysis", *Anal. Chem*. 74, 70A (2002)

24. A. Gragossian, S. H. Tavassoli, and B. Shorki, “Laser Ablation of Aluminum from Normal Evaporation to Phase Explosion”, J. Appl. Phys. 105, 103304 (2009).

25. P. Psyllaki and R.Oltra, “Preliminary Study on the Laser Cleaning of Stainless Steels after High Temperature Oxidation”, *Mater. Sci. Eng.* 282, 145 (2000).

26. R. G. Buchheit, R. K. Boger, M. C. Carroll, R. M. Leard, C. Paglia, and J. L. Searles, “The Electrochemistry of Intermetallic Particles and Localized Corrosion in Al Alloys”, *JOM* 53, 29 (2001).

27. N. Birbilis and R. G. Buchheit, “Electrochemical Characteristics of Intermetallic Phases in Aluminum Alloys: An Experimental Survey and Discussion”, *J. Electrochem. Soc.* 152, B140 (2005).

28. Y. Zhu, K. Sun, and G. S. Frankel, Intermetallic Phases in Aluminum Alloys and Their Roles in Localized Corrosion*”, J. Electrochem. Soc*. 165, C807 (2018).

29. B. Hirschorn, M. E. Orazem, B. Tribollet, V. Vivier, I. Frateur, and M. Musiani, “Determination of effective capacitance and film thickness from constant-phase element parameters.” Electrochim. Acta, 55, 6218 (2010).

30. G. O. Ilevbare and J. R. Scully, “Oxygen Reduction Reaction Kinetics on Chromate Conversion Coated Al-Cu, Al-Cu-Mg and Al-Cu-Mn-Fe Intermetallic Compounds”, *J. Electrochem. Soc.* 148, B196 (2001).

31. M.K. Cavanaugh, J.-C. Li, N. Birbilis, and R. G. Buchheit, “Electrochemical Characterization of Intermetallic Phases Common to Aluminum Alloys as a Function of Solution Temperature”, *J. Electrochem. Soc.* 161, 535 (2014).

32. N. Birbilis, M. K. Cavanaugh, and R. G. Buchheit, “Electrochemical Behavior and Localized Corrosion of Al_7Cu_2Fe Particles in Aluminum Alloy 7075-T651”, *Corros. Sci*. 48, 4202 (2006).

33. J. Evertsson, F. Bertram, J. F. Zhang, L. Rullik, L. R. Merte, M. Shipilin, M. Soldemo, S. Ahmadi, N. Vinogradov, F. Carla, J. Weissenrieder, M. Gothelid, J. Pan, A. Millelsen, J.-O. Nilsson, and E. Lundgren, “Thickness of Native Oxides on Aluminum Alloys and Single Crystals”, *Appl. Surf. Sci*. 349 826 (2015).

34. D. Schaepers and H. H. Strehblow, “Surface Analytical Investigations of Electrochemically Formed Passive Layers on Binary FE/AL Alloys”, *J. Electrochem. Soc.* 142, 2210 (1995).

35. M.A. Jakab, D.A. Little, and R. Scully, “Experimental and Modeling Studies of the Oxygen Reduction Reaction on AA2024-T3”, *J. Electrochem. Soc*. 152 B311 (2005).

36. H.C. Zeng, “Ostwald Ripening: A Synthetic Approach for Hollow Nanomaterials”, *Curr. Nanosci.*, 3 177 (2007).

37. IUPAC Compendium of Chemical Terminology, 2nd edition, 1977.

38. H.C. Zeng, “Synthetic Architecture of Interior Space for Inorganic Nanostructures”, *J. Mater. Chem.*, 16, 649 (2006).

39. C.C. Yec and H.C. Zeng, “Synthesis of Complex Nanomaterials via Ostwald Ripening*”, J. Mater. Chem.*, 2, 4843 (2014).

40. H.G. Yang and H.C. Zeng, “Preparation of Hollow Anatase TiO_2 Nanospheres via Ostwald Ripening”, *J. Phys. Chem.*, 108, 3492 (2004).

CHAPTER 6. EFFECT OF TCP COATING ON THE ELECTROCHEMICAL BEHAVIOR OF LASER CLEANED AND HYPERPASSIVATED ALUMINUM ALLOY 2024-T3

6.1 INTRODUCTION

Surface pretreatment (cleanliness, texture, and chemistry) is necessary to properly prepare alloys for adhesive bonding to other materials or for the application of a coating system for corrosion protection. Abrasives and wet chemical treatments are still routinely used for coating removal, cleaning, and surface pretreatment of aerospace materials. The use of abrasives and solution processing is time consuming, labor intensive, can be an issue for worker health and safety, and requires expensive environmental controls for chemical use and waste disposal.[1, 2]

For aluminum alloys there is a need to identify surface pretreatments that are more environmentally friendly than currently used wet chemical processes. These pretreatments needed to at least be as effective at cleaning and conditioning alloy surfaces as the pretreatments they are replacing. Laser cleaning is a surface pretreatment that has been shown to be beneficial and could provide the safety to the worker and environment needed.[3-11] Lasers can remove surface contaminants and oxide layers without detriment to the substrate if done properly.[1-9] By using lasers the hazardous waste for the chemical baths is eliminated, and it has many other advantages, such as being able to be done remotely and quickly.

Laser cleaning removes the contaminants from the surface of the substrate and ablates the surface oxide without altering the surface texture of the aluminum alloy. Depending on the parameters used, the surface can undergo localized melting and cooling and form periodic structures on the surface or can form more wavy or rippled surfaces.[3-13] The laser cleaning can,

depending on the conditions, cause surface oxidation in the ambient leading a thicker and less defective oxide layer than is formed after solution processing methods. A thicker passivating oxide layer provides added protection through barrier layer protection. This barrier layer protection can involve blocking active sites for oxygen reduction or diffusional resistance to dissolved oxygen. Both would decrease the rate of dissolved oxygen reduction and decreasing the rate of this cathodic reaction will automatically decrease the rate of aluminum oxidation and dissolution (*i.e.*, corrosion). The barrier layer properties of the oxide can also inhibit alloy contact with moisture and salt in the environment, thus improving the corrosion resistance of the alloy.[5]

Trivalent chromium process (TCP) conversion coatings are one type of surface finish being investigated to enhance the corrosion resistance of aerospace aluminum alloys in service.[14-24] The conversion coating is one of a multi-component coating system typically employed (conversion coating, primer, and topcoat). TCP is a more environmentally friendly conversion coating that are the legacy chromate conversion coatings that have historically been used. The function of the conversion coating is to provide some level of corrosion protection and to promote adhesion with the primer layer in the multi-component coating system.[15-17, 20, 22-26] TCP conversion coatings are the leading alternative replacement to the chromium (VI) coatings that have been used previously. The TCP is more environmentally friendly and safer for workers. There is still basic research needed to understand how to properly pretreat aluminum alloys for the application of a TCP surface finish. Key issues to understand and control are the surface texture, chemistry, and cleanliness after the pretreatment .

The TCP forms as a biphasic coating on aluminum alloys. The coating bath contains fluoride under acidic conditions (pH 3.8), which serves to dissolve the surface oxide and

underlying aluminum to form a fluoride-rich interfacial layer,/K_xAlF_{3+x}. This interfacial layer is ~10-100 nm thick.[20,23] On top of this, the conversion coating forms consisting of relatively insoluble, ZrO_2 and $Cr(OH)_3$, that deposit following the hydrolysis of the soluble coating bath precursors, H_2ZrF_6 and $Cr_2(SO_4)_3$. The hydrolysis occurs under more alkaline conditions and these are created in the interfacial region by proton-consuming cathodic redox reactions (oxygen reduction and water reduction) that commence on the aluminum after dissolution of the native passivating oxide layer by fluoride, $Al_20_3 + 6F^- \rightarrow 2AlF_6^{3-}$.[16, 20, 25] The formation of TCP coatings on laser cleaned/pretreated surfaces and the resulting improvement in corrosion resistance has not been investigated. Laser cleaning is a viable surface pretreatment, as opposed to mechanical abrasion and solution processing, especially for localized repairs.

Herein is a discussion of the formation of TCP conversion coatings on aluminum alloy, 2024-T3, after two different laser surface pretreatments: cleaning (5.2 J/cm^2) and hyperpassivation (10.8 J/cm^2). The objective of the work was to learn how TCP coatings form on these surfaces and to evaluate the degree of improved corrosion resistance imparted by the coatings in laboratory electrochemical tests and during accelerated degradation testing by neutral salt-spray exposure. Control experiments were performed with alloys pretreated by wet chemical processing (degreasing and deoxidation). The electrochemical behavior was evaluated in naturally aerated 0.5 M Na_2SO_4 at room temperature. Accelerated degradation testing was done in accordance with ASTM B117.

6.2 MATERIALS AND METHODS

Reagents

All chemicals were analytical grade quality, or better, and were used without additional purification. All cleaners, deoxidizers and coating baths were commercial grade quality and

used as received. Sodium sulfate (Na_2SO_4) was purchased from Fisher Chemical (Fairlawn, NJ). Sodium chloride (NaCl) was purchased from Sigma Aldrich (St. Louis, MO). Industrial grade Bonderite C-AK 6849 (also known as Turco 6849) and Bonderite C-IC Smut-go NC Aero (also known as Turco Liquid Smut-Go) solutions (Henkel Corp., Madison Heights, MI) served as the degreaser and deoxidizer, respectively. Both were diluted with ultrapure water to 20 vol. % for use. Bonderite T5900 (Henkel Corp., Madison Heights, MI) served as the TCP coating. All solutions were prepared with ultrapure water (Barnstead E-Pure) having a resistivity >17 MΩ - cm.

Specimen Preparation – Wet Chemical Processing

Wrought aluminum alloy, AA2024-T3, was obtained as 12" x 12" rolled sheets – so-called "as received" (www.onlinemetals.com). The nominal elemental composition of this alloy is presented in Table 6.1.[27, 28]

Table 6.1. Nominal Elemental Composition of AA2024-T3 in Weight Percent

	Al	Cr	Cu	Fe	Mg	Mn	Si	Ti	Zn
AA2024-T3	Bal.	Max 0.1	3.5-5.0	Max 0.5	1.2-1.8	0.3-0.9	Max 0.5	Max 0.1	Max 0.25

The laser pretreatments were performed on specimens "as received". As such, the surfaces were rough with rolling groove undulations and were covered by cutting oil, grease, fingerprints and other contaminants from past handling and processing. A 0.08" (2-mm)-thick sheet was cut into 1 in^2 specimens for the experiments. Specimens for control measurements were prepared by conventional solution (wet chemical) processing – degreasing and deoxidation. This involved specimen immersion in Bonderite C-AK 6849 degreaser at 55°C for 10 min. This was followed by a 2-min city tap water immersion rinse. The specimen was then immersed in Bonderite C-IC Smut-go NC Aero for deoxidation at room temperature for

2 min followed by another 2-min city tap water immersion rinse. All specimens were then dried with N_2 prior to use in additional experiments.

Specimen Preparation - Laser Cleaning and Hyperpassivation

"As received" alloy specimens were (i) laser cleaned (low fluence) or (ii) laser hyperpassivated (high fluence). Laser treatment was performed by Adapt-Laser (Kansas City, MO) using a pulsed Nd:YAG laser with output wavelength of 1064 nm. The spot size was 428 μm in both treatments with a spot overlap of 50% during the spatial treatment process. Only one laser pulse per spot was applied over a treatment area of *ca.* 1 in^2. The parameters used were selected based on the company's knowledge of cleaning aluminum alloys without introducing any microstructural alterations. No process parameter variation was performed in this work. For the laser cleaning, the following parameters were used: (i) a pulse frequency of 40 kHz, (ii) a pulse duration of 180 ns, (iii) a pulse intensity of 29 MW/cm^2, and a (iv) laser fluence of 5.16 J/cm^2. For the laser hyperpassivation, the following parameters were used: (i) a pulse frequency of 15 kHz, (ii) a pulse duration of 80 ns, (iii) a pulse intensity of 140 MW/cm^2, and (iv) a laser fluence of 10.84 J/cm^2. Treated specimens were stored in Ziploc storage bags and shipped back to MSU. The bagged specimens were stored in a refrigerator until time for TCP coating. The time between laser treatment and TCP coating was several weeks.

Fundamentals of Laser Treatment

Laser cleaning involves the use of a high power, pulsed (nanosecond) light source that is rastered across a surface point to point. Key process parameters are the wavelength, pulse spot size and spacing, pulse frequency (kHz), pulse duration (nsec), pulse power (MW/cm^2), and fluence (J/cm^2). The cleaning mechanism generally involves surface heating and ablation.[7-

[17,18,23-25] If the energy supplied is greater than the ablation threshold, the material will undergo sublimation or vaporization. Oxides have an ablation threshold well below that of most base metals. Hence, one can adjust the laser parameters so that the oxide is removed without damage to the metal. The source wavelength (1064 nm) and the absorption characteristics of the material are key factors in how the ablation proceeds. Materials with high laser light absorption will be removed easier than materials that do not absorb (*i.e*, reflect) the laser light. For example, oxides absorb 1064 nm light strongly while aluminum exhibits little absorption at this wavelength. At low fluence, energy is absorbed and melting of the surface can occur, which may induce surface alloying and or reduce the exposure of second-phase particles due to melting and cooling of the surrounding aluminum matrix around and over a particle. At higher fluence, athermal processes begin to be important, and ejection of material via formation of a hot, dense plasma is observed. Oxides absorb the laser light and are evaporated. Additionally, the interaction of the laser beam with the surface may generate significant thermal effects to induce follow-up thermal oxidation or even some near-surface melting.[8-11,23-25] The heating of the surface in air results in the reformation of an oxide layer that is thicker and perhaps less defective than the native oxide that forms in air at room temperature. Importantly, the laser cleaning can prepare and activate a surface for the application of a coating.

TCP Conversion Coating

Solution processed, laser cleaned, and laser hyperpassivated specimens were TCP immersion coated with RTU Bonderite T-5900 coating bath (pH 3.65) at room temperature for 10 min with very gentle beaker agitation, as needed, to dislodge any gas bubbles (H_2) that formed. This was followed by a 2 min city tap water soak and then a 30 s soak in ultrapure

water. Excess water was then carefully wicked off the coated surface with a Kim wipe. This was followed by overnight drying at room temperature before use of the specimen in further testing. The typical conversion coating thickness for this and the other TCP coatings was in the range of 100-300 nm, based on past published work.[23, 25, 29]

Deft Primer Application

A Deft® primer (02GN084) was applied over the TCP-coated alloy specimens by brush (PPG Aerospace). This is a chemically cured, chrome-free, two-component epoxy polyamide primer. The two-component primer is mixed right before application with 3 parts 02GN084 (base component) and 1 part 02GN084CAT (catalyst component) by volume. This primer is designed to provide a high degree of corrosion resistance to aluminum alloys. The primer is qualified for MIL-PRF-23377 (Performance Specification: Primer Coatings: Epoxy, High Solids) as a Type I, Class N (non-chromate) coating. The primer was applied within one week of the TCP application. Specimens were primed on one side and were aged for one week to allow for complete drying. The brush was dipped into the primer before each brush stroke. Seven brush strokes were applied from end to end across the specimen surface. The primer thickness was 0.01-0.02 in (250-500 μm) as measured using a caliper.

6.3 TESTING AND CHARACTERIZATION

Electrochemical Measurements

All electrochemical measurements were performed in a 1 cm^2 flat cell (Bio-Logic Science Instruments, France) using a computer-controlled electrochemical workstation (Gamry Instruments, Inc, Reference 600, Warminster, PA). An aluminum alloy specimen was mounted against a Viton® O-ring that defined the exposed geometric area, 1 cm^2. All currents reported herein are normalized to this geometric area. The counter electrode was a Pt flag, and the

reference was a home-made Ag/AgCl electrode (4 M KCl, E^0 = +0.197 V vs. NHE) that was housed in a Luggin capillary with a cracked glass tip. All measurements were made in naturally aerated 0.5 M Na_2SO_4 at room temperature (23 ± 2 ºC).

The following measurements were performed to evaluate the electrochemical behavior of the solution processed, laser treated, and TCP-coated alloy specimens: (i) a 30-min open circuit potential (OCP) measurement, (ii) an electrochemical impedance spectroscopy (EIS) measurement at the OCP at frequencies from 10^5 to 10^{-2} Hz, (iii) a linear polarization resistance measurement from ± 20 mV vs. OCP to determine the polarization resistance, R_p, and (iv) anodic and cathodic potentiodynamic polarization curves from the OCP to 0.2 and -1.0 V vs. Ag/AgCl, respectively. The scan rate was 1 mV/s. The cathodic potentiodynamic polarization curve was recorded first followed by the anodic curve on the same specimen. The polarization curves were recorded last after the OCP, EIS, and linear polarization measurements.

Neutral Salt-spray (ASTM B117) Testing

Primed specimens were placed at a ~20° angle (with respect to the vertical axis) on plastic racks inside a commercial salt-spray chamber (Associated Environmental Systems, MX-04, 4 ft^3). The chamber was filled with a circulating continuous salt fog generated from a 5 wt.% NaCl solution. The salt fog/mist test was conducted according to ASTM B117 for 14 days (35 ºC). At the end of the test period, the specimens were removed, rinsed thoroughly with ultrapure water, and dried under a stream of N_2 gas. Specimens were then ultrasonically cleaned in nitric acid in 2-min increments to remove any corrosion product until a stable weight was reached.

Scanning Electron Microscopy

Scanning electron microscopy (SEM) was performed using a field emission electron microscope (JEOL 6610LV) equipped with an energy dispersive x-ray microanalysis attachment (Oxford, AZtec Software). Electron micrographs were obtained using an accelerating voltage of 15 kV, a working distance of 11 mm, and an electron beam spot size of 30 with a dwell time 16 µs/pixel. EDS microanalysis was done by increasing the spot size to 50 and maps of elements present across the area were collected.

Digital Optical Microscopy

Digital optical microscopy was performed using a Keyence VHX-6000 microscope at magnifications of 50 and 2000x. Digital micrographs of an entire surface were captured as each different area comes into focus, combining them into one fully focused (stitched) image. The microscope uses a depth of defocus method to calculate three-dimensional information based on the amount of defocusing of two-dimensional images. The apparent surface roughness was assessed from line scans of 1 mm in length measured at different points near the center of each three-dimensional image. The depth resolution was ca. 0.2 µm.

Optical Profilometry

Optical profilometry was performed using a WYKO l profilometer along with the associated instrument software, Vision for RST Plus (version 1.8). The instrument uses an 10x magnification lens along with a field of view lens of 2x to produce images at a 20x magnification. Five areas across each specimen were probed in a grid like pattern to determine the surface roughness, feature heights, pit number density and nominal pit diameter. The topography was profiled by stitching focused images from 10 µm above focus to 10 µm below the surface for each scan. The profilometer collects this same image 5 times and reduces

unfocused areas of the image by averaging the scans together giving one fully focused image. 3D images and contour plots were collected over an area of 306 x 230 μm^2 to profile the surface texture and to calculate the surface roughness.

6.4 RESULTS

Electrochemical Behavior

Figure 6.1 shows representative cathodic potentiodynamic polarization curves for solution processed and laser pretreated AA2024-T3 specimens, with and without a TCP coating. The current at potentials between -0.4 and -0.8 V is due to the diffusion-limited reduction of dissolved oxygen. As can be seen in Figure 6.1A, the current at these potentials is similar for both TCP-coated specimens (laser cleaned and solution processed) and attenuated compared to the uncoated laser cleaned and solution processed specimens. The current decrease for both TCP-coated specimens is on the order of 10x. Clearly, the TCP coating reduces the diffusion limited rate of dissolved oxygen reduction by a couple of mechanisms: (i) blocking sites for O_2 chemisorption on exposed cathodically-active second-phase particles (e.g., Cu intermetallics) and (ii) serving as a diffusional barrier.[20,23] There are some significant differences in the OCP values for the different specimens, however. The OCP for the laser cleaned (uncoated) and solution processed (TCP coated) specimens is similar at ca. -0.2 V. The TCP coating has a different effect on inhibiting corrosion on the solution processed and laser cleaned specimens based on the shifts in the OCP. For the solution processed specimen, the TCP coating shifts the OCP positive by ca. 150 mV as compared to the value for the uncoated alloy. In contrast, for the laser cleaned specimen, the TCP coating shifts the OCP negative by ca. -300 mV as compared to the value for the uncoated alloy. Therefore, the TCP coating has a greater effect on reducing the anodic (aluminum oxidation) reaction rate for the solution

processed specimen (positive shift in OCP). In contrast, the TCP coating has a greater effect on reducing the cathodic (oxygen reduction) reaction rate for the laser cleaned specimen (negative shift in OCP).

Figure 6.1B presents potentiodynamic polarization curves for the laser hyperpassivated and solution processed specimens, with and without a TCP coating. The diffusion-limited current for dissolved oxygen reduction is similar in magnitude and lower for the laser hyperpassivated specimens with and without the TCP coating and for the solution processed specimen with the TCP coating. The current attenuation is on the order of 10x. the OCP values for the laser hyperpassivated and solution processed specimens with the TCP coating are shifted negative of the OCP values for their uncoated counterparts. Again, this suggests the coating has a greater effect on the cathodic reaction kinetics. The current for the laser hyperpassivated specimen is lower than the current for the laser cleaned specimen, both without a TCP coating. Recall that the hyperpassivation process produces a much thicker and presumably less defective oxide layer (see Chapter 5) and this serves to reduce the rate of dissolved oxygen reduction. Presumably, this is because the oxide serves as a diffusional barrier.

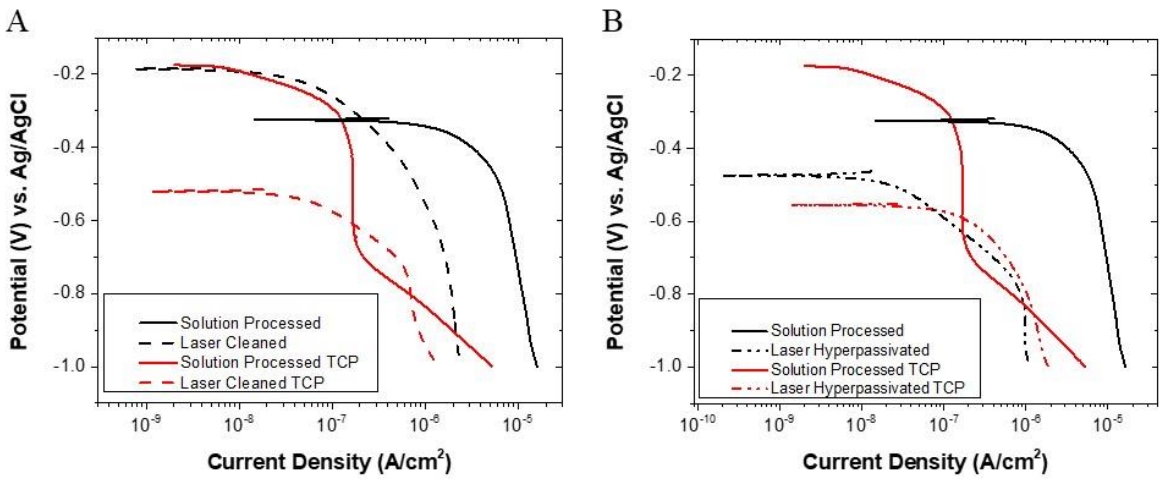

Figure 6.1. Cathodic potentiodynamic polarization curves for solution processed (controls) and (A) laser cleaned and (B) laser hyperpassivated AA2024-T3 specimens with and without a TCP coating. All measurements were made in naturally aerated 0.5 M Na_2SO_4 at room temperature. Scan rate = 1 mV/s.

Figure 6.2 presents anodic potentiodynamic polarization curves for solution processed and laser treated AA2024-T3 specimens with and without a TCP coating. The current at these potentials arises from the oxidation of the aluminum and formation of an oxide (Al_2O_3 layer or $AlOOH/Al_2O_3$ bilayer. There is no evidence in the curves for increased current associated with stable pit formation and growth, at least out to 0.2 V, as all show steady state currents consistent with the stable formation of an oxide layer. As was the case for the cathodic curves recorded first on these specimens, the OCP for the laser cleaned specimens is *ca.* -0.2 V, and for the laser hyperpassivated and control specimens is *ca.* -0.3 V. With the TCP coating applied both are shifted more negative to *ca.* -0.5 V. The negative shift in the OCP for the laser processed specimens again is suggestive of further passivation in the cathodic direction, but the alloy after laser processing alone is showing greater passivation to the alloy originally with the reformation of the oxide layer. It is difficult, however, to infer much about differences in the OCP because the same specimen was used in all the measurements, and this created changes in the surface condition over time.

Again, the current for the laser cleaned specimens with the TCP coating showed similar currents to the solution processed specimen that was TCP coated and both showed attenuation of current from the uncoated controls. The laser hyperpassivated specimen again showed an increase in total current after TCP coating when compared to the hyperpassivated specimen without TCP and was also higher in current when compared to the TCP coated solution processed specimen at 0.1 V but was not statistically different. This increase again is likely due to the incomplete fluoride etch during the TCP coating formation leaving the compact oxide that had formed after laser hyperpassivation more defective and producing an incomplete coating along the surface. The curves for all specimen types are reproducible in terms of current magnitude with potential.

The results demonstrate that the rate of aluminum oxidation is suppressed by an equivalent amount for the laser cleaned specimens and the solution processed specimens after TCP coating. The hyperpassivated specimens may not need a TCP coating to go into application, but this electrolyte is only mildly aggressive, and with chloride present even a poorly formed TCP coating may protect the surface further and will be investigated using accelerated degradation testing below.

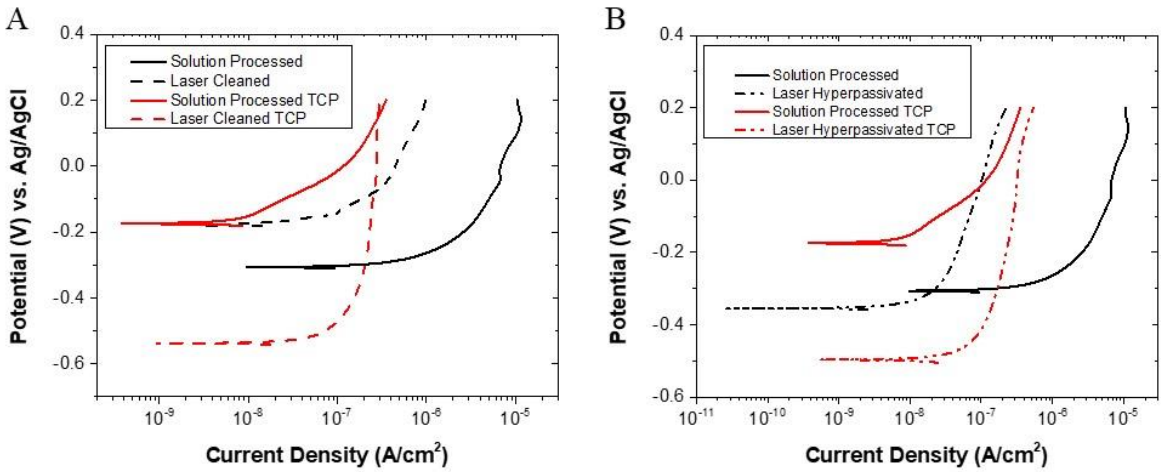

Figure 6.2. Anodic potentiodynamic polarization curves for solution processed (controls) and (A) laser cleaned and (B) laser hyperpassivated AA2024-T3 specimens with and without a TCP coating. All measurements were made in naturally aerated 0.5 M Na_2SO_4 at room temperature. Scan rate = 1 mV/s.

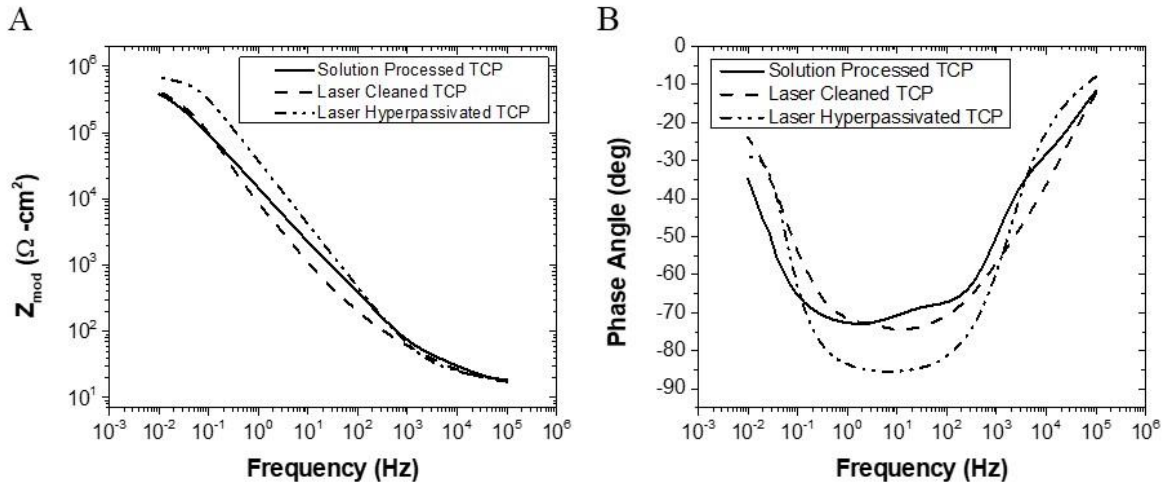

Figure 6.3. Electrochemical impedance spectroscopy data (Bode plots) for solution processed, laser cleaned and laser hyperpassivated TCP coated AA2024-T3 specimens showing (A) total impedance and (B) phase shift plots over a frequency range from 10^6 to 10^{-2} Hz. The measurements were made in naturally aerated 0.5 M Na_2SO_4 and recorded at the OCP. Specimens without TCP coating can be found in Chapter 5.[5]

Electrochemical impedance spectroscopic (EIS) data for the different TCP coated A2024-T3 specimens, recorded at the OCP, are presented in Figure 6.3. Figure 6.3A shows Bode plots of the total impedance as a function of frequency. Similar impedance profiles are seen for the laser cleaned and solution processed specimens. In fact, the $Z_{0.01\ Hz}$ values for the TCP coated

laser cleaned specimens are slightly smaller than the value for the TCP coated solution processed control, but there is no statistical difference in the values. As there is no statistical difference there is no difference in the polarization resistance (*i.e.*, corrosion resistance). The same can be said for the TCP coated laser hyperpassivated specimens, with the values for the TCP coated laser hyperpassivated specimens showing a slight improvement in the low frequency impedance modulus and a slight improvement in the polarization resistance. The high frequency range is dominated by the solution and electrode ohmic resistance, and for the three specimen types, there are no distinct differences.

Figure 6.3B shows Bode plots of phase shift as a function of frequency for the same specimens. All three TCP coated specimen types exhibit capacitive behavior at frequencies from 10^2 down to 10 Hz as evidenced by the -60 to -80 degree phase shift. The phase shift-frequency profiles in Figure 6.3 reveal two distinct time constants for the TCP coated solution processed specimens. These distinct time constants are not seen explicitly in the TCP coated laser processed specimens but are presumed to be there based on the equivalent circuit used to fit the data. The first is a high frequency peak at $\sim 10^2$ Hz and the second is a low frequency peak at ~1 Hz. Simulation results previously showed that increasing R_{po} from 1×10^3 to 1×10^4 caused the phase shift of the high frequency peak to proportionally increase while not affecting the other regions of the curve.[20, 24, 30] This suggests that this time constant is associated with the resistance of the hydrated channels and defects in the coating. Simulation results also showed that increasing R_p from 5×10^5 to 5×10^6 caused the maximum phase shift of the low frequency peak to progressively increase and shift to lower frequency.[20, 24, 30] This suggests that this time constant is associated with the charge transfer resistance of the metal corrosion reaction.[20] The highest phase angle was seen for the TCP coated laser

hyperpassivated specimen indicating that it provides the most corrosion resistance to the underlying alloy.

Table 6.2 presents a summary of electrochemical data for the three TCP coated AA2024-T3 specimen types obtained from the polarization curve and the EIS data. The first column presents the low frequency impedance modulus, $Z_{0.01\ Hz}$, determined from the EIS measurements at the OCP. The larger the impedance, the less susceptible the alloy is to corrosion under the open circuit conditions. The nominal values for the TCP coated laser cleaned specimens are not statistically different from the nominal value for the TCP coated solution processed controls. The TCP coated laser hyperpassivated specimens also showed no statistical difference from the TCP coated solution processed control, but on average the TCP coated laser hyperpassivated specimens showed a slightly increased low frequency impedance modulus. The data also reveal that the low frequency impedance modulus for the TCP coated specimens is reproducibly achieved.

The second column presents the OCP values for the different specimens. These are the OCP values measured initially for the different specimens before any of the other electrochemical measurements were performed. According to the trends, the OCP values for the TCP coated laser treated alloy are more negative of the nominal value for the TCP coated solution processed controls. The right two columns compare the cathodic and anodic current densities at -0.7 and 0.1 V vs. Ag/AgCl, respectively. The nominal currents at both potentials are not statistically different for any of the TCP coated specimens. Taken together, these numerical electrochemical parameters indicate that the laser cleaning and hyperpassivation produce a surface condition that renders the alloy more resistant to electrochemical corrosion than the solution processed specimens and when the TCP coating is applied to the laser cleaned

specimens some minor improvements are made to the corrosion resistance, but the hyperpassivated specimens may not need the TCP coating to provide the added protection as the application of the TCP actually decreases the corrosion resistance slightly.

Table 6.2. Summary of Electrochemical Parameters for the Solution Processed, Laser Cleaned, and Laser Hyperpassivated AA2024-T3 Specimens with and without TCP Coating

	$Z_{0.01\ Hz}$ ($k\Omega$-cm^2)	OCP (mV vs. Ag/AgCl)	Current Density at -0.7 V ($\mu A/cm^2$)	Current Density at 0.1 V ($\mu A/cm^2$)
Solution Processed	38 ± 11	-312 ± 35	80.9 ± 1.27	12.04 ± 4.99
Laser Cleaned	449 ± 16*	-178 ± 25*	1.66 ± 0.52*	0.83 ± 0.19*
Laser Hyperpassivated	1580 ± 650*	-344 ± 33	0.17 ± 0.06*	0.18 ± 0.05*
Solution Processed TCP Coated	725 ± 154*	-179 ± 36*	0.34 ± 0.27*	0.63 ± 0.58*
Laser Cleaned TCP Coated	609 ± 353	-477 ± 48**	0.56 ± 0.34	0.49 ± 0.02
Laser Hyperpassivated TCP Coated	870 ± 169	-554 ± 30**	0.43 ± 0.25	0.43 ± 0.17

Mean ± confidence interval (95%) values for solution processed (n=6), laser cleaned (n=3), and laser hyperpassivated (n=3) specimens. *Statistically significant difference determined, relative to the solution processed control, using a one-tailed Student's t-test at the 95% confidence interval. **Statistically significant difference determined, relative to the solution processed TCP coated control, using a one-tailed Student's t-test at the 95% confidence interval. Values for specimens not TCP coated are reprinted from elsewhere.[5]

The EIS data were fit (ZView® 3.0) using the equivalent circuit in Figure 6.4. The circuit used is that of a thin-film barrier layer consisting of some hydrated channels or defects to the underlying substrate. The equivalent circuit has been used previously to model the TCP coating on AA2024-T3. In the equivalent circuit, R_{el} is the resistance of the electrolyte, R_{po} and R_p represent the resistance of the electrolyte in the hydrated channels or defects of the TCP coating and the polarization resistance of the metal respectively. Constant phase elements (CPE-Q) were used in place of traditional double-layer capacitors. Q_{co} was the coating capacitance and

Q_{dl} was the capacitance for the electrolyte-metal interface in the hydrated channels or defects. The values are normalized to the geometric area of each specimen and can be found in Table 6.3.

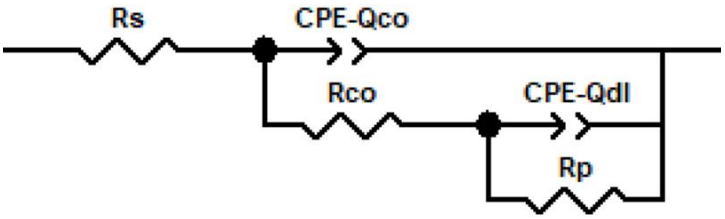

Figure 6.4. Equivalent circuit model used to represent the TCP coating on the aluminum alloy.

Table 6.3. Summary of the Fitting Parameters from the EIS Data Recorded at the OCP for the TCP Coated Solution Processed (SP TCP), Laser Cleaned (LC TCP), and Laser Hyperpassivated (LH TCP) AA2024-T3 Specimens

	R_s (Ω-cm^2)	CPE-Q_{CO} (s^n/Ω-cm^2) x 10^{-6}	α_{co}	R_{po} (Ω-cm^2)	CPE-Q_{dl} (s^n/Ω-cm^2) x 10^{-6}	α_{dl}	R_p (kΩ-cm^2)
SP TCP	16.37 ± 0.34	6.33 ± 2.17	0.82 ± 0.02	47.36 ± 6.58	5.60 ± 2.59	0.88 ± 0.03	687 ± 216
LC TCP	17.04 ± 0.50	3.35 ± 0.99	0.86 ± 0.04	81.36 ± 21.31	3.49 ± 0.14	0.85 ± 0.01	453 ± 71
LH TCP	18.35 ± 0.20	1.41 ± 0.25	0.97 ± 0.02	22.81 ± 3.13	3.23 ± 0.29	0.94 ± 0.01	987 ± 220

Mean ± confidence interval (95%) values for solution processed (n=6), laser cleaned (n=3), and laser hyperpassivated (n=3) specimens.

On the high frequency end the solution resistance showed no nominal differences as is anticipated with the same electrolyte being used for all measurements. The differences come on the low-frequency end, R_p, where the values for the TCP coated laser hyperpassivated specimens showed an elevated polarization resistance to the TCP coated solution processed controls. The higher polarization resistance is indicative of enhanced corrosion resistance which was seen in the accelerated degradation testing below. The values for the TCP coated

solution processed control are in good agreement with previously reported results for TCP coated AA2024-T3.[20, 24] The values for the laser processed specimens without the TCP coating are reported elsewhere,[5] but they showed no statistical difference for the laser cleaned specimens pre and post-TCP coating but there was a statistical difference for the laser hyperpassivated specimens. The hyperpassivated specimens showed a larger resistance to corrosion without the TCP coating present as is indicated by the larger R_p values for the specimens without the TCP coating (R_p= 6110 kΩ-cm^2).[5]

Accelerated Degradation Testing of the TCP Coated Specimens

Optical profilometry was used to generate contour plots of the surface texture enabling quantification of roughness, lay, and feature height for the specimens before and after accelerated degradation testing. Representative profiles for the three surface pretreated specimen types, with and without a TCP coating, are shown in Figure 6.5. The rolling grooves are distinguishable across the surface of both the (A) solution processed and (C) laser cleaned specimens. The lay of these is in the vertical direction. The periodicity of the features is similar for these two specimens and feature heights are 4-5 μm for both. The (E) laser hyperpassivated specimen has a much different surface texture. The surface consists of irregularly distributed; elongated features consistent with the wavy texture seen in the optical micrograph (Fig. 5.9C). The length of some of these features is *ca.* 100 μm. The height of these features is 8-10 μm. Clearly, the laser hyperpassivation with a higher pulse laser fluence produces changes in the surface texture of this alloy, more so than does the laser cleaning as there is greater near-surface heating during the hyperpassivation treatment. The greater heating leads to the flow of some of the near surface metal atoms and the growth of a thicker oxide layer as the pretreatment was performed in the ambient air.

The solution processed and laser treated specimens with a TCP coating are presented as (B) TCP-coated solution processed, (D) TCP-coated laser cleaned, and (F) TCP-coated laser hyperpassivated. The application of the TCP coating did not alter the surface texture of the specimens by much if at all. The TCP coating thickness has previously been reported to be between 100-300 nm and thus should not have much of an effect on the feature shapes or heights in the optical images.[15-17, 19, 20, 22, 23, 25, 26]

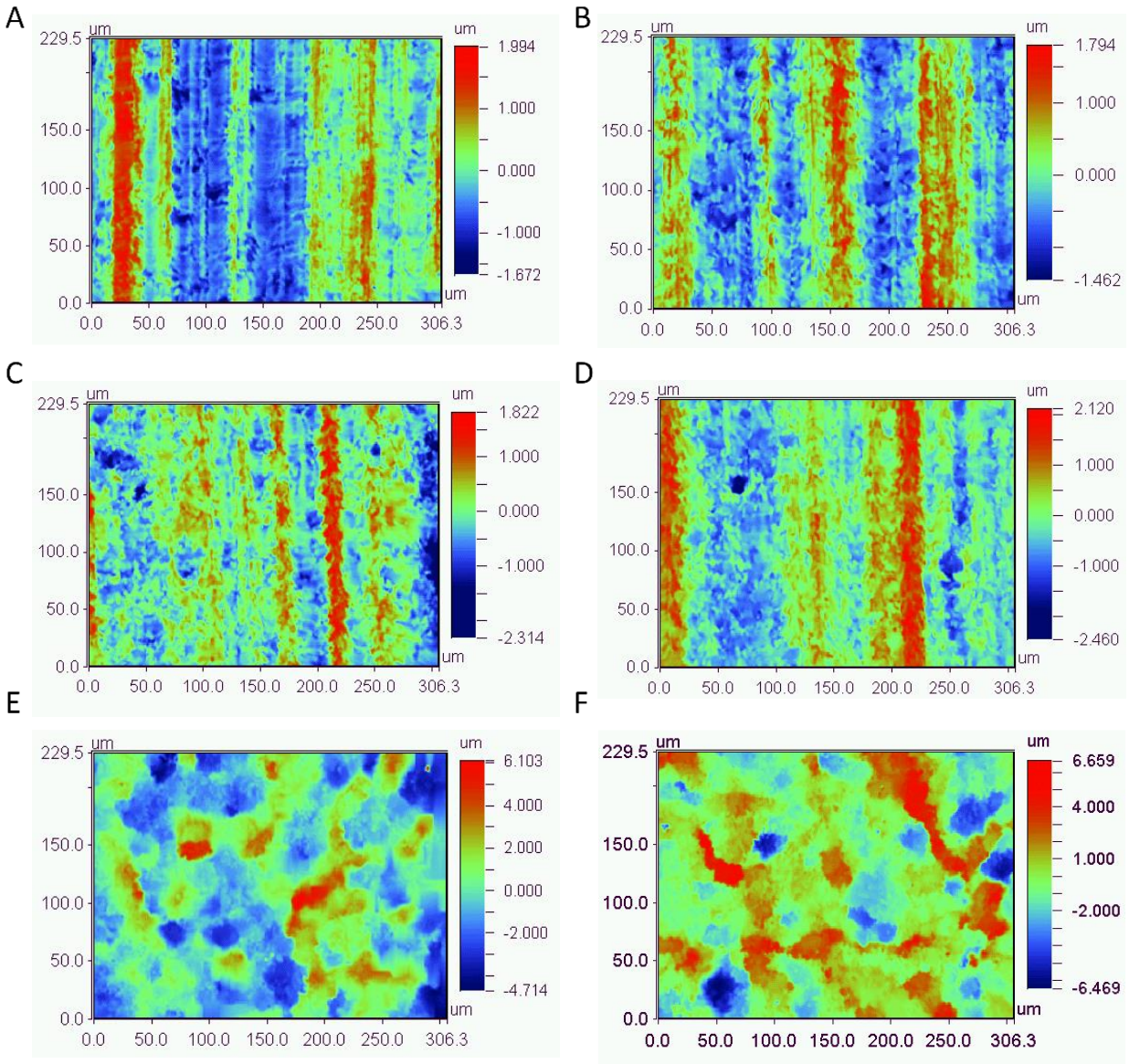

Figure 6.5. Contour plots of optical profilometry data before neutral salt spray exposure for AA2024-T3 specimens (A) solution processed, (B) solution processed and TCP-coated, (C) laser cleaned (5.2 J/cm^2), (D) laser cleaned and TCP coated, (E) laser hyperpassivated (10.8 J/cm^2), and (F) laser hyperpassivated and TCP coated. All plots are 300 x 230 μm^2 in dimension. The z-axis scales are different in each of the plots. The lay of the rolling grooves is from top to bottom in A-D. Maximum feature heights for the solution processed and laser cleaned specimens are 4-5 μm. In contrast, maximum feature heights for the laser hyperpassivated specimen are 10-12 μm.

Table 6.4 below summarizes the surface roughness (R_q) and feature height (R_z) data for the three surface pretreated specimen types, with and without a TCP coating, before and after neutral salt spray exposure. R_q and R_z values for before exposure for the laser cleaned specimens are statistically similar to the values for the solution processed ones. This indicates

the laser conditions used for cleaning produce no major changes in surface texture (roughness, lay, or waviness). There is, however, a statistically significant increase in the roughness and feature height of the laser hyperpassivated specimens, as compared to the solution processed controls. The TCP coating had little to no effect on the surface roughness or feature heights of any of the three pretreated specimens.

Representative contour plots for the three specimen types, with and without TCP coating, after neutral salt spray exposure are shown in Figure 6.6. The rolling grooves are still distinguishable across the surface of both the (A) solution processed and (C) laser cleaned specimens. The lay of these is in the horizontal direction. Across the specimen surfaces with no TCP coating (A, C, E), pits (dark blue spots) can be found. There was extensive pitting observed on the solution processed specimen after just 1 day of salt spray exposure (A). After the same exposure time, some minor pitting initiated on both the laser cleaned (C) and hyperpassivated specimens (E). The corrosion damage to all three specimen types would have been much more severe with longer exposure time. In contrast, the pretreated specimens coated with TCP remained in the salt spray for 10 days before being pulled for characterization. The TCP coated solution processed specimens showed pitting across the surface of each specimen and that caused the roughness of the surface to increase and the feature heights to increase as well after the 10-day exposure. There was much more damage found on the TCP coated solution processed specimens than the other TCP coated specimens. The TCP coated laser cleaned specimens did show some pits across the surface, but the pit depths were not as deep as those for the TCP coated solution processed. There was no to little pitting found on the TCP coated laser hyperpassivated specimens. The hyperpassivated specimen after TCP coating

provided the best corrosion protection to the underlying alloy out of the 6 specimen types exposed to the salt spray.

It should be noted here that the test chamber did experience a loss of solution due to a broken tube that caused the specimens to be in the heated chamber with no salt fog, but with salt then precipitating out on the surface of these specimens. This may have caused some extra pitting on the surface to occur as the salt fog was not continuously produced, but the specimens were still in the chamber where the temperature was elevated. This work should be repeated to ensure that the data found is true, however, it is anticipated that the laser hyperpassivated and TCP coated specimen would still provide the best corrosion protection as it did provide the extra protection in this more aggressive atmosphere.

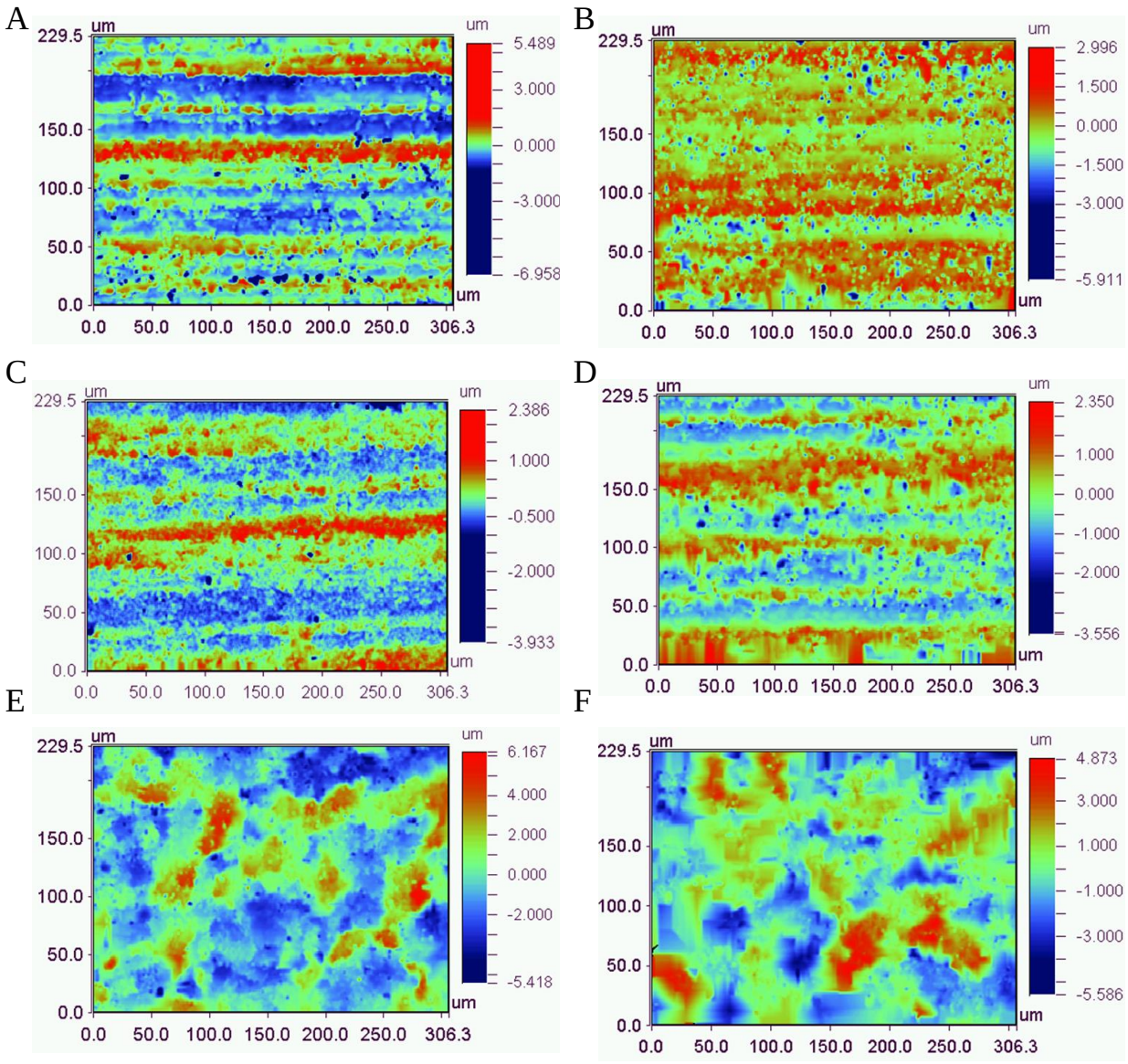

Figure 6.6. Contour plots of optical profilometry data after neutral salt spray exposure for AA2024-T3 specimens (A) solution processed, (B) solution processed and TCP coated, (C) laser cleaned (5.2 J/cm^2), (D) laser cleaned and TCP coated, (E) laser hyperpassivated (10.8 J/cm^2), and (F) laser hyperpassivated and TCP coated. All plots are 300 x 230 µm^2 in dimension. The z-axis scales are different in each of the contour plots. Maximum feature heights for the solution processed specimens are 7-11 µm giving an increase 3-6 µm. In contrast, maximum feature heights for the laser hyperpassivated specimen are 9-12 µm showing little change from before exposure. Specimens A, C, and E were all exposed to the neutral salt spray for just 1 day, while the specimens in B, D, and F were exposed for 10 days.

Table 6.4 summarizes the surface roughness (R_q) and feature height (R_z) data for the three specimen types both with and without TCP coating before and after neutral salt spray exposure. The values for after exposure the uncoated solution processed specimens showed that the while

the surface roughness was not statistically different at 95% confidence when compared to the data from before the test, the feature heights are statistically increased after exposure. This indicates that the pitting is deep into the alloy, but there was not any corrosion product buildup on the surface to increase the roughness. The same result was found for the uncoated laser cleaned specimen after the 1 day of exposure to the salt spray. The extent of the penetration of the pits on the uncoated laser cleaned specimen are not as deep as those found for the uncoated solution processed, so some slight protection was afforded by the laser cleaning process to the surface. The laser hyperpassivated specimen showed no statistical differences in the roughness or feature height after the exposure. The less defective and more compact oxide that is present after the laser hyperpassivation has provided extra protection to the underlying alloy.[5] The protection is far greater for the uncoated laser hyperpassivated specimen and even though there are some pits beginning to form, they do not penetrate deep into the specimen.

The TCP coated solution processed control showed a statistical difference in the feature height due to the deep penetrating pits found across the surface. The TCP coating broke down after the 10-day exposure and pitting began causing the increase in feature heights. The roughness was increased, but not statistically because there was no corrosion product buildup along the surface. The TCP coated laser cleaned specimens also showed similar results to the TCP coated solution processed specimen. The pitting was not as deep on the TCP laser cleaned specimens. The oxide that was present after the laser cleaning was not as defective as the natural oxide that forms from solution processes and this slightly less defective oxide provided added protection to the underlying alloy that was not provided by the solution processing.[5] The TCP did break down though on the laser cleaned specimen and the pitting did form across the surface of the specimens. The TCP coated laser hyperpassivated specimens did not show this

same trend. In fact, the TCP coated laser hyperpassivated specimens did not show an increase in feature height or roughness and few to no pits were visible across the surface of the specimens. Taken together the laser hyperpassivation to the surface does provide extra protection through the thicker and less defective oxide that forms after the laser treatment, and with the application of the TCP coating further protection was provided to the underlying alloy.

Table 6.4. Surface Texture Data Obtained from Contour Plots of Optical Profilometry Data for the Solution Processed, Laser Cleaned, and Laser Hyperpassivated Specimens With and Without TCP Coating for Before and After Neutral Salt Spray Exposure

	Solution Processed (μm)	Laser Cleaned (μm)	Laser Hyperpassivated (μm)	TCP Solution Processed (μm)	TCP Laser Cleaned (μm)	TCP Laser Hyperpassivated (μm)
R_q Roughness Before	0.54 ± 0.08	0.56 ± 0.09	1.47 ± 0.08*	0.62 ± 0.10	0.71 ± 0.12	1.67 ± 0.11*
R_z Height Before	3.43 ± 0.31	3.87 ± 0.74	9.20 ± 0.44*	3.37 ± 0.28	4.09 ± 0.37*	10.26 ± 0.69*
R_q Roughness After	0.66 ± 0.06	0.75 ± 0.20	1.62 ± 0.16	0.76 ± 0.04	0.69 ± 0.07	1.54 ± 0.08
R_z Height After	8.88 ± 1.96*	6.72 ± 1.89*	9.98 ± 0.68	7.08 ± 0.31*	5.15 ± 0.55*	9.73 ± 0.62

Mean ± confidence interval (95%) values for n=5 measurements across a single specimen of each type. Roughness values were determined over 300 x 230 μm^2 area on each specimen type at a 20x magnification. *Statistically significant difference determined, relative to the before exposure data found in Table 6.5, using a one-tailed Student's t-test at the 95% confidence interval.

Digital optical microscopy was used to characterize the specimens before and after the salt spray exposure. Figure 6.7 shows digital optical micrographs of representative (A) solution processed, (B) TCP coated solution processed, (C) laser cleaned, (D) TCP coated laser cleaned, (E) laser hyperpassivated, and (F) TCP coated laser hyperpassivated AA2024-T3 surfaces before neutral salt spray exposure. The surfaces for the solution processed and laser cleaned

specimens showed the rolling grooves as was previously reported, and the laser hyperpassivated exhibited the ripples along the surface that were previously reported as well.[5] Prior to the salt spray exposure there was no visible pitting or discolorations present along the surface for any of the specimens. These images were then compared to the surfaces after exposure. Digital optical micrographs in Figure 6.8 show the surfaces after exposure to the neutral salt spray. After the exposure time the specimens that were solution processed showed many pits along the surface that were visible to the naked eye. The TCP coated solution processed specimens also showed some pitting and some discoloration when compared to the specimen prior to exposure.

The laser cleaned specimen in Figure 6.8 C shows some minor discoloration and some pitting across the surface. The TCP coated laser cleaned specimen also showed some discoloration and some pitting along the surface. The uncoated laser hyperpassivated specimens showed no statistical differences in feature height or roughness as reported above and the uncoated specimen in Figure 6.8 E shows only some slight discoloration and minor pitting. The TCP coated laser hyperpassivated specimen shows no discoloration or pitting to the naked eye and when quantitatively assessed there was no statistical difference found for the surface roughness or feature heights. Taken together the optical profilometry and the digital optical microscopy indicate that the TCP coated laser hyperpassivated specimens provide the most protection to the underlying substrate when compared to all other specimen types investigated in this work.

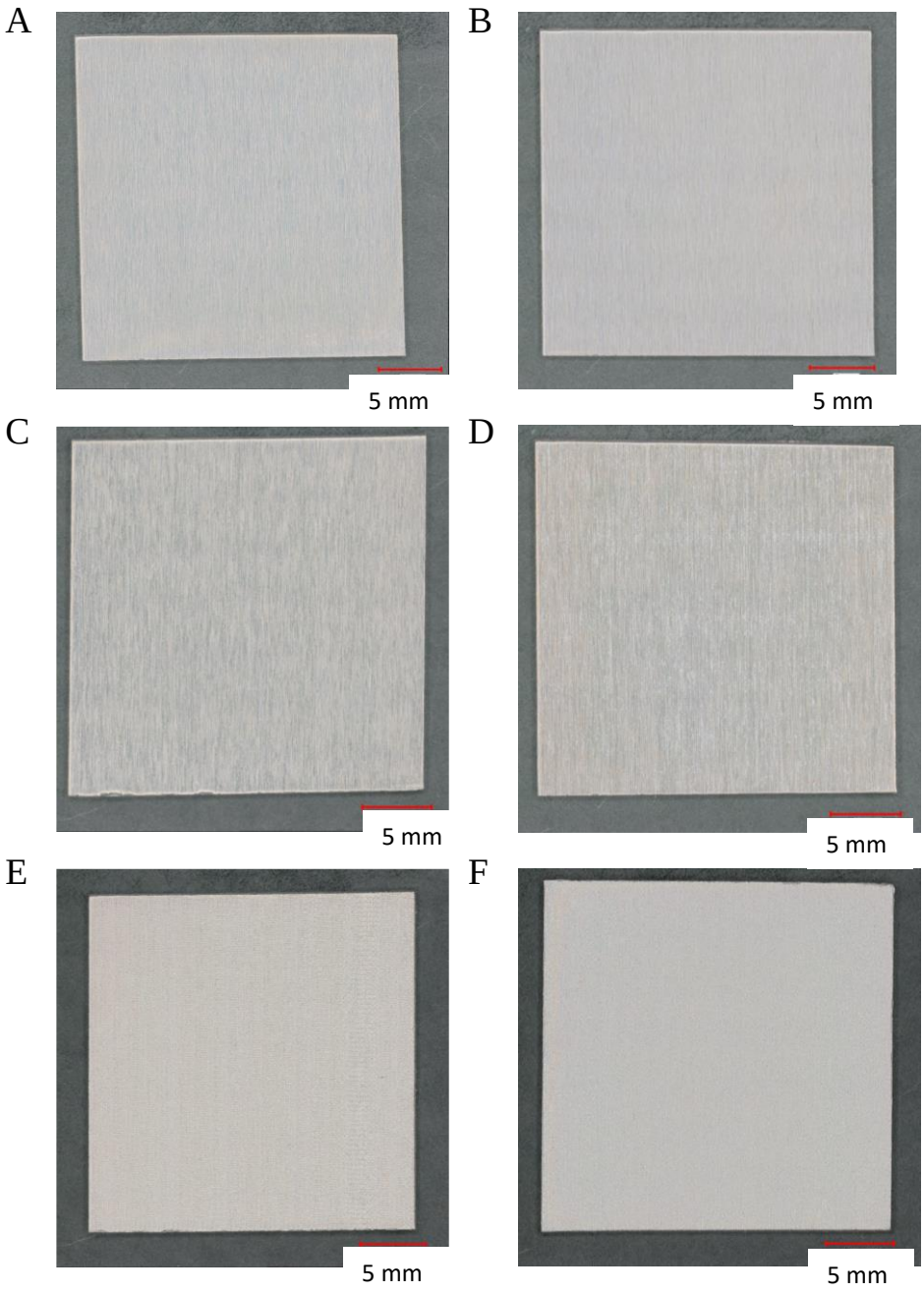

Figure 6.7. Digital optical micrographs from before neutral salt spray exposure of (A) solution processed, (B) TCP coated solution processed, (C) laser cleaned specimens (5.2 J/cm^2), (D) TCP coated laser cleaned, (E) laser hyperpassivated specimen (10.8 J/cm^2), and (F) TCP coated laser hyperpassivated AA2024-T3 specimens. The magnification for all the micrographs was the same, 50x.

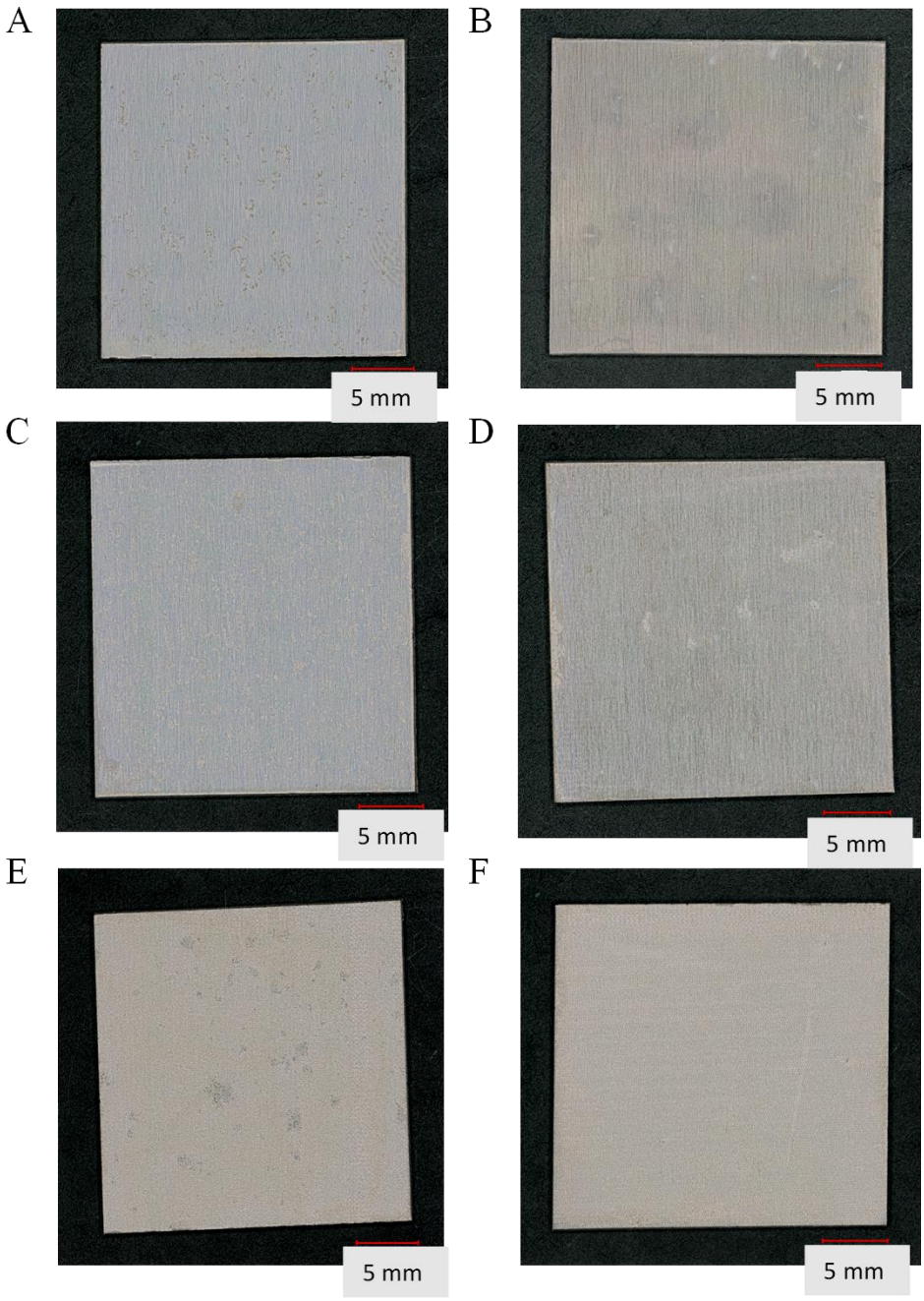

Figure 6.8. Digital optical micrographs from after neutral salt spray exposure of (A) solution processed, (B) TCP coated solution processed, (C) laser cleaned specimens (5.2 J/cm^2), (D) TCP coated laser cleaned, (E) laser hyperpassivated specimen (10.8 J/cm^2), and (F) TCP coated laser hyperpassivated AA2024-T3 specimens. Specimens A, C, and E were all exposed to neutral salt spray testing for 1 day, while the specimens in B, D, and F were exposed for 10 days to the neutral salt spray. The magnification for all the micrographs was the same, 50x.

Table 6.5. Weight Percent Change After Neutral Salt Spray Exposure

Solution Processed	Laser Cleaned	Laser Hyperpassivated	TCP Coated Solution Processed	TCP Coated Laser Cleaned	TCP Coated Laser Hyperpassivated
0.26 ± 0.01	0.22 ± 0.01*	0.17 ± 0.02*	0.14 ± 0.01	0.17 ± 0.01*	0.13 ± 0.01

Mean ± confidence interval (95%) values for n=3 for all specimen types. Uncoated specimens had exposure time of 1 day and the TCP coated specimens had an exposure time of 10 days. *Significant difference ($p \leq 0.05$) from solution processed specimens, assessed with One-tailed Students t-Test. TCP coated and laser treated specimens were compared to the solution processed and TCP coated specimen while the laser treated specimens without the TCP coating were compared to the solution processed specimen without TCP coating.

Mass loss data in Table 6.5 show the TCP sealants had a reduction in the mass loss after neutral salt spray exposure. The TCP coated laser cleaned specimens did show a statistically larger mass loss than the solution processed control, but the loss was decreased from the uncoated laser cleaned specimen which indicates the TCP does provide protection for the laser cleaned specimens. The TCP coated laser hyperpassivated specimens also showed improvement from the uncoated specimens in having a reduced mass loss, and the TCP coated laser hyperpassivated specimens were not statistically different from the TCP coated solution processed control. The laser treatments were shown to decrease the mass loss for the AA2024-T3 alloy for the uncoated specimens as well when compared to the solution processed controls. The less defective oxides that are slightly thicker than the native oxide provide that added protection to the substrate to help reduce the mass loss during the accelerated degradation tests.

Scanning electron microscopy coupled with energy dispersive X-ray spectroscopy was used to examine the surface morphology on a smaller length scale and to investigate the formation of the TCP coating on the surface of the laser treated specimens. Figure 6.9 shows a representative electron micrograph and EDX maps along the surface of the TCP coated laser cleaned specimen. The micrograph shows the formation of TCP precipitates along the surface

of the laser cleaned specimen and the EDX maps show that F, Cr, and Zr are all present across the surface. The TCP coating formed across the entire surface as has been previously reported on AA2024-T3.[20, 22, 25, 29-31]

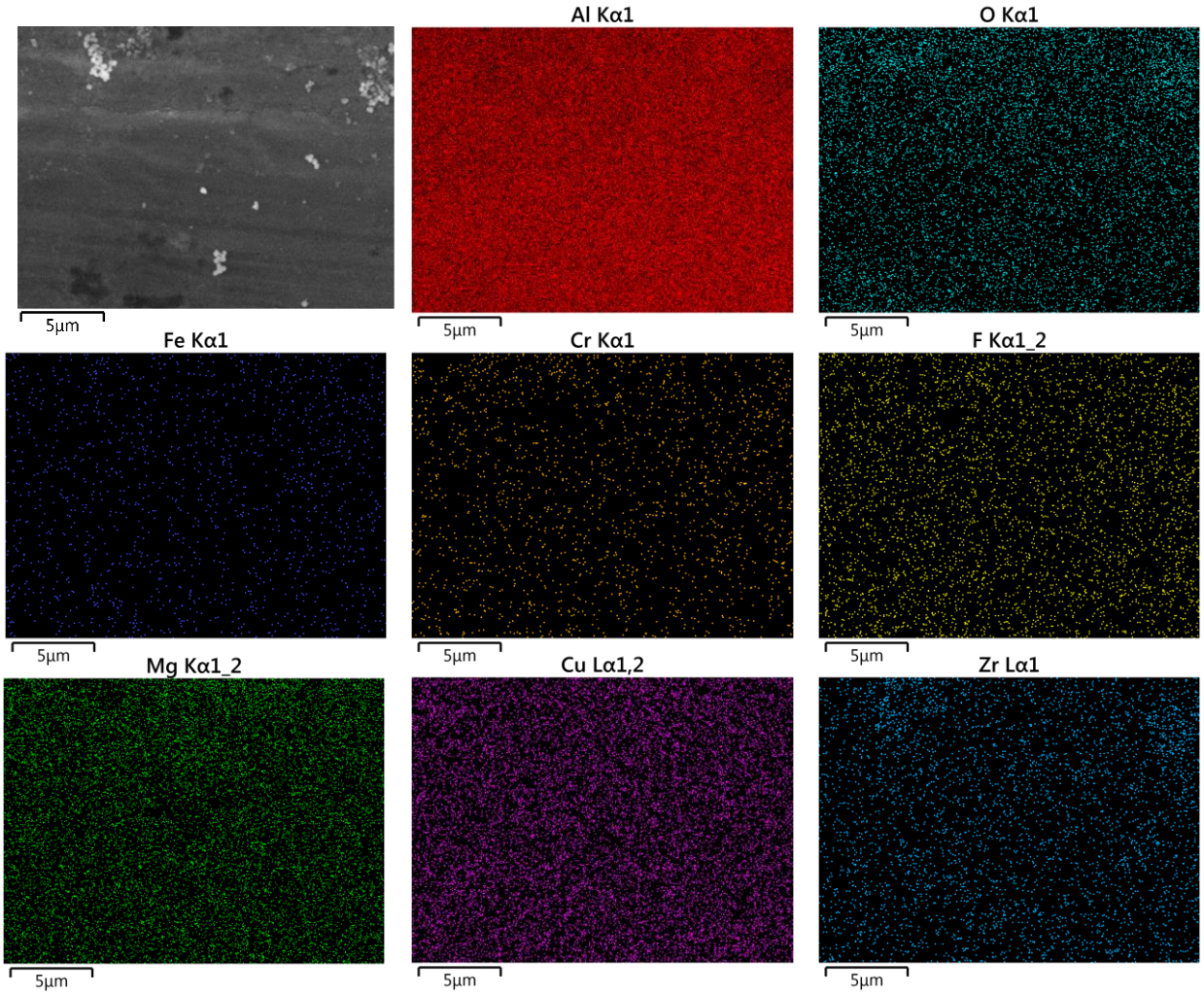

Figure 6.9. SEM micrographs of representative TCP coated laser cleaned (5.2 J/cm^2) Secondary electron micrograph and EDX maps are presented. Bright spots in the EDX maps indicate the presence of that element across the surface. All micrographs were recorded at a 500x magnification.

SEM micrograph and EDX maps are presented in Figure 6.10 for the TCP coated laser hyperpassivated specimen. The specimen shows the ripples that were previously reported along with the TCP components in the EDX maps across the surface. The only areas that the TCP coating elements were not found are in the deep crevices between the ripples. On the right

side of the ripples running through the micrographs there is evidence of mud cracking that is found when the specimen has been placed under high vacuum in the SEM. This has been previously reported on and does not mean that there is a break in the TCP coating under standard conditions.[17, 23, 32-34] In summary the TCP coating forms well across the surface for the laser cleaned and hyperpassivated specimens with only a few voids present along the surface of the hyperpassivated specimens where the ripples are present due to the localized melting and cooling caused during the laser processing.

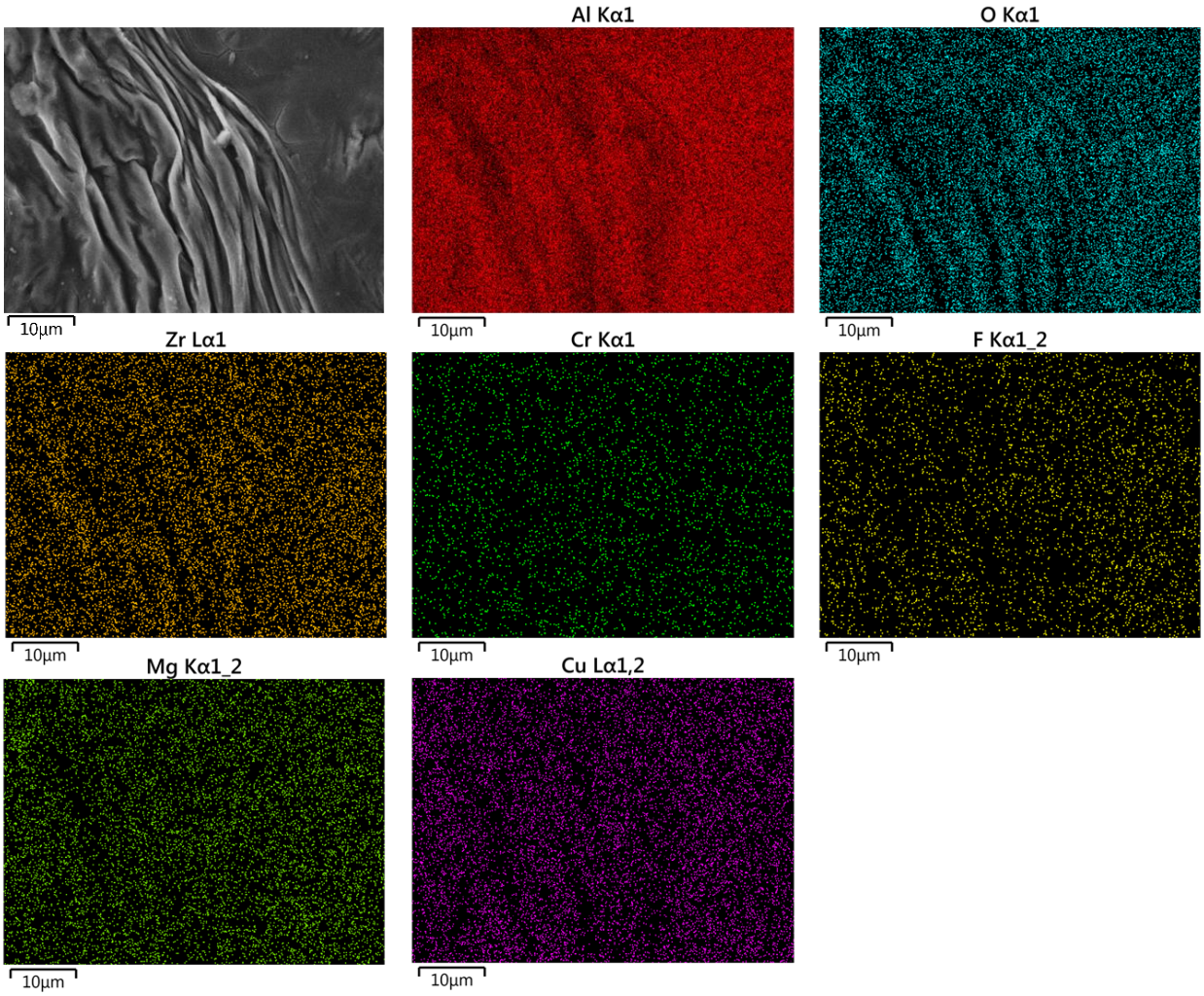

Figure 6.10. SEM micrographs of representative TCP coated laser cleaned (5.2 J/cm^2) Secondary electron micrograph and EDX maps are presented. Bright spots in the EDX maps indicate the presence of that element across the surface. All micrographs were recorded at a 1,000x magnification.

Figure 6.11 shows representative electron micrographs of TCP coated (A) solution processed, (B) laser cleaned, and (C) laser hyperpassivated specimens for specimens after 10-days of exposure to neutral salt spray. Both secondary electron and backscattered electron micrographs are presented. Bright spots in the backscattered electron micrographs reveal the location of second-phase particles exposed at the surface that consist of elements higher in atomic number than Al. The dark spots in the backscattered electron micrographs, also visible in the secondary electron micrographs, are the presence of pits along the surface. The electron micrographs reveal, consistent with the digital microscopy and optical profilometry data, that the TCP coated specimens that are solution processed and laser cleaned both have pitting along the surface, but with minimal other damage seen and no corrosion product buildup was found along the surfaces. Discoloration is not able to be investigated with the SEM but was found in the digital optical microscopy for both TCP coated specimen types. The TCP coated laser hyperpassivated specimen showed no changes along the surface after the exposure to the neutral salt spray for 10 days. The TCP coating provided excellent corrosion protection in the accelerated degradation test and provided the greatest protection to the underlying substrate.

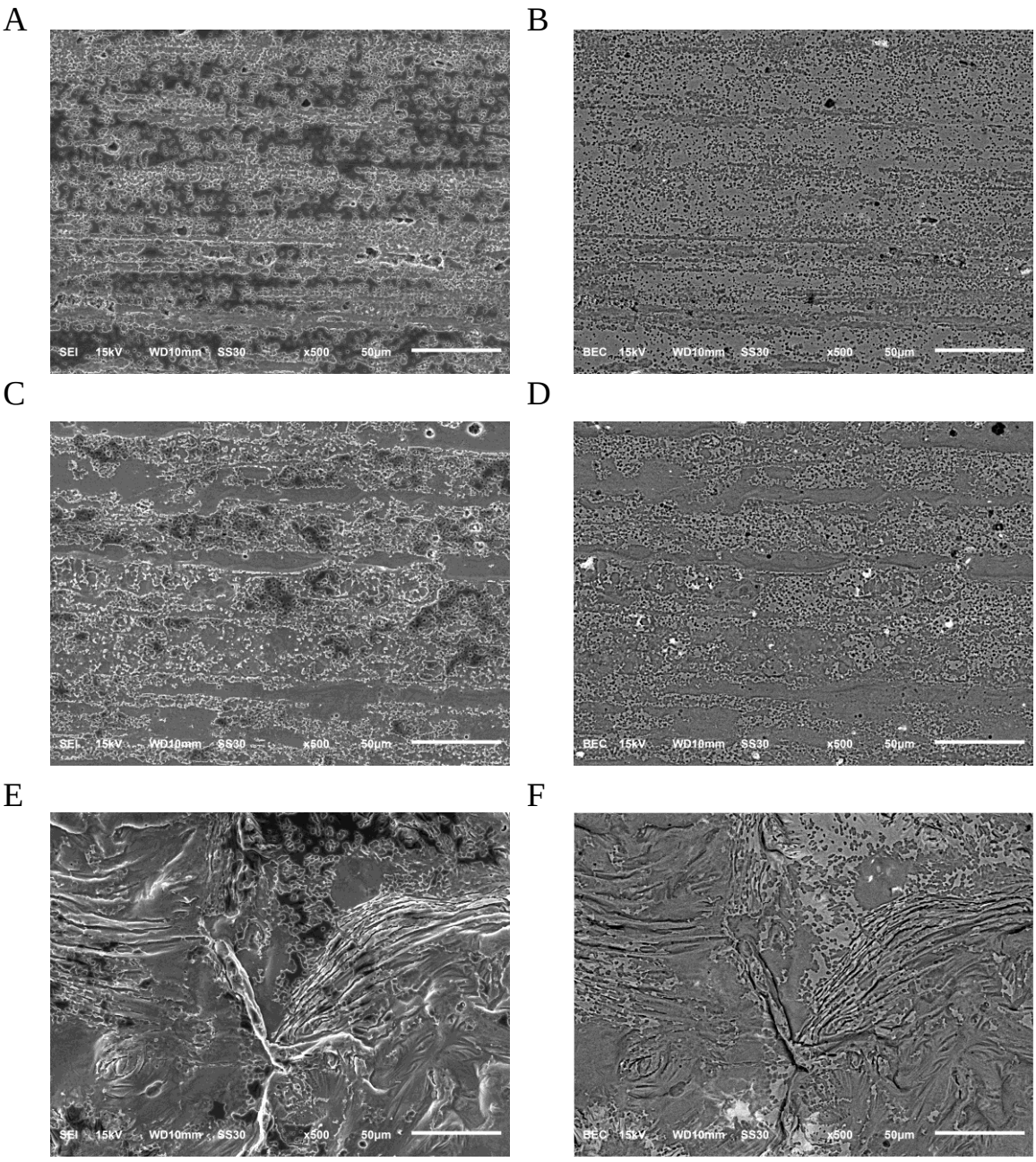

Figure 6.11. SEM micrographs of representative TCP coated (A, B) solution processed, (C, D) laser cleaned (5.2 J/cm^2), and (E, F) laser hyperpassivated (10.8 J/cm^2) specimens after 10 days of neutral salt spray exposure. Secondary electron (left) and backscattered electron (right) micrographs are presented. Bright spots in the backscattered electron micrographs indicate second-phase particles at the surface. All micrographs were recorded at a 500x magnification.

In summary, the accelerated degradation testing on the specimens that were uncoated showed damage after 1 day of exposure for the solution processed and the laser cleaned specimens. The laser hyperpassivated specimens did not show much damage to the surface

through pitting, corrosion product buildup, or discoloration. The surface features of the thicker and less defective oxide provide added protection to the underlying substrate. The TCP coated specimens, much like the uncoated specimens, showed that after 10 days of exposure the solution processed, and laser cleaned specimens both had some minor pitting present along the surface and some discoloration. The TCP coated laser hyperpassivated specimens did not show this same pitting or discoloration along the surface and, in fact, provided the greatest protection to the underlying substrate out of all types of specimens investigated.

Accelerated Degradation Testing of TCP Coated and Primed Specimens

As parts are not put into service as the bare alloy, the layered coating system was tested for adhesion and corrosion damage on the TCP coated solution processed and laser treated specimens after applying a chrome-free epoxy primer. The primer was applied to the front surface and was scribed with an "X" to initiate damage and to investigate undercutting of the primer layer and adhesion of the TCP and the primer to the substrate after laser treatment. Figure 6.12 shows the TCP coated and primed specimens before and after the 14-day neutral salt spray exposure. In Figure 6.12 the solution processed specimens in A and B show that prior to the test there was the scribe with no damage inside the scribe and after the salt spray exposure there is discoloration inside the scribe and some minor damage where the scribe was place, but there was no scribe widening or undercutting detected with digital optical microscopy. The primer adhered to the TCP coating well and did not peal up and away around the scribe and thus left the surface protected where there was primer present. The TCP coated and primed laser cleaned specimen in C and D also show there was no scribe widening or undercutting. Undercutting is usually evidenced with the visualization of blistering away from the scribe in the primer or with the primer layer being taller after the exposure when compared

to prior to exposure. This was not found for the laser cleaned or laser hyperpassivated specimens.

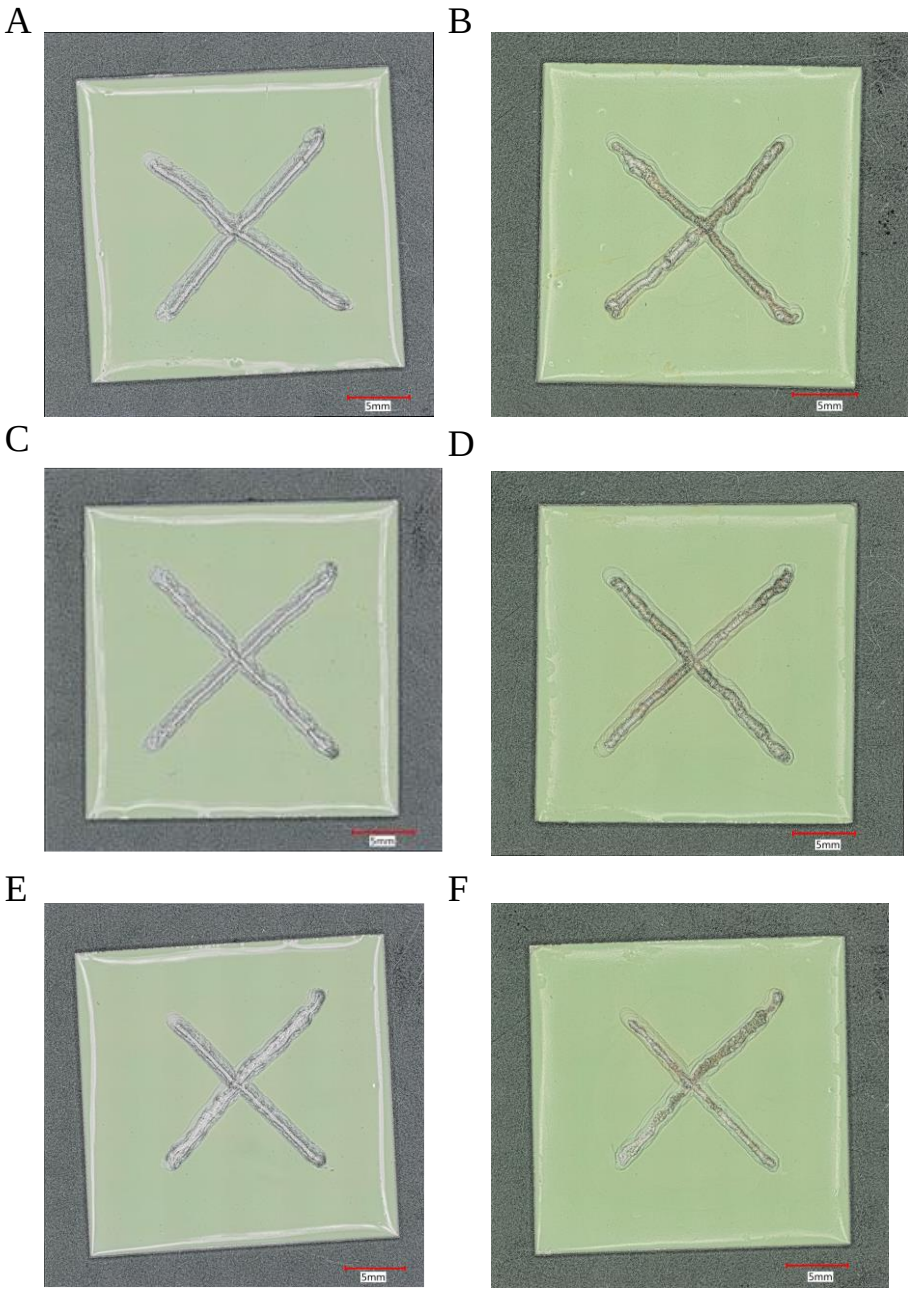

Figure 6.12. Digital optical micrographs from before and after 14-day neutral salt spray exposure of TCP coated and primed (A) solution processed before exposure, (B) solution processed after exposure, (C) laser cleaned specimens before exposure(5.2 J/cm^2), (D) laser cleaned after exposure, (E) laser hyperpassivated before exposure (10.8 J/cm^2), and (F) laser hyperpassivated after exposure AA2024-T3 specimens. The magnification for all the micrographs was the same, 50x.

Using the ASTM-D3359 the specimens that were primed were subjected to adhesion testing through the tape test. The specimens were cut according to the standards method to the substrate and then the tape was applied. Following the methods directions, the tape was removed within 90 s after being applied and then the grids were inspected for primer. If primer was present on the tape, it was scaled using the ASTM-D3359 griding system to give relative percentages of the deadhesion of the primer from the substrate. The tape being see through is not presented here but the results were as follows. For the TCP coated solution processed specimens on average 5% of the primer was removed via the tape, the TCP coated laser cleaned saw on average 2-3%, and the TCP coated laser hyperpassivated specimens were also 2-3%. Both the laser cleaned and hyperpassivated specimens showed great adhesion of the primer to the TCP coating and substrate. In summary, the application of further layers to the laser cleaned and laser hyperpassivated surfaces will result in excellent adhesion of the added layers and provide excellent corrosion protection.

6.5 DISCUSSION

The data reveal that both the laser cleaned and laser hyperpassivated specimens after TCP coating provide improved corrosion resistance of AA2024-T3, with the TCP coated laser hyperpassivated specimens providing excellent corrosion resistance more so than pretreatment by traditional solution processing. The electrochemical numerical parameters showed that the laser cleaned specimens were similar to the solution processed specimens after the application of the TCP coating with no statistical differences found except for the OCP. The low frequency impedance, $Z_{0.01\,Hz,}$ and the current densities at larger overpotentials in the anodic and cathodic direction from the OCP for the TCP coated laser cleaned showed no difference from the TCP coated solution processed controls but did show a marked improvement in corrosion resistance

when compared to the uncoated laser cleaned specimens. The TCP coated laser hyperpassivated specimens did on average show improvements in the corrosion resistance when compared to the TCP coated solution processed controls with an increase in the $Z_{0.01\ Hz}$ and decrease in the total current seen at -0.7 V and at 0.1 V. These differences were not statistically different but did show that the TCP coating on the laser hyperpassivated specimens would provide an added benefit to the specimen for corrosion resistance.

Taken together, these data indicate that the rate of diffusion-limited oxygen reduction on this alloy is lower for the laser cleaned and solution processed specimens after TCP coating as compared to the uncoated controls. This is attributed for the laser cleaned specimens to some surface melting and cooling of the aluminum matrix around second-phase particles that reduces their exposed area on the alloy surface, as these sites are the most active kinetically for the oxygen reduction reaction.[26-28] Additionally, aluminum oxide (Al_2O_3) reformation will occur around and over the second-phase particle at the end of the laser pulse. Given the brief elevated temperature of the surface at the end of a laser pulse, a thicker oxide layer is expected to reform, and this passivation layer could serve to inhibit oxygen reduction. The TCP coating also forms better along the aluminum surface and provides another barrier layer of protection with little defects in the coating that formed. For the solution processed specimens, the TCP acts as this barrier layer and protects the underlying substrate by covering the exposed particles as it also does for the laser cleaned specimens.

The laser hyperpassivated specimens do not show this same protection after TCP coating as it is likely that the TCP coating cannot form a defect free barrier layer with the highly roughened surface produced after hyperpassivation. The oxide that had originally formed after laser hyperpassivation was thicker and less defective than the native oxide found for the

solution processed specimen. The TCP coating first etches the oxide with the fluoride attack and then forms the fluoride and zirconium/chromium layers as described elsewhere. This etching was likely to be incomplete on the laser hyperpassivated specimens leaving a more defective oxide behind and a TCP coating that had not fully formed along the entire surface. This along with the increased surface roughness caused by the ripples previously reported cause the TCP to fully protect the underlying substrate and increase the kinetics for the diffusion-limited oxygen reduction reaction to take place. The increase is not large from before TCP coating, but the coating leaving the slightly defective oxide would suggest slightly reduced corrosion resistance.

The TCP coating was found to form well over both the laser cleaned and hyperpassivated specimens with the hyperpassivated specimens only showing any defects in the coating formation along the ripples formed from the local melting and cooling processes during the lasering of the surface. The TCP was found to cover the Cu-containing second phase particles and because of this the current in the cathodic direction was reduced. The reasoning behind this is the Cu-containing particles act as active sites for the oxygen reduction reaction and with those being blocked by the TCP coating the reaction kinetics would then be reduced.[35-38] The defects that were found in the area of the ripples was anticipated as there was some indications in the potentiodynamic polarization curves that the coating may not have been defect free. As the ripples are fairly steep and cause an increased roughness to the surface the TCP is not able to form a fully defect free layer like is able to on the laser cleaned specimens. It has been shown in the past that the defect walls are not able to be properly coated with the TCP[20, 25, 29, 30] and thus leaves the walls of the ripples exposed for the electrolyte to contact.

The incomplete coating formation does not result in a large current as it was previously shown that the laser hyperpassivated specimens form a thicker and more compact oxide layer with few defects after the lasering of the surface.[5] With this and the localized melting and cooling of the aluminum matrix the Cu-containing second phase particles are blocked which reduces the Cu presence on the surface. With the fewer sites the kinetics for the oxygen reduction reaction are reduced and the specimens will have improved corrosion resistance.

The specimens were subjected to accelerated degradation testing via neutral salt spray to investigate the inherent corrosion resistance of the uncoated specimens and then to see what, if any, improvements are made with the addition of the TCP coating to the surfaces. The uncoated specimens for the solution processed and laser cleaned both showed large amounts of pits forming on the surface after just 1 day of exposure, with the deepest pits found on the solution processed specimens. The laser hyperpassivated specimen did not show such extensive pitting across the surface, and when compared to before the test there was not a statistical difference in the surface roughness or feature heights.

The addition of the TCP coating to the specimens was done and they were exposed for 10 days to the neutral salt spray test. After the 10 days the solution processed and laser cleaned specimens again saw pitting across the surface, with the most damage seen on the solution processed specimens. They both showed statistical differences in the feature height after the exposure due to the depths of the pits. The TCP coated laser hyperpassivated specimens did not show this change in feature height as again it outperformed the other two types investigated in this work. The specimens did not show any discoloration or corrosion product buildup and no pits were detectable by the naked eye or in the imaging.

Adhesion of a primer layer to the TCP coating and the laser cleaned and hyperpassivated specimens was investigated through the use of tape test adhesion testing. The laser cleaned and hyperpassivated specimens each showed around 2-3% primer removal after 14-day neutral salt spray exposure. This is reduced from the ~5% for the solution processed specimens and is excellent for the application of the layered coating system employed by the aerospace industry. In total, the laser cleaned specimens did show improvement after TCP coating, but the laser hyperpassivated specimens in all areas showed marked improvement in corrosion resistance/protection and would be a viable alternative to use to the solution processing methods.

6.6 CONCLUSIONS

The results reported herein show how TCP coating of laser cleaned and hyperpassivated specimens affects the surface texture, corrosion resistance with accelerated degradation testing, and electrochemical behavior of AA2024-T3. The following are the key findings based on the data:

1) TCP coating laser cleaned specimens improves the corrosion resistance to be similar to the TCP coated solution processed controls, with slightly better results on average when looking at the currents at -0.7 V and 0.1 V.
2) Laser hyperpassivated specimens upon TCP coating do not change from the uncoated laser hyperpassivated specimens electrochemically and the TCP coating provides on average equal protection to the surface as the uncoated laser hyperpassivated specimen provides.

3) TCP coating is needed to extend the lifetime of the specimens in the accelerated degradation test. Uncoated specimens of all types lasted only 1 day in the exposure, where the TCP coated specimens were exposed for 10 days before seeing damage.
4) TCP coated laser hyperpassivated specimens provided the most corrosion protection in accelerated degradation testing by showing no signs of pitting and having no change in the surface roughness or feature heights after 10 days of neutral salt spray exposure.
5) The TCP coating adheres strongly to the laser cleaned and hyperpassivated specimens. Tape testing done on the TCP coated and primed specimens showed less than 5% primer removal for the laser treated specimens.

REFERENCES

REFERENCES

1. Xia, L.; Akiyama, E.; Frankel, G.; McCreery, R., Storage and Release of Soluble Hexavalent Chromium from Chromate Conversion Coatings: Equilibrium Aspects of Cr VI Concentration. *J. Electrochem. Soc.* **2000,** *147* (7), 2556-2562.

2. Reisch, M. S. Confronting the looming hexavalent chromium ban. https://cen.acs.org/articles/95/i9/Confronting-looming-hexavalent-chromium-ban.html (accessed March).

3. Lasagni, A.; D'Alessandria, M.; Giovanelli, R.; Mücklich, F., Advanced design of periodical architectures in bulk metals by means of Laser Interference Metallurgy. *Applied Surface Science* **2007,** *254* (4), 930-936.

4. D'Alessandria, M.; Lasagni, A.; Mucklich, F., Direct Micro-Patterning of Aluminum Substrates via Laser Interference Metallurgy. *Applied Surface Science* **2008,** *255*, 3210-3216.

5. McFall-Boegeman, S.; Yancey, D. F.; O'Neill, T.; Davidson, N.; Swain, G. M., Effect of Laser Cleaning and Hyperpassivation on the Electrochemical Behavior of AA2024-T3. *Journal of The Electrochemical Society* **2021,** *168* (3), 031501.

6. Kuo, T. Y.; Lin, H. C., Effects of pulse level of Nd-YAG laser on tensile properties and formability of laser weldments in automotive aluminum alloys. *Materials Science and Engineering: A* **2006,** *416* (1), 281-289.

7. Marczak, J.; Jach, K.; Sarzynski, A.; Ostrowski, R., Experimental and Theoretical Indications on Laser Cleaning. 2005; pp 103-111.

8. Razab, M. K. A. A.; Jaafar, M. S.; Abdullah, N. H.; Amin, M. F. M.; Mohamed, M., Influence of Elemental Compositions in Laser Cleaning for Automotive Coating Systems. *Journal of Russian Laser Research* **2016,** *37* (2), 197-206.

9. Milles, S.; Voisia, B.; Nitschke, M.; Lasagni, A. F., Influence of Roughness Achieved by Periodic Structures on the Wettability of Aluminum Using Direct Laser Writing and Direct Laser Interference Patterning Technology. *Journal of Materials Processing Tech.* **2019,** *270*, 142-151.

10. Lasagni, A.; Holzapfel, C.; Weirich, T.; Mücklich, F., Laser interference metallurgy: A new method for periodic surface microstructure design on multilayered metallic thin films. *Applied Surface Science* **2007,** *253*, 8070-8074.

11. Shamsul Baharin Ahmad, F.; Ghazali Mariyam, J.; Juyana, A. W., Laser surface texturing and its contribution to friction and wear reduction: a brief review. *Industrial Lubrication and Tribology* **2016,** *68* (1), 57-66.

12. Tam, A. C.; Leung, W. P.; Zapka, W.; Ziemlich, W., Laser-Cleaning Techniques for Removal of Surface Particulates. *Journal of Applied Physics* **1992,** *71*, 3515-3523.

13. Dieter, B. In *Perspectives of laser processing and chemistry*, Proc.SPIE, 2002.

14. Li, L.; Kim, D. Y.; Swain, G. M., Transient Formation of Chromate in Trivalent Chromium Process (TCP) Coatings on AA2024 as Probed by Raman Spectroscopy. *Journal of The Electrochemical Society* **2012,** *159* (8), C326-C333.

15. Dong, X.; Wang, P.; Argekar, S.; Schaefer, D. W., Structure and Composition of Trivalent Chromium Process (TCP) Films on Al Alloy. *Langmuir* **2010,** *26* (13), 10833-10841.

16. Munson, C. A.; Swain, G. M., Structure and chemical composition of different variants of a commercial trivalent chromium process (TCP) coating on aluminum alloy 7075-T6. *Surface and Coatings Technology* **2017,** *315*, 150-162.

17. Qi, J.; Walton, J.; Thompson, G. E.; Albu, S. P.; Carr, J., Spectroscopic Studies of Chromium VI Formed in the Trivalent Chromium Conversion Coatings on Aluminum. *Journal of The Electrochemical Society* **2016,** *163* (7), C357-C363.

18. Ely, M.; Swiatowska, J.; Seyeux, A.; Zanna, S.; Marcus, P., Role of Post-Treatment in Improved Corrosion Behavior of Trivalent Chromium Protection (TCP) Coating Deposited on Aluminum Alloy 2024-T3. *J. Electrochem. Soc.* **2017,** *164* (6), C276-C284.

19. Dardona, S.; Chen, L.; Kryzman, M.; Goberman, D.; Jaworowski, M., Polarization Controlled Kinetics and Composition of Trivalent Chromium Coatings on Aluminum. *Analytical Chemistry* **2011,** *83* (16), 6127-6131.

20. Li, L.; Doran, K. P.; Swain, G. M., Electrochemical Characterization of Trivalent Chromium Process (TCP) Coatings on Aluminum Alloys 6061 and 7075. *Journal of The Electrochemical Society* **2013,** *160* (8), C396-C401.

21. Suib, S. L.; La Scala, J.; Nickerson, W.; Fowler, A.; Zaki, N., Determination of hexavalent chromium in NAVAIR trivalent chromium process (TCP) coatings and process solutions. *Metal Finishing* **2009,** *107* (2), 28-34.

22. Munson, C. A.; McFall-Boegeman, S. A.; Swain, G. M., Cross comparison of TCP conversion coating performance on aluminum alloys during neutral salt-spray and thin-layer mist accelerated degradation testing. *Electrochimica Acta* **2018,** *282*, 171-184.

23. Guo, Y.; Frankel, G. S., Characterization of trivalent chromium process coating on AA2024-T3. *Surface and Coatings Technology* **2012,** *206* (19), 3895-3902.

24. Guo, Y.; Frankel, G. S., Active Corrosion Inhibition of AA2024-T3 by Trivalent Chrome Process Treatment. *Corrosion* **2012,** *68* (4), 045002-1-045002-10.

25. Li, L.; Swain, G. P.; Howell, A.; Woodbury, D.; Swain, G. M., The Formation, Structure, Electrochemical Properties and Stability of Trivalent Chrome Process (TCP) Coatings on AA2024. *J. Electrochem. Soc.* **2011,** *158* (9), C274-C283.

26. Dardona , S.; Jaworowski, M., In situ spectroscopic ellipsometry studies of trivalent chromium coating on aluminum. *Appl. Phys. Lett.* **2010,** *97*, 181908-1 –; 181908–3.

27. Davis, J. R.; Associates, *ASM International. Handbook Committee, Aluminum and Aluminum Alloys*. 1993.

28. Kaufman, J. G., Aluminum Alloy and Temper Designation Systems of the Aluminum Association. In *Introduction to Aluminum Alloys and Tempers*, ASM International 2000; pp 9-22.

29. Li, L.; Whitman, B. W.; Munson, C. A.; Estrada, R.; Matzdorf, C. A.; Swain, G. M., Structure and Corrosion Performance of a Non-chromium Process (NCP) Zr/Zn Pretreatment Conversion Coating on Aluminum Alloys. *J. Electrochem. Soc.* **2016,** *163* (13), C718-C728.

30. Li, L.; Swain, G. M., Effects of Aging Temperature and Time on the Corrosion Protection Provided by Trivalent Chromium Process Coatings on AA2024-T3. *Appl. Mater. Interfaces* **2013,** *5*, 7923-7930.

31. Whitman, B. W.; Li, L.; Swain, G. M., Anti-Corrosion Properties of a TCP Pretreatment Conversion Coating on Aluminum Alloy 2024-T3 during Moist SO_2 Atmospheric Testing: Effects of Galvanic Coupling. *J. Electrochem. Soc.* **2017,** *164* (4), C135-C147.

32. Arrowsmith, D. J.; Dennis, J. K.; Sliwinski, P. R., Chromate conversion coatings on aluminium: Growth of layers of spherical particles. *Transactions of the IMF* **1984,** *62* (1), 117-120.

33. Treverton, J. A.; Amor, M. P., High-resolution SEM studies of chromate conversion coatings. *Journal of Materials Science* **1988,** *23* (10), 3706-3710.

34. Laget, V.; Jeffcoate, C. S.; Isaacs, H. S.; Buchheit, R. G., Dehydration-Induced Loss of Corrosion Protection Properties in Chromate Conversion Coatings on Aluminum Alloy 2024-T3. *Journal of The Electrochemical Society* **2003,** *150* (9), B425.

35. Buchheit, R. G.; Boger, R. K.; Carroll, M. C.; Leard, R. M.; Paglia, C.; Searles, J. L., The electrochemistry of intermetallic particles and localized corrosion in Al alloys. *JOM* **2001,** *53* (7), 29-33.

36. Birbilis, N.; Buchheit, R. G., Electrochemical Characteristics of Intermetallic Phases in Aluminum Alloys. *Journal of The Electrochemical Society* **2005,** *152* (4), B140.

37. Jakab, M. A.; Little, D. A.; Scully, J. R., Experimental and Modeling Studies of the Oxygen Reduction Reaction on AA2024-T3. *J. Electrochem. Soc.* **2005,** *152* (8), B311-B320.

38. Ilevbare, G. O.; Scully, J. R., Oxygen Reduction Reaction Kinetics on Chromate Conversion Coated Al-Cu, Al-Cu-Mg, and Al-Cu-Mn-Fe Intermetallic Compounds. *Journal of The Electrochemical Society* **2001,** *148* (5), B196.

CHAPTER 7. CONCLUSIONS AND FUTURE WORK

7.1 CONCLUSIONS

Solution processes are very common to use as a pretreatment to the surface of aluminum alloys prior to use, but these chemical baths pose dangers to workers health and are very costly to dispose of. This dissertation focuses on 2 main alternatives, anodization and laser cleaning, to solution process cleaning to prepare the alloy for the next layers applied to the aluminum alloy prior to service. The other main focus of this dissertation is investigating how a Trivalent Chromium Process (TCP) coating helps to further protect the alternative cleaning/preparation methods from corrosion.

The solution processed specimens after TCP coating were exposed to neutral salt spray and then tensile strength testing was done to determine the protection that can be afforded to the alloy when galvanically coupled to a titanium screw and nut system. The damage that was seen depended on the TCP coating that was applied. The TCP coatings that were previously reported to have higher Zr/Cr ratios performed much better than those with lower ratios as the damage was minimal for higher ratios. The TCP coatings all provided protection from deep penetrations that would alter the mechanical strength as there was no statistical difference between them after the neutral salt spray exposure. This level of damage and coating protection for the solution processed specimens could then be compared to the further surface pretreatments to investigate the effectiveness of those treatments.

Anodization of the aluminum alloy helps to passivate the alloy. Two different acid baths were investigated, sulfuric acid and sulfuric acid/boric acid (SABA), to investigate the incorporation of the acid electrolyte effect on the resulting oxide layer. The sulfuric acid bath led to a linear porous oxide perpendicular to the substrate surface. This was in opposition to

the more compact oxide formed for the SABA bath. SABA produced an oxide that grew perpendicular to the substrate surface, but the oxide was more compact and was grown along the grains leaving channels only at the grain boundaries. These channels were not linear but were instead found to be tortuous in nature. Both oxides provided better corrosion protection to the alloy substrate when compared electrochemically, and after accelerated degradation testing to the solution processed specimens. The SABA bath formed and oxide coating that provided extra protection when compared to the sulfuric acid bath as the oxide was more compact and had fewer open pores for electrolyte to penetrate through.

Further protection can be given to the anodic oxide produced through anodization by sealing the resulting oxide layer. Typically, hot water or nickel acetate are used as sealants, but they are energy intensive. TCP coatings were investigated as alternatives to the common sealants to look for corrosion protection in accelerated degradation testing, improved or similar corrosion resistance, and finally the sealing mechanism by the TCP coating. The TCP as a sealant for the sulfuric acid anodized specimens showed improvements in corrosion resistance electrochemically and showed protection during accelerated degradation testing. The TCP was able to penetrate into the pores and from the barrier layer, at the oxide/substrate surface, to the top of the oxide layer the pores were sealed with the TCP. There was also a layer of TCP found as a barrier layer on top of the oxide to be around 150 nm thick. This provided excellent corrosion protection and further enhanced the corrosion resistance of the oxide further when compared to the unsealed alloy.

When applied to the SABA anodized specimen there were some slight improvements found in corrosion resistance and protection, but because the oxide grows differently the sealing processes for the TCP is different as well. The tortuous nature of the pores means that the TCP

was not able to fully reach the bottom of the oxide layer, but the region where the TCP did penetrate (~50% of the total oxide) was sealed and a 150-200 nm barrier layer was formed above the oxide. This did provide slightly better corrosion resistance, but with the oxide being the nature that it was, the oxide corrosion resistance was already very high.

The last surface pretreatment was investigating laser cleaning and hyperpassivation of the surface of the aluminum alloy. The laser cleaning did not alter the surface of the alloy in any way other than to remove some of the smaller secondary phase particles and the heat from the laser treatment helped to form a less defective oxide than that of solution processed specimens. Laser hyperpassivation provided the greatest corrosion protection by altering the surface morphology the Cu-containing secondary phase particles were buried below the remelted and cooled aluminum bulk and a thicker and less defect oxide layer was formed to further provide protection to the surface. This passivation was further improved after applying the TCP coating for the laser cleaned and hyperpassivated specimens. The TCP adhered well to the substrate and the primer that was applied also showed no delamination or undercutting.

In summary the anodizing and laser treatments would be viable alternatives to the solution processes for the pretreatment of AA2024-T3 depending on the service of the part. The TCP coating is an excellent source for added corrosion protection for both the laser treatments and the oxide sealant and improves corrosion resistance on AA2024-T3.

7.2 FUTURE WORK

Through this work AA2024-T3 was investigated as it is one of the main alloys used in the aerospace industry. However, solution processes are used for other alloys as well to pretreat the surface. The preliminary work done on AA6061-T6 and AA7075-T6 for the laser cleaning and hyperpassivation show that more information about the laser contacting those surfaces

would be needed, along with the application of the TCP coating to look for any further improvements to the other alloys. Research also needs to be conducted to understand the mechanical properties of the alloys that have been anodized or treated with the laser. The alloys are used due to the high strength to low weight ratio, and with the anodizing and the laser treatment it would be imperative to investigate the mechanical properties to ensure they would be alternatives to the solution process cleaning.